



**US Army Corps  
of Engineers**  
Waterways Experiment  
Station

Miscellaneous Paper GL-97-17  
August 1997

# Working Forum on the Manifold Method of Material Analysis, Volume I

Organized by *U.S. Army Engineer Waterways Experiment Station*

**DTIC QUALITY INSPECTED 4**

DTIC QUALITY INSPECTED 4

Approved For Public Release; Distribution Is Unlimited

19971007 032

The contents of this report are not to be used for advertising, publication, or promotional purposes. Citation of trade names does not constitute an official endorsement or approval of the use of such commercial products.

The findings of this report are not to be construed as an official Department of the Army position, unless so designated by other authorized documents.



PRINTED ON RECYCLED PAPER

Miscellaneous Paper GL-97-17  
August 1997

# **Working Forum on the Manifold Method of Material Analysis, Volume I**

U.S. Army Corps of Engineers  
Waterways Experiment Station  
3909 Halls Ferry Road  
Vicksburg, MS 39180-6199

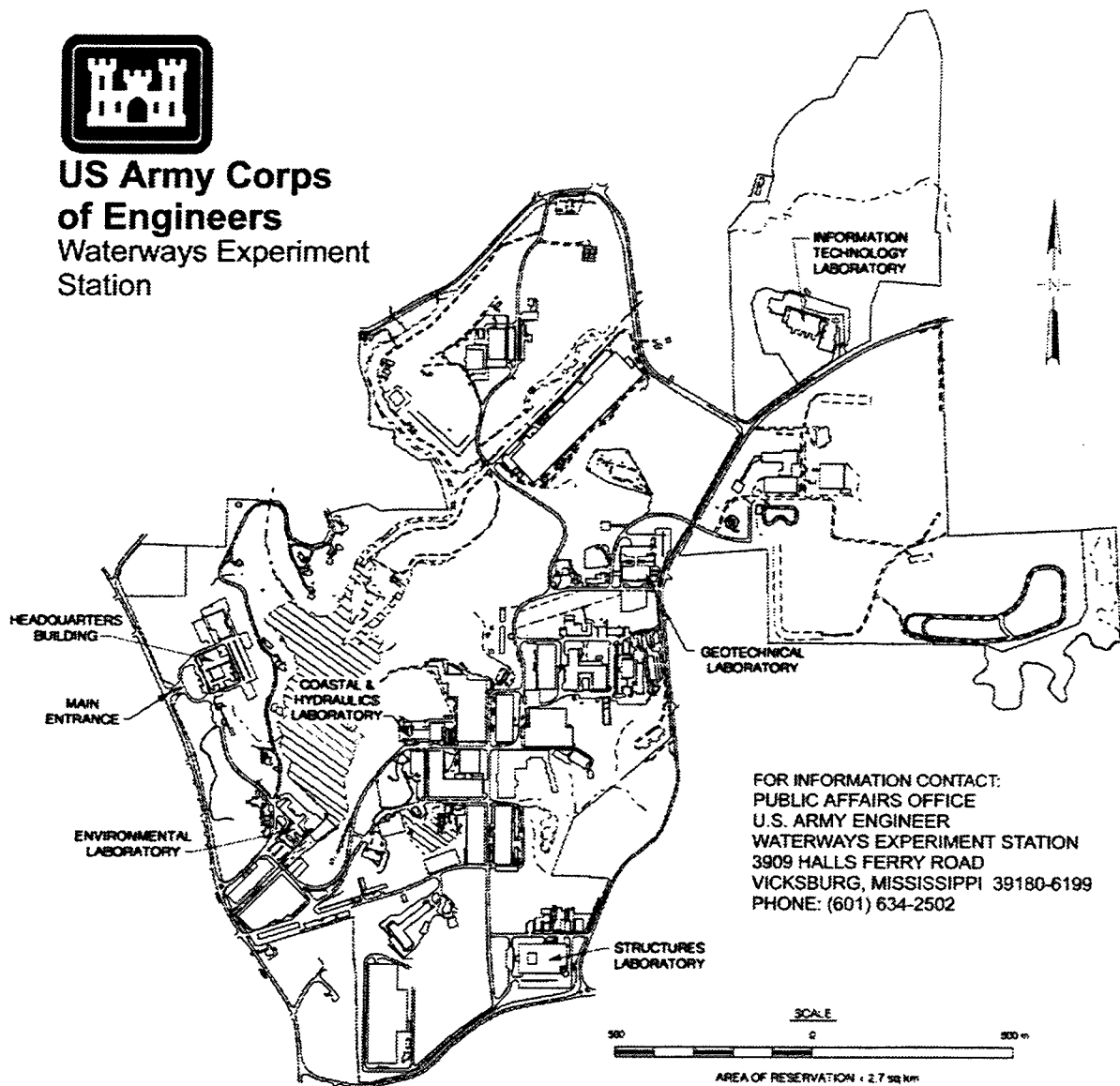
Volume 1 of 2

Approved for public release; distribution is unlimited

Prepared for U.S. Army Corps of Engineers  
Washington, DC 20314-1000



**US Army Corps  
of Engineers**  
Waterways Experiment  
Station



**Waterways Experiment Station Cataloging-in-Publication Data**

Maclaughlin, Mary M.

Working Forum on the Manifold Method of Material Analysis. Volume I / by Mary M. Maclaughlin, Chaio-Tung Chang ; prepared for U.S. Army Corps of Engineers.

252 p. : ill. ; 28 cm. — (Miscellaneous paper ; GL-97-17 v.1)

Includes bibliographic references.

Volume 1 of 2.

1. Materials — Analysis — Case studies. 2. Manifolds (Mathematics) — Case studies. I. Chang, Chaio-Tung. II. United States. Army. Corps of Engineers. III. U.S. Army Engineer Waterways Experiment Station. IV. Geotechnical Laboratory (U.S. Army Engineer Waterways Experiment Station) V. Working Forum on the Manifold Method of Material Analysis (1995 : Jenner, California) VI. Title. VII. Series: Miscellaneous paper (U.S. Army Engineer Waterways Experiment Station) ; GL-97-17 v.1.

TA7 W34m no.GL-97-17 v.1



# Contents

Continuous and Discontinuous Analysis Using the Manifold Method by Jeen-Shang Lin . . . . .	1
Artificial Joint-based Manifold Method by Te-Chih Ke . . . . .	21
Single Field Manifold Method using Fourier Function in Wave Propagation Analysis by Max Ma . . . . .	39
Approximation Theories for the Manifold Method by Chung-Yue Wang, Jopan Sheng, Ming-Hong Chen, and Ching-Chiang Chuang . . . . .	61
Estimation of Rock Mass Distribution Around a Repository Drift Using the DDA Method by Frank C. Tsai . . . . .	87
Automatic Creation of Mathematical Meshes in Manifold Method of Material Analysis by Guangqi Chen, Shigeru Miki, and Yuzo Ohnishi . . . . .	105
Nonlinear Entrance Level Manifold Method by Chiao-Tung Chang and Paulo J.M. Monteiro . . . . .	127
Manifold Method of Material Analysis by Dezhang Lin and Haihong Mo . . . . .	147
Manifold Method with Four-node Isoparametric Finite Element Mesh by Kuokai Shyu and M. Reza Salami . . . . .	165

Development of Second Order Displacement Function for DDA and Manifold Method	
by J. C. Chern, C. Y. Koo and S. Chen . . . . .	183
Applications of DDA Augmented Lagrangian Method and Fracturing Algorithms in the Manifold Method	
by C. T. Lin and B. Amadei . . . . .	203
Manifold Method Application: Tunnel Roof Deflection	
by Mary M. Maclaughlin . . . . .	241

## PREFACE

The Working Forum on the Manifold Method of Material Analysis, convened October 4 through 6, 1995, Timber Cove Inn, Jenner, CA, was sponsored by the Geotechnical Laboratory (GL), U.S. Army Engineer Waterways Experiment Station (WES), Vicksburg, MS. Funding for the forum was provided by the CWR&D Work Unit 31700, Special Studies for Civil Works Rock Problems.

Dr. Gen-hua Shi, Rock Mechanics Branch (RMB), Soil and Rock Mechanics Division (SRMD), GL, developed the original theory for the Manifold Method and wrote Volume 2 of the forum proceedings. Mr. Jerry S. Huie, Chief, RMB, SRMD, GL, organized and conducted the forum with the advice and assistance of Drs. Gen-hua Shi, Mary M. MacLaughlin, and Chaio-Tung Chang. Drs. MacLaughlin and Chang were then graduate students at the University of California, Berkeley. Dr. Nick Sitar was their advisor. Volumes 1 and 2 of the proceedings were compiled by Drs. MacLaughlin and Chang.

The forum was conducted under the general supervision of Dr. W. F. Marcuson III, Director, GL. Dr. Don C. Banks, Chief, SRMD, provided direct supervision.

At the time of publication of this report, Dr. Robert W. Whalin was Director of WES.

*The content of this report is not to be used for advertising, publication, or promotional purposes. Citation of trade names does not constitute an official endorsement or approval of the use of such commercial product.*

# **Continuous and Discontinuous Analysis Using the Manifold Method**

Jeen-Shang Lin  
Department of Civil and Environmental Engineering  
University of Pittsburgh  
Pittsburgh, PA 15261

## **Abstract**

The manifold method is a new numerical method which provides a unified framework for solving problems dealing with continuous media, discontinuous media, or both. Furthermore, in the manifold method the response function can either be continuous or discontinuous. One of the most innovative features of the method is that it employs two sets of meshes, the physical mesh and the mathematical mesh. The physical mesh is dictated by the physical boundaries of a problem; the mathematical mesh by the computational considerations. These two are inter-related through an ingenious application of weighting functions. The fundamental concepts central to the manifold method are discussed in detail that include the concepts of the generalized node, the generalized element, the definition of discontinuity, and the role of weighting functions. Whenever possible, the essential elements of the manifold method are explained by using the finite element analogy. Finally, illustrative examples are presented.

## **Introduction**

Materials often are characterized very differently depending upon the nature of a problem, the scale or dimension of interest, or even the focus of an investigation. Under some circumstances, a material may be modeled as a continuous medium, while under others as a discontinuous medium. Then there are occasions to characterize it as a mixture of both. For the purposes of analysis, the available methods of analysis frequently dictate how a material is to be modeled. Time and again, we find ourselves forced to neglect some important features of a problem in order to attain a solution. This, in turn, casts doubts on the validity of the analysis results.

The manifold method is a novel numerical method which provides a new approach for that gives us a better grip on the modeling. The method was conceptualized by Shi (1991, 1992). In the manifold method, the independent response variables, such as displacements, can be continuous or discontinuous throughout a problem domain. This paper provides an overview of the method and presents a computational procedure. Some results from a on-going study are also given.

The term "manifold" originates from topology. Topology is a branch of geometry which studies the properties of geometric figures under continuous transformation (Stillwell, 1993). The manifolds is one of the most important geometric figures it studies. Briefly stated, a manifold is simply a collection of objects, such as points, that satisfies certain homogeneity and continuity requirements. For instance, a two-dimensional manifold, or 2-manifold, is a geometric figure in that every point has a neighborhood equivalent to the interior of a disk. Therefore, surfaces of a sphere and torus are both 2-manifold. In a broad view, engineering analysis also falls into the general areas studied by topology. This is because a problem domain of an engineering analysis is, mathematically speaking, a manifold, and its response such as deformation is simply a transformation of the manifold. It is therefore not surprising that the methods of topology also have important bearings. For example, when a manifold is subjected to a complicated transformation, it is frequently decomposed into simpler shapes such as triangles or polygons through a process called triangulation. These simpler shapes are then covered by other figures that are easier to analyze. By so doing, a complicated problem is converted into smaller and simpler problems on these covering figures. For problems of engineering interests, often the number of the covering figures is finite. The concept of finite covers is the basis of the manifold method.

Because the concepts involved may be abstract and , at times, difficult to engineers, this paper also presents an explanation as to how different parts of the manifold method are formulated and put together. Whenever possible this study employs the finite element analogy to facilitate the explanation. The essential issues addressed include how to cover a manifold, what constitute the generalized elements and the generalized nodes, how to derive the stiffness matrix and the force vector, and how to obtain a solution.

## **A Two-layer Description of a Problem**

Shi's proposal of using a two-layer description for a problem is perhaps one of the most innovative features of the manifold method. The first layer of the description is called

a physical mesh. A physical mesh is a unique portrait of the physical domain of a problem that should include all the discontinuities. It defines the manifold whose response is being sought. The second layer of description is called a mathematical mesh. A mathematical mesh can be a mesh of some regular pattern, or a combinations of some of arbitrary figures. The mesh or shape size may be chosen according to the problem geometry, solution accuracy requirements, and the physical property zoning. The mathematical mesh is used for building covers and has to be large enough to cover every point of the physical mesh.

This two-layer description concept is illustrated here with a retaining wall example. The soil behind the retaining wall above the potential sliding plane is modeled as consists of several thin slices to facilitate the occurrence of a particular mode. These decisions define a physical mesh for the problem which is depicted in Fig. 1(b). A triangular mesh, as shown in Fig. 1(a), is arbitrarily selected as the mathematical mesh. A superposition of these two meshes, shown as Fig. 1(c), gives a covered manifold of the problem. It is important to note that the manifold method does not require a mathematical mesh to conform to the physical boundary of a problem. This greatly simplifies an input preparation.

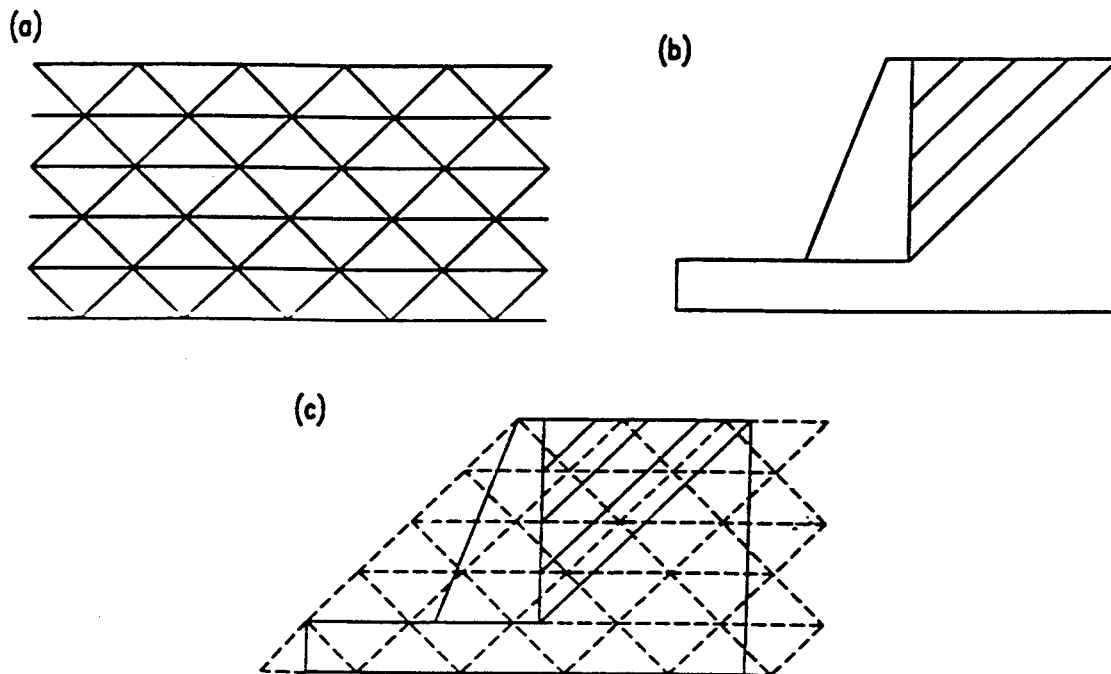


Figure 1. A manifold example (a) an arbitrary triangular mathematical mesh  
(b) a physical description of a retaining wall problem (c) a covered manifold

In the narrow scope of this study the manifold method can be viewed as a combination of the finite element and the discrete element methods. Thus many features of the finite elements and the discrete elements, particularly those of the Discontinuous Deformation Analysis, DDA, (Shi, 1988; 1993), are incorporated into the current manifold method formulation.

## Generalized Nodes and Elements

The key to the manifold method as an analysis tool lies in the generalization of the node and element concepts. The manifold method, by not requiring a mathematical mesh to coincide with the physical boundary of a problem, departs significantly from the finite element, or the discrete element methods for that matter. Two generalizations in the manifold method make it possible for a rather arbitrary selection of the mathematical mesh. First, it constructs the interpolation on the basis of the mathematical mesh. Second, it uses weighting functions to track the physical boundary of a problem.

Without losing generality, the following discussion considers displacements as the only independent variables. In other words, the so-called assumed displacement method (e.g., Macneal, 1994) is adopted here. Other considerations include the use of a triangular mesh as the mathematical mesh and the use of a linear displacement field within a basic triangle. To avoid confusion, an intersection point on a physical mesh is denoted as a vertex, while one on a mathematical mesh is denoted as a node. Also, a basic triangle refers to a triangle formed by three neighboring nodes.

Within a basic triangle bounded by three nodes, say 0,1, and 2, the assumption of a linear displacement field leads to the following linear equations,

$$\begin{aligned} u(x,y) &= a_0 + a_1x + a_2y \\ v(x,y) &= b_0 + b_1x + b_2y \end{aligned} \quad (1)$$

where,  $u(x,y)$  and  $v(x,y)$  are the x- and y- displacements, respectively, at a point  $(x,y)$ . Evaluation of  $u(x,y)$  at all three nodes gives

$$\begin{bmatrix} u_0 \\ u_1 \\ u_2 \end{bmatrix} = \begin{bmatrix} 1 & x_0 & y_0 \\ 1 & x_1 & y_1 \\ 1 & x_2 & y_2 \end{bmatrix} \begin{bmatrix} a_0 \\ a_1 \\ a_2 \end{bmatrix} = [X][a_d] \quad (2)$$

The coefficients  $[a_i]$  can be expressed as a function of nodal displacement  $[u_i]$  as

$$[a_d] = [A][u_d] \quad (3)$$

where,  $[A]$  is the inverse of the nodal coordinate matrix  $[X]$ . A similar relationship can also be written for the coefficients  $[b_i]$ :

$$[b_d] = [A][v_d] \quad (4)$$

Substituting (4) and (3) to (1), the internal displacement within a basic triangle can be written in terms of nodal values by

$$\begin{bmatrix} u(x,y) \\ v(x,y) \end{bmatrix} = \begin{bmatrix} N_0(x,y) & 0 & N_1(x,y) & 0 & N_2(x,y) & 0 \\ 0 & N_0(x,y) & 0 & N_1(x,y) & 0 & N_2(x,y) \end{bmatrix} \begin{bmatrix} u_0 \\ v_0 \\ u_1 \\ v_1 \\ u_2 \\ v_2 \end{bmatrix} \quad (5)$$

where,  $N_i(x,y)$  is the so-called interpolation function or shape function of a node  $i$ , which has a peak value of 1 at  $i$ , and 0 at the rest of the nodes.  $N_i(x,y)$  can be found as,

$$N_i(x,y) = \frac{1}{\det [X_i]} (n_{i0} + n_{i1}x + n_{i2}y) \quad (6)$$

and using the arithmetic of mod 3, one can write,

$$\begin{aligned} n_{i0} &= x_{i+1}y_{i+2} - x_{i+2}y_{i+1} \\ n_{i1} &= y_{i+1} - y_{i+2} \\ n_{i2} &= x_{i+2} - x_{i+1} \end{aligned} \quad (7)$$



Fig. 2 shows a plot of the interpolation function  $N_i(x,y)$  and the domain area it affects. This area affected by a node  $i$  is the combined area of all triangles with a common node  $i$ . In topology, such an area is called a star, or a neighborhood star. A nodal response, such as  $u_i$  or  $v_i$ , is but a scaling factor for the interpolation function that resides on a star. Adopting this geometric view, the manifold method considers stars as the generalized nodes. The benefits of such a viewpoint become apparent when a discontinuity is encountered.

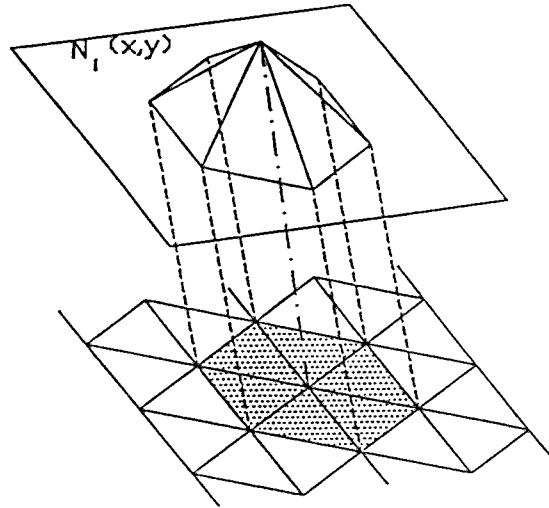


Figure 2. A geometric view of an interpolation function and the star it covers

Another generalization can be realized from a different interpretation of (5). What (5) implies is: "Within a basic triangle bounded by three nodes, the internal displacement is determined once the nodal displacements are known." If the statement is recasted in terms of stars, a generalization emerges. (5) may be interpreted as-- "Any physical area that is covered by three stars has its displacement field defined." This is significant: Within any such an area, the strain, stress, strain energy can all be computed from the defined displacement field, and it is, therefore, possible to apply to it mechanical theories such as the minimum energy principle. Using the finite element analogy, such a physical area constitutes an element. In the manifold method, a generalized element is hence defined as "any physical area that is covered simultaneously by a certain number of stars". This number of covering stars required depends upon the type of interpolation functions used. Using a triangular mesh with a linear interpolation function, a generalized element is an area covered by three stars. If, however, a rectangular mesh is used together with a four-term bilinear interpolation function, a generalized element becomes a physical area covered by four stars. On the other hands, a rigid object is a star by itself.

Thus from this very simple generalization, a new way of generating elements is established. Considering the basically infinite ways of defining response functions-- which may be different physical entities, the possibility of coming up new elements are therefore without limit.

## Discontinuities and Weighting Functions

In order to conduct a continuous-discontinuous analysis, the issue of continuity and discontinuity has to be clarified first. This study finds the issue can easily be resolved using the concept of "connectedness" from topology which is central to question such as if a figure is of one piece (e.g., Mendelson, 1990). Among the various types of connectedness, the concept of path-connectedness is found particularly useful. A domain is called path-connected if any pair of its points can be connected by a path in it. For example, the domain as depicted in Fig. 3 is path-connected because any pair of points, such as 1 and 2, can be connected by a path. It can readily be shown that a path-connected domain has a continuous response. On the other hand, a discontinuity is a figure, or a curve in a 2-dimensional case, that makes it impossible for a domain to stay path-connected. Thus a discontinuity always divides a domain into components each of which is path-connected, and no points from different components can be connected without crossing the discontinuity.

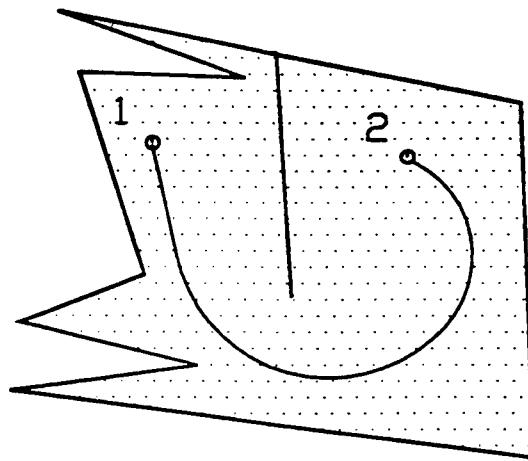


Figure 3. A path-connected domain

Discontinuities may enter an analysis because they are present physically. Or, they may be introduced by a mathematical mesh. This study is concerned mainly with the star discontinuity. Because whenever a star is divided, its components may response independently, and the interpolation function resides on the divided star becomes discontinuous.

Fig. 4 shows a physical domain a-b-c-d which contains a physical discontinuity e-f that divides it into two components a-e-f-d and e-b-c-f. A partial mathematical mesh is also depicted on it. The star associated with the node 5, shown in hatch, covers the polygon of 1-2-6-9-8-4, is divided by e-f into two components. This reflects the fact that a physical discontinuity always causes a discontinuity in the star it crosses. On the other hand, the curves g-h and mn are not physical discontinuities since the components they are in remain path-connected. But g-h nonetheless introduces a discontinuity in the star associated with the node 6 that covers the polygon 2-3-7-10-9-5, while m-n does not introduce a discontinuity in the stars that cover it. This clearly illustrates that the selection of a mathematical mesh reflects our view of the scale effects. We would choose a mathematical mesh with a size compatible to the scale of discontinuity of concern to us.

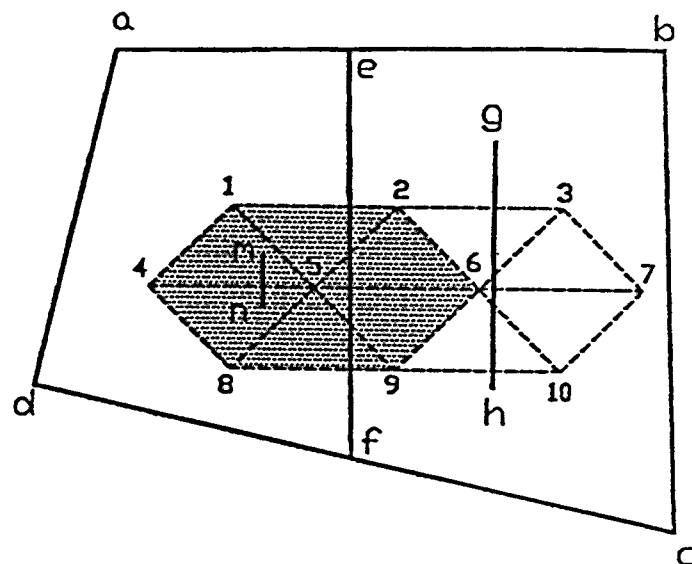


Figure 4. Physical discontinuities and star discontinuities

The manifold method uses an elegant approach to model a discontinuous interpolation over a divided star. Whenever a star is divided a new star is added for each additional component. Following Shi's notation, this study denotes a star with a node

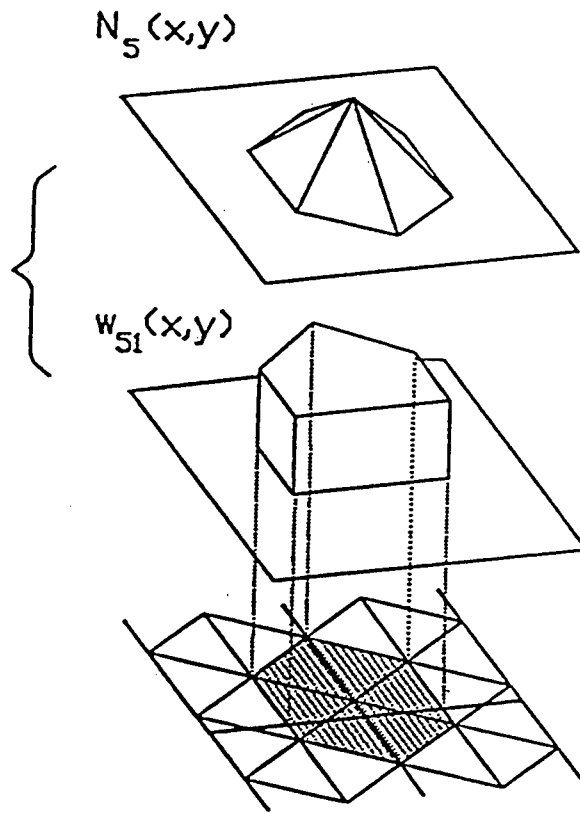


Figure 5. Construction of the interpolation function for the star  $5_1$

number and a subscript that starts from 1 onward to distinguishes all its components. In the case of the node 5 of the above example, two independent stars are needed since two components are formed. Two stars are independent only if they are scaled by two independent nodal values. To accomplish this, two sets of nodal values are stored at node 5. For the two stars at 5, let  $5_1$  represent the component to the left of e-f and  $5_2$  to its right. For each one of them, its interpolation function is constructed in two steps. First, the same interpolation function,  $N_5(x,y)$ , as defined by (2) are used for both  $5_1$  and  $5_2$ . Second, different weighting functions,  $w_{5_1}(x,y)$  and  $w_{5_2}(x,y)$ , are then introduced. Each weighting function has the value of 1 over its corresponding component area, and 0 elsewhere. For example, the weighting function,  $w_{5_1}(x,y)$ , for  $5_1$  is depicted in Fig. 5. The actual interpolation function used in an analysis is obtained by multiplying the interpolation function with the weighting function. That is, the actual displacement field, say  $u(x,y)$ , due

to  $S_1$  is

$$u(x,y) = w_{S_1}(x,y)N_5(x,y)u_{S_1} \quad (8)$$

where  $u_{S_1}$  is nodal value assigned for scaling the star  $S_1$ . Similar equation can be written for  $S_2$ . The displacement over the combined  $S_1$  and  $S_2$  area, i.e., the polygon 1-2-6-9-8-4 due to these two 5 stars becomes

$$u(x,y) = w_{S_1}(x,y)N_5(x,y)u_{S_1} + w_{S_2}(x,y)N_5(x,y)u_{S_2} \quad (9)$$

which is continuous within  $S_1$  or  $S_2$ , but becomes discontinuous when crossing e-f. In general, the displacement  $u(x,y)$  within an element can be written as,

$$u(x,y) = \sum_i \sum_j w_{ij}(x,y)N_j(x,y)u_{ij} \quad (10)$$

where  $i$  is a sum over all the covering stars on an element,  $j$  is a sum over all the component within an  $i$  star.

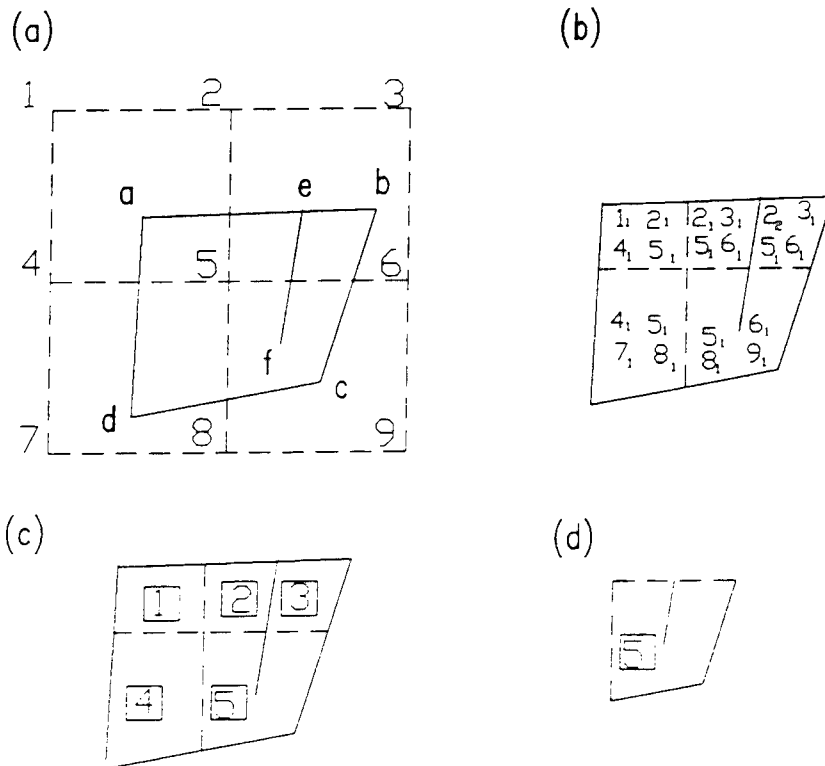


Figure 6. Identification of stars and elements

Fig. 6 further illustrates how to integrate the concepts of stars and discontinuities into identifying the generalized elements. Just to illustrate the liberty we have in selecting the mathematical mesh, a rectangular mesh is adopted here for this example. The underlying response is assumed to be bi-linear within each star. Here except for the node 2, each node is associated with one star only. A 2 star covers the quadrilateral area 1-4-6-3 which is divided into two components by e-f. Here, the star  $2_1$  is designate as the cover over the domain left of e-f, while star  $2_2$  to its right. There are therefore 10 stars in this problem:  $1_1, 2_1, 2_2, 3_1, 4_1, 5_1, 6_1, 7_1, 8_1$ , and  $9_1$ . Each generalized element in this example is an area covered by four stars. There are, therefore, five elements for this problem. Element 1 is covered by  $1_1, 2_1, 4_1$  and  $5_1$ ; element 2 by  $2_1, 3_1, 5_1$  and  $6_1$ ; element 3 by  $2_2, 3_1, 5_1$  and  $6_1$ ; element 4 by  $4_1, 5_1, 7_1$  and  $8_1$ ; and element 5 by  $5_1, 6_1, 8_1$  and  $9_1$ . It is important to note that each element can take a rather arbitrary physical shape.

## Basic Formulations on Elements

Since most engineers are familiar with the finite element method, the following discussions use the finite element terminology. Stiffness matrix of an element due to the strain energy is derived here to illustrate the basic formulations. Here, the strain energy over a basic triangle is derived first, which is then modified by a weighting function to give the real strain energy over its physical domain.

In a plane strain small deformation problem, the strain-displacement relationship can be expressed as follows,

$$[\epsilon] = \begin{bmatrix} \epsilon_{xx} \\ \epsilon_{yy} \\ \gamma_{xy} \end{bmatrix} = \begin{bmatrix} \frac{\partial u}{\partial x} \\ \frac{\partial v}{\partial y} \\ \frac{1}{2} \left( \frac{\partial u}{\partial y} + \frac{\partial v}{\partial x} \right) \end{bmatrix} \quad (11)$$

Rewriting (5) as

$$[u(x,y)] = [N(x,y)] [u_d] \quad (12)$$

the element strain can be related to the nodal displacement with

$$[\varepsilon] = [B(x,y)][u_d] \quad (13)$$

where,  $[B(x,y)]$  is a linear derivative of  $[N(x,y)]$ . Furthermore, let the constitutive relationship be

$$[\sigma] = [C][\varepsilon] \quad (14)$$

then the strain energy density,  $u_o(x,y)$ , may be written as

$$u_o(x,y) = \frac{1}{2}[\varepsilon]^T[\sigma] = \frac{1}{2}[u_d]^T[B(x,y)]^T[C][B(x,y)][u_d] \quad (15)$$

and the total strain energy of an element can be obtained through integration. To account for the physical area of a generalized element, again, the weighting function is introduced. The true total strain energy of an element is obtained as follows,

$$U = \int_A w(x,y) u_o(x,y) dA \quad (16)$$

Employing the minimum potential energy principle, the stiffness matrix associate with the straining of the element can be found as follows,

$$[K] = \int_A w(x,y)[B(x,y)]^T[C][B(x,y)] dA \quad (17)$$

In a similar fashion, other components of the stiffness matrix and the force vectors can be derived. Among the factors that are considered for a general applications are initial strains, initial stresses, body forces, inertia forces, interactions through contacts, boundary loadings, and other structures components such as earth anchors or rock bolts.

## Formulations Across Discontinuities

Discontinuities pose two sets of constraints. First, objects should not penetrate each

other across the discontinuities that separate them. Second, the motion of one object against another along a discontinuity is affected by the surface strength characteristics. In the manifold method, the first constraint is modeled via the use of a penalty formulation, namely, a very stiff normal spring is inserted at the point of contact. Any tendency to penetrate is restrained by the spring's high stiffness. The second constraint is modeled by inserting a shear spring which yields if its strength governed by Mohr-Coulomb's law is reached. The strain energy in the contact springs is modeled as part of the overall potential energy of the system. This results in the coupling of the stiffness matrices of the elements that are in contact. It is important that the stiffness matrices are coupled because it allows the motion constraints be imposed as soon as interactions take place.

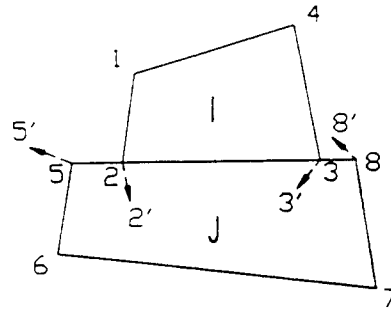


Figure 7. Modeling the constraints between element boundaries

A simple example is depicted in Fig.7 to illustrate how a discontinuity is modeled. Here only the physical boundaries of elements are shown. Initially, edge 2-3 of an element I is in contact with edge 5-8 of an element J. As the loading is applied, both elements may move. Before a constraint across the discontinuity is imposed, the edge 2-3 may move, say to 2'-3', while the edge 5-8 to 5'-8'. In the manifold method, just like in DDA, edge contacts are modeled via vertex-edge contacts. For this example, the two edge contacts are modeled as two contacts, one between vertex 2' and edge 5'-8', and the other between vertex 3' and edge 5'-8'. Here only the formulation for the first one is detailed. If the vertex 2' penetrates the edge 5'-8', the movement from 2 to 2' is first decomposed into a normal and a shear components against the edge 5'-8' and they are denoted as  $d$  and  $s$  respectively. From a geometric consideration using vector cross product,  $d$  can be written as (Shi, 1988),

$$d = \frac{\Delta}{l_{58}} = \frac{1}{l_{58}} \begin{vmatrix} 1 & x_2 + u_2 & y_2 + v_2 \\ 1 & x_5 + u_5 & y_5 + v_5 \\ 1 & x_8 + u_8 & y_8 + v_8 \end{vmatrix} \quad (18)$$



where,  $l_{58}$  is the length of 5-8,  $u_i$  and  $v_i$  are unknown vertex displacements,  $x_i$  and  $y_i$  are known vertex coordinates and  $\Delta$  can be expressed as

$$\Delta = d_o + [(y_5 - y_8) (x_8 - x_5)] \begin{bmatrix} u_2 \\ v_2 \end{bmatrix} + [(y_8 - y_2) (x_2 - x_8)] \begin{bmatrix} u_5 \\ v_5 \end{bmatrix} + [(y_2 - y_5) (x_5 - x_2)]$$

In this expression,  $d_o$  is a function of known vertex coordinates and is a constant; while the displacements at vertices 2, 5 and 8 are functions of the unknown nodal displacements. For instance,  $u_2$  and  $v_2$  can be expressed in terms of the nodal displacements of the element I by substituting the  $(x_2, y_2)$  coordinates into the interpolation relationship of element I as follows,

$$\begin{bmatrix} u_2 \\ v_2 \end{bmatrix} = [M(x_2, y_2)]_I [u]_I \quad (20)$$

Similarly,  $u_4, v_4$  and  $u_5, v_5$  can be expressed in terms of those of the element J. Thus  $d$  can be expressed as a linear functions of unknown nodal displacements of elements I and J in the following form,

$$d = d_o + [a][u]_I + [b][u]_J \quad (21)$$

where,  $[a]$  and  $[b]$  are constant row vectors. Since 2' is not to penetrate 5'-8', a correct solution should make this normal penetration  $d$  zero. As stated, this is carried out by inserting a very stiff spring in the penalty formulation. The potential energy,  $\Pi$ , of a contact spring is

$$\Pi = \frac{k_n d^2}{2} \quad (22)$$

A solution obtained from a minimum potential energy of the complete system generally gives negligible penetration. It is important to note that in a penalty formulation, which is an approximation to the Lagrange multiplier (Hughes, 1987), a constraint is only approximately satisfied. A small penetration always takes place. If the penetration is deemed too large, improvements can be made by increasing the spring stiffness or by reducing the

time step size. The penalty method has the advantage, however, that the spring constant does have physical meaning and can be selected to match laboratory test results be they linear or nonlinear.

The shear deformation,  $s$ , of point 2' along 5'-8' causes shear stresses which is modeled by a shear spring,  $k_s$ . Expressing  $s$  in terms of nodal displacements, the potential energy of the spring is also formulated. The corresponding stiffness and forcing terms can be similarly determined. Again, the stiffness matrices due to shear movements are coupled in this approach. Iteration is required if the shear spring yields.

Elements may form new contacts or may disengage from existing contacts. Because of the coupling in the stiffness matrix, how large a memory area should be reserved for an analysis becomes an important issue as the number of elements increases.

## Construction of Physical Boundaries of Elements

To show that the computational geometry also plays an important role in the manifold method, the construction of the physical boundaries of elements from a covered manifold is described here.

1. First of all, the physical mesh is obtained which includes the boundary of blocks and discontinuities with them. A computational algorithm devised by Shi for DDA can be adopted for this purpose. The algorithm uses tree-cutting analogy and the "coherent orientation" scheme in topology (e.g., Giblin, 1977).

2. One may choose to work on all blocks simultaneously, or one block a time. The latter approach is described here. For instance, Fig. 8 (a) depicts a rather general block. One may easily determine a rectangular box that covers the block. Let the lower left corner be  $(x_{min}, y_{min})$  and the upper right corner be  $(x_{max}, y_{max})$ .

3. According to the size of the mathematical mesh selected, the mathematical mesh may be generated starting from  $(x_{min}, y_{min})$ , until the mesh covers  $(x_{max}, y_{max})$ .

4. For each point on the mesh, determines if the point or its immediate neighbors fall on the boundary or within the interior of the block. If so, the point is retained for constructing stars. In Fig. 8(b), it shows 12 points are retained. This means that at least 12 stars are need to cover the block.

5. For each point retained, the corresponding star or stars are constructed. If a star falls completely within the block, no thing needs to be done. If it intersects with the block, the intersected region is the real star area. This step can be achieved with some polygon intersection algorithm. If a star is divided by discontinuities, the number of components are determined. For instance, there are two 2-stars as depicted in Fig. 8 (c).

6. Obtain the total number of elements and their physical boundaries. This is equivalent to obtain the area overlapped by three stars associated with the triangles of the underlying mesh.

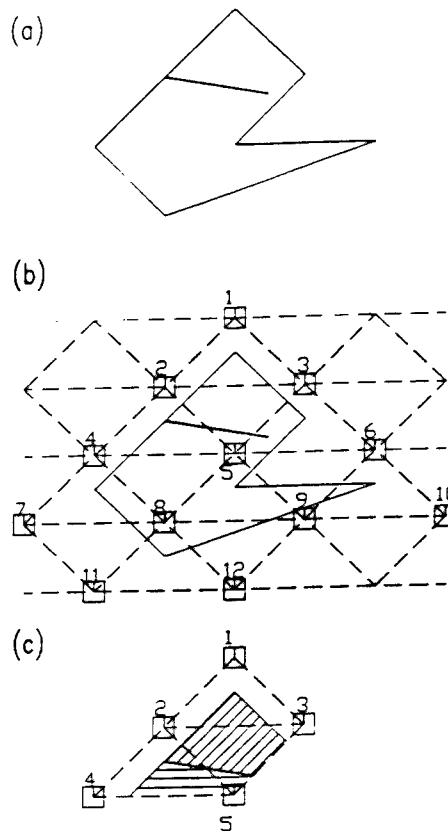


Figure 8. Construction of physical boundaries of elements (a) A typical object (b) after identifying the relevant nodes (c) construction of stars

## Example Applications

Two problems are solved here for illustration. For the purpose of illustration, these examples are much simplified: large size mathematical meshes are used together with linear interpolation functions. All the elastic objects have a Poisson ratio of 0.3, a mass density

of  $1.8 \text{ Mg/m}^3$ , a unit weight of  $18 \text{ kN/m}^3$ , and elastic moduli ranging from  $1500$  to  $4000 \text{ kN/m}^2$ . All the rigid bodies are marked by hatch dots in the following drawings.

The first problem tackles an elastic medium with rigid inclusions. In this problem the elastic medium has both exterior and interior boundaries. Here, two rigid plates are pressed against an elastic medium with two rigid inclusions placed unsymmetrically. Initially, there are perfect contacts between the elastic medium and the rigid inclusions, as well as between the elastic medium and the rigid plates. The covered manifold is depicted in Fig. 9 (a). All contacts are modeled as frictional with a friction angle of  $5^\circ$ . The deformed configuration after experiencing a  $14.7\%$  vertical strain is shown in Fig. 9(b). Because of the way inclusions are placed, the elastic medium deformed unsymmetrically. Part of the contacts between the inclusions and the medium are separated. The contacts between the rigid plates and the elastic medium also shift.

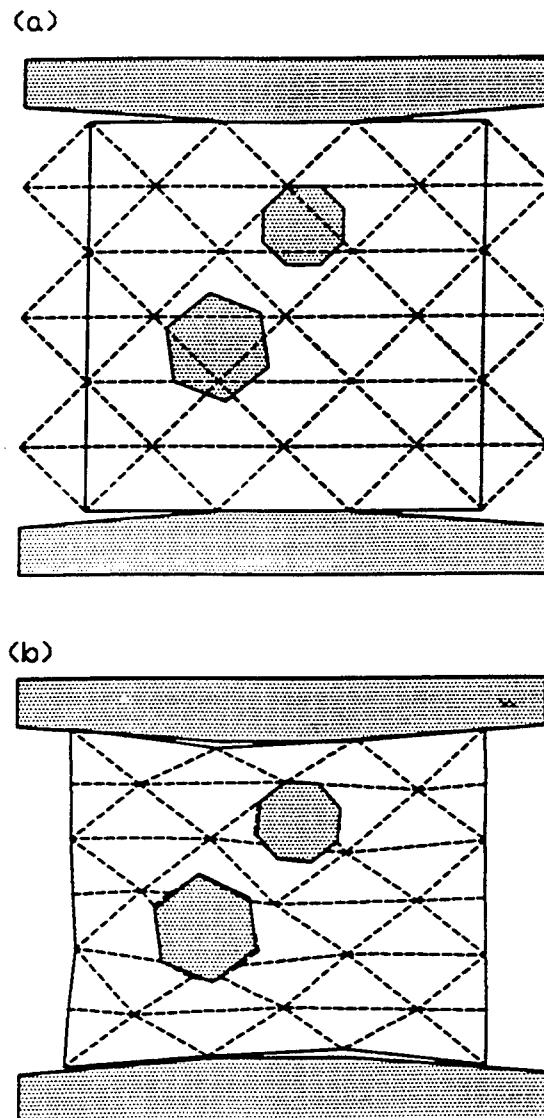


Figure 9. An elastic medium with rigid inclusion problem (a) a covered manifold (b) its deformed configuration

The second problem, as shown in Fig. 10(a), studies an elastic object, which contains a set of well-defined fissures, and is being pressed from the sides. Surfaces of the fissures are characterized by a friction angle of  $5^\circ$ . This problem is presented here to illustrate the capability of the manifold method in modeling discontinuities. For this purpose, tips of the fissures are not allowed to propagate. Even with this simplification, this is still a rather difficult problem. Pressing the sample from sides, the fissures show a complicated movement pattern. The side rigid blocks in this example are assumed smooth frictionless surfaces. The deformed configuration at a horizontal strain of 20.8 % is summarized in Fig. 10(b). In order to show the deformed configuration clearly, the mathematical mesh is not shown in this plot. Because of the rough mesh used, this result is only a crude approximation. Although much simplified, the example shows the manifold method may have a potential use in solving problems involving clusters of discontinuities in various arrangements.

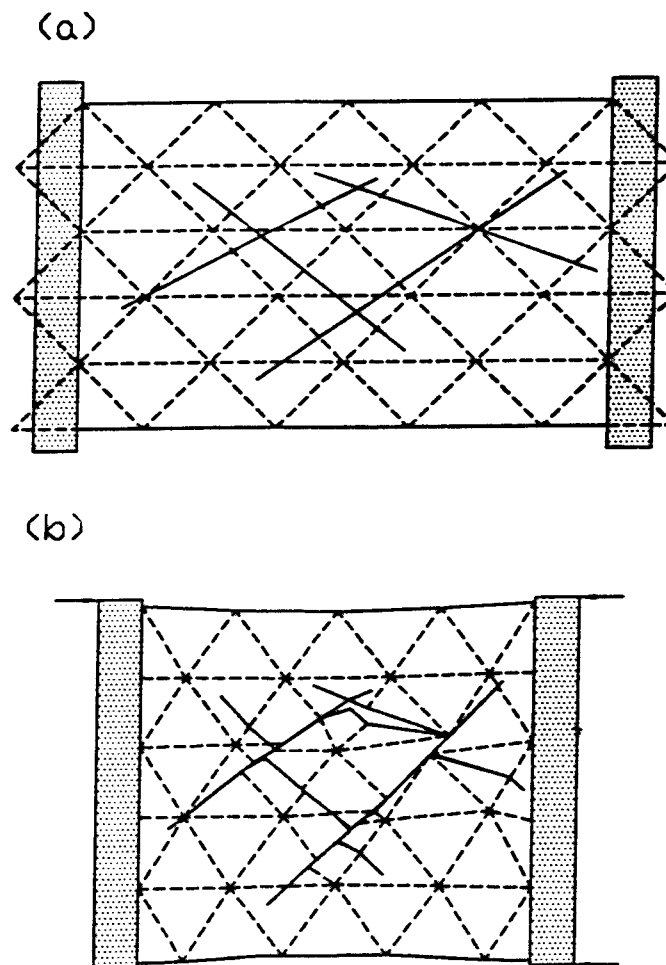


Figure 10. An elastic medium with non-propagating fissures (a) a covered manifold (b) its deformed configuration

## Conclusions

This study explains the fundamentals of the manifold method using concepts with which engineers are familiar, and shows how different parts are put together for an engineering analysis. The illustrative examples may also shed lights on what problems may be benefited from its use.

The manifold method has several distinctive features that are important from engineering analysis point of view. First and foremost, by using a covered manifold it opens up a new way for the continuous and the discontinuous methods of analysis. Second, it satisfies the minimum energy principle globally, namely both within elements and across elements. Except for the discretization simplifications, the procedure is rigorous both analytically and numerically. Third, the unifying underlying formulations allows extensions be introduced, such as the inclusion of rigid bodies, in a consistent manner.

## Acknowledgments

The author would like to acknowledge the support of a grant ( 1434-94-G2434 ) from National Earthquake Hazard Reduction Program for the present work. This program has been administered by United States Geological Survey. The author would also like to thank Dr. Gen-Hua Shi of the Waterways Experiment Station, USAE, for his comments and suggestions. The computer program developed for this research also benefits from adapting some code from a DDA program written by Dr. Shi.

## References

- Cuthill E., and McKee, J. (1969). "Reducing the Bandwidth of Sparse Symmetric Matric." ACM Proceeding of 24th National Conference, New York.
- Giblin, P.J. (1977). "Graphics, Surfaces and Homolog." Chapman and Hall, London.
- Hughes, T.J.R. (1987). "The Finite Element Method, Linear Static and Dynamic Finite Element Analysis." Prentice-Hall, Inc., Englewood Cliffs.
- Macneal, R. H. (1994). " Finite Elements: Their Design and Performance." Marcel Derkkere Inc. New York.
- Mendelson, B. (1990). "Introduction to Topology." 2nd Edition, Dover.

- Shi G. W. (1988). "Discontinuous Deformation Analysis--A New Numerical Model for the Statics and Dynamics of Block Systems," Ph.D. diss., Department of Civil Engineering, University of California at Berkeley.
- Shi, G. W. (1991). "Manifold Method of Material Analysis." Proceeding, ninth Army Conference on Applied Mathematics and Computing.
- Shi, G. W. (1993). "Block system modeling by discontinuous deformation analysis." Computational Mechanics Publication, Southampton, UK.
- Shi, G. W. (1992). "Modeling rock joints and blocks by Manifold Method." Proceeding of the 33rd U.S. Symposium on Rock Mechanics, SanTa Fe, New Mexico, pp. 639-648.
- Stillwell, J. (1991). "Classical topology and combinatorial group theory." 2nd Ed., Spriner-Verlag, New York.

# Artificial Joint-based Manifold Method

Te-Chih Ke

Department of Civil Engineering  
Chung-Yuan University, Taiwan 32023, R.O.C.

## Abstract

This paper presents a 2D simplified version of Shi's manifold method when combined with the *artificial joint* concept. The physical solid blocks are refined into a system of sub-blocks by a certain pattern of artificial joint mesh. The displacement function used and modelling of block interactions are directly extracted from Shi's discontinuous deformation analysis. This simplified version can determine the refined stress distribution within selected blocks of any shape, and permit simulating fracture propagation of intact solids.

## Introduction

Since the manifold method was first introduced by Shi in 1992, the concept and potential use of this method has drawn great attention from international researchers in both the mathematical and engineering fields. It is foreseen that the manifold method will become one of the most flexible tools to deal with material problems of complex geometry or mixed phases, as encountered in composite materials, fracture propagation, multi-phase flows, etc.

As a key issue in the method, the separation of mathematical and physical meshes makes it possible to solve problems involving complex/different material domains. The mathematical mesh does not only relate to the physical behavior of a material (i.e. some partial differential equations), but also includes the numerical discretization scheme on the space as well as the shape function used. The selection of shape functions might be quite arbitrary. However, in order to handle complex material boundaries, the simplest and lowest-ordered are preferred. The physical mesh represents the complex space occupied by a material domain, and subsequently indicates the integration domain in a numerical analysis. The physical mesh is given and can not be changed arbitrarily. It is emphasized in the manifold method that a simple mathematical function is used to integrate over a complex geometrical domain.



With the finite covering concept, the manifold method can model a wide variety of continuous or discontinuous materials. If a local function  $f_i(x,y)$  is defined over Cover  $U_i$

$$f_i(x, y) \quad (x, y) \in U_i \quad (1)$$

then the global function for the whole finite cover system can be given by

$$F(x, y) = \sum_{i=1}^n \omega_i(x, y) f_i(x, y) \quad (2)$$

where  $\omega_i(x,y)$  is the weight function, and is defined by

$$\begin{aligned} \omega_i(x, y) &\geq 0 \quad (x, y) \in U_i; \\ \omega_i(x, y) &= 0 \quad (x, y) \notin U_i; \\ \sum_{(x, y) \in U_j} \omega_j(x, y) &= 1 \end{aligned} \quad (3)$$

According to this concept, both the finite element method and Shi's discontinuous deformation analysis (DDA) are special cases of the manifold method.

DDA (Shi, 1988) adopts displacements as unknowns which are solved implicitly, fully satisfies dynamic equilibrium, and has complete block kinematics for block contacts. For Block  $i$  of a 2D space, the displacements of any interior point  $(x,y)$  is given by

$$\begin{pmatrix} u \\ v \end{pmatrix}_{(x, y)}^i = [T_i]_{(x, y)} [D_i] \quad (4)$$

where

$$\begin{aligned} [T_i]_{(x, y)} &= \begin{pmatrix} 1 & 0 & -(y-y_0) & x-x_0 & 0 & \frac{1}{2}(y-y_0) \\ 0 & 1 & x-x_0 & 0 & y-y_0 & \frac{1}{2}(x-x_0) \end{pmatrix}^i \\ [D_i]^T &= (u_0 \quad v_0 \quad \gamma_0 \quad \epsilon_x \quad \epsilon_y \quad \gamma_{xy})^i \end{aligned} \quad (5)$$

where  $(u_0, v_0, \gamma_0)$  are the three components of rigid-body movements, and  $(\epsilon_x, \epsilon_y, \gamma_{xy})$  the three components of strain. The local function is  $[T_i]_{(x,y)}[D_i]$ , and the weight function is

$$\begin{aligned} \omega_i(x, y) &= 1 \quad (x, y) \in U_i \\ \omega_i(x, y) &= 0 \quad (x, y) \notin U_i \end{aligned} \quad (6)$$

where  $U_i$  is the physical domain of Block  $i$ . Accordingly, DDA blocks are totally discontinuous to each other. Besides, it is seen in Eqn(5) that each DDA block possesses a state of constant stress, regardless of its shape.

In the early computer code of the manifold method developed by Shi (1992), the mathematical mesh used for the blocks is the three-noded finite elements, and block

interactions are modelled according to the block kinematics in DDA. This code can analyze a system of discrete deformable solid blocks of complex geometry.

This paper presents a 2D simplified version of the manifold method when combined with the *artificial joint* concept. The physical solid blocks are refined into a system of sub-block by a certain pattern of artificial joint mesh. The displacement function used and modelling of the interactions between solid blocks are the same as in DDA. This simplified version can determine the refined stress distribution within selected blocks of any shape or even containing complex interior features, and permit simulating fracture propagation of intact solids. In this paper, the *artificial joint* concept is first introduced, followed by illustration of several numerical examples. Discussions on the comparison of various schemes and selection of adequate artificial joint meshes are also included.

## The Artificial Joint Concept

The artificial joint concept includes two parts: *cutting* and *patching*. Cutting is a process of *dividing* a block domain into sub-blocks by artificial joints so that the block becomes an assemblage of sub-blocks created by imaginary boundaries. These added artificial joints represent "additional" physical boundaries within the block. Figure 1 shows a quadrilateral block (solid lines) and a regular pattern of artificial joint mesh (dashed lines) which creates equilateral triangular sub-blocks. It can be seen in the figure that the block is divided into six sub-blocks, among which only one is equilateral triangular, and the others have irregular shapes produced by the block outer boundaries and adjacent artificial joints. With a regular artificial joint mesh, the resultant regular sub-blocks are generally present much within the refined block and the irregular ones near the block outer boundaries.

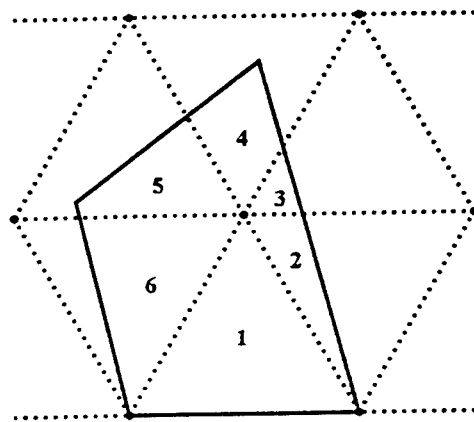


Figure 1. A solid block and artificial joint mesh

Patching is a process of assigning strengths to the artificial joints to *glue* sub-blocks together. If the artificial joints are infinitely strong, the contacts between sub-blocks never fail, leading to continuous connection of two adjacent sub-block by contact springs. As the stiffness of contact springs increases, the contact sides of two adjacent sub-blocks will displace similarly. As a result, the assemblage of sub-blocks behaves as a continuous body like the original block but with refined stress distribution since each sub-block has its own stress state. If the artificial joints are assigned finite strengths, they provide potential cracking paths wherever contact forces exceed limiting values. The energy loss due to cracking is represented by the strain energy release of failed contact springs. Accordingly, fracture propagation of an intact block along a predestined path can be simulated. The failure criterion for  $(\tau, \sigma)$  along the contacts between sub-blocks follows Mohr-Coulomb's law with a tensile strength *cut-off*. Ke (1993) coded the procedures to deal with joints having cohesion and tensile strength, in which contact pairs, each composed of two contact points, need to be sought first. Artificial joints intersecting the cracks, or boundaries of holes and interior blocks, allow these complex features to be modelled.

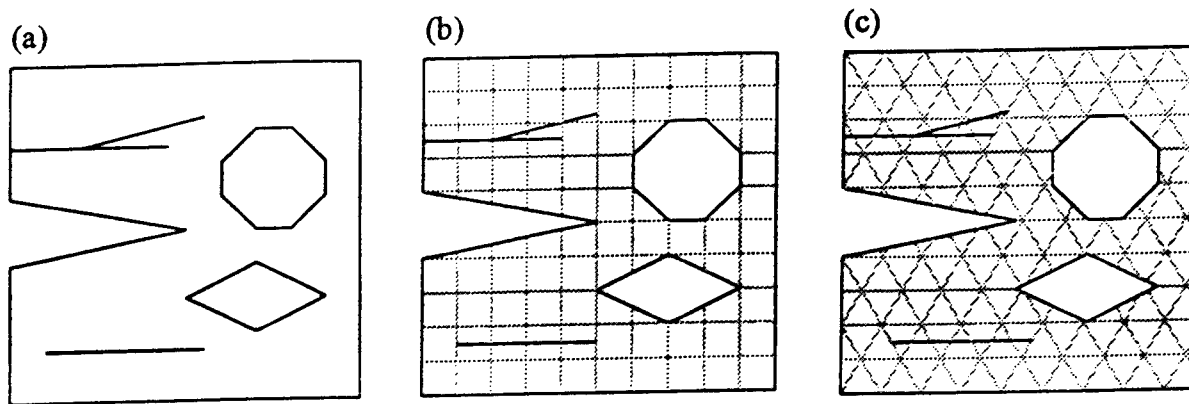


Figure 2. (a) A block with complex geometry and interior features; and refined geometry by: (b) Type A artificial joints; (c) Type C artificial joints

Figure 2a depicts a complex block domain with a notch at the left, one isolated crack below and another with a branch above the notch, and two interior boundaries at the right. Figures 2b and 2c show the resultant sub-block systems of the block domain in Figure 2a by adding regular artificial joint meshes. Note that any portions of the added artificial joints outside the refined domain have been automatically deleted by the joint mesh generator. Type A artificial joint mesh (Figure 2b) contains two orthogonal joint sets and generates rectangular sub-blocks; Type C artificial joint mesh (Figure 2c), which also appeared in Figure 1, contains three joint sets to produce equilateral triangular sub-blocks. There are another three artificial joint mesh types available to refine a homogeneous and isotropic

block domain, as follows.

Type	Number of joint sets	Sub-blocks formed
B	4	Right-angle triangular
D	2	Diamond-shaped
E	3	Hexagon-shaped

## Numerical Examples

The applicability of the artificial joint-based manifold method is illustrated by the following five examples. The 'static' mode is used in the first three examples; while the 'dynamics' mode (in which the velocity of each block is updated step by step) is used in the last two where a progressive failure is involved.

### Cantilever beam

This example examines the performance of Types A and C artificial joint meshes for stress analysis in a cantilever beam. The beam, 8m long and 1m high, is fixed at its left end and is loaded at its right tip. The Young's modulus and Poisson's ratio of the beam are 100 MPa and 0.2, respectively; the tip load is 100 kN. Type A artificial joints divide the beam into 128 sub-blocks; while Type C artificial joints cut the beam into 228 sub-blocks. The added artificial joints have infinite strength.

Figure 3a shows the deformed geometry and principal stress field<sup>1</sup> of the Type A refined beam. The results are unsatisfactory; all sub-blocks have the same tensile principal stress at  $-45^\circ$  and the same compressive stress at  $45^\circ$ . The whole beam responded in simple shear rather than bending, because the deformed shape of the rectangular sub-blocks generated by Type A artificial joint mesh is restrained by, the first-order displacement function used, to deform only into parallelograms<sup>2</sup>.

Figure 3b depicts the deformed geometry and principal stress field of the beam refined by Type C artificial joints. In contrast to Figure 3a, Type C mesh allows the beam

---

the principal stress field described in this paper means the computed graphic output showing the principal stresses of each block at its centroid; compressive stresses are indicated by solid lines and tensile stresses by dotted lines.

this is no longer true when using a higher-order displacement function.

to deflect, developing a neutral axis with tensile fiber stress in its upper part and compressive fiber stress in its lower part. This example shows the adequacy of Type C artificial joints to detail beam structures. Ke (1993) examined other cases with smaller deflection, in which Type C artificial joint mesh yielded results agreeing with those calculated using classical simple beam theory.

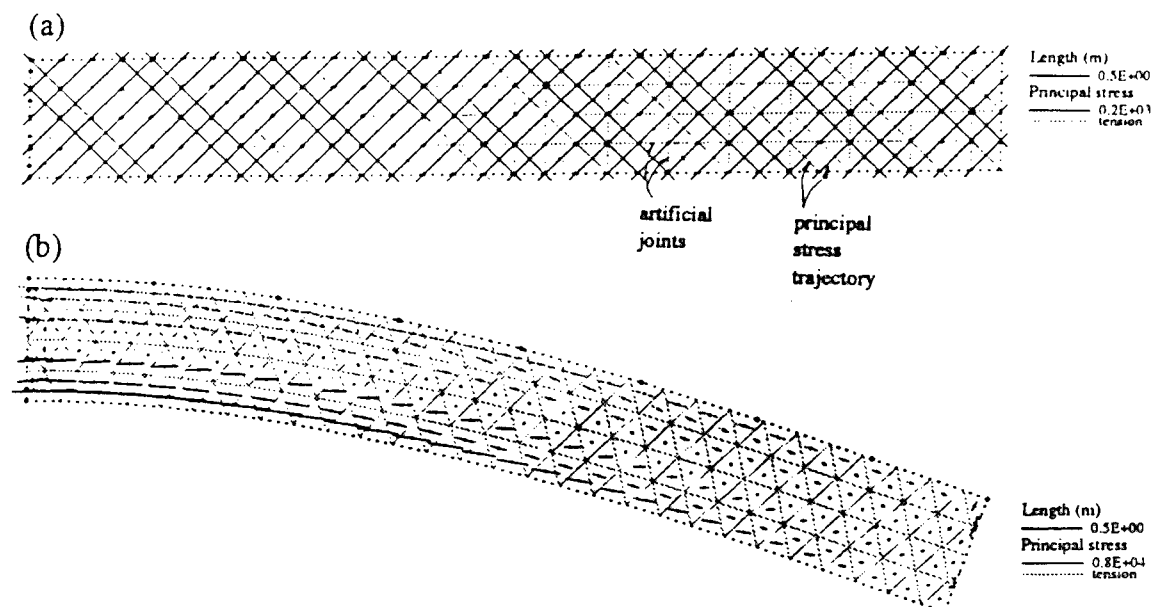


Figure 3. Principal stress field of: (a) Type A refined beam; (b) Type C refined beam

### Stress concentration near a crack tip

Analytical solutions to two-dimensional crack problems for various loading conditions show that the stresses at a small distance  $r$  from the crack tip always vary as  $r^{-1/2}$  (Rice, 1968). Two behavioral modes of a crack, Mode I (in-plane opening) and Mode II (in-plane shearing), are investigated here. Figures 4a or b show a block, 1m high and 1m wide, with a horizontal crack extending six tenths of the way across its width; the block is fixed at its two bottom corners. In Figure 4a, a vertical load  $P$  pulls the upper-left corner of the block upward, causing crack opening (Mode I); in Figure 4b, a horizontal load  $H$  at the left end of the top crack wall causes sliding (Mode II crack shearing). The block has the same Young's modulus and Poisson's ratio as in the cantilever beam example and the crack is assigned zero friction to signify the sliding behavior in Mode II. The cracked block was refined into 252 sub-blocks by Type C artificial joints with infinite strength.

Figure 4c shows the deformed geometry and principal stress field of the cracked block subjected to  $P=10$  kN. In this figure, the crack is open, and higher values of tensile

principal stresses are present near the crack tip in the radial direction. If more sub-blocks are used, the stress concentration near the crack tip in Mode I will be more precisely described.

Figure 4d depicts the deformed geometry and principal stress field of the cracked block subjected to  $H=100$  kN. The adjacent crack walls are in contact at the tip and on the left end, but open between these two points. Higher compressive principal stresses run from the loading point, along the top crack wall, around the tip, then attenuate finally to merge toward the lower-right fixed corner: tensile stress is distributed below the crack wall and concentrated near the lower-left fixed corner.

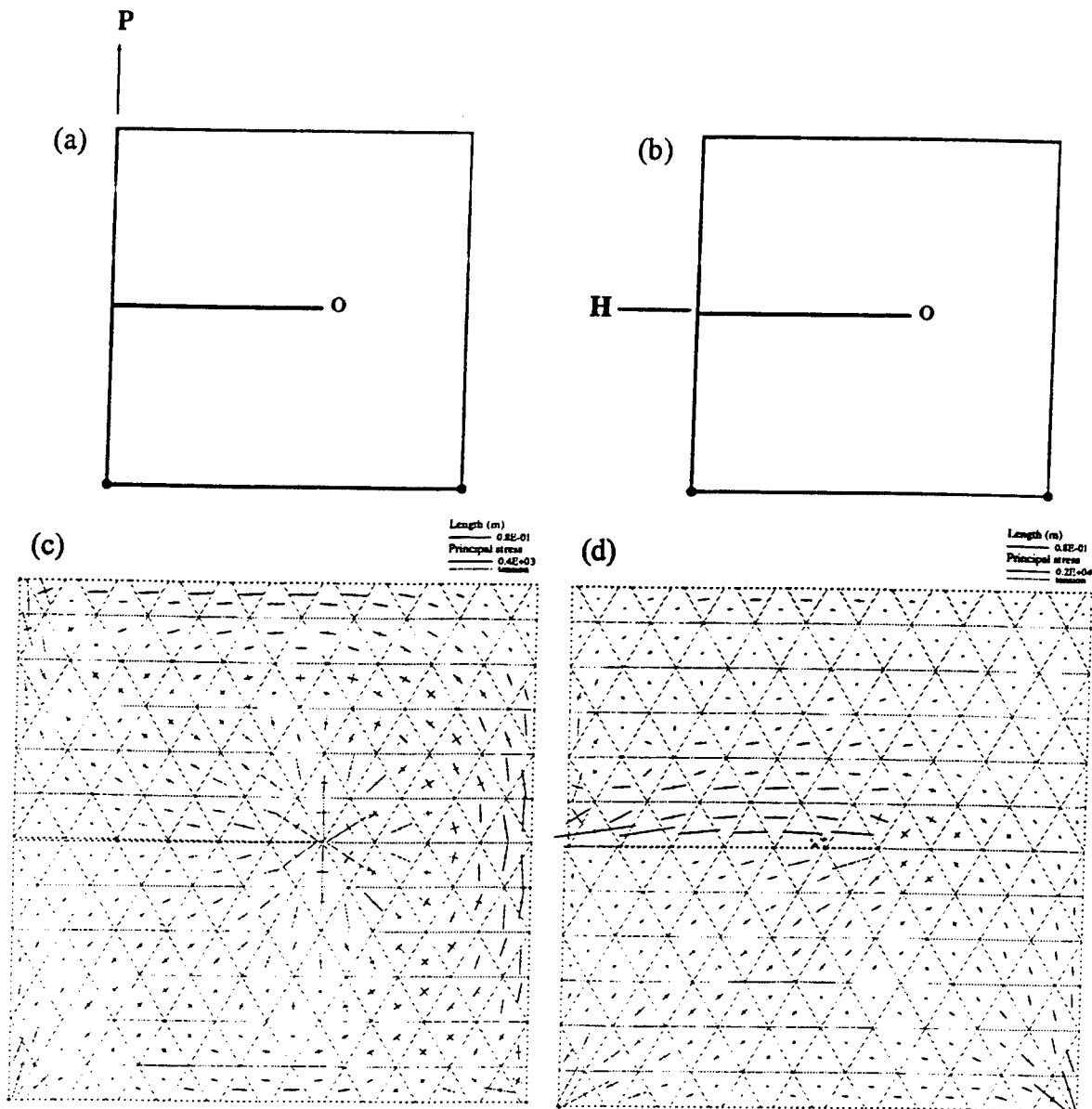


Figure 4. A block with a crack: (a) vertical load  $P$  (Mode I); (b) horizontal load  $H$  (Mode II); (c) principal stress field (Mode I); (d) principal stress field (Mode II)

## Block-in-matrix materials

A block-in-matrix material contains isolated (interior) blocks which are embedded within a matrix. The properties of the matrix and interior blocks may not be the same; the interfaces between the matrix and interior blocks are inherent discontinuities. The global behavior of a block-in-matrix material is a function of the proportion, orientation, arrangement, and size of interior blocks and, especially, the interface strengths (Ke, 1995).

Figure 5 shows two specimens from a particular case of block-in-matrix materials, *melange*, found in the subduction zones paralleling present and ancient convergent plate margins. Melange is distinguished by its oriented lenticular interior blocks. The specimen in Figure 5a contains 19 horizontally oriented blocks (shaded areas) which occupy 40% of the total "volume"; that of Figure 5b has 27 vertically oriented blocks covering 58% of the "volume".

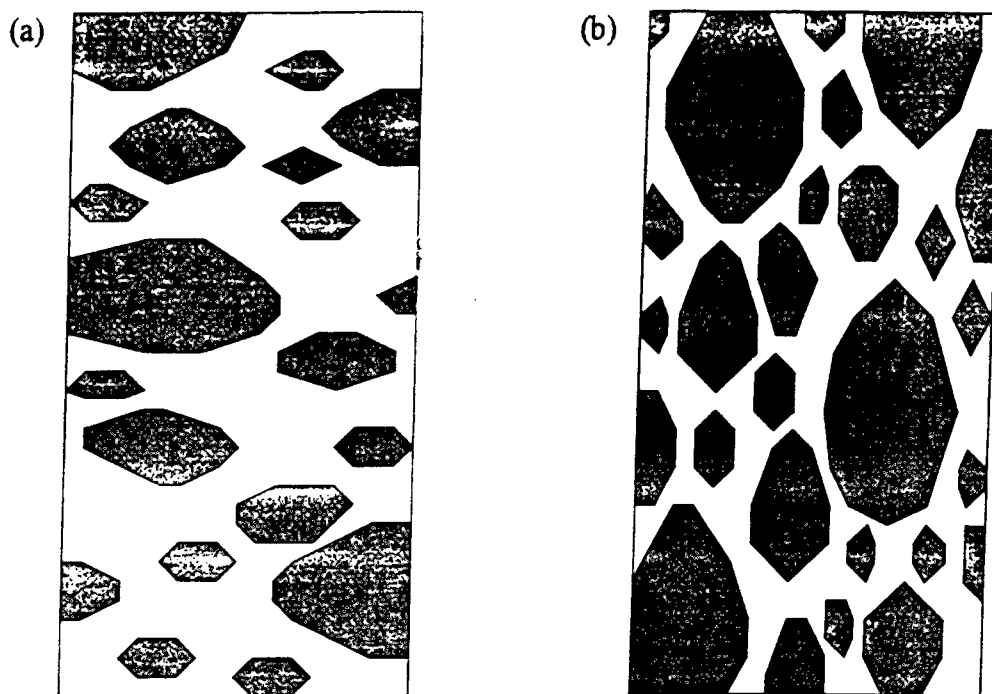


Figure 5. Melange specimens: (a) specimen 1 with 19 horizontally oriented blocks; (b) specimen 2 with 27 vertically oriented blocks

Young's moduli of the matrix and interior blocks are 250 and 420 MPa, respectively; both materials have the same Poisson's ratio of 0.4. The interfaces are assumed to be frictionless. A *numerical* uniaxial compression test was conducted on both specimens (Figure 5) by adding stiff loading plates on the top and bottom of the *specimen*. The bottom

plate is fixed; a vertical load,  $P$ , is applied to the top of the upper plate. The displacements of selected points around the specimens were used to compute their overall secant moduli and Poisson's ratios<sup>3</sup>. The matrix domain was refined by Type C artificial joints with infinite strength.

Table 1 Computed secant moduli and Poisson's Ratios in Example 3

	$P=1(\text{kN})$	$P=2(\text{kN})$	$P=5(\text{kN})$	$P=10(\text{kN})$
Secant moduli: Specimen 1	298.5	298.0	297.9	297.9
Secant moduli: Specimen 2	312.2	310.3	309.9	309.9
Poisson's ratios: Specimen 1	0.4819	0.5165	0.5262	0.5205
Poisson's ratios: Specimen 2	0.5986	0.6595	0.8422	0.8755

Table 1 lists the computation results of two specimens, in which moduli are expressed in units of MPa. Both specimens behave non-linearly, indicated weakly by the computed secant moduli and more convincingly by Poisson's ratios<sup>3</sup>. The non-linear behavior derives from the large number of frictionless interfaces that undergo sliding in several directions, leading to continuous reduction in stiffness with increasing load. Some of the interfaces intersect the outer boundaries, especially on the free side walls of the specimens (Figure 5), further degrading the overall stiffness. Table 1 also indicates that although the block proportion of Specimen 2 is higher than that of Specimen 1 by 18%, the increase in modulus is not proportionally large. This is probably because Specimen 2 loses some stiffness due to increased chance for sliding along its longer frictionless interfaces.

### An arch dam subjected to impact

As an example of showing the fracture propagation capability, cracking and destruction of an arch dam subjected to enormous impact is simulated here. Figure 6a gives a plan view of an arch dam abutting on jointed rock and a huge block at  $t=0$  approaching the dam in the indicated direction. Points 1 to 11 are fixed. Because an arch dam is always

---

ratios of average horizontal to vertical displacements revealed by the output.



made of rectangular concrete blocks, Type A artificial joints were used to refine the dam into 36 concrete sub-blocks, as depicted in Figure 6a. Each concrete sub-block was not further refined at the stage of this study.

Young's modulus and Poisson's ratio of the dam are 1000 MPa and 0.2, respectively, and those of the abutments are 200 MPa and 0.2, respectively. All joints in the abutments are cohesionless and have a friction angle of  $15^\circ$ ; the interfaces between the dam and abutments have a friction angle of  $30^\circ$  and a cohesion of 0.1 MPa. The added artificial joints (interfaces between concrete blocks in the dam) have a limited strength: a friction angle of  $30^\circ$ , a cohesion of 0.1 MPa and a tensile strength of 0.03 MPa. The velocity of the approaching rock is 141.1 m/sec.

Figure 6b shows the deformed geometry of the dam at  $t=0.002\text{sec}$  when the rock just hit the dam. Many interfaces near the collision point fail (indicated by solid lines), and lose their initial cohesion and tensile strength. Two gaps form in the interfaces of concrete blocks below the impact point. At  $t=0.003\text{sec}$ , cracking of interfaces is propagating into the two wings of the dam, as revealed in Figure 6c. Figure 6d depicts the significantly deformed geometry of the dam at  $t=0.01\text{sec}$ . In this figure, no interface survives at this time, and remarkable gaps arise between the concrete blocks below the hitting point. At this stage, imagine that water at a reservoir pressure enters these gap, leading to the total collapse of the dam.

### **A flying object hitting a shelter roof**

This imaginary example provides a second illustration of fracture propagation within a solid structure. As depicted in Figure 7a, the structure subjected to impact resembles a military shelter for tanks or aircraft, which is composed of 80 concrete blocks (this was also done using Type A artificial joints). A warhead-like object is approaching the middle point of the shelter at a downward velocity of 100 m/sec. The foundation block are fixed at its three corners.

Young's modulus and Poisson's ratio of the shelter and foundation are 1000 MPa and 0.2, respectively. The interfaces between the shelter and foundation have a friction angle of  $30^\circ$  and a cohesion of 0.1 MPa. The added artificial joints (interfaces between concrete blocks in the shelter) have a finite strength: a friction angle of  $40^\circ$ , a cohesion of 0.05 MPa and a tensile strength of 0.01 MPa.

Figure 7b shows the deformed geometry of the cracking shelter at  $t=0.0015\text{sec}$  when the object started to penetrate the shelter roof. Many interfaces near the collision point fail (indicated by solid lines), and lose their initial cohesion and tensile strength. At  $t=0.01\text{sec}$ , cracking is propagating into the two wings of the shelter, as revealed in Figure 7c. Figure

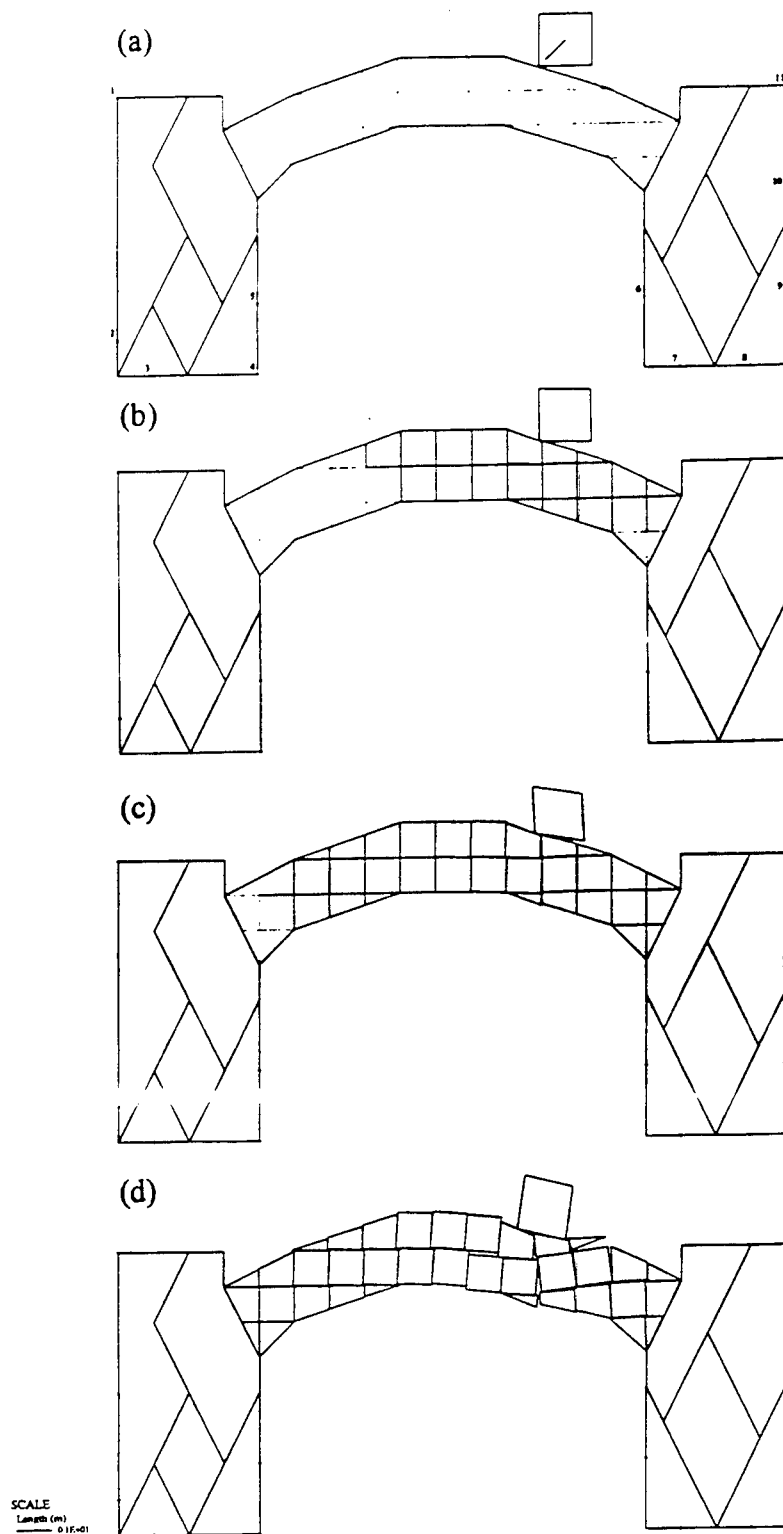


Figure 6. Cracking of an arch dam at  $t =$ : (a) 0; (b) 0.002; (c) 0.003; (d) 0.01sec

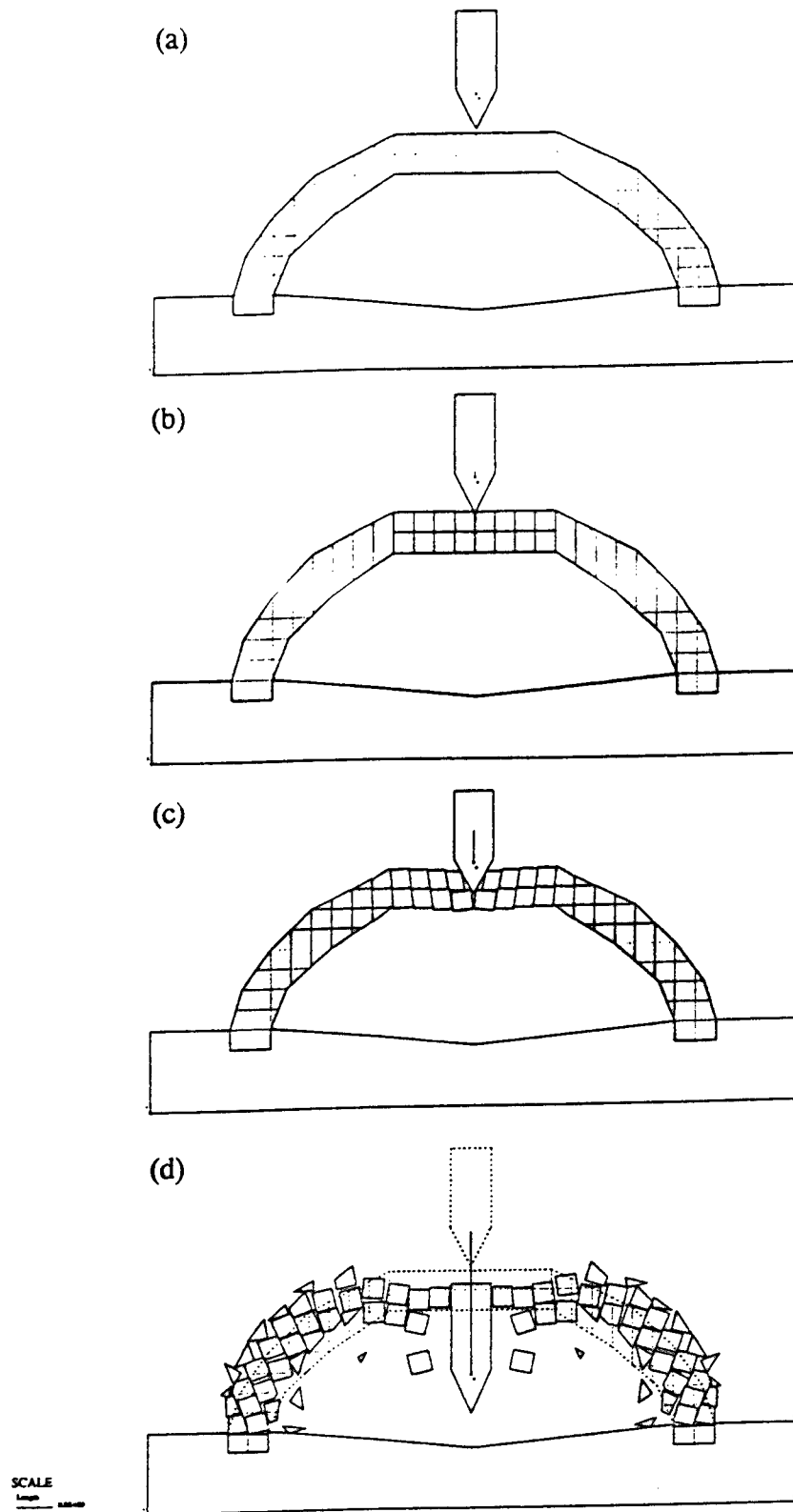


Figure 7. Cracking of an shelter at  $t =$ : (a) 0; (b) 0.0015; (c) 0.01; (d) 0.05sec

7d depicts the total collapse of the initially intact shelter at  $t=0.05\text{sec}$ . In this figure, the intruding object has already dug into the shelter and the protected object(s) inside will be destroyed shortly.

## Discussions

### Comparison of various schemes

In addition to the artificial joint-based manifold method, there are at least three schemes which can handle variable stress and fracture propagation within a continuous block. They include using a higher-order displacement function in DDA, finite element-based DDA (Shyu 1993 and Chang 1994), and the original form of manifold method (Shi 1992). Tables 2 and 3 compare these schemes with respect to refined stress distribution and fracture propagation capabilities.

Adopting a higher-order displacement function in DDA is the most straight-forward to attain a variable stress field and to indicate a point where stress concentration occurs and cracking initiates. In this case, since straight block sides become curved after deformation, additional nodes must be added along those long straight block sides for better detection of contacts. The computation time and complexity of block integration involved increase with the order of the displacement function used. However, this scheme alone can not resolve a block domain having extremely irregular shape and containing non-crossing cracks or interior blocks. Also because it does not identify and allow non-crossing cracks within a block, it can only simulate the fragmentation of blocks, i.e. a block breaks into two or four pieces instantly.

In a finite element-based DDA, the original block unknowns are now replaced by finite element nodal displacements. To refine a complex block domain containing non-crossing cracks, a versatile mesh generator is required. It is possible for this scheme to simulate fracture propagation if the element boundaries are allowed to break down. The energy loss due to cracking can be modelled by damping or reduction in stress, which may require input from physical tests.

The original code of manifold method developed by Dr. Shi contains a versatile finite element mesh generator which can refine a block domain even containing swirling non-crossing cracks. With adopting adequate failure criteria, the fracture propagation within a solid can be readily simulated. However, the energy loss due to cracking must be represented by the same way as used in the above scheme.

When attaining a refined stress distribution within the same order of solution precision, the total number of degree of freedom required by the artificial joint concept-

Table 2 Comparison of Various Schemes for Stress Variation Capability

Scheme	Computation Need	Complex Block Shape	Inclusions <sup>1</sup>
Higher-order displacement function <sup>2</sup>	- <sup>3</sup>	- <sup>3</sup>	Impossible
FE-based DDA	O.K.	Need good mesh generator	Need good mesh generator
Original manifold method	O.K.	O.K.	O.K.
Artificial joint-based scheme	Higher	O.K.	O.K.

<sup>1</sup> such as non-crossing cracks, holes and interior blocks.

<sup>2</sup> additional nodes needed along the initial long straight block sides.

<sup>3</sup> depending on the order of displacement function.

Table 3 Comparison of Various Schemes for Fracture Propagation Capability

Scheme	Capability	Energy Loss	Cracking Direction
Higher-order displacement function	Fragmentation only	Damping/ $\Delta\sigma$	Any
FE coupling	Possible	Damping/ $\Delta\sigma$	Along element boundaries
Original manifold method	O.K.	Damping/ $\Delta\sigma$	Any
Artificial joint-based scheme	O.K.	Strain energy release of failed contact springs	Along artificial joints <sup>1</sup>

<sup>1</sup> relaxed by allowing the breakage of sub-blocks.

based scheme are about 40% larger than the other schemes, leading to longer computation time. However, this does not remain true when modelling fracture propagation, in which an intact solid is gradually fractured and finally broken into pieces. In this scheme, the energy-loss associated with cracking is naturally modelled by the strain energy release of failed contact springs, with no need of inputting other measured or artificial quantities. The cracking direction is constrained by the artificial joint mesh selected, but this limitation can be overcome by allowing the breakage of sub-blocks according to a certain failure criterion.

### Selection of adequate artificial joint meshes

Solid materials are usually composed of crystals or grains in the micro scale, as ideally shown in Figure 8. The crystal/grain boundaries are essentially softer and weaker than the solid parts of crystal/grains. Therefore, these boundaries are more deformable and represent potential cracking routes. If an artificial joint mesh could match exactly these boundaries or mostly their macro-pattern which would be mappable, then the computation results with an adequate displacement function should be much more compatible to the actual behavior of the solid domain, in terms of mechanical behavior.

For a homogeneous and isotropic solid with unknown crystal boundary pattern, a regular artificial joint mesh should be used, like those as described in the Section of THE ARTIFICIAL JOINT CONCEPT. If a first-order displacement function is used, only those generating triangular sub-blocks (such as Types B and C) should be used. In the case of a higher-order displacement function used, all joint mesh types can be adopted. When a transversely isotropic material is encountered, Type A joint mesh may be applied, with one closely-spaced joint set being parallel to the geological structure like foliation.

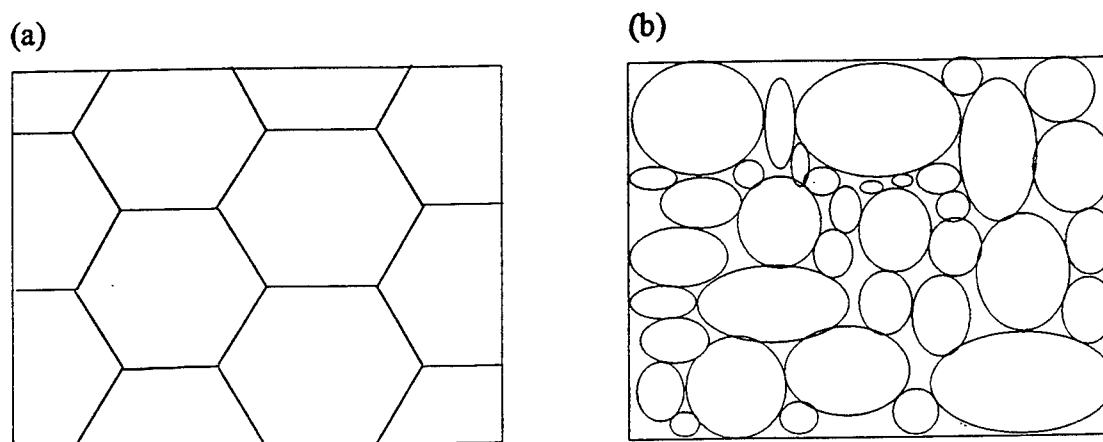


Figure 8. Ideal representation of a solid composed of: (a) crystals; (b) grains

## Conclusions

Since the concept of separating mathematical and physical meshes, the manifold method has been becoming one of the most flexible tools to deal with material problems of complex geometry or mixed phases. This paper presented a 2D simplified version of the manifold method when combined with the *artificial joint* concept. This simplified version can determine the refined stress distribution within selected blocks of any shape or even containing complex interior features, and permit simulating fracture propagation of intact solids. When compared with other schemes, the artificial joint-based scheme seems to be more flexible and practical. Selection of an adequate artificial joint mesh depends upon the understanding of the solid material under investigation.

## Acknowledgements

The author wishes to thank Dr. G.-H. Shi of U.S. Army Corps for sharing his DDA and manifold method work with him and for many invaluable discussions. The author is also indebted to Prof. R. E. Goodman of University of California at Berkeley for continuous inspiration and encouragement during his graduate study.

## References

- Chang, C.-T (1994). " Nonlinear Dynamic Discontinuous Deformation Analysis with finite Element Meshed Block Systems." Ph.D dissertation, Department of Civil Engineering, University of California, Berkeley, CA.
- Ke, T.-C. (1993). " Simulated testing of two-dimensional heterogeneous and discontinuous rock masses using Discontinuous Deformation Analysis." Ph.D dissertation, Department of Civil Engineering, University of California, Berkeley, CA.
- Ke, T.-C. (1995). " Application of DDA to Block-in-Matrix Materials." *Proceedings of the 35th U.S. Symposium on Rock Mechanics*, Lake Tahoe, 4-7 June, 1995: 33-38.
- Rice, J. R. (1968). " Mathematical analysis in the mechanics of fracture." *Fracture, and Advanced Treatise* (2): 191-311.

Shi, G.-H. (1988). " Discontinuous Deformation Analysis - A new numerical model for the statics and dynamics of block systems." Ph.D dissertation, Department of Civil Engineering, University of California, Berkeley, CA.

Shi, G.-H. (1992). " Modeling rock joints and blocks by Manifold Method." *Proceedings of the 32rd U.S. Symposium on Rock Mechanics*, Santa Fe, New Mexico: 639-648.

Shyu, K. (1993). " Nodal-based Discontinuous Deformation Analysis." Ph.D dissertation, Department of Civil Engineering, University of California, Berkeley, CA.



# Single Field Manifold Method using Fourier Function in Wave Propagation Analysis

Max Y. Ma

C.W. Associates dba Geolabs-Hawaii  
2006 Kalihi Street, Honolulu, Hawaii 96819, U.S.A

## 1. Introduction

The wave propagation analysis in an either elastic continuous or discontinuous medium is of great importance in geotechnical, rock and earthquake engineering. However, the limitation of analytical solution due to the complex boundary condition, and numerical error due to the temporal and spatial discretization in Finite Element Method (FEM) analysis for wave propagation of continuous system has posed a long-standing challenge. In addition, the questionable dynamic solution of the existing discontinuous computations methods such as FEM with large number of joint element or Discrete Element Method (DEM) in wave analysis of discontinuous system resulted fairly less confidence among researchers and engineers on the computation results.

Manifold Method (MFM) is a novel numerical method developed by Dr. Gen-hua Shi early 90's (Shi, 1991). Mathematical field (mesh or domain) and physical mesh are defined separately and integrally incorporated to model the continuous or discontinuous material with complex internal geometry like composite structure, inherent or growing crack, sliding failure plane. The mathematical fields may overlap each other, cover the entire material space to form a finite cover system. Mathematical field is always approximated by regular grids, FEM type mesh or randomly distributed convergence regions of series function, whichever is the closest. Since any vibration of a system can be solved into the natural modes of vibration in general case and the natural modes of vibration can be well represented by trigonometric (Fourier) series. Fourier function naturally become the best candidate for representing the mathematical field of MFM in wave propagation analysis. Using Fourier function, FEM type numerical error of spatial discretization can be eliminated since no spatial discretization is needed.

A simplest fashion, one dimensional single field using Fourier function, MFM has been developed and examined for better understanding of MFM's principal, potential and for further development. Single field means that physical mesh is covered by only one single field represented by a displacement function. For instance of a block system, every block is only

covered by a single mathematical field and has no overlaps. In this paper, manifold method using Fourier function is referred as *MFM<sub>f</sub>*. Major formulations are presented and followed by three classic examples. Comparison made in three examples show the great potential, advantage of MFM as well as its beauty.

## 2. The Best Displacement Function

The physical meshes in MFM are based on the external boundary and internal joints or interface and represent the material boundary and joints. The displacement function defines the mathematical field. Integration over the mathematical field is based on the selected displacement function or mathematical mesh, and boundaries defined by physical meshes. Since virtually displacement function can any format as long as it converges in the area of defined mathematical field, the best displacement is possibly to be found. The best displacement means that a displacement function has higher degree accuracy or less degree of approximation to represent the mathematical field with reasonable unknown variables.

A general one-dimensional series approximation can be served as a displacement function:

$$u = \sum_{j=1}^N a_j f_j(x). \quad (1)$$

where  $a_j$  is the coefficient of the series approximation and referred as the deformation variables here. Equilibrium conditions is reached only when the total potential energy ( $\Pi$ ) is a minimum. By minimizing the total potential energy with respect to these variables, a set of simultaneous equilibrium equation is set up as the following equation:

$$\frac{\partial \Pi}{\partial \mathbf{a}} = \begin{pmatrix} \frac{\partial \Pi}{\partial a_0} \\ \frac{\partial \Pi}{\partial a_1} \\ \vdots \\ \frac{\partial \Pi}{\partial a_N} \end{pmatrix} = 0 \quad (2)$$

Minimum can be sought only within the constraint of an assumed displacement pattern, which varies with a finite set of undermined displacement variables. A assumed displacement function with a set of displacement variables limits the infinite degree of freedom and may not be the best approximation for a specific problem. As a result, the true minimum

of the energy may not have been reached. Therefore, the displacement function should be able to represent the true displacement distribution as closely as possible. One beauty and powerful feature of MFM is to incorporate the best displacement function, if it exists, into its formulations. For dynamic problems such as wave propagation, since any vibration of a system can be resolved into the natural modes of vibration in general case and the natural modes of vibration can be well represented by trigonometric (Fourier) series approximation, which can be considered as the best displacement function (see Equation 3).

$$f(x) = a_0 + \sum_{n=1}^N \left[ a_{2n-1} \sin \frac{n\pi(x-x_i)}{2l_i} + a_{2n} \cos \frac{n\pi(x-x_i)}{2l_i} \right] \quad (3)$$

where  $x_i$  is the center point of  $i$ th single field in a  $n$ -field system, or a  $n$ -block system.  $l_i$  is the length of  $i$ th block.  $N$  can be any number of integer. The displacement of point  $x$  can be expressed as:

$$\begin{aligned} u = & a_0 + a_1 \sin \frac{\pi(x-x_i)}{2l_i} + a_1 \cos \frac{\pi(x-x_i)}{2l_i} + \dots \\ & + a_{2n-1} \sin \frac{n\pi(x-x_i)}{2l_i} + a_{2n} \cos \frac{n\pi(x-x_i)}{2l_i} + \dots \\ & + a_{2N-1} \sin \frac{N\pi(x-x_i)}{2l_i} + a_{2N} \cos \frac{N\pi(x-x_i)}{2l_i} \end{aligned} \quad (4)$$

The greater the degrees of freedom of approximation, the more closely the solution approximates to the true one ensuring complete equilibrium will be. To ensure the best approximation, the greater degrees of freedom in terms of larger number of  $N$  in equation 3 is essential. In addition, each field can have its own displacement function, which does not have to be the same type approximation, if necessary, or the same number of  $N$ .

In this paper, formulations of MFM given in program coding-ready format is based on a general Fourier approximation. Any number of  $N$  can be chosen in the final formulations or inputted in the program depending on the specific problem.

### 3. Simultaneous Equations and Submatrices

Equilibrium equations are derived by minimizing the total potential energy  $\Pi$  done by the forces and stresses as Equation 5 for field or block  $i$ :

$$\frac{\partial \Pi}{\partial d_{ri}} = 0 \quad r = 0, 1, \dots, 2N, \quad (5)$$

These equations represent the equilibrium of all the loads and contact forces acting on block  $i$  along the moving direction or deformation defined by  $d_{ri}$ . Equation 6 can be obtained from equation 5:

$$[K_{ii}][D_i] = [F_i] \quad (6)$$

One block has  $2N+1$  degree of freedom or deformation variables.  $K_{ii}$  in the coefficient matrix of equation 6 is a  $(2N+1) \times (2N+1)$  matrix.  $D_i$  and  $F_i$  are  $(2N+1) \times 1$  matrices where  $D_i$  represents the deformation variables. The total potential energy  $\Pi$  is the summation over all the potential energy of individual stress and force. In MFM, the potential energy of each force or stress and their differentiation are computed separately. The differentiation

$$\frac{\partial^2 \Pi}{\partial d_{ri}^2}, \quad r = 0, 1, \dots, 2N, \quad (7)$$

are the coefficients ( $K_{ii}$ ) of unknown  $d_{ri}$  of the equilibrium equation 6 for variables  $d_{ri}$ . The differentiations

$$-\frac{\partial \Pi(0)}{\partial d_{ri}}, \quad r = 0, 1, \dots, 2N, \quad (8)$$

are the free terms  $[F_i]$  of equation 6 after shifting it to the right. Total  $K_{ii}$  and  $F_i$  are the sum of  $K_{ii}$  or  $F_i$  due to the different potential energy.

Simultaneous equations of a  $n$ -block system are written as:

$$\begin{pmatrix} K_{11} & K_{12} & K_{13} & \cdots & K_{1n} \\ K_{21} & K_{22} & K_{23} & \cdots & K_{2n} \\ K_{31} & K_{32} & K_{33} & \cdots & K_{3n} \\ \vdots & \vdots & \vdots & \ddots & \vdots \\ K_{n1} & K_{n2} & K_{n3} & \cdots & K_{nn} \end{pmatrix} \begin{pmatrix} D_1 \\ D_2 \\ D_3 \\ \vdots \\ D_n \end{pmatrix} = \begin{pmatrix} F_1 \\ F_2 \\ F_3 \\ \vdots \\ F_n \end{pmatrix} \quad (9)$$

where  $K_{ij}$  is determined by contact between block i and block j.  $K_{ij}$  is zero if block i and block j do not contact.  $\Pi_c$  is the potential energy due to the contact, so:

$$K_{ij} = \frac{\partial^2 \Pi_c}{\partial d_{ri} \partial d_{sj}}, \quad r, s = 0, 1, \dots, 2N. \quad (10)$$

In equation 10,  $K_{ij}$  and  $F_i$  have a number of submatrices such as elastic submatrice, point loading submatrice, inertial force submatrice, previous stress submatrice, contact submatrice, etc. In this paper, elastic, initial stress, volum loading, point loading, inertial force, fixed point and contact force are given in some detail. The more detail can be found in reference 1. All the submatrices are expressed in the general fashion.

### 3.1 Elastic Submatric

Equation 4 is written in maxtrix form:

$$(u) = \begin{pmatrix} 1 & \sin \frac{\pi(x-x_i)}{2l_i} & \cos \frac{\pi(x-x_i)}{2l_i} & \dots & \sin \frac{N\pi(x-x_i)}{2l_i} & \cos \frac{N\pi(x-x_i)}{2l_i} \end{pmatrix} \begin{pmatrix} a_0 \\ a_1 \\ \vdots \\ a_{2n-1} \\ a_{2n} \\ \vdots \\ a_{2N} \end{pmatrix} \quad (11)$$

donte:

$$[T_i] = \begin{pmatrix} 1 & \sin \frac{\pi(x-x_i)}{2l_i} & \cos \frac{\pi(x-x_i)}{2l_i} & \dots & \sin \frac{N\pi(x-x_i)}{2l_i} & \cos \frac{N\pi(x-x_i)}{2l_i} \end{pmatrix} \quad (12)$$

$$[D_i] = \begin{pmatrix} a_0 \\ a_1 \\ \vdots \\ a_{2n-1} \\ a_{2n} \\ \vdots \\ a_{2N} \end{pmatrix} \quad (13)$$

Then:

$$\begin{pmatrix} u \end{pmatrix} = [T_i][D_i] \quad (14)$$

Strain ( $\epsilon_x$ ) of any point in block is the differntial of  $u$ :

$$\epsilon_x = \begin{pmatrix} \frac{\partial u}{\partial x} \end{pmatrix} = \begin{pmatrix} 0 \\ \frac{\pi}{2l_i} \cos \frac{\pi(x-x_i)}{2l_i} \\ -\frac{\pi}{2l_i} \sin \frac{\pi(x-x_i)}{2l_i} \\ \vdots \\ \frac{N\pi}{2l_i} \cos \frac{N\pi(x-x_i)}{2l_i} \\ -\frac{N\pi}{2l_i} \sin \frac{N\pi(x-x_i)}{2l_i} \end{pmatrix} \begin{pmatrix} a_0 & a_1 & a_2 & \cdots & a_6 \end{pmatrix} = [D][P] \quad (15)$$

The potential energy due to elastic stresses is expressed:

$$\begin{aligned} \Pi_e &= \int \frac{1}{2} \epsilon_x \sigma_x dx \\ &= \int \frac{1}{2} \epsilon_x E \epsilon_x dx \\ &= \frac{1}{2} \int \int [D_e]^T [P_e]^T [E] [P_e] [D_e] dx \\ &= \frac{1}{2} [D_e]^T \left( \int [P_e]^T [E] [P_e] dx \right) [D_e] \end{aligned} \quad (16)$$

$$k_{rs} = \frac{\partial^2 \Pi_e}{\partial d_{ri} \partial d_{si}} = \int ([P_e]^T [E] [P_e] dx = [E] \left( \int [P_e]^T [P_e] dx \right) \rightarrow [K_{ii}] \quad (17)$$

Donte

$$[A] = \int [P_e]^T [P_e] dx \quad (18)$$

$$a_{pq} = \begin{cases} \frac{n^2 \pi^2}{4l_i} & p = q = 1, 2, \dots, 2N \\ Q & p = 2n-1 \text{ \& } q = 2m-1 \text{ or } p = 2n \text{ \& } q = 2m, n \leq m \leq 2N \\ 0 & \text{others} \end{cases} \quad (19)$$

$$Q = (-1)^{p+1} \frac{mn\pi}{4l_i} \left[ \frac{1}{m+n} \sin \frac{(m+n)\pi}{2} + (-1)^{p+1} \frac{1}{m-n} \sin \frac{(m-n)\pi}{2} \right] [1 + (-1)^{p+q}] \quad (20)$$

### 3.2 Initial Stress

The initial stress ( $\sigma_x^i$ ), which is not necessarily constant along the block, is a function of  $x$  and can be represented by a Fourier approximation function in term of the initial strain and Young's modulus:

$$\sigma_x^i = E \epsilon_x^i = E[P][D^i] \quad (21)$$

where  $[P]$  is the same as the equation 15 and  $[D^i]$  is  $(2N+1) \times 1$  matrix depending on the initial stress. The potential energy of initial stress is

$$\Pi_i = - \int \epsilon_x \sigma_x^i dx = -[E] \int [D_e]^T [P_e]^T [P^i] [D^i] dx \quad (22)$$

Minimizing  $\Pi_i$  by taking the derivatives:

$$\begin{aligned} f_r &= - \frac{\partial \Pi_i(0)}{\partial d_{ri}} \\ &= [E] \int [P_e]^T [P^p] [D^p] dx \rightarrow [F_i] \\ &= E \int_{x_i-l_i}^{x_i+l_i} \left( \frac{\pi}{2l_i} \right)^2 (1 + 2^2 + 3^2 + \dots + N^2) [D^p] dx \\ &= E \left( \frac{\pi^2}{12l_i} \right) N(N+1)(2N+1) [D^p] \rightarrow [F_i] \end{aligned} \quad (23)$$

which is added to  $F_i$  in the global equation 9.

### 3.3 Point Loading Matrix

The potential energy due to the point load ( $F_x$ ) at point  $x$  is

$$\Pi_p = -F_x u = -[D_i]^T [T_i]^T F_x \quad (24)$$

where  $u$  is the displacement of loading point. To minimize  $\Pi_p$ , the derivatives are computed:

$$\begin{aligned} f_r &= -\frac{\partial \Pi_p(0)}{\partial d_{ri}} \\ &= [T_i]^T F_x + \longrightarrow [F_i] \end{aligned} \quad (25)$$

This  $(2N+1) \times 1$  submatrix is added in the global equation 9

### 3.4 Volume Loading Matrix

Volume loading ( $f_x$ ) is constant and acts on the block with length of  $l_i$ . The potential energy due to this loading is

$$\Pi_w = - \int u f_x dx = - \int [D_i]^T [T_i]^T f_x dx = - [D_i]^T f_x \left( \int [T_i]^T dx \right) \quad (26)$$

The derivatives of  $\Pi_w$  are taken to minimize the potential energy:

$$\begin{aligned} f_r &= -\frac{\partial \Pi_w}{\partial d_{ri}} \\ &= \int [T_i]^T dx F_x + \longrightarrow [F_i] \end{aligned} \quad (27)$$

$$f_r = \begin{cases} 2l_i f_x & r = 0 \\ \frac{4l_i f_x}{n\pi} \sin \frac{n\pi}{2} (1 + (-1)^r) & r = 2n \text{ or } 2n-1, n = 1, 2, \dots, N, \end{cases} \quad (28)$$

which is added to  $[F_i]$  in the global equation 9.

### 3.5 Matrix of Inertia Force

The inertia force acting on the point of  $x$  can be written as:

$$F_x = -M \frac{\partial u(t)}{\partial t^2} \quad M \text{ is unit mass} \quad (29)$$

and results in the time dependent displacement,  $u(t)$ . The potential energy of inertia force over the block is:



$$\Pi_i = - \int u F_x dx = \int M u \frac{\partial^2 u(t)}{\partial t^2} dx \quad (30)$$

where:

$$\frac{\partial^2 u(t)}{\partial t^2} = [T_e] \frac{\partial^2 [D_i]}{\partial t^2} \quad (31)$$

Using Taylor approximation to obtain the following equation:

$$[D] = [D(\Delta)] = D(0) + \Delta \frac{\partial D(0)}{\partial t} + \frac{\Delta^2}{2} \frac{\partial^2 D(0)}{\partial t^2} \quad (32)$$

where  $\Delta$  is time interval of this time step and  $[D]$  is the displacement at the end of this time step. The displacement at the beginning of time step,  $D(0)$  is zero. This equation becomes:

$$[D] = \Delta \frac{\partial D(0)}{\partial t} + \frac{\Delta^2}{2} \frac{\partial^2 D(0)}{\partial t^2} \quad (33)$$

Assuming the constant acceleration at each time step, so Equation 33 can be written as:

$$\frac{\partial^2 D(t)}{\partial t^2} = \frac{2}{\Delta^2} [D] - \frac{2}{\Delta} \frac{\partial D(0)}{\partial t} = \frac{2}{\Delta^2} [D] - \frac{2}{\Delta} [V_0] \quad (34)$$

$[\frac{\partial D_e(0)}{\partial t}]$  is the velocity,  $[V_0]$  at the beginning of the time step. The equation 34 becomes:

$$\begin{aligned} \Pi_i &= M \int [D]^T [T]^T \left( \frac{\partial^2 u(t)}{\partial t^2} \right) dx \\ &= M [D]^T \left( \int [T]^T [T] dx \right) \left( \frac{\partial^2 D(t)}{\partial t^2} \right) \\ &= M \frac{2}{\Delta^2} [D] [D]^T \left( \int [T]^T [T] dx \right) - M \frac{2}{\Delta} [D]^T \left( \int [T]^T [T] dx \right) [V_0] \end{aligned} \quad (35)$$

To reach equilibrium,  $\Pi_i$  is minimized with respect to displacement variables.

$$\frac{2M}{\Delta^2} \left( \int [T_e]^T [T_e] dx \right) + \longrightarrow [K_{ii}] \quad (36)$$

$$\frac{2M}{\Delta} \left( \int [T_e]^T [T_e] dx \right) [V_0] + \longrightarrow [F_i] \quad (37)$$

which are added into the global equations. if denote  $[B] = \int [T_e]^T [T_e] dx$

$$b_{pq} = \begin{cases} 2l_i & p = q = 0 \\ \frac{4l_i f_x}{n\pi} \sin \frac{n\pi}{2} [1 + (-1)^p] & p = 0 \text{ or } q = 0 \\ l_i & p = q \\ Q & p = 2n \text{ and } q = 2m \text{ or } q = 2n-1 \text{ and } q = 2m-1 \\ 0 & \text{others} \end{cases} \quad (38)$$

where  $n, m = 1, 2, \dots, N$  and  $Q$  is expressend as:

$$Q = b_{pq} = (-1)^p \frac{l_i}{\pi} \left[ \frac{1}{m+n} \sin \frac{(m+n)\pi}{2} + (-1)^p \frac{1}{m-n} \sin \frac{(m-n)\pi}{2} \right] [1 + (-1)^{p+q}] \quad (39)$$

### 3.6 Displacement Constraint at a Point

As a boundary condition, some of the blocks are fixed at specific points. The constraint can be applied to the block system with very stiff springs. Assume the fixed point  $x_f$ . so:

$$u(x) = 0$$

The stiffness of springs is  $p$ . The spring forces are

$$f_x = -pu \quad (40)$$

The strain energy of the spring is  $\Pi_m$ , then

$$\begin{aligned} \Pi_m &= \frac{p}{2} u^2 \\ &= \frac{p}{2} [D_i]^T [T_i]^T [T_i] [D_i] \end{aligned} \quad (41)$$

The derivatives are computed to minimize the spring strain energy  $\Pi_m$ :

$$k_{rs} = \frac{\partial^2 \Pi_m}{\partial d_{ri} \partial d_{si}} = \frac{K_n}{2} \frac{\partial^2}{\partial d_{ri} \partial d_{si}} [D_i]^T [T_i]^T [T_i] [D_i] \quad (42)$$

which is added to  $[F_i]$  in the global equation 9.

$$p[T_i]^T [T_i] + \longrightarrow [K_{ii}] \quad (43)$$

### 3.7 Contact Spring

Assume there are two points ( $x_i$  of block i and  $x_j$  of block j) contacting. the inte-penetration distance is d as following:

$$d = x_i + u_i - x_j - u_j$$

Denote the stiffness of the spring as  $k_n$  and the strain energy of the contact spring is

$$\begin{aligned}\Pi_k &= \frac{1}{2} K_n d^2 \\ &= \frac{k_n}{2} (x_i + u_i - x_j - u_j)^2 \\ &= \frac{k_n}{2} (d_0 + u_i - u_j)^2 \\ &= \frac{k_n}{2} (d_0 + [D_i][T_i] - [D_j][T_j])^2\end{aligned}\tag{44}$$

where  $d_0 = x_i - x_j$ , the derivatives of  $\Pi_k$ :

$$k_{rs} = \frac{\partial^2 \Pi_k}{\partial d_{ri} \partial d_{sj}} = \frac{K_n}{2} \frac{\partial^2}{\partial d_{ri} \partial d_{sj}} [D_i]^T [T_i]^T [T_i] [D_i] \tag{45}$$

$$K_n [T_i]^T [T_i] + \longrightarrow [K_{ii}] \tag{46}$$

$$K_n [T_i]^T [T_j] + \longrightarrow [K_{ij}] \tag{47}$$

$$K_n [T_j]^T [T_j] + \longrightarrow [K_{jj}] \tag{48}$$

The derivatives of  $\Pi_k$  at 0:

$$\begin{aligned}f_r &= -\frac{\partial \Pi_k(0)}{\partial d_{ri}} \\ &= -\frac{\partial}{\partial d_{ri}} (K_n [D_i]^T [T_i])\end{aligned}\tag{49}$$

$$-K_n d_0[T_i] + \longrightarrow [F_i] \quad (50)$$

$$K_n d_0[T_j] + \longrightarrow [F_i] \quad (51)$$

which are added into the global equations 9.

## 4. Illustrative Examples

Three examples presented here are simple and classic. The detail of first two examples can be found in Reference 2. The first case presents both static and dynamic solution. In the second example, the original solution of Discontinuous Deformation Analysis (DDA) was computed along with  $MF M_f$  and analytical solution. The third examples, although extremely simple to save analytically, is a source of considerable insight as regards impact and separation phenomena. Discussion will be given with regard to the contact or impact behavior under influence of displacement function.

### 4.1 Force Suddenly Removed in a Beam with Fixed Ends

There are two stages in this case. At the beginning the constant force was applied at middle points of beam which is a static case (Figure 1), then the force was suddenly removed. The initial displacement essentially caused the vibration inside beam.

As displacement under a static loading,  $P$ , showed in Figure 2,  $MF M_f$  provides fairly accurate results. When larger number of  $N$  ( $N=24$ ) was used,  $MF M_f$  displacement is almost identical with the theoretical solution, even in a static case. After  $P$  is suddenly removed, vibration due to the initial displacement within beam starts. The time history of displacement at middle point of beam was computed by  $MF M_f$  with  $N = 3$  and is compared with solution provided by Timoshenko and Young(1955), which is:

$$\begin{aligned} \varepsilon &= \frac{P}{2AE} \\ u &= \frac{4\varepsilon l}{\pi^2} \sum_{N=1,3,..} \frac{(-1)^{\frac{N-1}{2}}}{i^2} \sin \frac{N\pi x}{l} \cos \frac{N\pi at}{l} \end{aligned} \quad (52)$$

where  $A$  is the section area of beam,  $l$  is the length,  $\gamma$  represents density and  $a = \sqrt{Eg/\gamma}$ .  $N$  of 30 was used in Timoshenko's solution. It is noted that the peak displacement has small attenuation. It is because of time disceretation in  $MF M_f$  using the first order of Taylor approximation (Equation 32). Higher order of time discretation will reduce such attenuation. The time interval used in this case was 1/10,000 sec. It appeared to have little affect on such attenuation if time interval is significantly reduced.

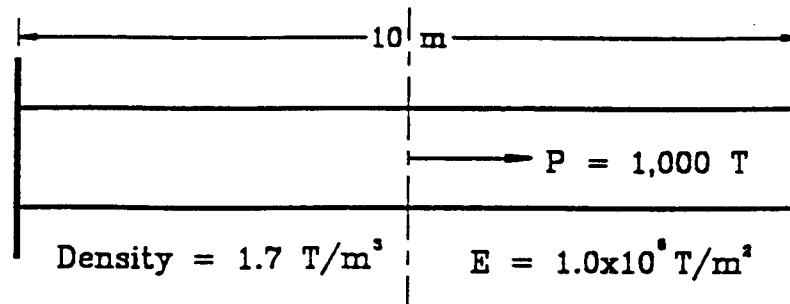


Figure 1. Configuration of Example 1.

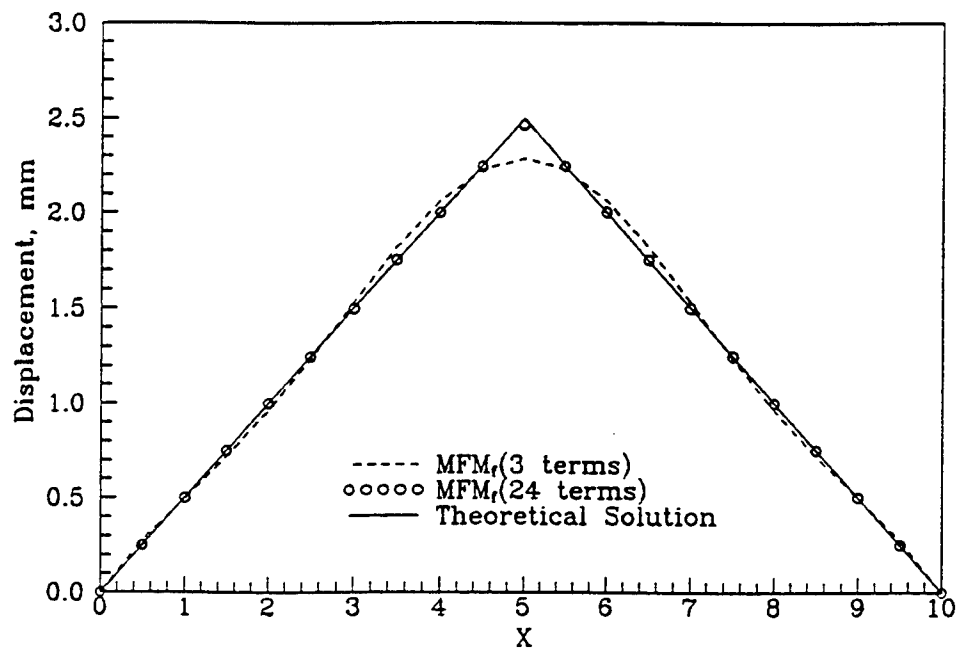


Figure 2. Static Displacement.

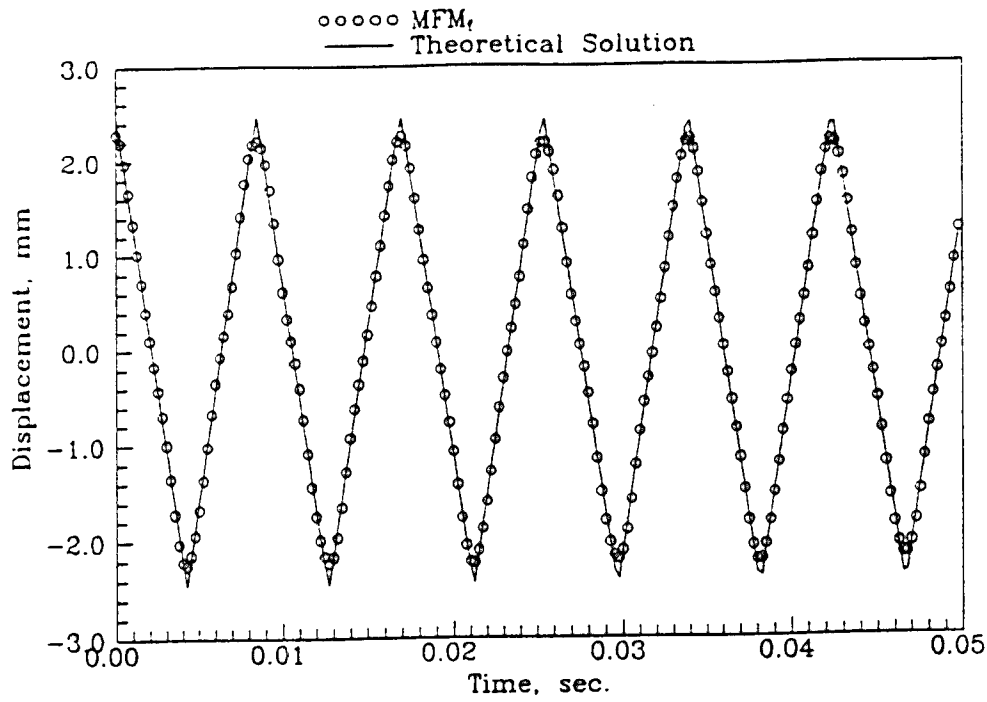


Figure 3. Time History of Middle Point Displacement.

#### 4.2 Forced Longitudinal Vibrations of a Beam

In this case (Figure 4), the left end of which is a fixed and to the right end of which a disturbing force  $P$  is applied. The solution provided by Timoshenko and Young(1955) is :

$$u = \frac{8glP}{a^2\pi^2\gamma A} \sum_{N=1,3,5,\dots} \frac{(-1)^{\frac{N-1}{2}}}{N^2} \sin \frac{N\pi x}{2l} \left(1 - \cos \frac{N\pi at}{2l}\right) \quad (53)$$

where  $a$ ,  $l$ ,  $\gamma$  and  $A$  are defined as the same as the first case. Static displacement was computed and shown in Figure 5. In addition to the theoretical and  $MFM_f$  solution. This case was computed by DDA (2.0) as well. The current DDA versions can be considered as a single field MFM using the first order Taylor displacement function. Displacement time history of middle point of beam from three solution are shown in Figure 6. There were thirty terms of fourier approximation used in Timeoshenko's solution and only three terms incorporated in  $MFM_f$ . The solution from DDA was quite different with other two solutions in terms of frequency when the vibration amplitude are close. The more evidence can be found in Figure 7, which suggests that the points in blocks vibrate as same phase and different amplitude, in other words, the wave can not propagate through the block.  $MFM_f$  takes the benefit of the fourier approximation to characterize the wave propagation inside block as demonstrated in Figure 8. Figure 9 illustrates the displacement distributions at 0.01 and 0.04 sec. The displacement in only small portion of beam have slightly difference in Timeoskenko ( $n=30$ ) and  $MFM_f$  ( $n=3$ ) solution.

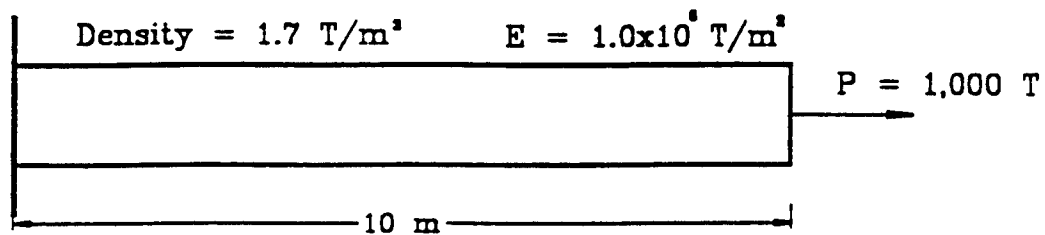


Figure 4. Configuration of Example 2.

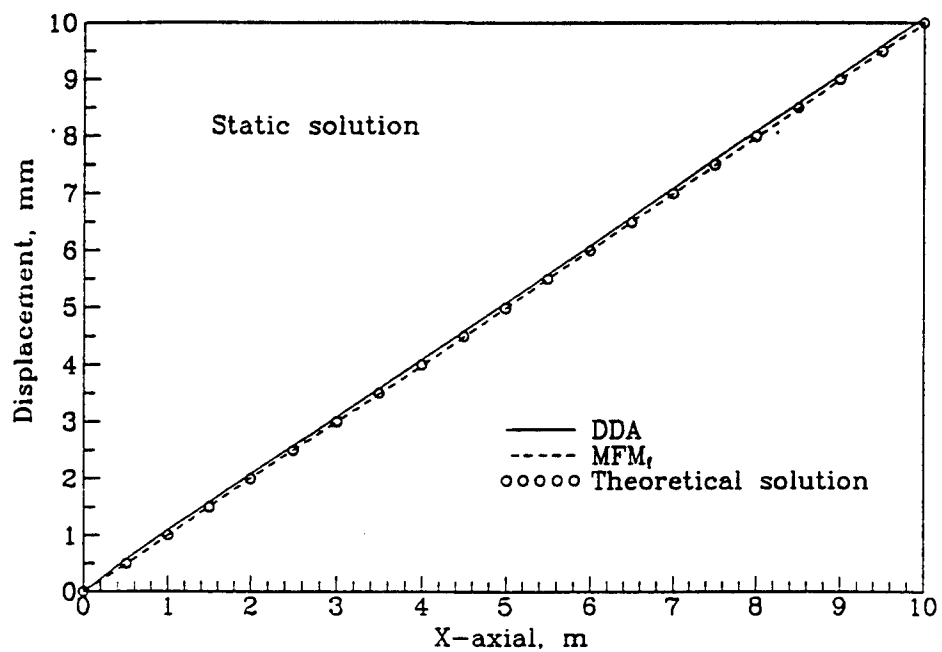


Figure 5. Static Displacement.

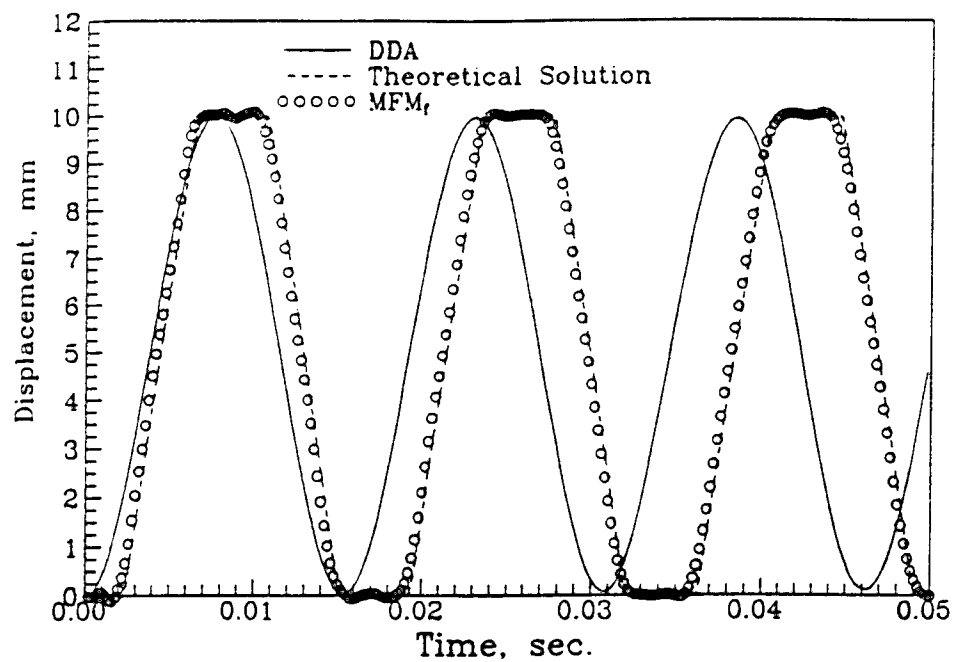


Figure 6. Time History of Middle Point Displacement.

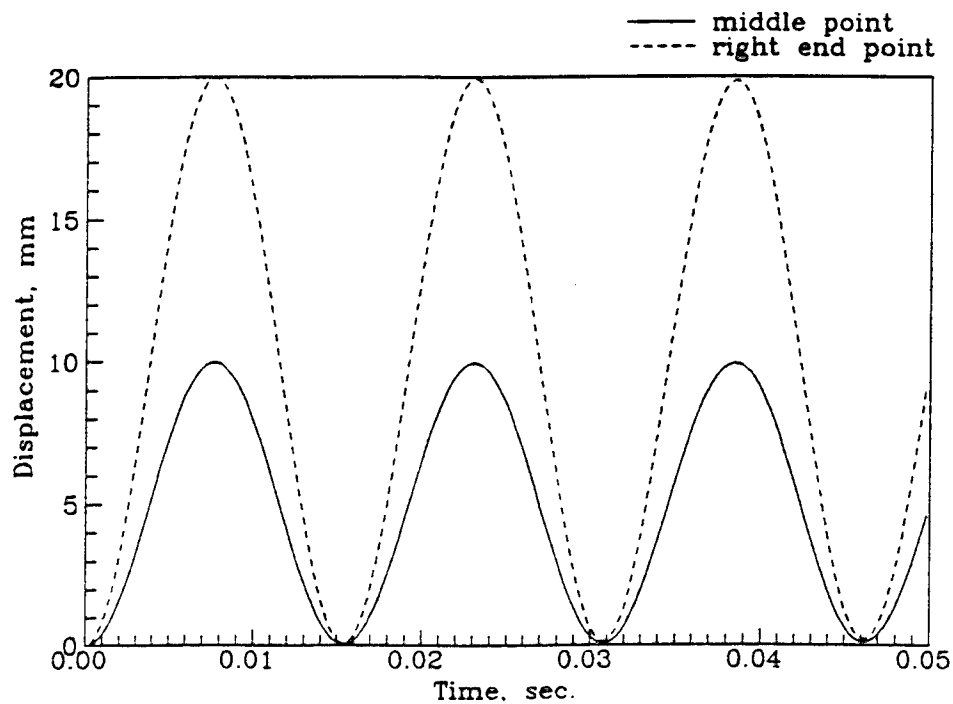


Figure 7. Time History of Displacement (DDA).



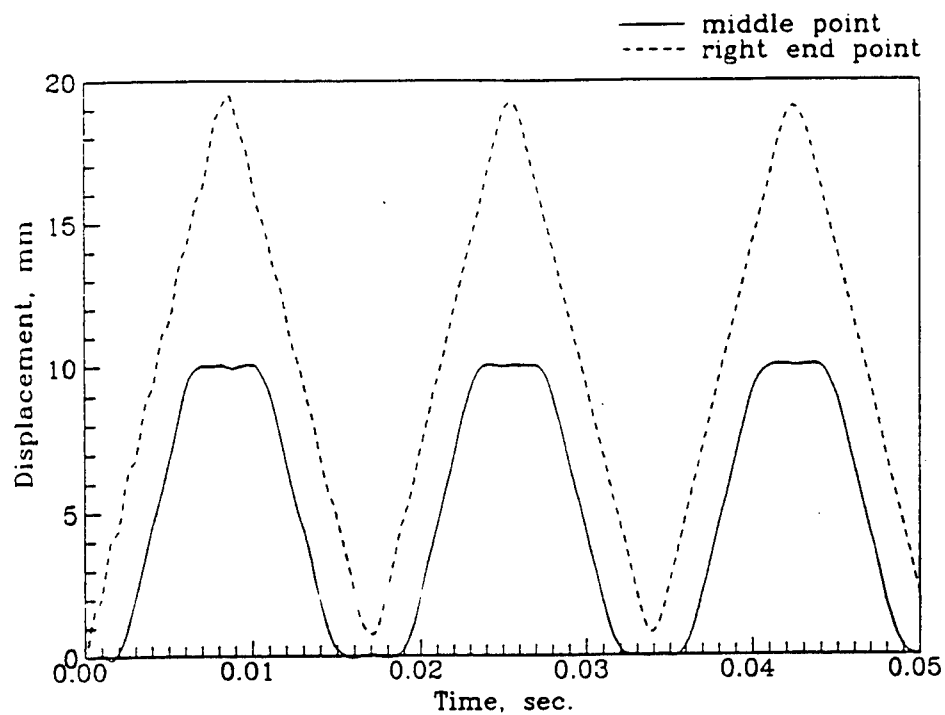


Figure 8. Time History of Displacement ( $MFM_f$ ).

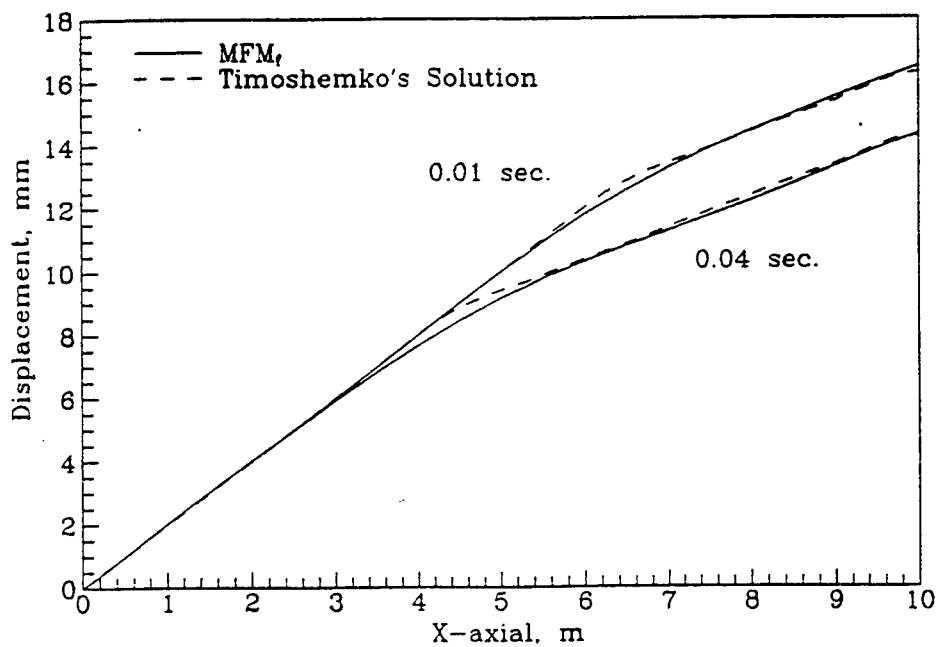


Figure 9. Displacement at 0.01 sec. and 0.04 sec.

### 4.3 Impact of Two Identical Elastic Beam

Previous examples were only a single block problem. In this example, two-beam system has been investigated in case of one beam moves at constant velocity toward to another rest beam. It involved the impact at contact and consequence wave propagation in each beam. Two identical beams with  $E=100$ ,  $\gamma = 0.01$  and length  $l=10$  were lined up horizontally. This problem has been investigated using FEM by Huges et al.(1977). Comparison between two solutions were made.

Figures 10a-10d show the time history of displacement, velocity at the contact point, contact force and stress at middle point of beam 2 obtained from  $MFM_f$  with  $N = 9$ . The negative stress means the compression stress. As seen in figures, not only  $MFM_f$  results are comparable with Huges et al.'s solution, but also present the stress oscillation after separation, which was difficult to capture numerically, especially with coarse grid mesh in FEM solution as pointed by Huges et al. (1977).

The contact period computed by  $MFM_f$  is about 0.205 sec. compared to 0.2 sec. of theoretical solution. The contact algorithm of  $MFM_f$  is different from one used by Huges et al. and is a spring approximation as described in section 3.7. The contact spring stiffness is an essential element in this computation. The more stiff of contact spring will result in the higher maximum the contact force and less contact duration. It is consist with the physical observations in general cases to assign it as the Young's modulus. There was a contact element in Huges et al.'s solution. The contact behavior of two beam was mainly controlled by this no-exist element based on 'theoretical estimation'. However, such approach will be much less effective when slightly complicated contact problem is considered. On another hand, spring approximation of contact is effective, simple and has been adopted in many discontinuous methods. Moreover, when a great deal of attention was given to improve the contact model alone, it was found from this case, the approximation of contact body seems to be a fact which influences the contact behavior. Figures 11 and 12 show the contact force and stress history when only  $N = 3$  was used. More rough contact force and less smooth stress were resulted from reducing  $N$  value from 9 to 3. It may indicate that contact behavior can be improved by increasing number of freedom in the approximation.

In this case, there are total 19 unknown variables in  $MFM_f$  compared to 41 unknown variables in FEM (Huges et al., 1977). Without spatial discretization,  $MFM_f$  avoids the numerical error induced by such discretization, which has been a major concern in wave propagation analysis using FEM.

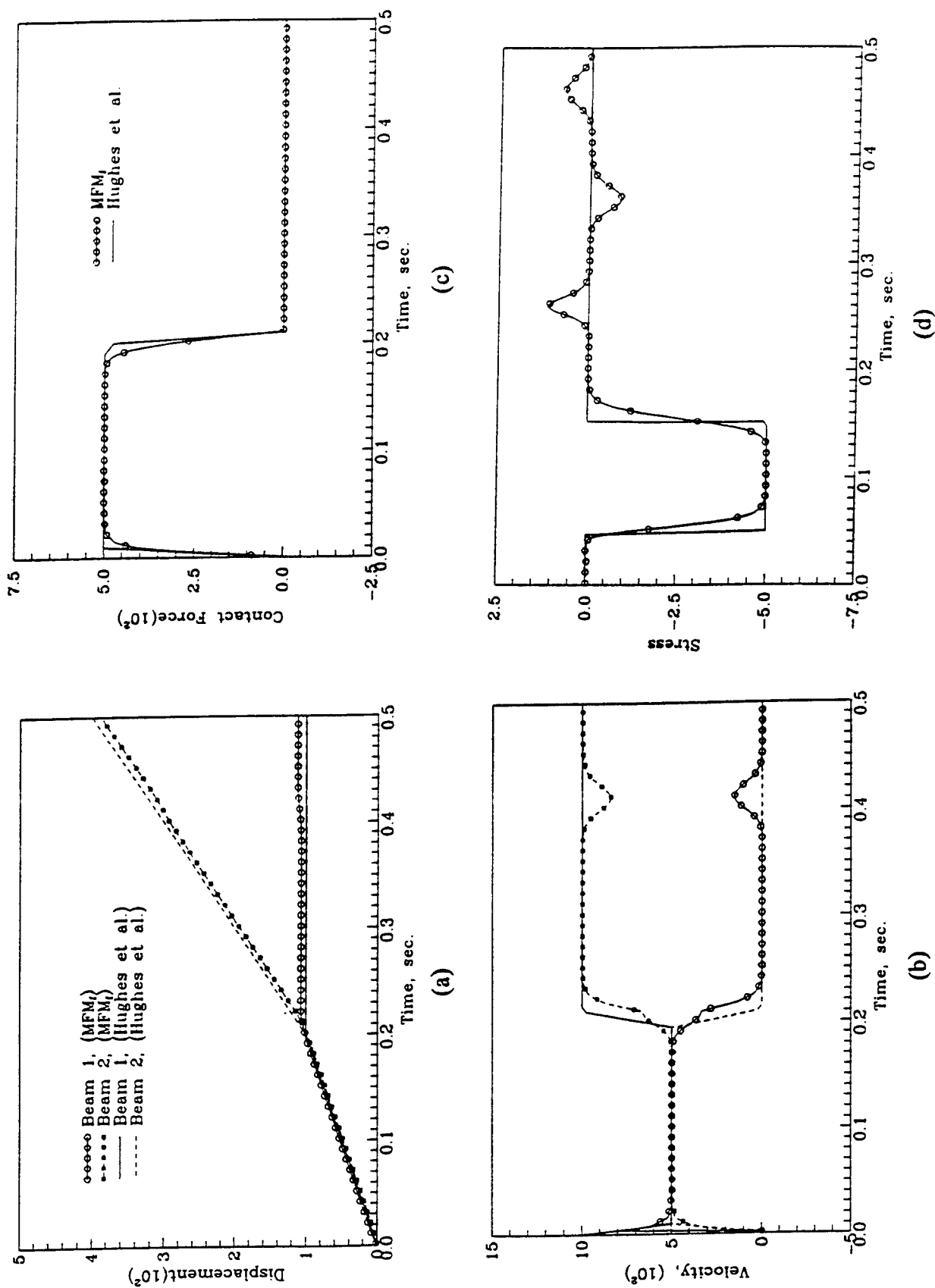


Figure 10. Time History of Contact Point Displacement (a), Velocity (b), Contact Force (c) and Stress at Middle Point of Beam 2 (d).

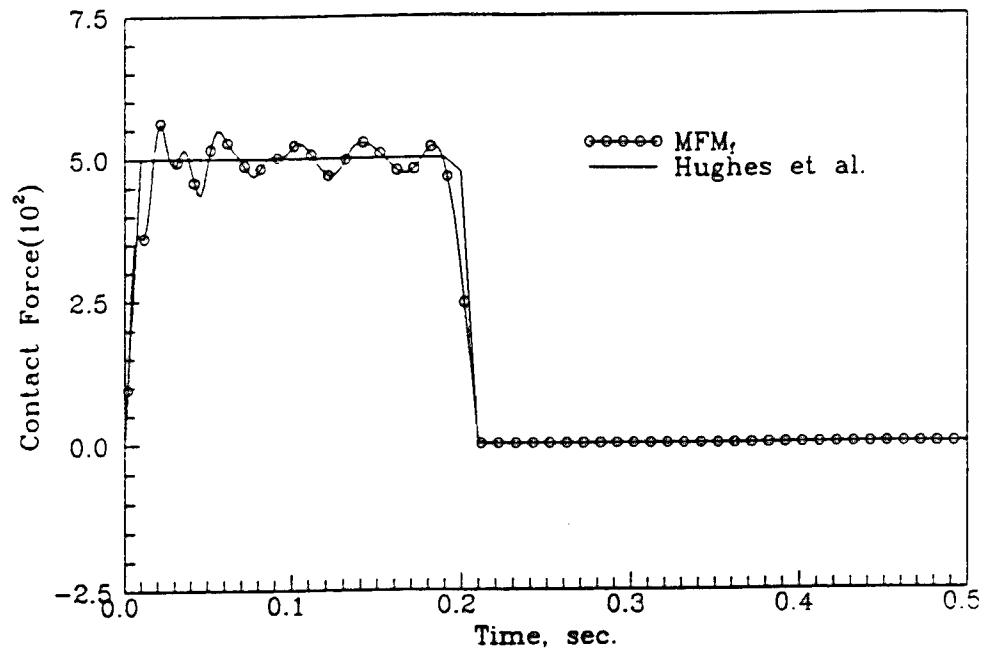


Figure 11. Time History of Contact Force ( $N = 3$ ).

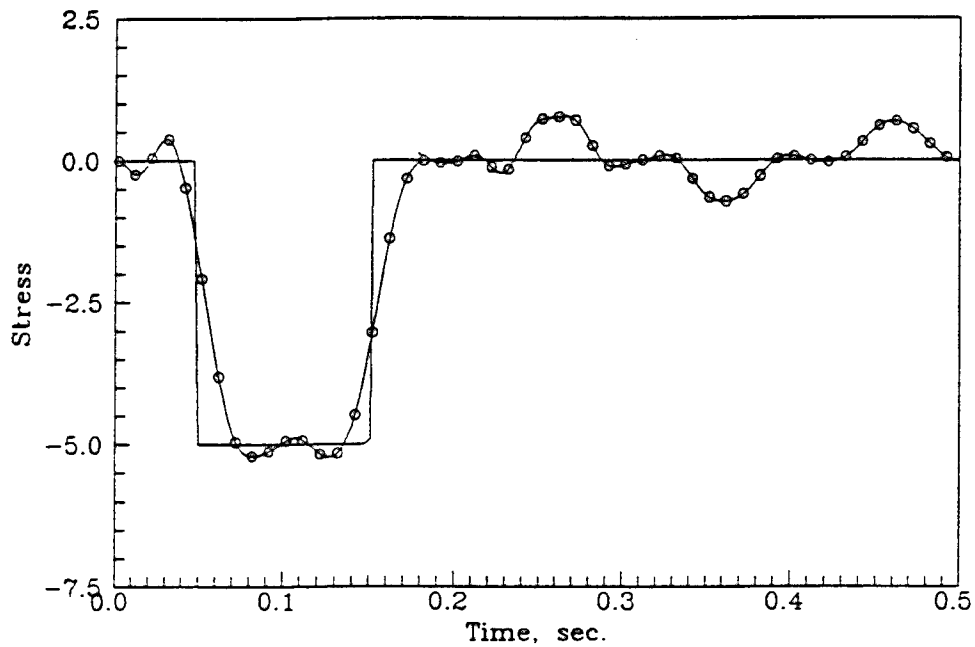


Figure 12. Time History of Stress at Middle Point of Beam 2 ( $N=3$ ).

## 5. Closure Remarks

The study presented in this paper demonstrates that Manifold method with Fourier displacement function can provide a reasonable solution with higher degree of accuracy, specially for wave propagation analysis. From example 3, it is noted that Fourier function with high number of terms can facilitate to model the contact or impact behavior in a more realistic way.

Implementation and development of manifold theory in numerical computation open a new avenue to reach a point, where the numerical method can be truly used in design and analysis for real world problems, especially for failure analysis, composite structure analysis, contact or impact problem in civil engineering. Significance of this new movement is far beyond what were presented in this paper. This study is only part of starting point for further understanding and development.

## Acknowledgments

This study was initiated in late 1992 with funding of National Science Foundation (Grant No. MSS-9021973) at Clarkson University, Potsdam, New York. Constructive input and suggestions provided by Drs. An-Bin Huang and Jone S. Lee are highly appreciated. Support from C.W. Associates dba Geolabs-Hawaii on this study is gratefully acknowledged.

The writer would like to thank Dr. Gen-hua Shi for his continued encouragement and guidance in past six years. Without his support, this study would not have been possible.

## References

- Shi, G. (1991). "Manifold Method of Material Analysis." Proceeding of the 9th Army Conference on Applied Mathematics and Computing.
- Timoshenko, S. and Young, D.H. (1955) "Vibration Problems in Engineering." D. Van Nostrand Company, Inc. Princeton, New Jersey.
- Hughes, T.J., Taylor, R.L., Sackman, J.L., Curnier, A. and Kanoknukulchai, W. (1977). "A Finite Element Method for a Class of Contact-Impact Problems." Computer Method in Applied Mech. and Eng., No.8, 249-276.

# Approximation Theories for the Manifold Method

Chung-Yue Wang, Jopan Sheng, Ming-Hong Chen, and Ching-Chiang Chuang

Department of Civil Engineering  
National Central University  
Chungli, 320, Taiwan, R. O. C.

## Abstract

Approximation theories for the manifold method (MM) which is applicable to the analysis of dynamic, continuous or discontinuous, large displacement deformation of materials is studied. In this paper, finite covers concept proposed by the manifold method is used to evaluate the approximation theories of finite element method and the moving least-squares method (MLSM). This comparison study provides some reference information for the further development of the manifold method. The finite cover concept can provide a more general sense to classify those existed approximation methods like finite element method (FEM), finite difference method (FDM), discontinuous deformation analysis method (DDA) and diffuse element method (DEM). In contrast to the conventional approximation methods, two independent meshes called mathematical mesh and physical mesh are introduced by the manifold method to gain more freedom in selecting effective approximation functions and conducting integral evaluation during the simulation process. At the end of this paper, a modified manifold method with adaptive covers and quadrature cells is proposed for future study.

## Introduction

Due to mechanical loading, chemical reactions, thermal treatments during manufacturing process or damage during service, there might be discontinuities existed in the physical field of engineering system at different scope levels. Complicated behaviors due to these discontinuities lead to difficulties of interpretation and analysis. In the past few years, topics concerning discontinuities like the behaviors of jointed rock masses, ice plates, granular materials, delamination of layered medium, blasting fragmentation and

damage/fracture progression of materials etc. have been worked by a number of researchers and engineers.

It has become clear that researchers are expedient to explore methods which may simulate the whole deformation process of solid bodies within a mechanical or electromagnetic physical field from a state of continuous system to a discontinuous one. According to Rice and Ting's (1992) classification, there are two common groups of numerical methods used in the study of structural response. One of these groups can be classified as numerical analysis and consists of the finite element method (FEM), finite difference method (FDM) and boundary element method (BEM), etc. These techniques are intended mainly for the pre-failure and failure analysis of a continuous medium by giving quantitative predictions of stress, strain, and displacement values. The second group can be termed numerical simulation and consists of the finite block method, distinct element method, discontinuous deformation analysis method (DDA), etc. This group is utilized chiefly in modeling discontinuous media to qualitatively recreate the behavior of granular or jointed materials through motion histories using the contact forces acting on the discrete bodies (Babosa and Ghaboussi 1990; Heuze, et. al.; Shi 1988; Cundall 1974; Munjiza 1992).

In the past few years, the author with his colleagues have applied Shi's DDA method to study some fundamental problems in solid mechanics (Wang et al.; Chen et al.) Through those study, it is found that DDA method with its outstanding contact detection and numerical simulation algorithm can well model the dynamic interaction behaviors among deformable bodies. But in the original DDA formulation (Shi 1988), constant strain field is assumed in each block that will lead some computational difficulties and inaccuracy when dealing problems of blocks with complicated strain fields. Due to this disadvantage, it is a natural thought of attaching a finite element mesh on the block to have a better deformation description. This concept also motivates Shi's development of his newly proposed manifold method (Shi 1991). The manifold method retaining most of the DDA's attractive features can be identified as the generalized finite element and discontinuous deformation analysis method. From the theory of manifold method, one can realize its potential of solving various challenging mechanical problems up to date in an effective and straightforward manner. In this paper, it is planned to present some point of views extended from the finite element method (Axelsson and Barker 1984), diffuse element method (Nayroles et al. 1992) and manifold method (Shi 1991) to evaluate the correspondence among these three methods. Finally, a modified manifold method is proposed based on the approximation theories discussed in this paper. This new method is designed to have the capability of analyzing continuous/discontinuous deformation of solid bodies accurately and efficiently.

## **Approximation Theories**

The basic concept of the finite element method is not new. Kardestuncer (1988) had the following statements: " Today's understanding of the finite-element method, however, is finding an approximate solution to a boundary- and initial-value problem by assuming that the domain is divided into well defined subdomains (element) and that the unknown functions of the state variable is defined approximately within each element. With these individually defined functions matching each other at the element nodes or at certain points at the interfaces, the unknown function is approximated over the entire domain." It can be concluded that the approximation theory play a paramount role in the Galerkin type analyses. The values of physical variable at nodal points or at certain points will be the basic unknown parameters of the problem, just as in the simple, discrete, structural analysis.

Recently, there are two similar approximation theories have been developed and can be considered as the generality of the finite element method. One group is the diffuse element method introduced by Nayroles et al. (1992) and the element-free Galerkin method developed by Belytschko et al. (1994); the other group is the manifold method developed by Shi (1991). Both groups of methods are very interesting and promising. In Shi's manifold method, the finite covers theory in mathematics is introduced to develop the approximation theory of unknown functions. Two independent meshes called mathematical mesh and physical mesh were created to formulate the whole numerical analysis procedure. In diffuse element method, only a group of nodes and a boundary description is needed to develop the Galerkin equations. It is surprising to realize that there are some common features existed between these two independently developed methods. Hence, the main goal of present paper is to reinvestigate and readdress the manifold method imbued with the superiority of the diffuse element method and the element-free Galerkin method.

## **Basic concepts of the manifold method**

### **Finite covers approximation theory**

For the manifold method, the local displacement function is independently defined on individual covers. Local displacement functions can be connected together to form a global displacement function on the whole material volume. As shown by Fig. 1, manifolds connect many individual folded domain together to cover the entire material volume. The global displacement function is general and flexible enough to represent the



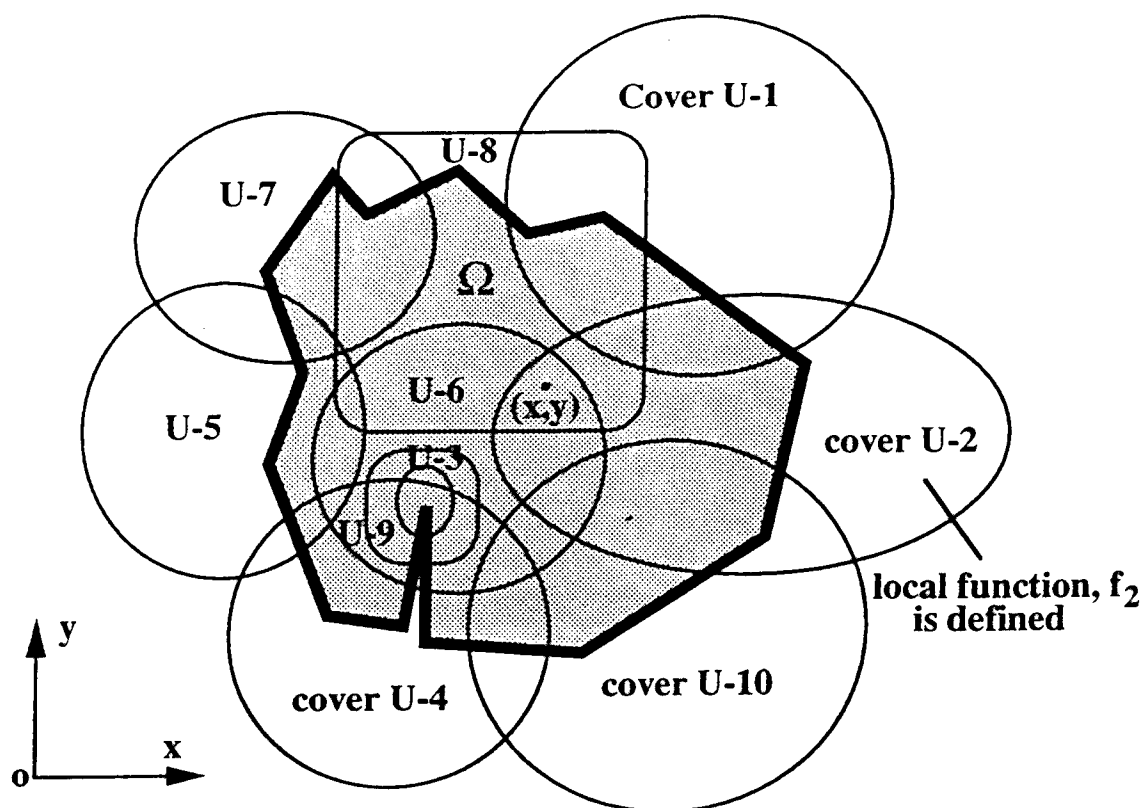


Fig. 1 A material volume is covered by individual folded domains.

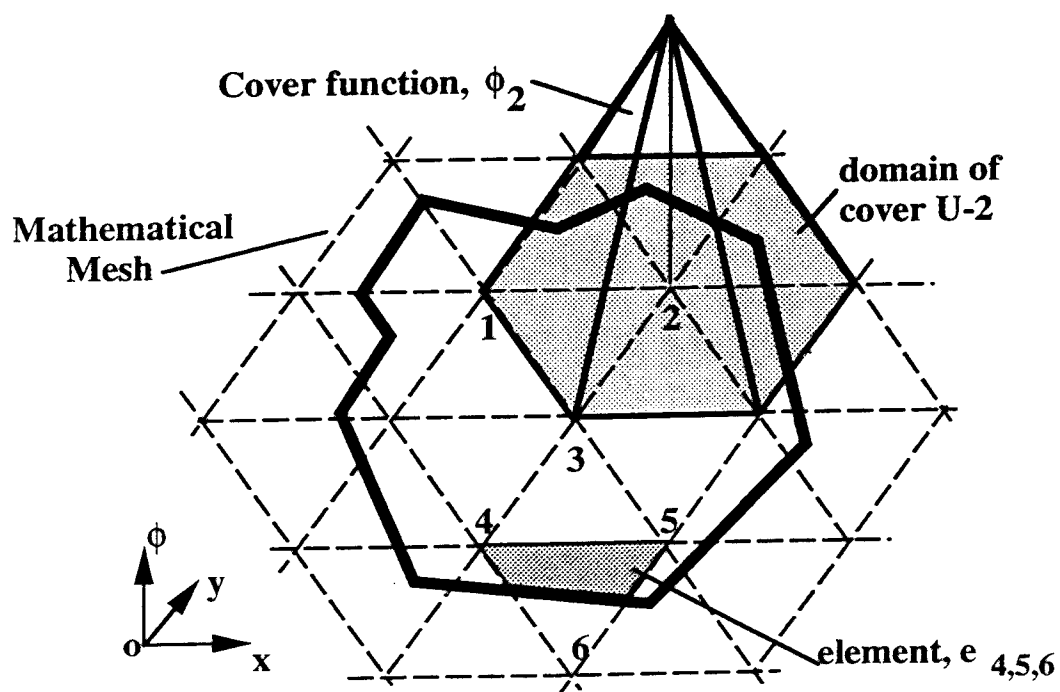


Fig. 2 Mathematical mesh and physical mesh in the manifold method.

wide variety of continuous or discontinuous materials located within moving boundary. The local functions  $f_i(x,y)$  defined on physical cover  $U_i$

$$f_i(x, y) \quad (x, y) \in U_i \quad (1)$$

can be constant, linear, high order polynomials or locally defined series. These local functions are connected together by the weight function  $W_i(x, y)$

$$W_i(x, y) \geq 0 \quad (x, y) \in U_i \quad (2)$$

$$W_i(x, y) = 0 \quad (x, y) \in U_i \quad (3)$$

with

$$\sum_{(x, y) \in U_j} W_j(x, y) = 1 \quad (4)$$

The meaning of the weight functions  $W_i(x, y)$  is weighted average, which is to take a percentage from each local function  $f_i(x, y)$  for all physical covers  $U_i$  containing point  $(x, y)$ . Using the weight functions  $W_i(x, y)$  a global function  $F(x, y)$  on the whole physical cover system is defined from the local functions

$$F(x, y) = \sum_{i=1}^n W_i(x, y) f_i(x, y) \quad (5)$$

From the forementioned basic concept of the finite covers approximation one can realize that there are some important issues have to be discussed:

- (1) How do the weighting functions  $W_i$ ,  $(i=1, n)$  corresponding to the selected local functions of all physical covers be effectively generated?
- (2) How do we formulate a numerical scheme based on this newly proposed finite covers theory?
- (3) What are the relations with the conventional finite element method?

To solve these questions, Shi (1991) has proposed two independent discretization meshes named mathematical mesh and physical mesh to construct the computational scheme of his manifold method. The mathematical mesh is used to construct the domain of covers  $U_i$  and the associated local trial functions  $f_i$  while the physical mesh formed by the geometrical boundary of the solid body and the mathematical mesh is used to define the zone of numerical integration in a discretization sense. As shown in Fig. 2, the element  $e_{4,5,6}$  is

within the common part of the hexangular mathematical covers U-4, U-5 and U-6. Each node in the mathematical mesh represents a cover function. For the finite element type mathematical mesh, the cover function can be chosen as the global basis function in the traditional finite element method.

### Finite element approximation theory

If the finite element theorem is used to construct the global approximation function, then the mathematical mesh of manifold method is related to the finite element mesh. According to the FEM, a function  $F(x,y)$  belongs to a finite element space  $V_n = \text{SPAN} \{\phi_1, \phi_2, \phi_3, \dots, \phi_n\}$ , spanned by the finite element basis functions  $\phi_i$  ( $i=1,n$ ), can be expressed as

$$F(x,y) = \sum_{i=1}^n c_i \phi_i(x,y), \quad (x,y) \in \Omega_e \quad (6)$$

where the global basis functions,  $\phi_i$  ( $i=1,n$ ) defined on a domain  $U_i$  satisfy the following properties (Axelsson and Barker 1984):

(I) The restriction of  $\phi_i$  to any element  $e_k$  has the polynomial form

$$\phi_i(x,y) = \sum_{s=1}^T C_{ik}^{(s)} x^{p(s)} y^{q(s)} \quad (x,y) \in e_k \quad (7)$$

where the power  $p(s)$  and  $q(s)$ ,  $s=1,2,\dots,T$ , are independent of  $i$  and  $k$ .

$$(II) \quad \phi_i(N_j) = \delta_{ij} \quad \text{for } i, j = 1, 2, \dots, n \quad (8)$$

where  $N_j$  is the coordinates of node  $j$ .

(III)  $\phi_i$  is uniquely determined on every element edge by its values at the nodes belonging to that edge.

Property (II) implies that  $\phi_1, \phi_2, \phi_3, \dots, \phi_n$  are linearly independent. The coefficients in Eq. (7) are determined from Eq.(8) through the linear system of equations

$$\sum_{s=1}^T C_{ik}^{(s)} x_{i_r}^{p(s)} y_{i_r}^{q(s)} = 1, \quad \text{for } i_r^{(k)} = i, \\ = 0, \quad \text{otherwise,} \quad r = 1, 2, \dots, T \quad (9)$$

where  $i_r^{(k)}$  is the global node number of node  $r$  in element  $k$ . This system can be expressed in the matrix-vector form

$$S_m C_{im} = d_{im} \quad (10)$$

where

$$S_m = \begin{bmatrix} x_{i_1}^{p(1)} y_{i_1}^{q(1)} & x_{i_1}^{p(2)} y_{i_1}^{q(2)} & \dots & x_{i_1}^{p(T)} y_{i_1}^{q(T)} \\ x_{i_2}^{p(1)} y_{i_2}^{q(1)} & x_{i_2}^{p(2)} y_{i_2}^{q(2)} & \dots & x_{i_2}^{p(T)} y_{i_2}^{q(T)} \\ \cdot & \cdot & \dots & \cdot \\ \cdot & \cdot & \dots & \cdot \\ x_{i_T}^{p(1)} y_{i_T}^{q(1)} & x_{i_T}^{p(2)} y_{i_T}^{q(2)} & \dots & x_{i_T}^{p(T)} y_{i_T}^{q(T)} \end{bmatrix} \quad (11)$$

Except in very special "degenerate" case  $S_m$  is nonsingular and  $\phi_i$  is well defined on  $e_m$ . Further, property (III) ensures that  $\phi_i$  is continuous at element edges. This, together with the continuity of polynomials, implies that

$$(IV) \quad \phi_i \in C(\Omega_e) \quad (12)$$

Suppose node  $N_i$  is not in element. Then  $d_{im} = 0$ , and it follows from Eq.(10) and Eq.(9) that  $\phi_i$  vanishes everywhere in  $e_m$ . Hence,

$$(V) \quad \phi_i \text{ assumes nonzero values only in those elements to which } N_i \text{ locates.}$$

In finite element theory, it calls the union of elements to which  $N_i$  belongs the "support" of  $\phi_i$ . It is analogical to the domain of the cover in the manifold method. Thus, property (V) states that  $\phi_i$  vanishes outside of its support. By definition, a function  $F(x,y)$  belongs to  $V_n$  can be approximated by the interpolation function  $F_I(x,y)$  for the  $k$ -th element as

$$F_I(x,y) = \sum_{i=1}^n F(N_i) \phi_i(x,y) \quad (x,y) \in \Omega_e \quad (13)$$

or can be written by inserting Eq.(7) into it as

$$F_I(x,y) = \sum_{i=1}^n \sum_{s=1}^T F(N_i) C_{ik}^{(s)} x^{p(s)} y^{q(s)} \quad (x,y) \in \Omega_e^{(k)} \quad (14)$$

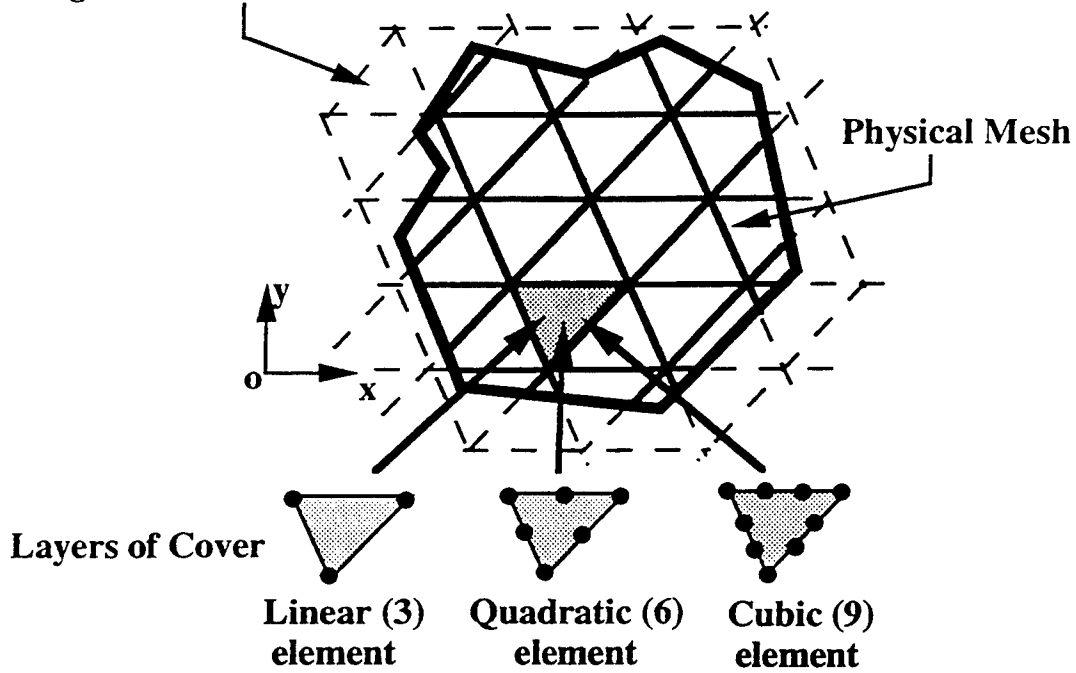
By comparison between Eq.(1) and Eq.(13), we can hardly identify that the exact correspondence among basis function  $\phi_i$ , nodal constant  $F(N_i)$  in the FEM and the weighting function  $W_i(x, y)$ , cover function  $f_i$  in the manifold method. It seems that the basis function in the FEM contained both the characters of cover function and weighting function defined by the manifold method. The basis functions  $\phi_i$  ( $i=1,n$ ) used to span the finite element interpolation space can be treated as the finite cover functions in the manifold method. Actually, the statements between Eq.(6) to Eq.(14) denotes the implementation of the Ritz-Galerkin method with finite element basis functions, i.e., basis functions that are continuous, piecewise polynomials and that have local support in the sense that each function vanishes outside of small subregion of the domain  $U_i$  (the cover).

Here it has to be pointed out that the number of cover functions on the physical variable function at the point to be interpolated is restricted by the finite element type that mathematical mesh used. That is, for a  $n$  nodes element there are  $n$  layers of covers with theirs corresponding local functions above the element domain for constructing the global interpolation function. For example, as shown in Fig. 3(a), if the 6-node quadratic triangular element is used in the mathematical mesh, then there are 6 layers of cover laying above this element used to construction the interpolation function.

## Finite Covers of Finite Element Mesh

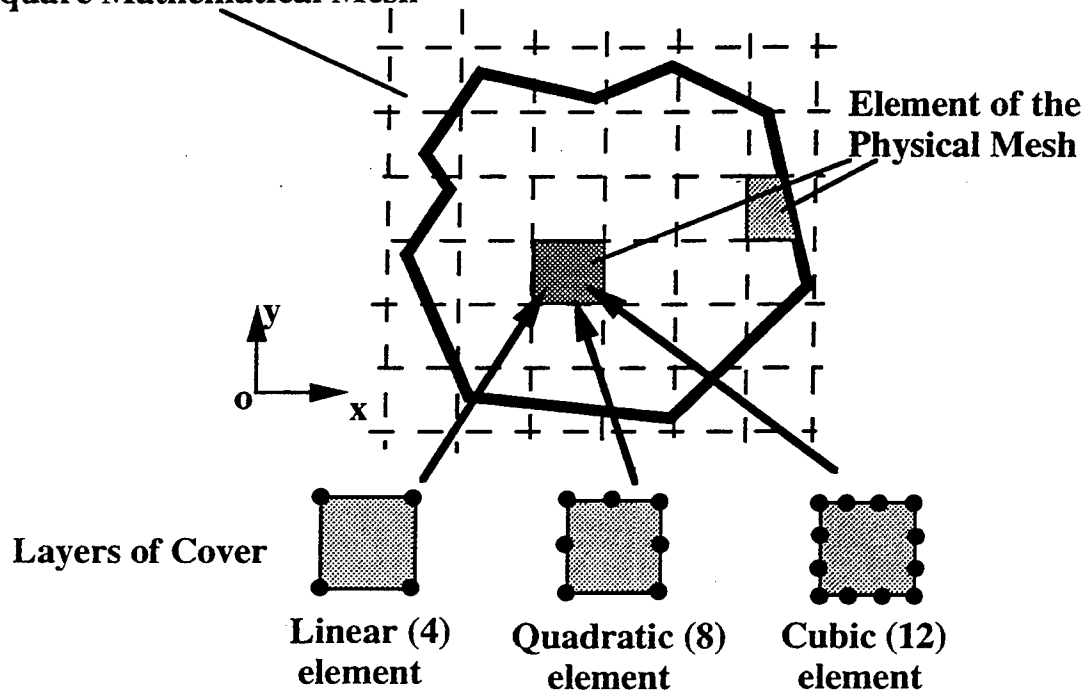
At present time, the attachment of finite element mesh on analysis domain of discrete blocky system has been conducted (Shi 1991, 1994) and it is just a special case of the manifold method. As seen in Fig. 4(a), the domain of the mathematical mesh outside the physical domain  $V$  has little contribution to the analysis and causes the shape of the element around the boundary to be irregular. These irregular shaped elements lead some difficulty in the numerical integration of element stiffness matrices. Although this difficulty can be conquered by applying the simplex integration theorem recently derived by Shi (1994). But for the simplicity, the conventional triangular finite mesh ( see Fig. 4(b))

Triangular mathematical Mesh



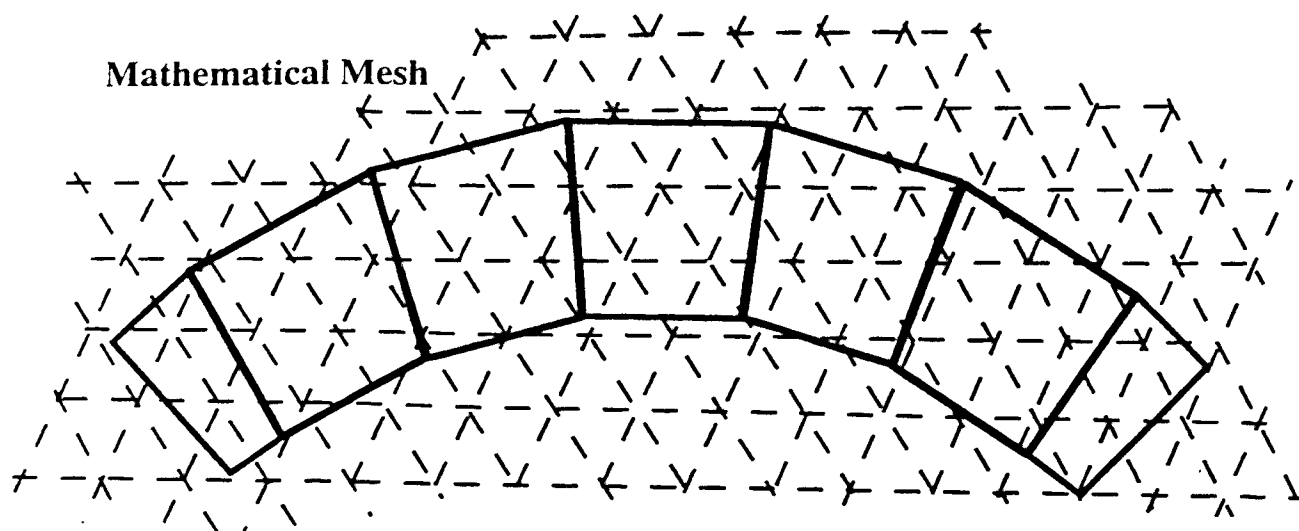
(a)

Square Mathematical Mesh

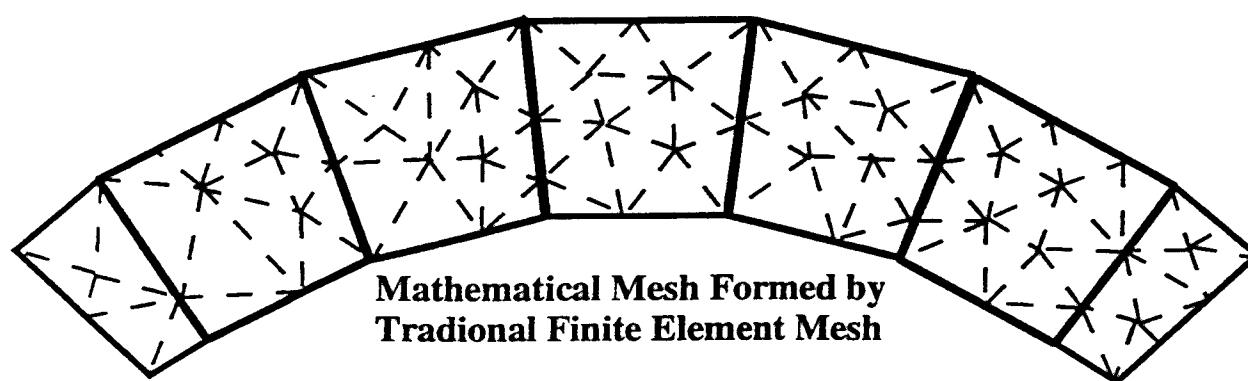


(b)

Fig. 3 Mathematical mesh and physical mesh of the manifold method



(a)



(b)

**Fig. 4 Finite Covers of Finite Element Mesh**

attached on each physical body is suggested to be used to proceed the numerical analysis. A computation code based on the formulation presented in Shi (1991) together with the contact detection scheme of DDA method can be developed. Recently, Shyu (1993) has developed a this type of code to simulate the large and vibration characteristics of an automobile's leaf spring-dashpot suspension system. This research work verifies the accuracy and capability of the manifold method.

## **Basic concepts of the diffuse element method & element-free Galerkin method**

Nayroles et al. (1992) and Belytschko et al. (1994) have recently introduced a very interesting and promising method which they called the diffuse element method and element-free Galerkin method respectively. In this type of method, only a group of nodes and boundary description is needed to develop the Galerkin equations. The interpolants are polynomials which are fit to the nodal values by a least-squares approximation. The conventional finite element mesh is totally unnecessary in this method. As Nayroles et al. (1992) stated, the motivations of developing the diffuse element method are to provide smoother approximations and no explicit elements to avoid difficulty in generating adequate discretization meshes for complex tridimensional domains. Belytschko et al. (1994) have successfully extended this concept to develop their element-free Galerkin methods and demonstrated that the methods does not exhibit any volumetric locking, the rate of convergence can exceed that of finite elements significantly and a high resolution of localized steep gradients can be achieved. The main reason of the success of this diffuse element, element-free or implicit element type method is due to its application of the moving least-squares interpolation theory. Different from the traditional FEM, the moving least-squares methods interpolants do not pass through the data because the interpolation functions are not equal to unity at the nodes unless the weighting functions are singular. In the following of this paper, a brief introduction of this type of method mainly from Nayroles et al. (1992) and Belytschko et al. (1994) is given and the correlation with respect to the manifold method are discussed in detail.

### **Moving least-squares interpolant**

Similar to the finite element approximation, the moving least squares (MLS) interpolant  $u^h(\mathbf{x})$  of the function  $u(\mathbf{x})$  is defined in the domain  $\Omega$  by



$$u^h(\mathbf{x}) = \sum_{j=1}^m p_j(\mathbf{x}) a_j(\mathbf{x}) \equiv \mathbf{p}^T(\mathbf{x}) \mathbf{a}(\mathbf{x}) \quad (15)$$

where  $\mathbf{p}(\mathbf{x})$  is a vector of "m" independent functions, most often polynomial terms, and  $\mathbf{a}(\mathbf{x})$  is a vector of "m" approximation parameters which are position dependent in the domain  $\Omega$ . For example, a quadratic basis in a two-dimensional domain is provided by  $\mathbf{p}^T(\mathbf{x}) = [1, x, y, x^2, xy, y^2]$ ,  $m=6$ . Compared with the interpolant of FEM expressed by Eq.(6), the position dependency of the coefficient vector  $\mathbf{a}(\mathbf{x})$  is the main character of this MLS type approximation and makes it become a more general method. The  $\mathbf{a}(\mathbf{x})$  is obtained at any point  $\mathbf{x}$  by minimizing a weighted discrete  $L_2$  norm as follows:

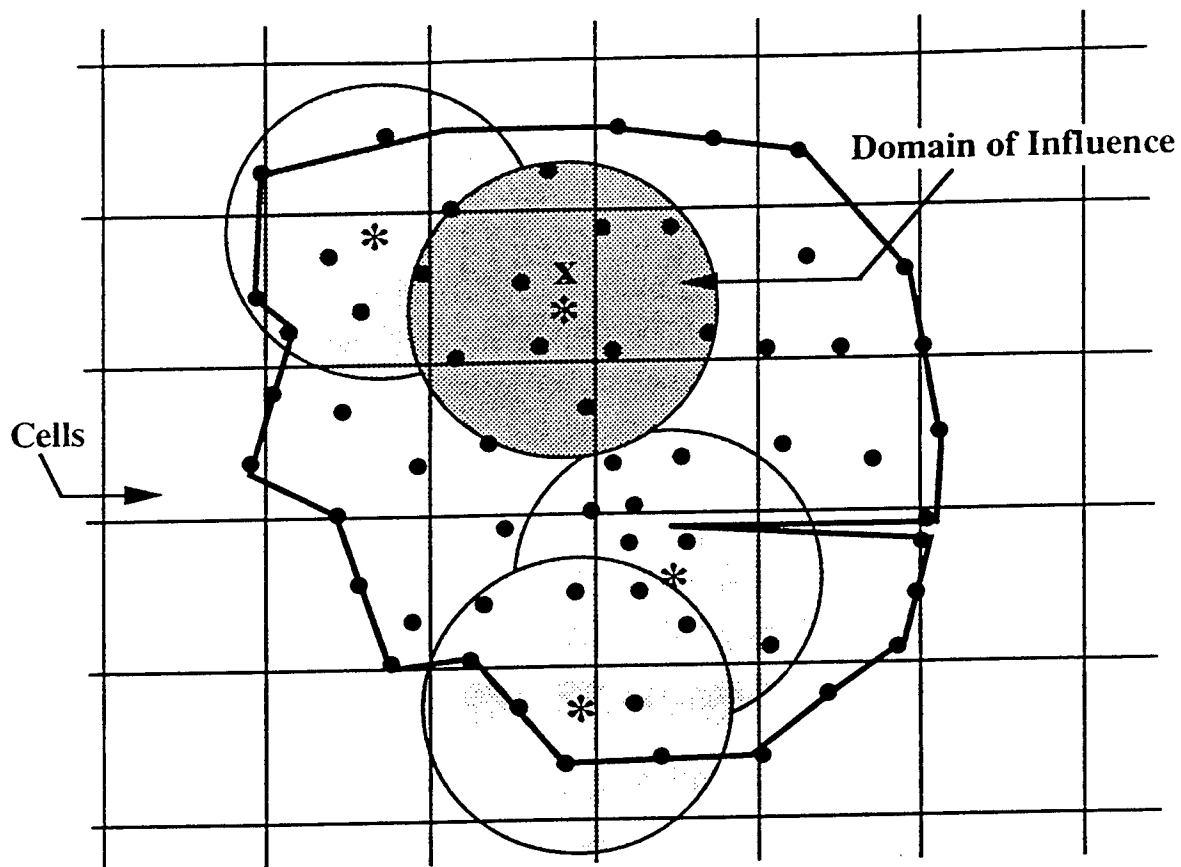
$$J = \sum_{I=1}^n w(\mathbf{x} - \mathbf{x}_I) [\mathbf{p}^T(\mathbf{x}_I) \mathbf{a}(\mathbf{x}) - u_I]^2 \quad (16)$$

where  $n$  is the number of points in the neighborhood of  $\mathbf{x}$  for which the weight function  $w(\mathbf{x} - \mathbf{x}_I) \neq 0$ , and  $u_I$  is the nodal value of  $u$  at  $\mathbf{x} = \mathbf{x}_I$ .

This neighborhood of  $\mathbf{x}$  is called the domain of influence of  $\mathbf{x}$ , or circle of influence in two dimension. Actually, this domain of influence can be identified as the circular shaped implicit element of this diffuse element method. From the manifold method point of view, the mathematical mesh of this moving least-squares method is composed of infinite overlapped circular elements centered at the point where the approximation is required (see Fig. 5(a)). This implicit element is the common domain of the  $n$  covers associated with those  $n$  nodes within the element. The exact form of the cover function will be presented in the latter part of this section.

The connectivity of an interpolated point depends on the nodes in the domain of influence. Fig. 5(b) shows the connectivity of the nodes to the evaluation point in the diffuse element method and in the finite element method respectively. In the finite element method the connecting lines are restricted inside the element which the evaluation point  $\mathbf{x}$  located and the connected nodes are the nodes associated with the element. It is also noted that the connectivity lines can not intersect any geometrical boundary of the material volume.

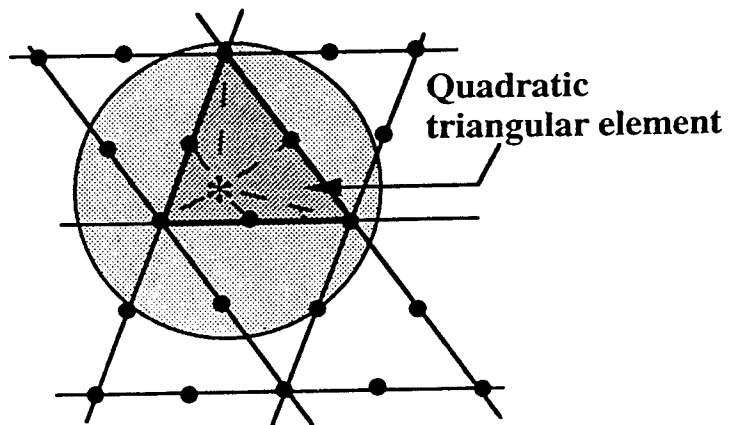
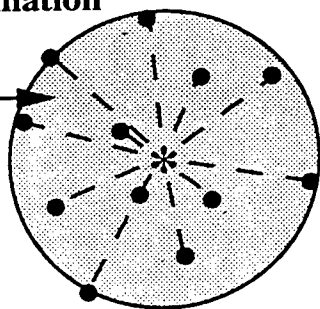
In this approximation theory, the number of nodes used to construct the interpolation function can be freely adopted and removed from the domain of influence zone. Compared with conventional finite element method of fixed number of nodes, this moving least squares approximation can provide various type of interpolants. Even more



\* center of influence domain for the interpolated point  $x$   
 ● nodal point for the moving least-squares approximation theory

(a)

implicit element of  
MLS approximation



(b)

Fig. 5 (a): Element-free Galerkin method and the moving least-squares approximation.  
 (b): Connectivity in the MLS approximation and the finite element approximation.

exciting are its potential in adaptive methods for the portion of material required more accuracy as in the crack and damage progression problems.

The stationary of  $J$  in Eq.(16) with respect to  $\mathbf{a}(\mathbf{x})$  leads to the following linear relation between  $\mathbf{a}(\mathbf{x})$  and  $u_j$ :

$$\mathbf{a}(\mathbf{x}) = \mathbf{A}^{-1}(\mathbf{x}) \mathbf{B}(\mathbf{x}) \mathbf{u} \quad (17)$$

where  $\mathbf{A}(\mathbf{x})$  and  $\mathbf{B}(\mathbf{x})$  are the matrices defined by

$$\mathbf{A}(\mathbf{x}) = \sum_{I=1}^n w_I(\mathbf{x}) \mathbf{p}^T(\mathbf{x}_I) \mathbf{p}(\mathbf{x}_I) \quad (18)$$

$$w_I(\mathbf{x}) \equiv w(\mathbf{x} - \mathbf{x}_I) \quad (19)$$

$$\mathbf{B}(\mathbf{x}) = [w_1(\mathbf{x}) \mathbf{p}(\mathbf{x}_1), w_2(\mathbf{x}) \mathbf{p}(\mathbf{x}_2), \dots, w_n(\mathbf{x}) \mathbf{p}(\mathbf{x}_n)] \quad (20)$$

$$\mathbf{u}^T = [u_1, u_2, \dots, u_n] \quad (21)$$

Hence, we have

$$u^h(\mathbf{x}) = \sum_{I=1}^n \sum_{j=1}^m p_j(\mathbf{x}) (\mathbf{A}^{-1}(\mathbf{x}) \mathbf{B}(\mathbf{x}))_{jI} u_I \equiv \sum_{I=1}^n \phi_I u_I \quad (22)$$

where the basis function  $\phi_I(\mathbf{x})$  is defined by

$$\phi_I(\mathbf{x}) = \sum_{j=1}^m p_j(\mathbf{x}) (\mathbf{A}^{-1}(\mathbf{x}) \mathbf{B}(\mathbf{x}))_{jI} \quad (23)$$

This is the global basis function or called cover function used to span the space of the approximation functions. Compared with the basis functions in the finite element method, the MLS approximation does not exactly verify the interpolation property expressed by Eq. (8). In practice, this property is verified with good accuracy except in the vicinity of points where the function  $\mathbf{u}$  is discontinuous or the gradients of  $\mathbf{u}$  are very large.

The partial derivatives of can be obtained as follows:

$$\phi_{I,i} = \sum_{j=1}^m \{p_{j,i} (A^{-1}B)_{ji} + p_j (A_{,i}^{-1}B + A^{-1}B_{,i})_{ji}\} \quad (24)$$

where

$$A_{,i}^{-1} = -A^{-1} A_{,i} A^{-1} \quad (25)$$

and the index following a comma is a spatial derivative. The rank and conditioning of matrix  $A$  depend on the relative locations of the nodes belonging to the certain neighborhood of the point  $x$  called the influence domain. A necessary condition to get a non singular  $A$  matrix is the existence of at least "m" nodes in the neighborhood of  $x$ . An advantage of this MLS approximation is that it requires no postprocessing for the output of strains and stresses or other field variables which are derivatives of the primary-dependent variables since these quantities are already very smooth.

### Choice of weighting functions

The weighting function  $w_I(x) \equiv w(x - x_I)$  play an important role in the performance of the moving least-squares method. They should decrease in magnitude as the distance from  $x$  to  $x_I$  increase. The approximate function is made smooth by replacing the discontinuous coefficients in Eq.(16) by continuous weighting function. Vanishing of these weighting functions  $w_I(x)$  at a certain distance from the point  $x$  preserves the local character of the approximation. If the weighting function is continuous with respect to  $x$ , the basis function (Eq.(23)) and the approximation function (Eq. (22)) are continuous with respect to  $x$ , as well as the shape functions of the derivatives and the estimates of the derivatives up to order "m". The standard finite element method can be obtained if the weight function  $w_I(x)$  is defined as piecewise-constant over each subdomain or element. For example,  $w_I(x)=1$  if node  $I$  belongs to element and  $w_I(x) = 0$  otherwise. By comparison equations (7), (14) with (22), (23), it is easy to realize the relationship between the finite element approximation and the moving least-squares approximation. The accuracy of the moving least-squares approximation method is directly related to the choice of the weighting functions. The rational fraction type weighting function, Gauss like function and triangular function have been successfully tested by Nayroles et al. (1992). While Belytschko et al. (1994) have considered the exponential and conical type of weighting functions. Belytschko et al. (1994) have found that the performance of

exponential function which is essentially a truncated Gauss distribution, performs far better than a conical weight function. These weight functions depend only on the distance between two points as follow:

$$w_I(\mathbf{x}) \equiv w(\mathbf{x} - \mathbf{x}_I) = w_I(d) \quad (27)$$

where  $d = ||\mathbf{x} - \mathbf{x}_I||$  is the distance between the two points  $\mathbf{x}$  and  $\mathbf{x}_I$ . That is, the functions present a symmetry around  $\mathbf{x}$ . But it may be helpful to use anisotropic weighting function, for instance to fit a steep front.

## **Modified Manifold Method —Adaptive Covers with Quadrature Cells**

At the present time, both the diffuse element method and element-free Galerkin method (EFGM) are at their infant stage. Compared with the manifold method which is developed from the discontinuous deformation analysis method (DDA), the EFGM has not included the multi-body dynamic interaction mechanism into the analysis procedure. But the concept inherited inside its approximation theory do inspire the manifold method on its future development.

From the discussion on the finite element approximation and moving least squares approximate, it can be found that in the conventional finite element method the number of basis functions (or called covers) is fixed for each element (domain of integration). While for the element-free Galerkin method, the number of cover functions used for interpolation is free to be adopted or abandoned. Therefore, we can characterize these two types of approximation theory as the "fixed covers approximation" and the "adaptive covers approximation" respectively.

Here we propose a modified manifold method in which the finite element approximation as discussed in the previous section is replaced by the moving least-squares approximation theory. In this newly proposed method there is no explicit mathematical mesh but with distributed nodes and the physical mesh is represented by quadrature cells (see Fig. 6). In each cell, Gauss quadrature is used to evaluate the integrals for the formulation of system governing equations. The number of quadrature points depends on the number of nodes in a cell. Belytschko et al. (1994) have suggested  $n_Q \times n_Q$  Gauss quadrature for square shaped cell structure where

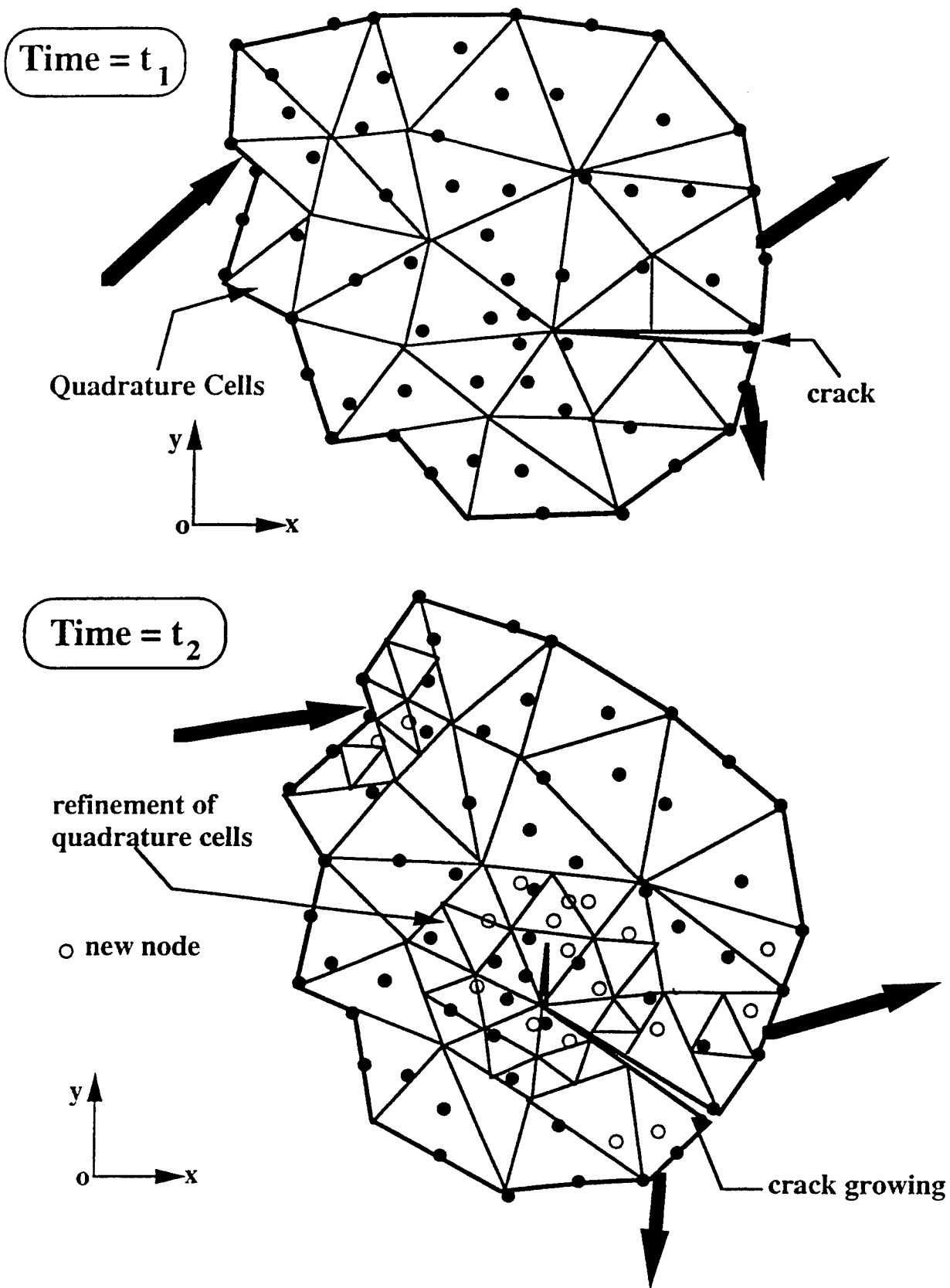


Fig. 6 Modified manifold method of adaptive covers with quadrature cells

$$n_Q = \sqrt{m} + 2$$

and  $m$  is the number of nodes in a cell. The number of cells to be used in most of Belytschko et al. (1994) analysis by using  $m_c \times m_c$  cells, where

$$m_c = \sqrt{n_N}$$

and  $n_N$  is the total number of nodes in the solid body. In our modified manifold method, triangular cellular mesh is used due to its capability of discretizing solids of irregular shape. When high accuracy requires, either mesh refinement or increasing number of nodes per cell can be considered. One technique for refining a triangular mesh is by placing new nodes at the midpoints of all element edges. (See Fig. 6) In this adaptive covers manifold method the cellular structure is designed for the numerical quadrature of integrals. Therefore, the refinement of a coarse grid can be proceeded locally within an element without considering of the connectivity condition between adjacent elements as discussed in conventional FEM. This is very effective for crack propagation problems. The quadrature scheme is the same as the one used in EFGM (1994). Based on these adaptive covers and quadrature cell concepts, then just follows the formulation procedure of the finite covers finite element mesh in Shi (1991) and substitutes the cover functions  $f_i$  by the basis functions obtained by Eq.(22). According to this proposal, one can formulate a scheme which is capable to simulate the whole deformation process of solid body system within a mechanical or electromagnetic physical field from a state of continuous system to a discontinuous one.

## Numerical Examples

Based on the formulation proposed in Shi (1991, 1994), a manifold analysis code of triangular finite element mesh is developed. It is noted that the manifold method is an incremental dynamic formulation. Hence it can be applied to analyze the elastodynamic problems of large displacements. To evaluate the capability and accuracy of the computer code, a simple problem was studied first. As shown in Fig. 7, a 10 cm x 40 cm elastic strip ( $E = 2 \times 10^6$  kg/cm<sup>2</sup>,  $\nu = 0.2$ ) of thickness  $t = 1$ cm without any constraint sustains a pair of suddenly applied 30,000 kg constant loads. Triangular finite element mesh is used to construct the approximation function. In the manifold method terminology this is a

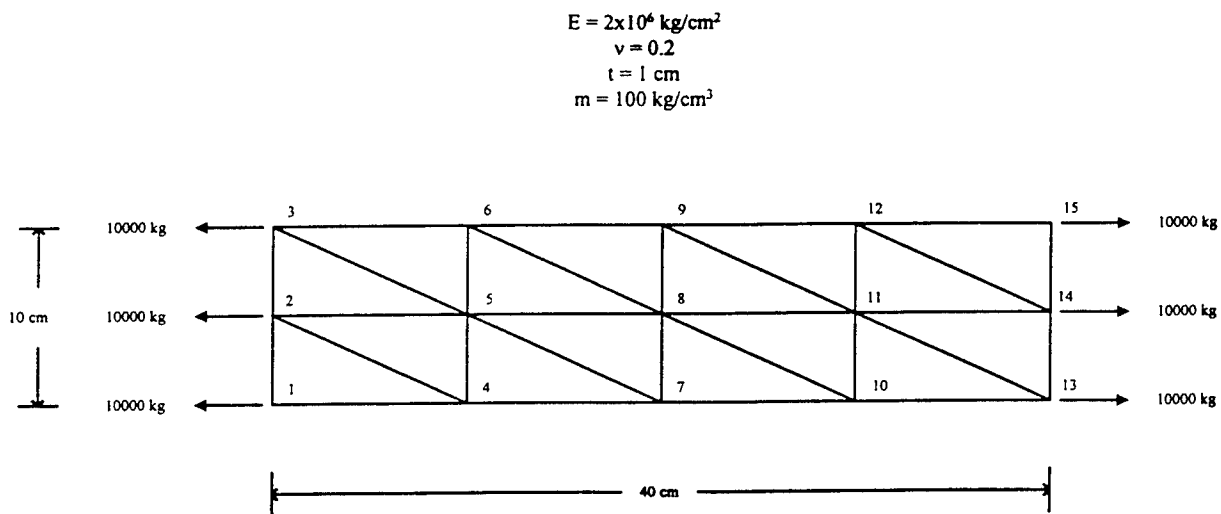


**Fig. 7** An elastic strip sustains a pair of suddenly applied constant loads.

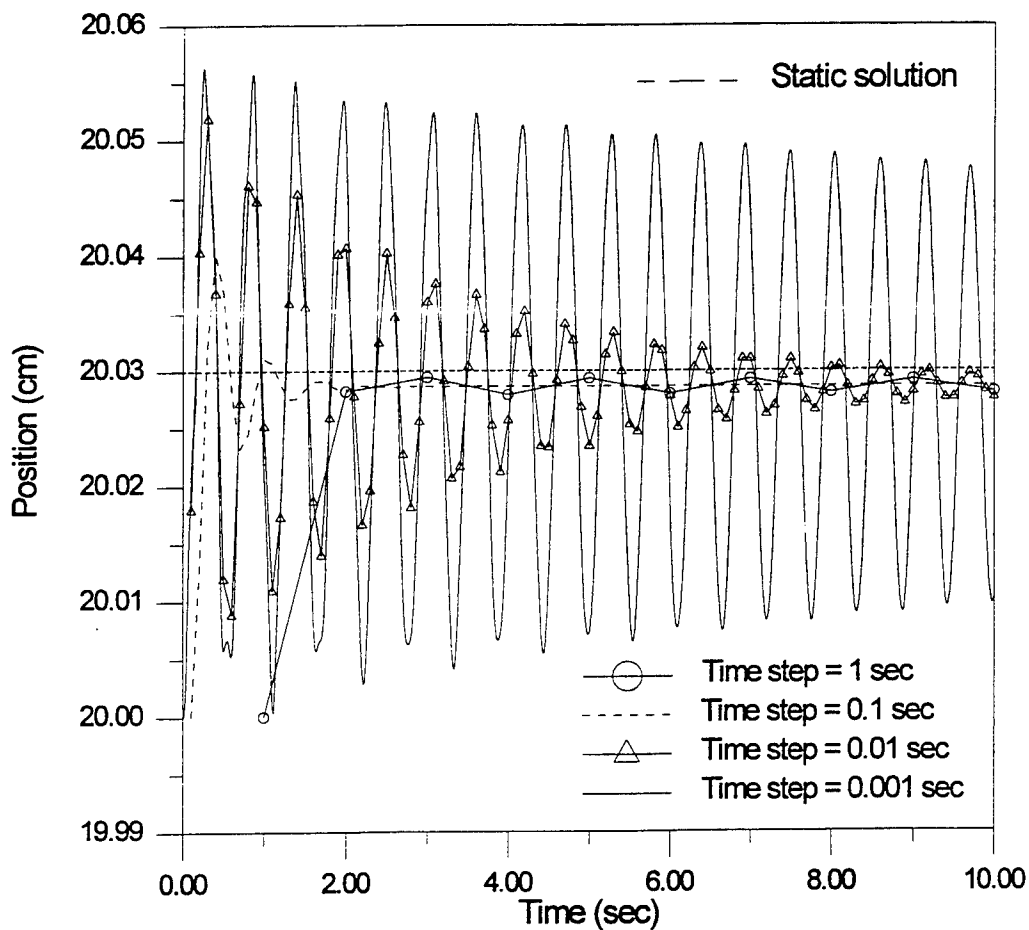


**Fig. 8** Dynamic behavior of a suddenly loaded elastic strip simulated by constant acceleration time integration scheme at different time step.



block with finite covers of finite element mesh. The analytical solution of this 2D elasticity problem is difficult to obtain due to the Poisson's effect. But it is sure that the axial displacement of the tip is oscillation about it static solution. Transverse vibration shares some strain energy from the axial deformation. This effect causes the oscillation amplitude of the tip varying at a low frequency mode during the vibration.

Two kinds of time integration schemes, namely constant acceleration method and linear acceleration method, were used to simulate the problem. The time integration schemes used in the DDA formulation and the Newmark-  $\beta$  method ( $\beta = 1/4$ ,  $\delta = 1/2$ ) belong to the constant acceleration type and both are unconditional stable with respect to the time step size. Fig. 8 shows the simulations of the problem with different time step size by constant acceleration time integration scheme. From this figure it is found that there is some numerical damping existed in the numerical algorithm. The damping effect is proportional to the time step size. Exact solution can be approached if very small time step size is used. For the same time step size, the linear acceleration time integration scheme can provide better approximation as shown by Fig. 9. But this scheme becomes unstable after

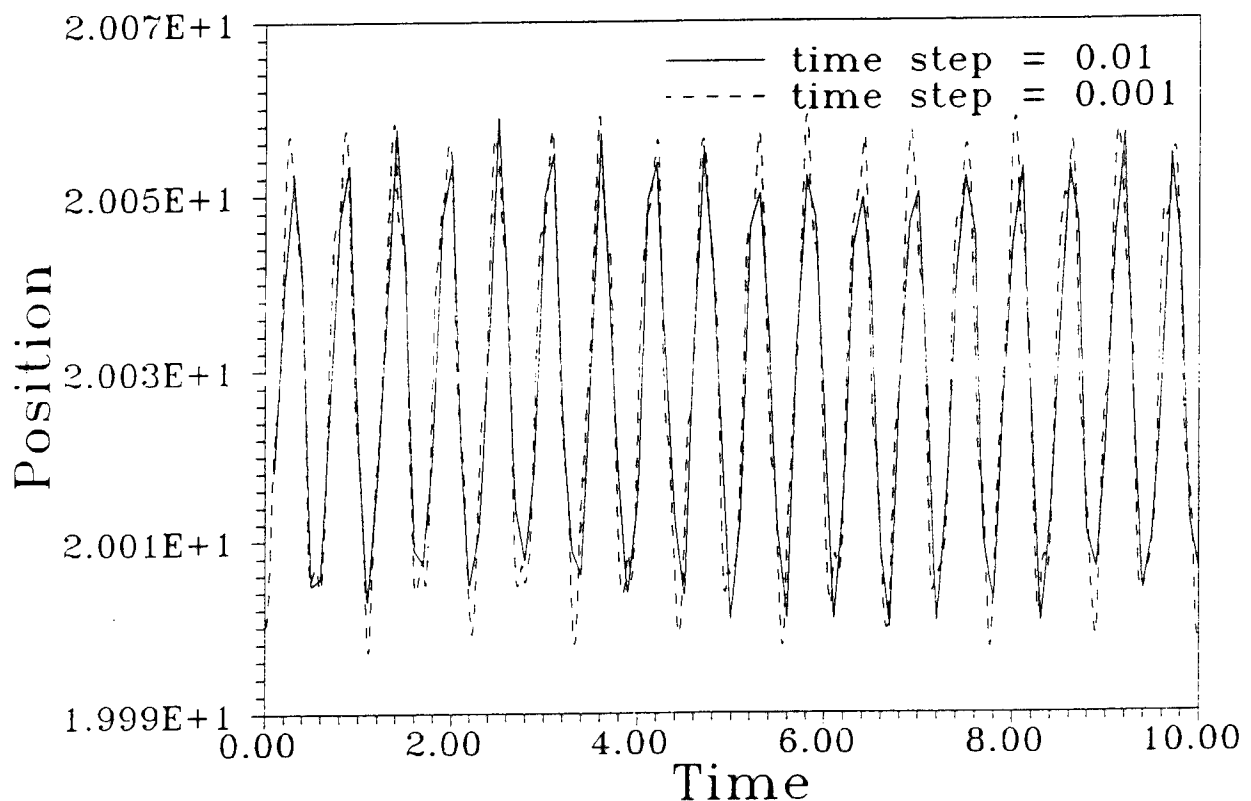


**Fig. 9** Dynamic behavior of a suddenly loaded elastic strip simulated by linear acceleration time integration scheme at different time step.

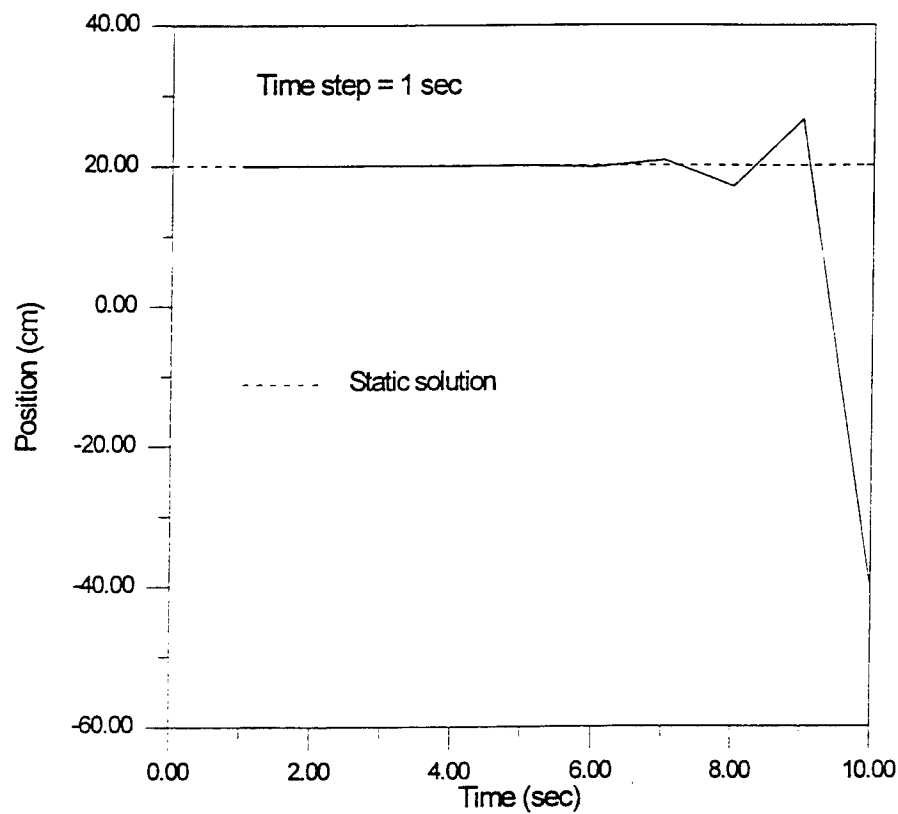
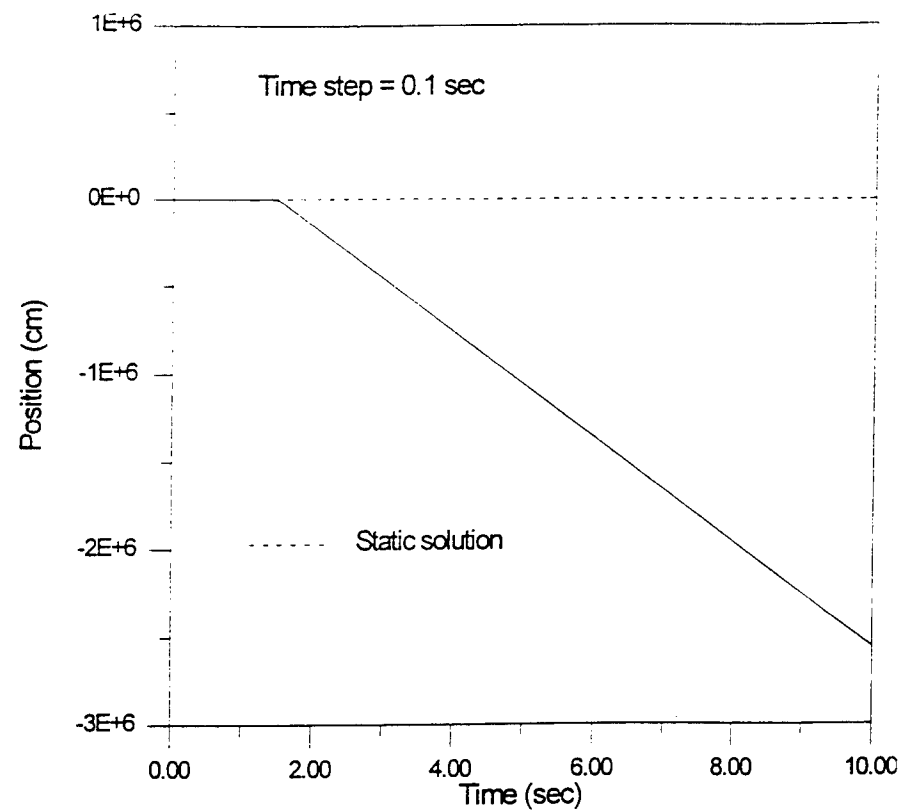
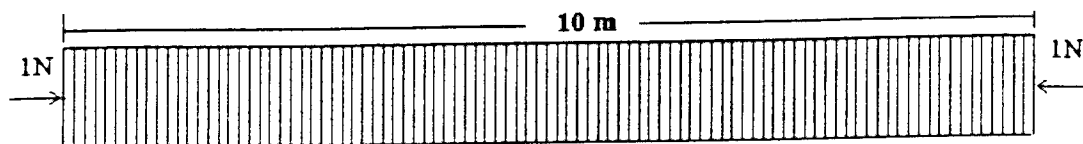


**Fig. 10 The divergent of linear time integration scheme at time step size**  
 (a)  $\Delta t = 0.1$  sec, (b)  $\Delta t = 1$  sec.



$$E = 10,000 \text{ N/m}^2, \rho = 1 \text{ Kg/m}^3$$

**Fig. 11** Computation mesh of manifold method for a rod composed of 100 connected blocks under step loading.

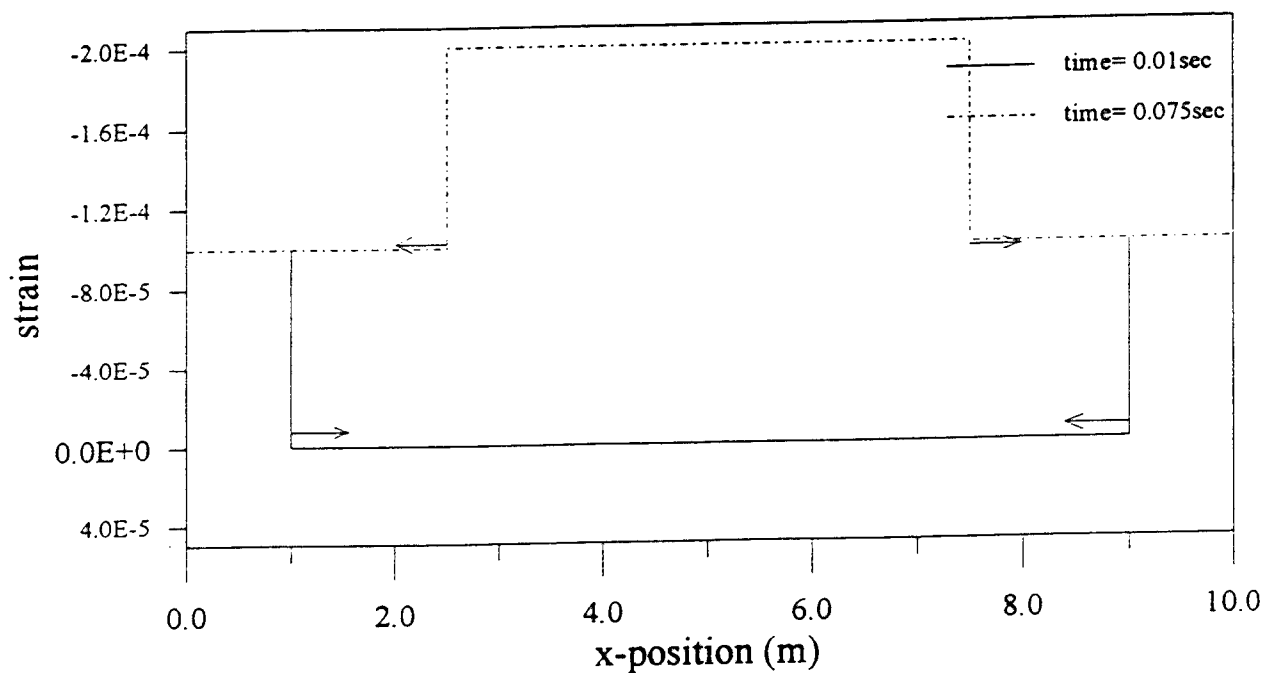


**Fig. 12** Analytical solution of stress states and locations of wave front at different time of a rod under step loading.

$$\Delta t = 2 \cdot 10^{-5} \text{ sec}$$

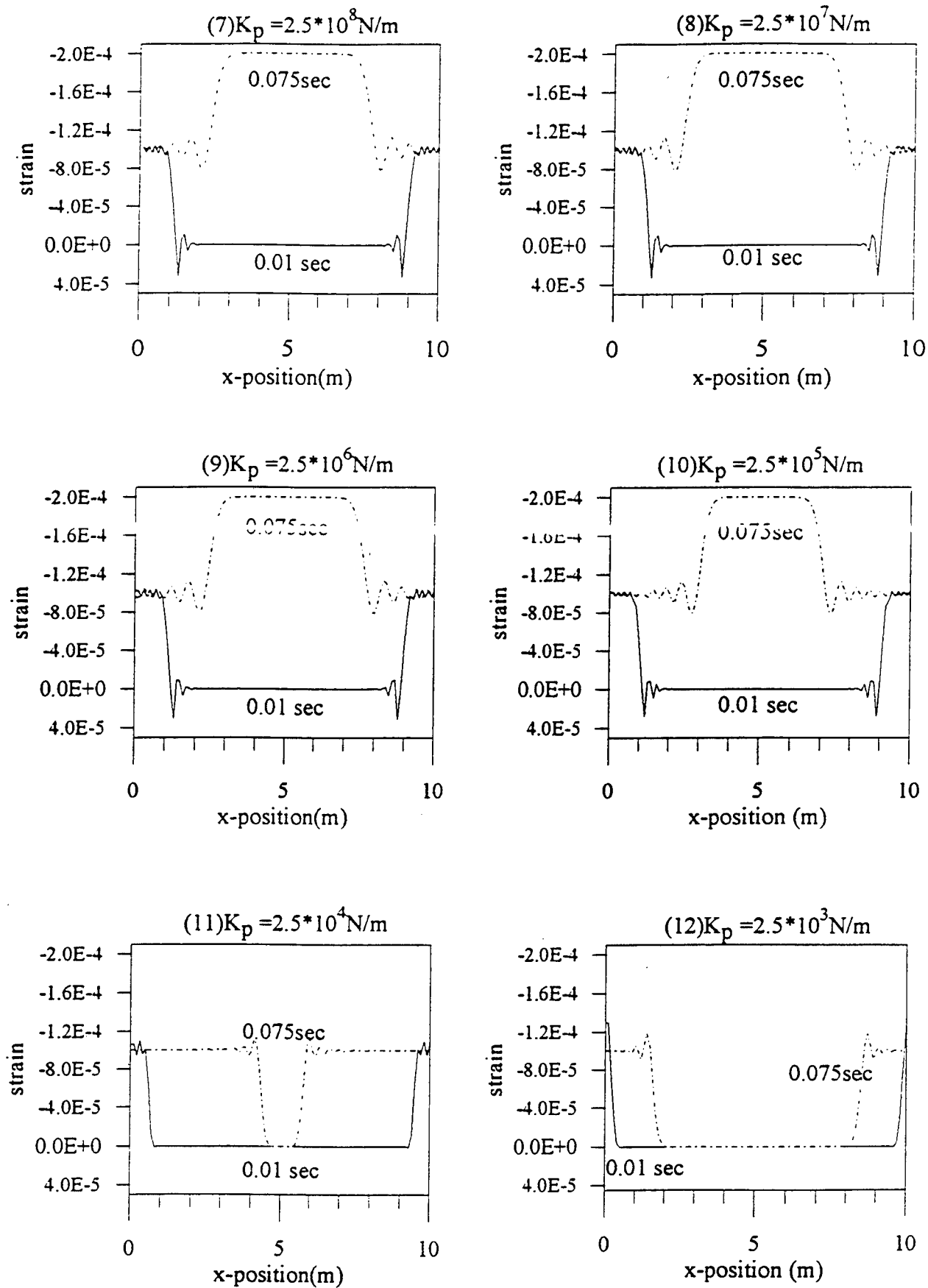


**Fig. 13** Manifold simulation for the rod composed of 100 connected blocks under step loading with different values of contact spring constant and time step size  $\Delta t = 2 \times 10^{-5} \text{ sec}$ .

certain iteration steps at bigger time step size as shown in Fig. 10 (a) and Fig. 10 (b). The reason of the deviation of the center line of vibration from the static solution is mainly due to the finite element mesh used in the model. From this numerical example, one can realize that the time integration scheme plays an important role in applying the manifold method to analyze dynamic problems effectively and accurately.

Another important factor which affects the simulation results of applying manifold method to multibody dynamics is the penalty value of the contact spring. Fig. 11 shows the configuration of 100 blocks shocked by a step loading at the outer blocks. Stress wave propagation behavior at different time is tried to be studied (see Fig. 12). In this example, for each block its mathematical mesh coincides with the physical mesh. This is a special case of the manifold method. Contact detection actions among blocks are performed during the simulation. With properly selected values of time step size and its associated contact spring constant as the way suggested by the author in his previous study<sup>7</sup>, the simulation results approaches the analytical solution quite well (see Fig. 13).

## Discussion and Conclusions

The finite element method, diffuse element method, element-free Galerkin method and even the manifold method can be grouped as a Ritz-Galerkin type method based on its characters of constructing the approximation function of the analysis domain for finding the solution of a boundary value problem. It is interesting to find that the concept of finite covers already has been embedded in the Ritz-Galerkin type approximation theories. The concepts of the moving least-squares approximation are more general than the finite element method.

The moving least squares approximation theory has its superiority in analyzing crack or damage propagation problems due to its high rate of convergence and the achievement of a high resolution of localized steep gradients. It is sure that the adoption of those superior features of element-free Galerkin method and retaining the dynamic multibody interaction scheme of discontinuous deformation method can make the manifold method be a more powerful tool for the continuous-discontinuous analysis. Nevertheless, the potential benefits in many problems are so attractive that this manifold method deserves consideration and further development.

## Acknowledgment

The support of National Science Council and the National Central University of Taiwan, R. O. C. is gratefully acknowledged.

## References

- Axelsson, O. and Barker, V. A. (1984) "Finite element solution of boundary value problems, theory and computation." Academic Press, Inc., London.
- Babosa, R. and Ghaboussi, J. (1990). "Discrete finite element method." *J. Geotech. Eng., ASCE*, Accepted for publication.
- Belytschko, T., Lu, Y. Y. and Gu, L. (1994). "Element-free Galerkin methods." *International Journal for Numerical Methods in Engineering*, vol. 37, 229-256.
- Chen, M.-H., Sheng, J., Wang, C.-Y. and Sun, P.-T. "Application of Discontinuous Deformation Analysis to continua." Submitted to the *International Journal for Numerical and Analytical Methods in Geomechanics*.
- Cundall, P. A. (1974) "A computer model for rock-mass behavior using interactive graphics for the input and output of geometric data.", Report AD/A-001, 602, U. S. national Technical Information Services.
- Heuze, F. et. al., "Models for rock mass dynamics." *Mechanics Computing in 1990's and Beyond*, ASCE, Conf. Proc., vol. 2, 1169-1173.
- Kardestuncer, H. (1988). "Basic concepts of the finite-element method." *Finite Element Handbook*, McGraw-Hill International Editions, 2.75-2.108.
- Munjiza, A. (1992) "Discrete elements in transient dynamics of fractured media." Ph. D. Thesis, University of Wales.
- Nayroles, B., Touzot, G. and Villon, P. (1992). "Generalizing the finite element method: Diffuse approximation and diffuse elements." *Computational Mechanics*, vol. 10, 307-318.
- Rice, D. L. and Ting, E. C. (1992). "Fragmentation algorithm for finite element failure simulation and analysis." *Structural Engineering Report, CE-STR-92-21*, Purdue University, West Lafayette, IN.
- Shi, G. H. (1988). "Discontinuous Deformation Analysis: A new numerical model for the statics and dynamics of block system." Ph. D. Dissertation, University of Calif., Berkeley, CA.

- Shi, G. H. (1991). "Manifold method of material analysis." *Proc. Ninth Army Conference on Applied Mathematics and Computing*, Minneapolis, Minnesota, U. S. A.
- Shi, G. H. (1994). "Modeling dynamic rock failure by Discontinuous Deformation Analysis with simplex integrations." *Proc. 1st North American Rock Mech. Symp.*, 591-598.
- Shyu, K. (1993) "Nodal-based Discontinuous Deformation Analysis." Ph. D. Dissertation, University of California at Berkeley.
- Wang, C.-Y. and Lin, H.-C. "A Discontinuous Deformation Analysis (DDA) model for circular shaped granular congregated medium." Submitted to the *International Journal for Numerical and Analytical Methods in Geomechanics*.
- Wang, C.-Y., Sheng, J. and Chen, M.-H. "Dynamic-contact analysis scheme applied in the DDA method." Submitted to the *International Journal for Numerical and Analytical Methods in Geomechanics*.

# Estimation of Rock Mass Disturbance Around a Repository Drift Using the DDA Method

Frank C. Tsai  
Woodward Clyde Federal Services  
101 Convention Center Drive, Suite P-110  
Las Vegas, NV 89109

## Introduction

In fractured rock, the hydraulic conductivity is extremely sensitive to changes in fracture aperture because hydraulic conductivity is a function of aperture to the third power (i.e., is based on the cubic law). When a nuclear waste repository drift is excavated in a rock mass, the introduction of the boundary surfaces (drift walls) reduces their traction to zero from that corresponding to the natural state of stress. Such traction reduction induces the change of the stress state in the host rock around the drift, as well as displacements in the vicinity of the excavation. Fractures in the rock mass may be extended or initiated, and existing fractures can be opened or closed by the change of the stress state. Thermally-induced stresses in rock can greatly enhance the above described responses. The change in fracture aperture can be estimated using a thermomechanical model of the rock mass, where the rock mass is represented by discrete rock blocks between the fractures. Whether the change could have a significant effect on repository performance can be determined based on the change in hydraulic conductivity and the amount of flow path length affected.

The purpose of this study is to demonstrate the use of the Discontinuous Deformation Analysis (DDA) code, [Shi, 1993], for estimating the changes in the fracture aperture in the vicinity of the repository openings caused by mechanical and thermomechanical effects (i.e., caused by construction and heat). The simulated opening and closing of fracture apertures in the vicinity of a waste emplacement drift, together with the induced stress state, may be used to provide information for assessing the rock mass disturbance. Since the DDA code cannot model the initiation of new fractures (cracking) due to the change of stress state, only the dislocation and the opening/closing of existing fractures are simulated. This approach may be sufficient because the cracking of intact rock only occurs in a very limited zone adjacent to the drift wall as compared to the mechanically and thermomechanically disturbed zone (i.e., such model limitation will have little influence on the results because of the small zone in which they may occur).



## Description of Numerical Method

The DDA code is a two-dimensional numerical model for simulating mechanical processes of a discrete system which is physically divided into a finite number of blocks that are bounded by preexisting discontinuities. The code models the relative movement between rock blocks that may be undergoing block deformation and rigid body motion. Rock blocks are considered to be elastic. Individual blocks are connected by contacts between blocks. A contact is defined by the force/displacement relationship between a corner of a block and an edge of another block. If the contact corner of one block has invaded (overlapped) into the other block through the reference edge, this contact is closed. Otherwise, the contact is open. For a closed contact, the corner of one block may be locked or sliding on the reference edge of another block. The Coulomb Frictional Law as a function of frictional angle and cohesion of the discontinuous surfaces is applied to govern the contact lock/slide mechanisms. For a locked contact, there is a relative shear movement between the corner and the reference edge if an external force parallel to the reference edge is acting on one of the blocks in contact. Hence, the mechanism of the penetration and shear movement of a locked contact can be modeled by inserting a pair of stiff springs between the block corner and the reference edge. The pair of springs are oriented in the directions normal to and parallel with the reference edge. For a sliding contact, the stiff spring parallel to the reference edge is substituted with a pair of external forces governed by the sliding criterion.

The method of approximation used in the DDA code is similar to that used in the finite element method where the solution of the complete system, as an assembly of its elements (blocks), follows precisely the same rules as applicable to a standard discrete system. A discrete time system is used to simulate the dynamic behavior of the discontinuous system. In other words, motion over a long period of time is the accumulation of motion over multiple small time intervals. The recurrence relationship for the system behavior in a small discrete time interval is formulated using the minimum total potential energy theorem where the governing equations, Newton's law of motion, the elastic constitutive law, and the prescribed boundary conditions of all contiguous blocks are solved simultaneously. The nonlinear contact behavior between blocks, which involves the frictional energy dissipation, is solved iteratively by choosing the trial contact positions between the blocks. Although the DDA code is a numerical method used for simulating the dynamics of a mechanical system, it can be used for quasi-static analyses. By resetting the velocity vectors of all blocks to zero at the beginning of each computational time step, the solution of the governing equations after many time steps represents the quasi-static condition of the mechanical system. Therefore, the time steps used in the quasi-static simulation are just a means to reach convergence through an iterative solution process. The theoretical detail and the formulation of the DDA code can be found in Shi (1993) and Tsai (1993).

The DDA code was modified to consider the effect of thermal loads. The thermal

loads are included using the change in temperature between two time increments for each block. The immediate mechanical response of rock blocks caused by temperature changes is a variation of block strains. Under the linear thermal expansion law,

$$[\Delta \epsilon_{kl}] = \alpha \Delta T [\delta_{kl}]$$

where  $[\Delta \epsilon_{kl}]$  is the incremental strain tensor,  $\delta_{kl}$  is the Kronecker delta,  $\alpha$  is the thermal expansion coefficient of the block at the current temperature, and  $\Delta T$  is the change in temperature. The variation of block strains is considered as a perturbation to the strain field. Using the linear elastic stress-strain relationship, a stress perturbation corresponding to the strain perturbation of a block can be expressed as

$$[\Delta \sigma_{ij}] = [E_{ijkl}] [\Delta \epsilon_{kl}]$$

where  $[E_{ijkl}]$  is the elastic tensor for the block, and  $[\Delta \sigma_{ij}]$  is the incremental stress tensor. Hence, the stress perturbation in a block can be expressed as

$$[\Delta \sigma_{ij}] = \alpha \Delta T [E_{ijkl}] [\delta_{kl}]$$

When the potential energy corresponding to the stress perturbation is taken into account as a part of potential energy for obtaining the quasi-static equilibrium condition of the system, movements (deformation, rotation, and translation) of blocks generated by the thermal loads are induced. During a small discrete time interval of the computation for the iterative solution process, the thermal expansion coefficient of a block is considered to be constant (according to the linear thermal expansion law). The nonlinearity of the thermal expansion coefficient is modelled using the updated thermal expansion coefficient computed from the nonlinear function using the updated temperature at the beginning of each time step.

## Description of Model

To conduct the numerical analyses using the DDA code, information is required about block geometries, fixed points or directions on the boundaries, block material constants, discontinuity properties, initial stresses, body forces, and various external loads. The input information about the jointed-rock pattern, the in situ stress condition, and the material properties of intact rock and rock joints for this study was adopted from the Reference Information Base (RIB) for Yucca Mountain (DOE, 1994) and from a site characterization report by Lin et al. (1993). Some of this information was modified to obtain a simple model which could be reasonably analyzed using the DDA code. The input data for the DDA simulation is listed in Table 1. The nonlinear thermal expansion coefficients for the rock blocks, shown in Figure 1, were adopted from the preliminary results of a laboratory test performed by Sandia National Laboratories (SNL). The specimen used for this laboratory test was taken from borehole USW NRG-6 at the Yucca Mountain site.

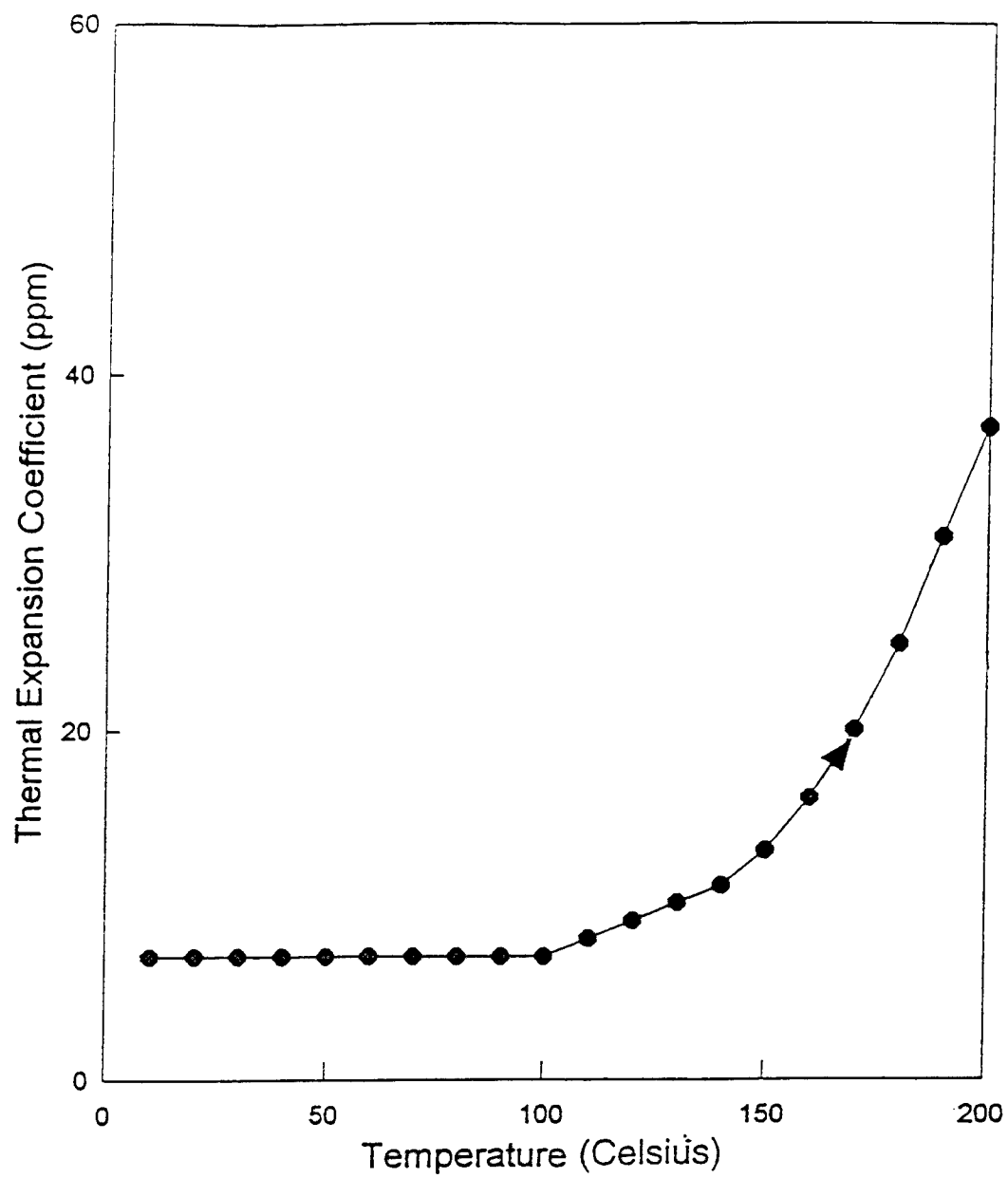


Figure 1. Instantaneous Coefficient of Thermal Expansion.

The computer simulation was performed in three stages: an initial stress loading stage, an excavation stage, and a thermal loading stage. For analysis of the initial stress loading, the region analyzed is composed of a jointed-rock mass, 40 m in height (20 m above and 20m below the centerline of the drift) with a width that corresponds to the drift spacing. Using the joint orientations and spacings listed in Table 1, the mesh generator in the DDA code produces a discrete system of rock blocks. In order to simulate the mechanical behavior of rock mass before and after excavation of a drift, the shape of each rock block in the center of the region is modified to fit the shape of the drift. To simplify the application of displacement and force boundary conditions on the problem domain, these rock blocks are bounded by rigid frames. The prescribed boundary displacements and forces are applied on these rigid frames rather than individual rock blocks at each edge of the mesh.

Table 1. Model Input Parameters

<u>Joint Properties</u>	<u>Vertical Joints</u>	<u>Horizontal Joints</u>	<u>Intact Rock</u>	
Orientation	100° dipping	10° dipping	Young's Modulus	32.7 GPa
Spacing	0.4 m	2.8 m	Poisson's Ratio	0.22
Frictional Angle	43 degrees	43 degrees	Bulk Density	2.3 g/cm <sup>3</sup>
Cohesion	7.3 MPa	25.2 MPa		
Normal Stiffness	1.7×10 <sup>6</sup> MPa/m	1.7×10 <sup>6</sup> MPa/m		
Shear Stiffness	6.9×10 <sup>4</sup> MPa/m	6.9×10 <sup>4</sup> MPa/m		
<u>Others</u>				
Depth of Tunnel Invert		311 m		
Vertical In Situ Stress @ 311 m		7.00 MPa		
Horizontal In Situ Stress @ 311 m		3.85 MPa		
Ratio of Horizontal to Vertical Stresses		0.55		

In a conventional finite element analysis, it is not necessary to conduct the initial stress-loading simulation. The initial stresses can be a part of the input parameters to describe the initial condition. In the DDA analyses, the initial condition of the system also includes the relative position of block interfaces, although the initial stresses may be input parameters. Contacts between blocks are established by the compression of contact springs which have no initial length. In other words, when two blocks are in contact, a small amount of geometrical overlap exists between them. Within a given space occupied by the initial system of nonoverlapping blocks, the contact overlap between blocks produces voids in the initially assigned system space. Hence, the stress relaxation in rock blocks caused by the existence of such voids may be a meaningless numerical result. Although very stiff springs (as compared to the stiffness of rock blocks) can be used where only a very small amount of stress reduction is generated in each block, the large

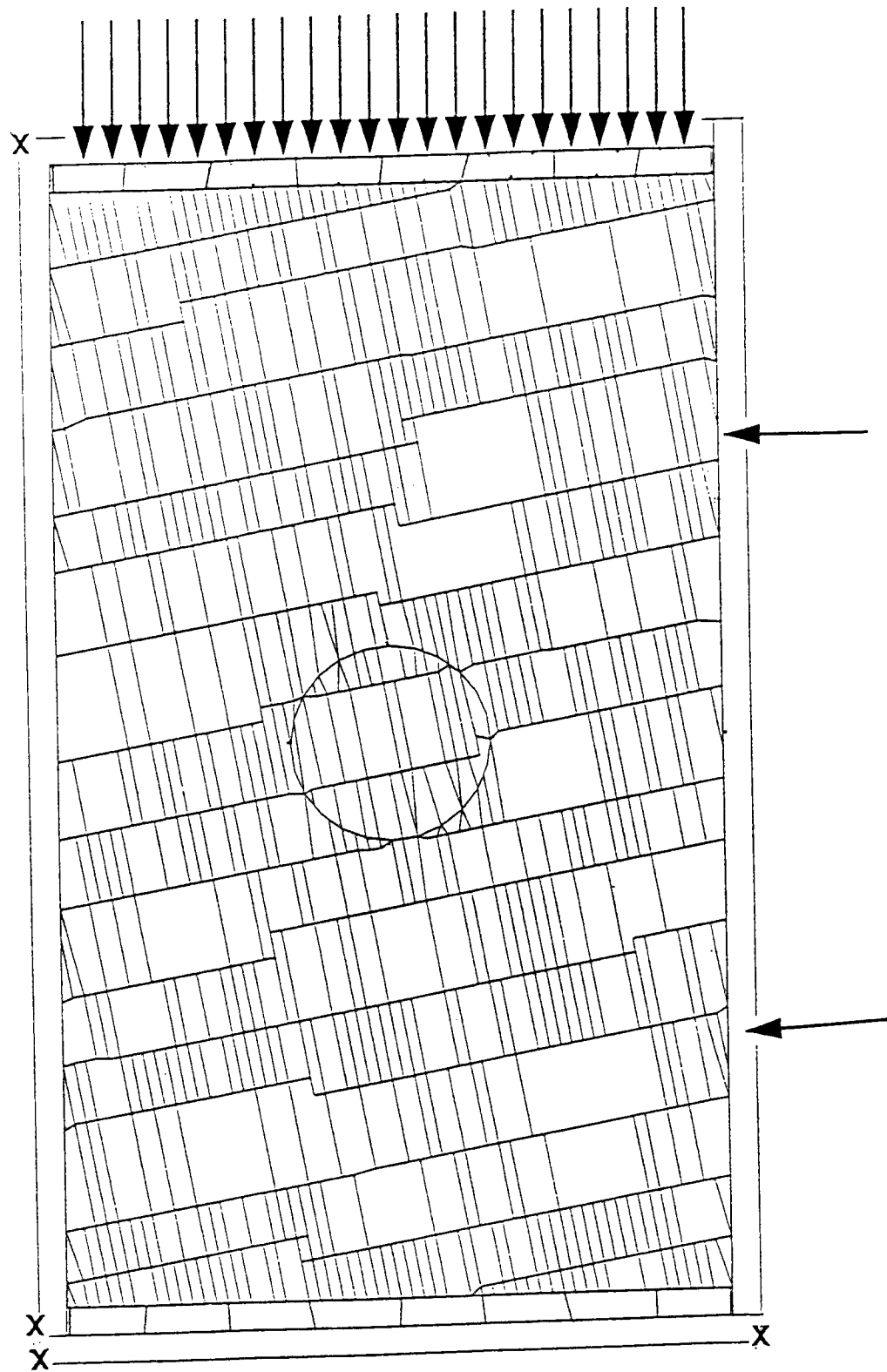


Figure 2. DDA Mesh

stiffness of contact springs creates the numerical difficulty for solving the system equations. To avoid this difficulty, a DDA model can start with the initial stresses and the geometries of overlapped blocks or with null initial stresses and rock blocks without overlapping surfaces. In the case of non-overlapped blocks with null initial stresses, the initial internal contacts are established by compacting the system using the external loads, which are statically equivalent to the in situ stresses.

Figure 2 shows the DDA model's representation of the jointed-block-rock mass which contains a 7.0-m diameter drift with 23.3-m drift spacing. This is the mesh used for the initial stress-loading simulation. The left and bottom boundary frames are fixed in the reference space. External point loads (the arrows shown in Figure 2) which are in static equilibrium with the horizontal in situ stresses are acting on the right boundary frame. The weight of the overburden is applied as the external vertical load that acts on a number of boundary frames at the top of the mesh. Since the overburden load is applied through a number of small frames (rather than one long piece of rigid frame), non-uniformly distributed displacements across the top of the mesh are modeled. At the bottom of the mesh, the non-uniformly distributed displacements are modeled by adding a layer of load-bearing blocks between the bottom of the jointed rock mass and the bottom rigid frame which is fixed in the reference space. The Young's Modulus for these load-bearing blocks is therefor assumed to be one order magnitude smaller than the corresponding value for the rock blocks in the jointed-rock mass and the joint surface of load-bearing blocks is assumed to be frictionless.

After the quasi-static solution of the initial stress loading simulation has been obtained, the rock blocks within the drift are removed to simulate the excavation process. The remaining rock blocks with their deformed/displaced geometry are then used as the initial geometry for the excavation simulation. The corresponding final block stresses generated by the initial stress loading simulation are adopted as the initial block stresses for the excavation simulation. The right frame for applying the external loads corresponding to the horizontal in situ stresses is then fixed in the reference space (without any external loads) to simulate the line of symmetry for the rock response induced by excavation of multiple drifts whose center-to-center distance is constant. The external vertical point forces remain the same as those for the initial stress-loading simulation to represent the weight of the overburden formation. The rock mass response induced by excavation is then obtained by obtaining the quasi-static solution that corresponds to the updated initial geometry and stresses and the revised load and displacement boundary conditions.

The thermal load is expressed by the value of areal mass loading (AML). For a given thermal load, the waste package spacing is adjusted according to the drift spacing. Lingineni (1994) computed the temperatures of the waste package and surrounding host rock as a function of time after waste emplacement. Thermal profiles in the near field were predicted for various thermal loads, package spacings, and drift diameters. The thermal model calculation is applicable to the in-drift emplacement mode where the

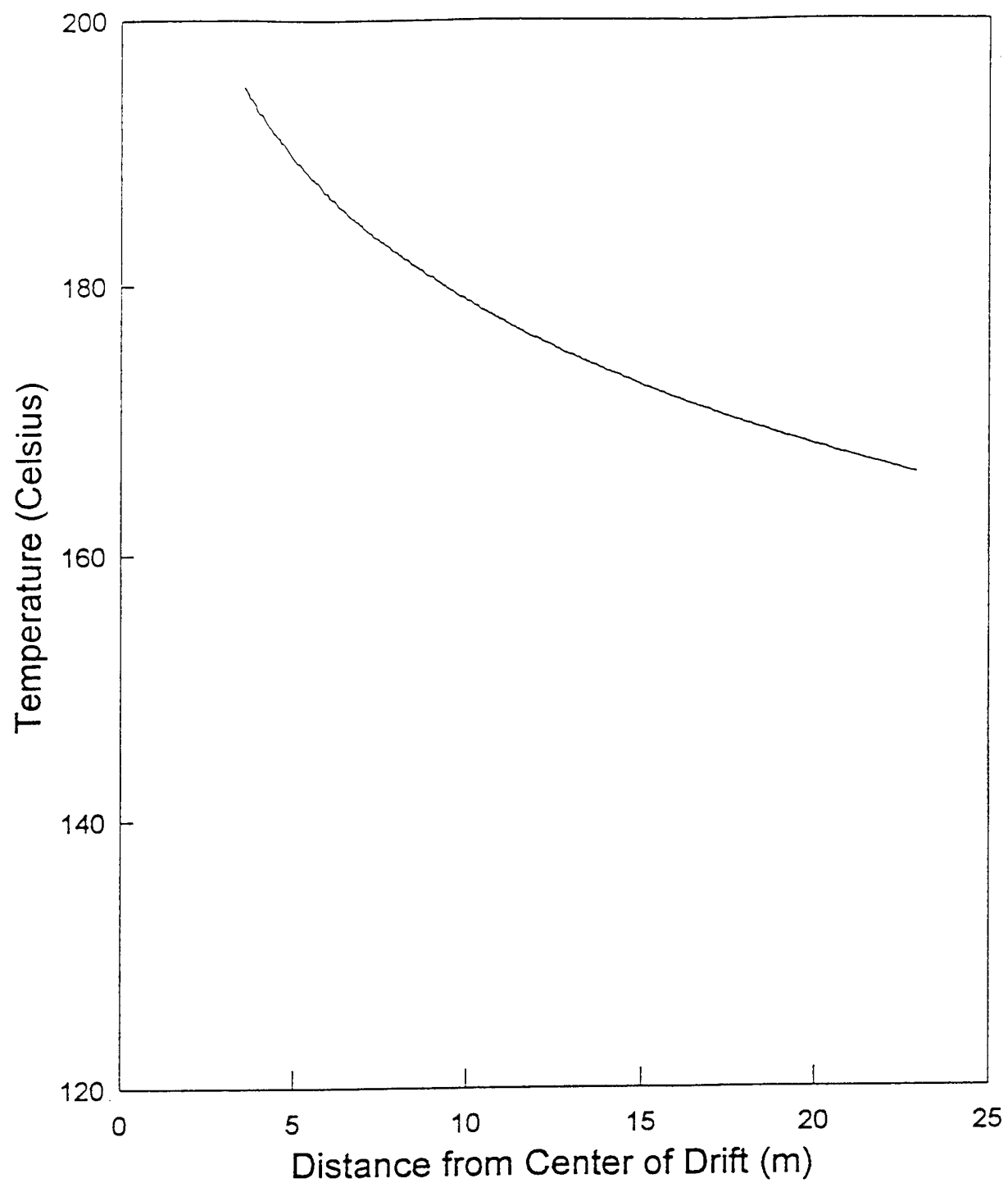


Figure 3. Temperature Profile

modelled region consists of a single, infinitely long emplacement drift surrounded by the host rock. These computations were carried out in a one-dimensional, radial coordinate system. The temperatures induced by thermal loads in neighboring drifts were computed. The superimposition of temperature fields for many drifts was then calculated to simulate the effects of thermal loads in multiple drifts. As part of the input data for this study, Lingineni provided the 100-year post-emplacement temperature distribution. These temperatures were reported at the center of each rock block in the deformed region generated by the excavation simulation. For a one-dimensional radial coordinate system, the computed temperature profile for thermal loading as a function of the radial distance from the center of the drift is shown in Figure 3.

To analyze the thermal loading effects, the DDA model was restarted (without any change in the boundary and loading conditions) from the quasi-static solution found in the excavation simulation using the concept that a perturbation of the block strain corresponds to a change in block temperature. By minimizing the total potential energy, which includes the variation of the strain energy generated by the change of block temperatures, the DDA model computes the thermally induced block deformation and rigid body motion of the blocks.

## Discussion of Results

To observe the change of the character of the joints, the status of contacts in the system has been presented graphically. A segment of a joint is represented by two edges of different blocks which are assumed to be nearly parallel. Therefore, a joint segment is referenced by a pair of contacts defined by corners and reference edges. If either contact corner is close to but not touching the referenced contact edge, the joint between these two blocks is open. A joint is closed only if the two contacts used to reference the joint segment are both closed. As shown in Figure 4, the size of a joint opening can be represented approximately using the associated contact opening which is the distance from the corner of a block to the referenced contact edge measured perpendicular to the edge. Each open contact can be represented by a vector normal to the referenced contact edge. The length of the vector represents the magnitude of the contact (joint) opening.

For the initial stress-loading simulation, a fairly uniformly distributed stress field was generated by the external loads which are in static equilibrium with the in situ stresses. The vertical stresses are about 6.5 MPa in the rock blocks near the top of the modeled region and about 7.4 MPa in the rock blocks near the bottom of the region (see Table 1). The ratio of the horizontal stress to the vertical stress remains at about 0.55 in each rock block. Since non-uniform contact forces are generated among blocks of various sizes, the principal stresses for each rock block are slightly different. As a result of the initial stress-loading, all joints in the modeled rock mass are closed.

The final stress distribution and joint openings from the excavation simulation are shown in Figures 5 and 6. The stress concentration around the drift after excavation



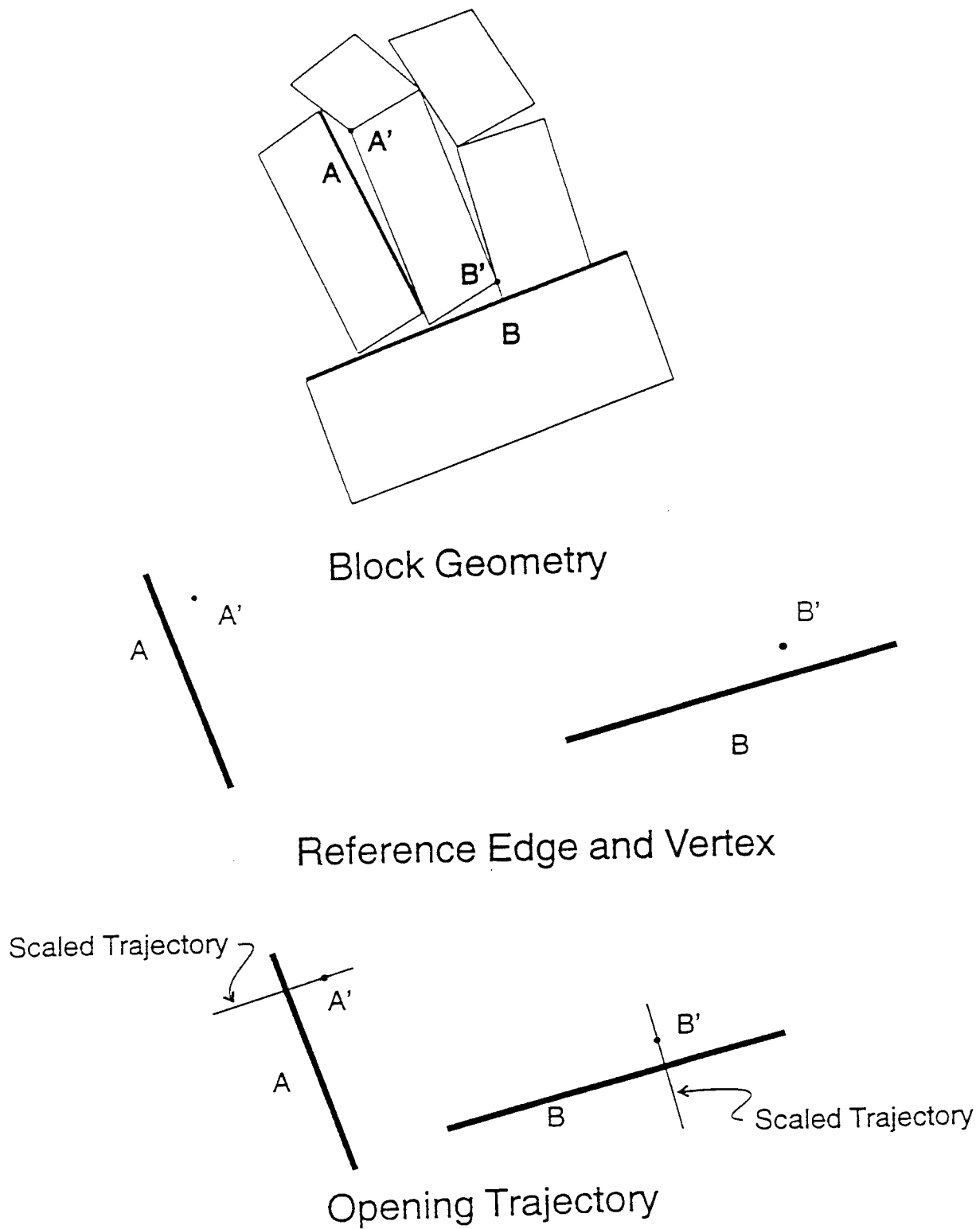
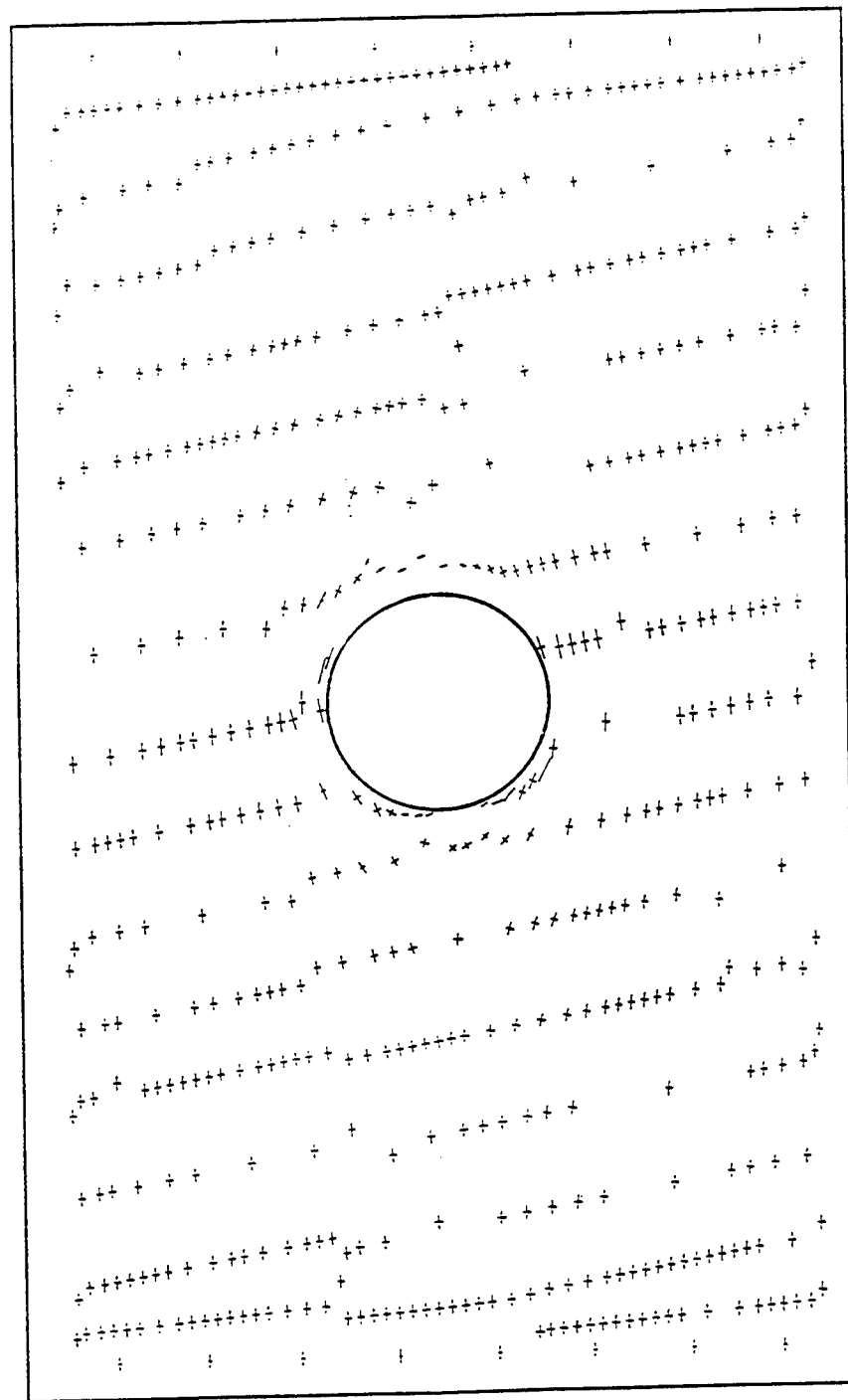


Figure 4. Joint Opening Representation



Scale: 100MPa

Figure 5. Principal Stresses After Excavation

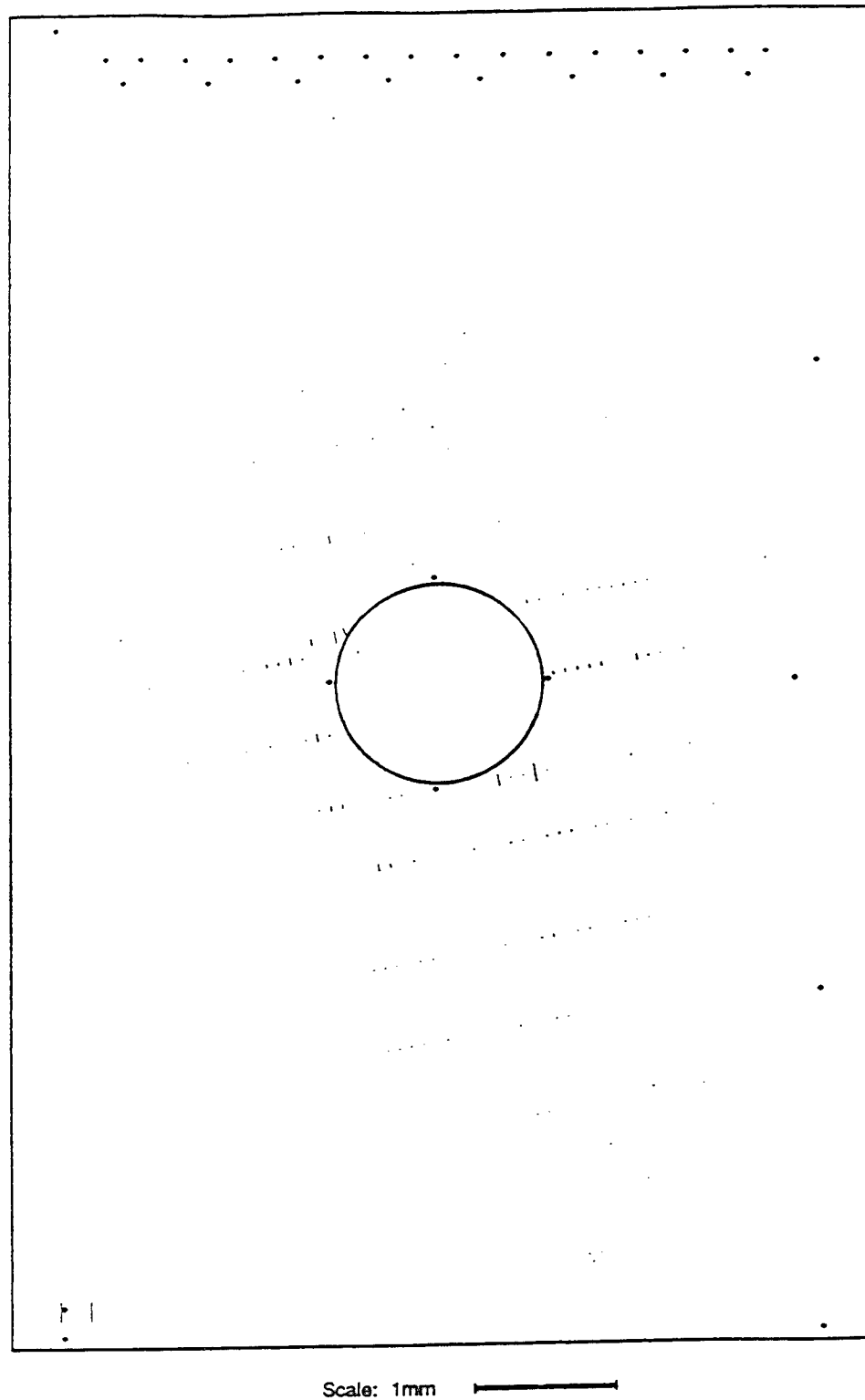


Figure 6. Joint Opening After Excavation

forms a pressure arch that makes the drift opening structurally stable. Noticeable joint opening appears after the excavation, as shown in Figure 6. The openings in the rock mass only occur in the immediate vicinity of the drift walls (the invert and the roof). This effect is limited to a distance of less than the half the diameter of the drift (3.5 m). Except for joints formed by a few rock wedges at the upper left and the lower right corners of the drift, the size of joint openings in the immediate area of the drift wall is on the order of 0.03 mm. The vertical and horizontal drift closures after the excavation loading stage are about 1.6 and 0.3 mm, respectively.

## Thermomechanical Effects

Figures 7 and 8 show the final stress distribution and joint opening after the thermal loading stage. The vertical stresses of all blocks after thermal loading remains at about the level of the block initial values (6.5 to 7.4 MPa) due to upward rock mass thermal expansion. The horizontal stresses after thermal loading are increased significantly over the entire region, due to the fixed lateral displacement boundary conditions on both sides of the region. In general, the horizontal stresses in the rock mass, a few meters away from the drift are about 55 to 60 MPa. The model with a fixed lateral displacement boundary condition represents the center of the repository only. At the edge of the repository, a certain amount of lateral thermal expansion of rock mass would occur. Therefore, less horizontal stress would build up at this location because of thermal loading.

In the immediate area around the drift, the major principal stress may reach 90 MPa. This high principal stress in the jointed rock mass around the drift may cause rock spalling to occur at the drift wall. After thermal loading, the large number and magnitude of joint openings in the rock mass immediately around the drift suggests that some rock wedges at the drift wall may become detached. Figure 8 also shows that the amount of the disturbance (joint opening) extends to the boundary of the modeled domain. This indicates that a larger domain (more than 20 m above and 20 m below the drift centerline) should have been modeled in order to determine the full extent of the disturbance. The opening of horizontal joints is about 0.2 to 0.7 mm in an area within about a 10 m radius of the drift wall. In general, all of the vertical joints remain closed after the thermal load is applied. In contrast to the 1.6 mm vertical drift closure and 0.3 mm horizontal drift closure generated in the excavation stage, the drift height measured through the center of the drift increases (expands) 13.4 mm, while the drift width measured through the center of the drift closes 13.3 mm during the thermal loading stage.

The Reference Information Base (DOE, 1994) indicated that the rock mass strength is about 49 MPa at the confining pressure of about  $\sigma_3 = 7$  MPa. After thermal loading the horizontal stress in the area a few meters away from the drift is about 55 MPa. This prediction indicates the rock mass failure in the entire domain of the modeled rock mass may occur due to the compressive stresses generated by the 111 MTU/acre

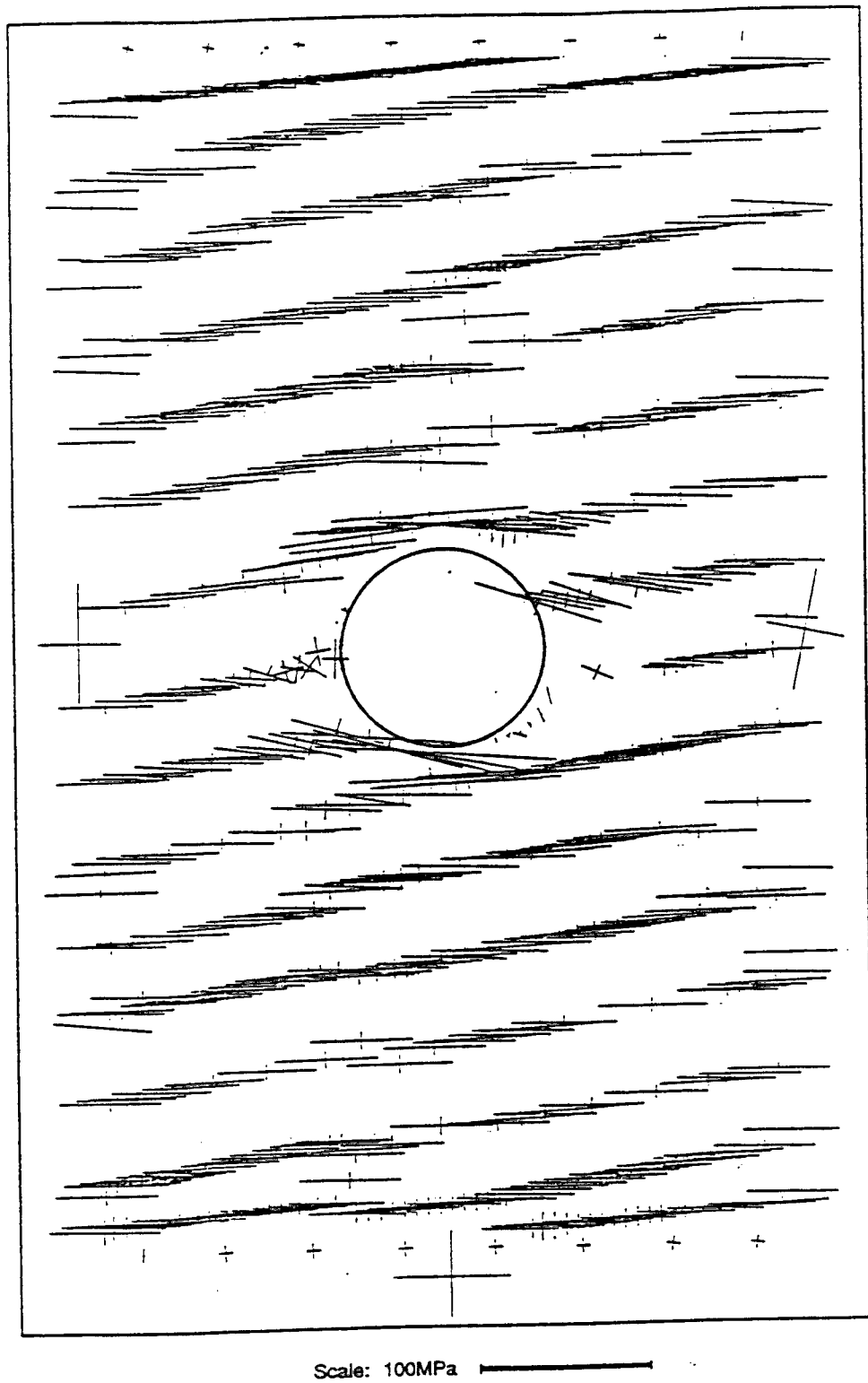
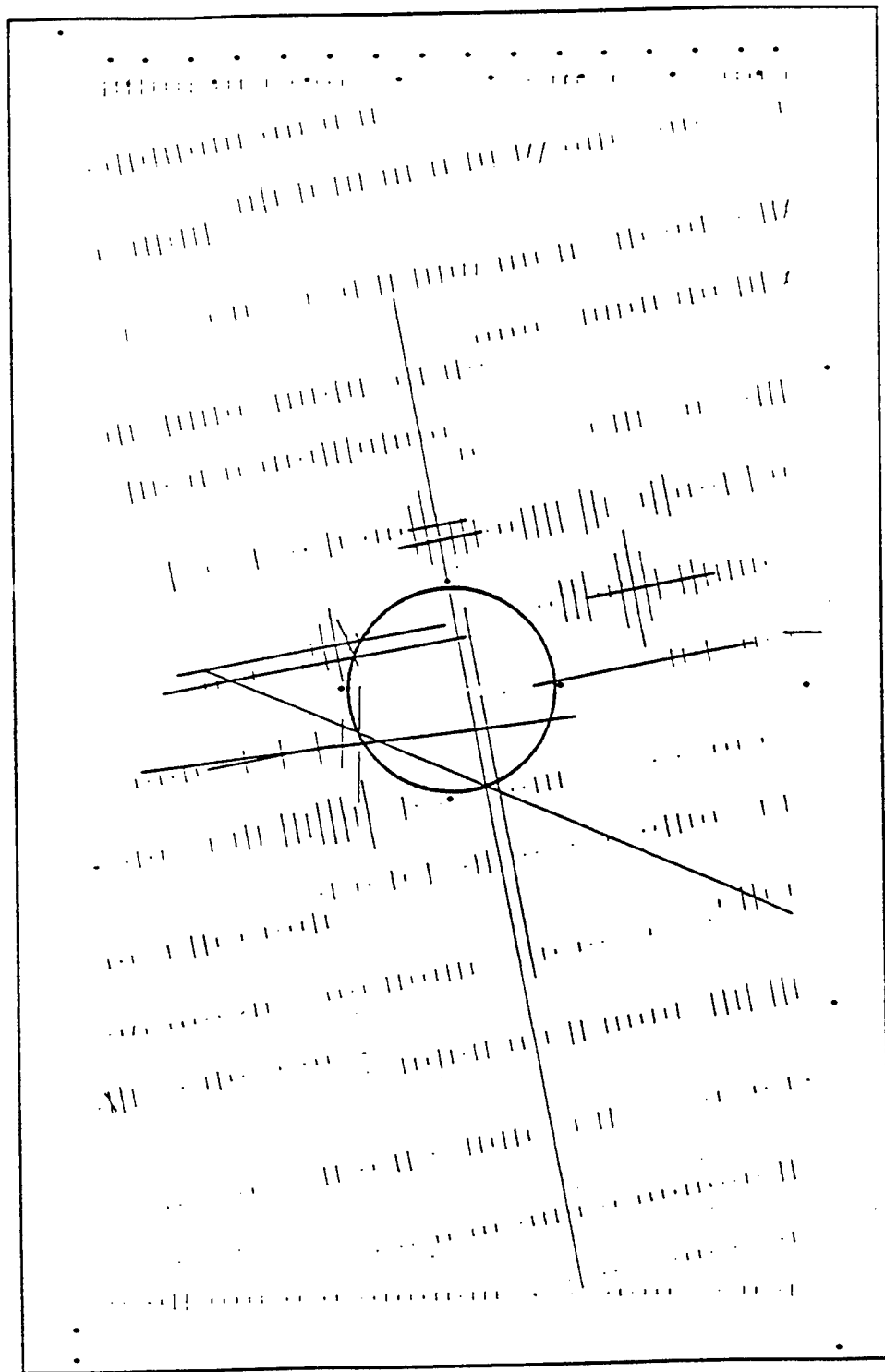


Figure 7. Principal Stresses After Thermal Loading



Scale: 1mm 

Figure 8. Joint Opening After Thermal Loading

thermal load. The high horizontal stresses with thermal load predicted by the DDA model was validated using a simple one-dimensional analytic solution based on the theory of linear elasticity, the theory of linear thermal expansion, and the boundary condition that there is no displacement at the ends of the one-dimensional segment.

The prediction of rock mass failure in the entire modeled domain (near field) is dependent on the validity of the criterion for rock mass strength and the assumption of fixed boundary displacement in the horizontal direction provided by boundary frames at both sides of the region, as well as the free sliding against the boundary frame in the vertical direction for the thermal loading stage simulation. Such assumptions are widely used for simulating the rock mass response to a mining layout using multiple parallel drifts. It is believed that this assumption is reasonable for simulating the rock mass response around the drifts at the center of the entire repository. If the rock mass strength criterion and the boundary frame assumptions are shown to be valid, the 111 MTU/acre thermal load may not be feasible because the entire near field rock mass may become mechanically unstable.

## **Estimated Change in Hydraulic Conductivity**

Existing fracture aperture sizes may be used to help estimate the undisturbed hydrologic properties of the fracture network beyond the zone affected by the drift excavation and thermal loads. The change in the fracture network hydrologic properties of the disturbed rock mass may be assessed by comparing the change of fracture apertures caused by excavation and thermal loading.

Montazer et al. (1986) and Thordarson (1983) reported bulk permeability for the TSw in the range of  $1 \times 10^{-13}$  to  $1 \times 10^{-11}$  m<sup>2</sup> for fracture aperture sizes in the range of 0.1 to 1 mm. The corresponding bulk permeabilities in the composite fracture/matrix porosity model have been estimated to be about  $1 \times 10^{-15}$  and  $1 \times 10^{-12}$  m<sup>2</sup> using cubic law for fracture permeability (Shenker et al, 1995). The bulk permeabilities used by Dunn and Sobolik (1993) for flow calculation in TSw fractured rock are  $3 \times 10^{-16}$  m<sup>2</sup> and  $1 \times 10^{-12}$  m<sup>2</sup> roughly corresponding to 0.005 mm and 0.07 mm fracture apertures, respectively. Fracture aperture sizes in Topopah Spring welded hydrogeologic unit (TSw), reported by Peters et al., (1984) are in the range of 0.004 to 0.005 mm. The average fracture aperture in the Tiva Canyon is about 0.5 mm and the fracture apertures of TSw are expected to be much smaller (personal communication, Lawrence Anna, USGS). Based on the wide range of values described here, we conservatively estimate that the average undisturbed fracture aperture for TSw is about 0.005 mm.

Through a literature review, it was found that the fracture aperture can increase up to 1 mm in a 10 meter wide mechanically disturbed zone around a drift, if the drift is excavated by drill-and-blast methods. Based on the DDA model calculations for the case of an 111 MTU/acre thermal load, the fracture aperture will be increased about 0.03

mm and 0.2 mm for the mechanically- and thermally-disturbed zones, respectively, if the drift is mechanically excavated. Compare to the undisturbed fracture aperture estimated in the last paragraph, the disturbed fracture aperture is about the same as the change of aperture size caused by thermal load. Hence, the change of bulk permeabilities in the thermally-disturbed zones for the case of an 111 MTU/acre thermal load is predicted to be significant.

## CONCLUSIONS

This paper has demonstrated that the mechanical and thermomechanical effects caused by excavation and thermal load can be analyzed using the DDA method. Based on the analysis, the following conclusions can be drawn:

- Quantitative descriptions of the joint openings induced by excavation and 111 MTU/acre thermal load are estimated to be of the order of 0.01 and 0.2 mm, respectively, in the near field of the potential repository. The corresponding bulk permeabilities in the composite fracture/matrix porosity model are estimated to be about  $1 \times 10^{-15}$  and  $1 \times 10^{-12}$  m<sup>2</sup>.
- The zone of disturbance caused by excavation was found to extend about half a drift diameter beyond the drift wall. Because of the limited extent of this disturbed zone and the small change in fracture aperture (0.01 mm) it can be assumed that this zone would not affect ground-water travel time significantly over the path length from the repository to the accessible environment (about 5300 m).
- The results of modeling of the stress distribution around the repository drift for the 111 MTU/acre thermal load indicate that stresses may be higher than the strength of the rock mass. This indicates that the rock mass could fail if this thermal load is applied and if the rock mass strength criterion and the boundary frame assumptions are shown to be valid.
- The increase in hydraulic conductivity caused by thermal loading is about three orders of magnitude. A change of this magnitude could be significant with respect to ground-water travel time depending on the extent of the disturbance.
- For the region modeled using DDA the thermal disturbance occurred throughout the entire region, 20 m above to 20 m below the center line of the drift. Based on this result the thermally disturbed zone is more than 20 m beyond the drift (more than one drift diameter).



## References

- DOE. (1994). "Yucca Mountain site characterization project - reference information base," version 3, YMP/93-02, Yucca Mountain Site Characterization Project, Las Vegas, NV.
- Dunn, E., and S. R. Sobolik. (1993). "Evaluation of the effects of underground water usage and spillage in the exploratory studies facility," SAND93-1182, Sandia National Laboratories, Albuquerque, NM.
- Lin, M., M. P. Hardy, and S. J. Bauer. (1993). "Rock mass mechanical property estimations for the Yucca Mountain site characterization project," SAND92-0450, Sandia National Laboratories, Albuquerque, NM.
- Linginini, S. (1994). "Near-field thermal calculations for individual waste package placement." *Proceedings of Fifth International High-Level Radioactive Waste Management Conference*, Las Vegas, NV.
- Montazer, P., E. P. Weeks, F. Thamir, S. N. Yard, and P. B. Hofrichter. (1986). "Monitoring the Vadose Zone in Fractured Tuff, Yucca Mountain, Nevada." *Proceedings of the NWWA Conference on Characterization and Monitoring of the Vadose (Unsaturated) Zone*, National Well Water Association, Worthington, OH, 439-469.
- Peters, R. R., R. L. Williams, F. B. Nimick, B. C. Blair, P. R. Heller, and G. W. Gee. (1984). "Fracture and matrix hydrologic characteristics of tuffaceous materials from Yucca Mountain, Nye County, Nevada." SAND84-1471, Sandia National Laboratories, Albuquerque, NM.
- Schenker, A. R., T. H. Robey, C. A. Rautman, and R. W. Barnard. (1994). "Stochastic hydrogeologic units and hydrogeologic properties development for total-system performance assessments." SAND94-0244, Sandia National Laboratories, Albuquerque, NM.
- Shi, G. (1993). "Block system modeling by Discontinuous Deformation Analysis." Computational Mechanics Publication, South Hampton, UK.
- Thordarson, W. (1983). "Geohydrologic data and test results from Well J-13, Nevada Test Site, Nye County, Nevada." USGS/WRI-83-4171, U.S. Geological Survey, Denver, CO.
- Tsai, F. (1993). "Dynamic interaction of discrete continuum - the theory of non-overlapping continuum." Ph. D. dissertation, Department of Engineering-Material Science and Mineral Engineering, University of California at Berkeley, Berkeley, CA.

# Automatic Creation of Mathematical Meshes in Manifold Method of Material Analysis

Guangqi CHEN\*, Shigeru MIKI\* and Yuzo OHNISHI\*\*

\* Kiso-Jiban Consultants Co., Ltd., Tokyo 102, Japan

\*\* Kyoto University, Kyoto 606-01, Japan

## Abstract

The Manifold Method (MM) of Material Analysis is a very flexible and powerful numerical analysis method, which contains and combines widely used Finite Element Method (FEM) and joint or block oriented Discontinuous Deformation Analysis (DDA) method in a unified form.

However, up to now, there is no effective means to make MM models, and it is not easy to make such a model by hand. As a result, the practical applications of the MM method are limited considerably.

For this reason, we present a method to create MM models from the corresponding DDA models automatically. Since we have already developed a very powerful DDA software called DDAWorkTool, which contains a model-maker module, it is easy to make a DDA model by use of the tool.

The program for the method has been developed, and it has been shown to be very efficient by transferring a lot of DDA models into MM models. It will be put into practical use soon. We expect that the powerful MM method will get more and more widely practical applications by using the program.

## 1 Introduction

The Manifold Method (MM) of Material Analysis, as we know, is a very flexible and powerful numerical analysis method. It contains and combines widely used Finite Element Method (FEM) and joint or block oriented Discontinuous Deformation Analysis (DDA) method in a unified form (Shi, 1994).

The meshes of the manifold method are finite covers, which overlap each other and cover the entire material volume. The cover system of a model is formed by both mathematical and physical meshes. The major work of creating a MM model is to delimit these meshes. However, up to now, there is no effective means to do this, and it is not easy to make such a mesh by hand. As a result, the practical applications of such a new good method are limited considerably.

Here, we present a method to create the mathematical meshes automatically based on the physical meshes for any MM models. We also propose to use a block system of DDA for the same problem as the physical meshes. Since we have already developed a very powerful DDA software called DDAWorkTool, which contains a model-maker module (Chen *et al.*, 1995), it

now is very easy to make a DDA block system by use of the tool.

The program for the proposed method has been developed, and it has been shown to be very efficient by transferring a lot of DDA models into MM models.

## 2 Outline of the proposed method

The physical meshes outline the boundaries of the material volume, joints and blocks. Obviously, they correspond to the assemblage of blocks for DDA models. For us, it is convenient to use DDA models to make MM models since DDA models are easily made by use of our newly developed DDAWorkTool.

The mathematical meshes of a MM model can arbitrarily be chosen by user and it does not matter even if some meshes extend outside the material volume. This is one of the major advantages of the MM method, which makes it possible to create mathematical meshes automatically for any shape of materials.

It is common to use triangular meshes like FEM to form mathematical meshes. Both the formulation and the program of MM for a triangular element of mathematical mesh have been developed by Shi, 1994. We also choose those meshes in our method.

For simple description and better understanding, we only use the term *element* for this specific choice instead of using the concepts of *cover* and *mesh* in the general meaning.

An *element* means a mathematical element and a physical element (Fig.1).

A *mathematical element* is a triangle represented by three element nodes like FEM. The displacements of the element nodes are unknowns of MM. An *element node* has both the coordinate and the node number, and it can be outside the physical region.

A *physical element* is a part of the mathematical element in which the material exists, and the integration will be carried out. It is represented by the vertices of the area, called *element vertices* here (Fig.1).

If an element vertex lies on the physical boundaries of a block system, it is also a *boundary point*. All the boundary points are needed to be specified for the purpose of checking the contacts between blocks in the MM calculation.

For example, in Fig.1, the triangle is the mathematical element represented by three element nodes  $i, j$  and  $k$ ; the shaded area is the corresponding physical element with vertices 1, 2,  $\dots$ , 7; all the element vertices except for 7 are the boundary points of the physical block delimited by dotted lines.

In fact, the major task of creating a MM model is to make all the elements, that is, to

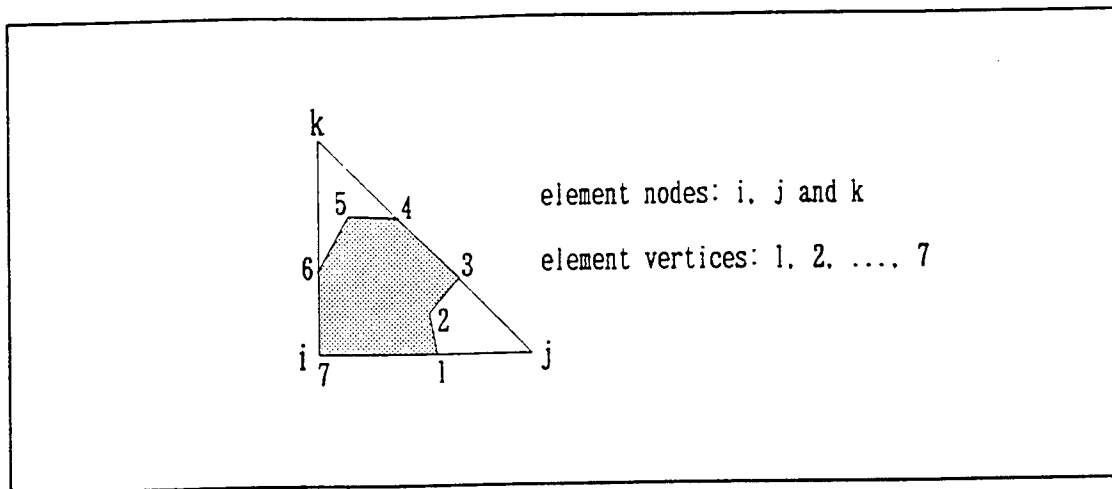


Fig.1. A mathematical element (the triangle) and the corresponding physical element (the shaded area)

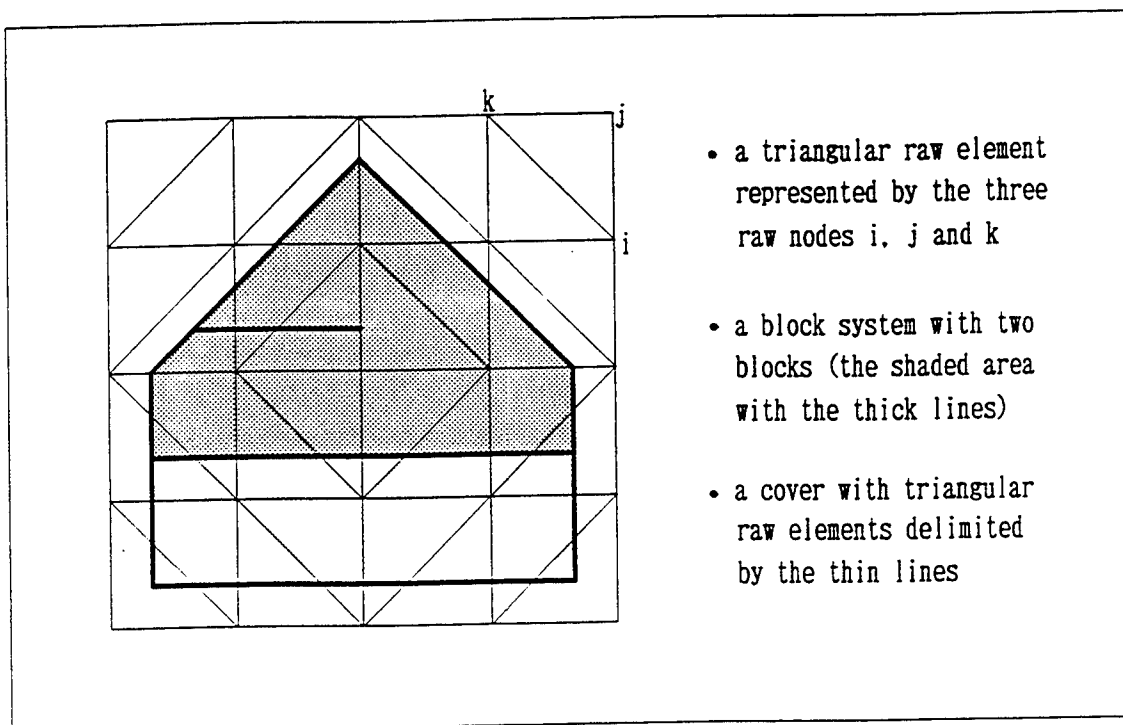


Fig.2. A cover with triangular raw elements over a block system

determine the coordinates and node numbers of all the element nodes; to specify the three element node numbers of each mathematical element and to obtain element vertices of each physical element.

For this purpose, we, in the first place, create a rectangular cover with regular triangles over the whole block system, i.e. the blocks of a DDA model. Fig.2 shows an example in which the cover with 32 triangles delimited by the thin lines covers the block system of two blocks (the shaded areas with the thick lines).

The grid points of the cover are called *raw nodes*, and the triangles are called raw elements here. A *raw element* is represented by three raw nodes as shown at the upper right corner of the cover in Fig. 2. We use the terms *raw element* and *raw node* here to distinguish them from the elements and the element nodes of MM.

In the second place, we produce all the elements from the raw elements based on the block system. If a raw element has a common area with a block, an element will be produced. The physical element corresponds to the common area and the mathematical element corresponds to the raw element. In other words, the element vertices directly take the vertices of the common area, and the element nodes take either the corresponding raw nodes or their copies. The copy of a raw node is a new raw node with the same coordinate as the original but a new different number next to the last raw node number.

Finally, we compress the element nodes by deleting the nodes which are not used by any elements, and find out all the boundary points for each block.

The major procedures of making a MM model are shown in Fig.3.

### 3 Creation of the Cover with Triangular Raw Elements

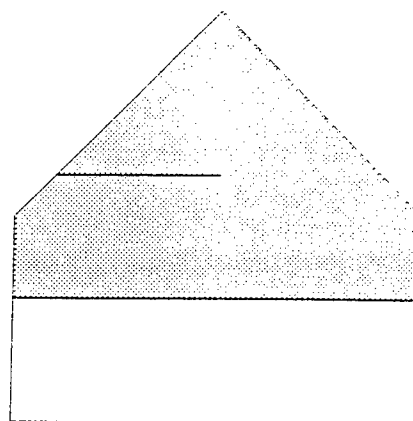
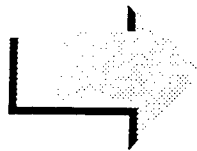
The cover with triangular raw elements in a rectangle region is adaptable to any shape of materials in our method. It should be large enough to cover the whole block system.

Fig.4(a) shows the outline of the cover to be created, and it is divided into four quadrants from the axis center  $(x_0, y_0)$ . There are  $n_r \times n_t$  grids in quadrant 1,  $n_l \times n_t$  grids in quadrant 2,  $n_l \times n_b$  grids in quadrant 3 and  $n_r \times n_b$  grids in quadrant 4 respectively. All grids have the same size with  $\Delta_x \times \Delta_y$ , and a grid contains two triangular raw elements.

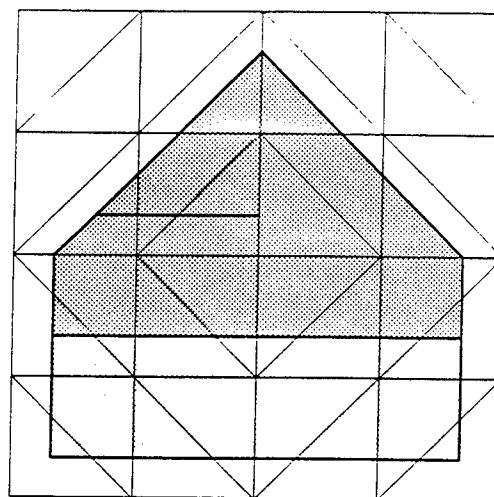
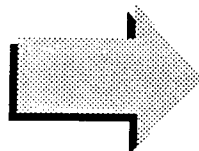
The number of the grids in each quadrant is determined by the following formulas according to the dimension of the block system:

$$n_r = \text{int}\left(\frac{x_{maz} - x_0}{\Delta_x}\right) + 1$$

1. Create the block system by use of DDAWorkTool



2. Create a cover with raw elements over the block system



3. Determine all the elements and the boundary points

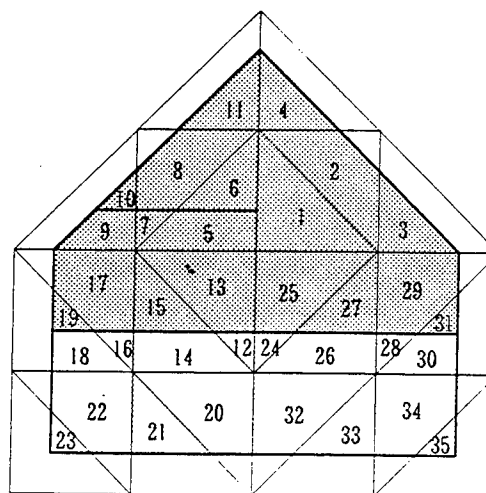
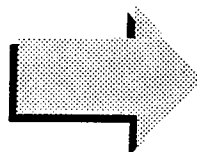


Fig.3. The major procedures of making a MM model

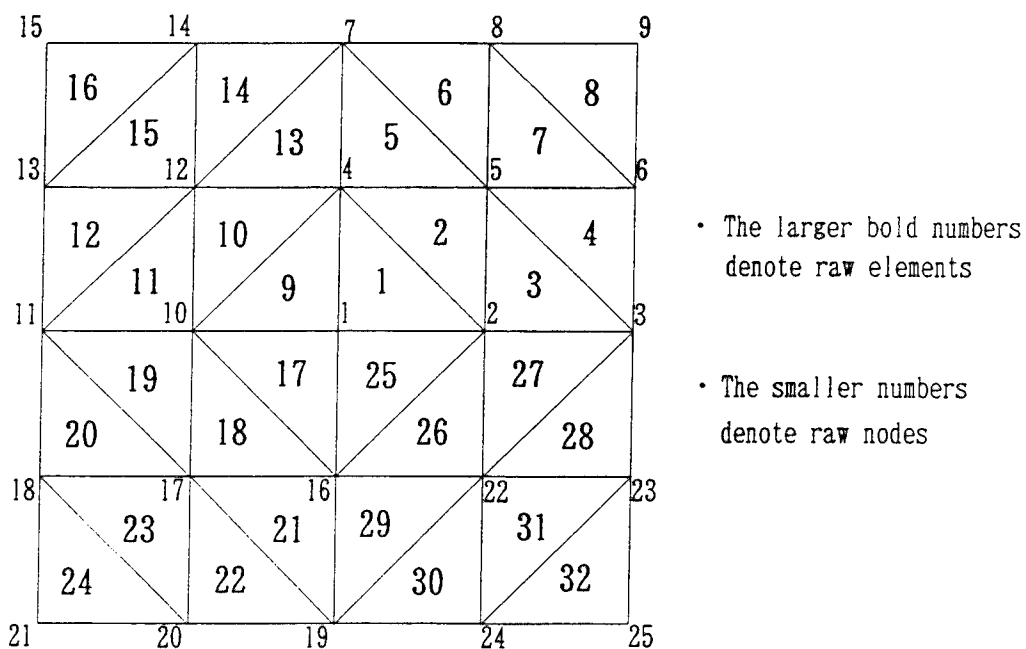
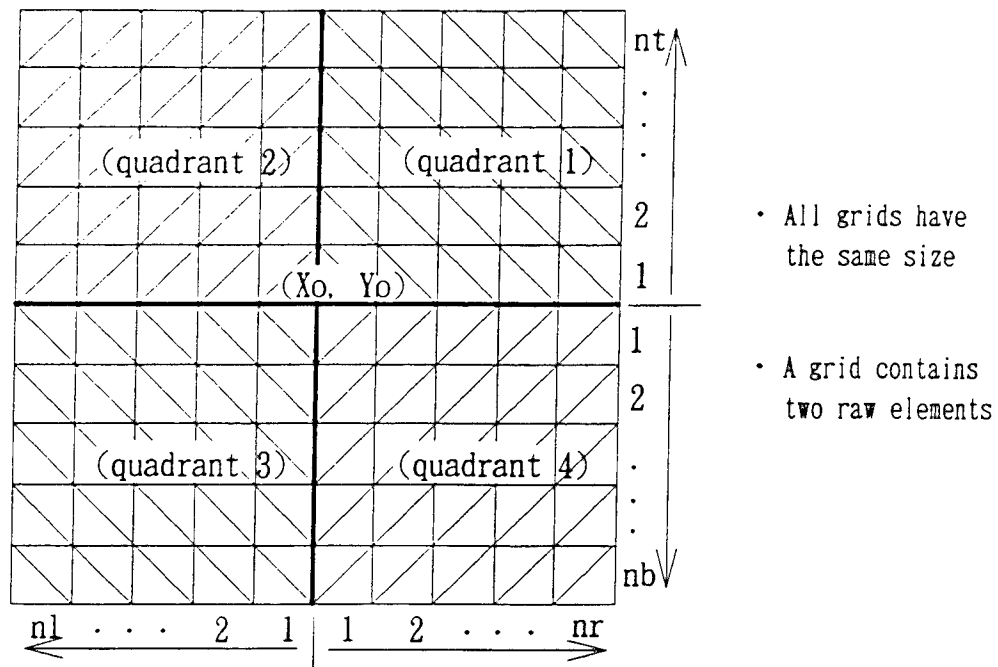


Fig. 4. The cover with triangular row elements

$$n_l = \text{int}\left(\frac{x_0 - x_{\min}}{\Delta_x}\right) + 1$$

$$n_t = \text{int}\left(\frac{y_{\max} - y_0}{\Delta_y}\right) + 1$$

$$n_b = \text{int}\left(\frac{y_0 - y_{\min}}{\Delta_y}\right) + 1$$

where  $(x_{\min}, y_{\min})$  and  $(x_{\max}, y_{\max})$  are the coordinates of the lower left and upper right corner points of the rectangle which just encloses the whole block system.

In creation of such a cover, we need to calculate the coordinates of all the raw nodes, to assign a unique number to each of them, and to specify the three raw node numbers of each raw element.

In quadrant 1, there are  $N_1 = (n_r + 1)(n_t + 1)$  raw nodes to be determined. The node number of the raw node in  $j$ th row and  $i$ th column from the center is noted as  $k1_{ji}$  and its coordinate is noted as  $(X_{k1_{ji}}, Y_{k1_{ji}})$ , which are determined as follows:

$$\begin{cases} k1_{ji} = i + 1 + j(n_r + 1) \\ X_{k1_{ji}} = x_0 + i\Delta_x \\ Y_{k1_{ji}} = y_0 + j\Delta_y \\ i = 0, 1, 2, \dots, n_r \\ j = 0, 1, 2, \dots, n_t \end{cases}$$

The three raw node numbers of the lower raw element of a grid in this quadrant are

$$\begin{cases} k1_{j-1, i-1} \\ k1_{j-1, i} \\ k1_{j, i-1} \\ i = 1, 2, \dots, n_r; \quad j = 1, 2, \dots, n_t \end{cases}$$

while those of the upper raw element of a grid are

$$\begin{cases} k1_{j-1, i} \\ k1_{j, i} \\ k1_{j, i-1} \\ i = 1, 2, \dots, n_r; \quad j = 1, 2, \dots, n_t \end{cases}$$

In quadrant 2, there are  $N_2 = n_t(n_t + 1)$  raw nodes to be determined. The node number of the raw node in  $j$ th row and  $i$ th column from the center is noted as  $k2_{ji}$  and its coordinate is



noted as  $(X_{k2ji}, Y_{k2ji})$ , which are determined as follows:

$$\begin{cases} k2ji = N_1 + i + jn_l \\ X_{k2ji} = x_0 - i\Delta_x \\ Y_{k2ji} = y_0 + j\Delta_y \\ i = 1, 2, \dots, n_l \\ j = 0, 1, \dots, n_t \end{cases}$$

Since the raw nodes in the boundary between quadrant 1 and 2 have already been determined in quadrant 1, they are just copied to quadrant 2 as follows:

$$k2j0 = k1j0 \quad \text{for } j = 0, 1, 2, \dots, n_t.$$

The three raw node numbers of the lower raw element of a grid in quadrant 2 are

$$\begin{cases} k2j-1,i \\ k2j-1,i-1 \\ k2j,i-1 \\ i = 1, 2, \dots, n_l; \quad j = 1, 2, \dots, n_t \end{cases}$$

while those of the upper raw element of a grid are

$$\begin{cases} k2j-1,i \\ k2j,i-1 \\ k2j,i \\ i = 1, 2, \dots, n_l; \quad j = 1, 2, \dots, n_t \end{cases}$$

In quadrant 3, there are  $N_3 = (n_l + 1)n_b$  raw nodes to be determined. The node number of the raw node in  $j$ th row and  $i$ th column from the center is noted as  $k3ji$  and its coordinate is noted as  $(X_{k3ji}, Y_{k3ji})$ , which are determined as follows:

$$\begin{cases} k3ji = N_1 + N_2 + i + 1 + (j - 1) * (n_l + 1) \\ X_{k3ji} = x_0 - i\Delta_x \\ Y_{k3ji} = y_0 - j\Delta_y \\ i = 0, 1, \dots, n_l \\ j = 1, 2, \dots, n_b \end{cases}$$

Since the raw nodes in the boundary between quadrant 2 and 3 have already been determined in quadrant 2, they are just copied to quadrant 3 as follows:

$$k30i = k20i \quad \text{for } i = 0, 1, 2, \dots, n_l.$$

The three raw node numbers of the lower raw element of a grid in quadrant 3 are

$$\begin{cases} k3_{j-1,i} \\ k3_{j,i} \\ k3_{j,i-1} \\ i = 1, 2, \dots, n_l; \quad j = 1, 2, \dots, n_b \end{cases}$$

while those of the upper raw element of a grid are

$$\begin{cases} k3_{j-1,i-1} \\ k3_{j-1,i} \\ k3_{j,i-1} \\ i = 1, 2, \dots, n_l; \quad j = 1, 2, \dots, n_b . \end{cases}$$

In quadrant 4, there are  $N_4 = n_r n_b$  raw nodes to be determined. The node number of the raw node in  $j$ th row and  $i$ th column from the center is noted as  $k4_{ji}$  and its coordinate is noted as  $(X_{k4_{ji}}, Y_{k4_{ji}})$ , which are determined as follows:

$$\begin{cases} k4_{ji} = N_1 + N_2 + N_3 + i + (j-1)n_r \\ X_{k4_{ji}} = x_0 + i\Delta_x \\ Y_{k4_{ji}} = y_0 - j\Delta_y \\ i = 1, 2, \dots, n_r \\ j = 1, 2, \dots, n_b . \end{cases}$$

Since the raw nodes in the boundaries between quadrants 4 and 1 as well as 4 and 3 have already been determined in quadrant 1 and 3 respectively, they are just copied to quadrant 4 as follows:

$$k4_{0i} = k1_{0i} \quad \text{for } i = 0, 1, 2, \dots, n_r$$

$$k4_{j0} = k3_{j0} \quad \text{for } j = 0, 1, 2, \dots, n_b .$$

The three raw node numbers of the lower raw element of a grid in quadrant 4 are

$$\begin{cases} k4_{j-1,i} \\ k4_{j,i-1} \\ k4_{j,i} \\ i = 1, 2, \dots, n_r; \quad j = 1, 2, \dots, n_b \end{cases}$$

while those of the upper raw element of a grid are

$$\begin{cases} k4_{j-1,i} \\ k4_{j-1,i-1} \\ k4_{j,i-1} \\ i = 1, 2, \dots, n_r; \quad j = 1, 2, \dots, n_b . \end{cases}$$

Fig.4(b) shows an example of the created cover, in which the numbers of grids are

$$n_t = n_b = n_r = n_l = 2 .$$

There are 32 raw elements denoted by the larger bold numbers and 25 raw nodes denoted by the smaller numbers in the example.

## 4 Creation of the Elements of MM

All the elements of MM are derived from raw elements based on the block system. An element will be produced if there is a common area between a raw element and a block. Therefore, we need to check, one by one, every raw element with every block to find out all the common areas.

### 4.1 Common Areas

How to detect all the common areas efficiently and correctly is the crucial point of this new method, which is explained in detail as follows.

Suppose that a block is represented by the ordered vertices which is numbered counterclockwise (Fig.5(a)), a raw element is represented by the three raw nodes with numbers  $i$ ,  $j$  and  $k$  also counterclockwise, and the edges are also labelled as shown in Fig.5(b).

In general, the following types of common areas are possible:

1. When a raw element is inside a block completely (Fig.6(a)), the common area is the whole raw element, and the vertices of the common area are the three raw nodes.
2. When a block is inside a raw element completely (Fig.6(b)), the common area is the whole block, and the vertices of the common area are those of the block.
3. When a raw element is partially overlapped on a block (Fig.6(c)), the common area is enclosed by both the block boundaries and the edges of the raw element.
4. When a raw element is divided into several parts by the boundaries of a block or joints within a block, multiple common areas are possible (Fig.6(d)), The common areas are enclosed by both the block boundaries and the edges of the raw element.

Type 1 and type 2 are easily detected. However, types 3 and 4 are a little difficult to be detected. For this reason, we mainly introduce how to detect the common areas like types 3 and 4 as follows.

We link the consecutive boundaries inside the raw element to obtain an oriented line called *crossed line* here. In general, a crossed line consists of an entering point, an exiting point and,

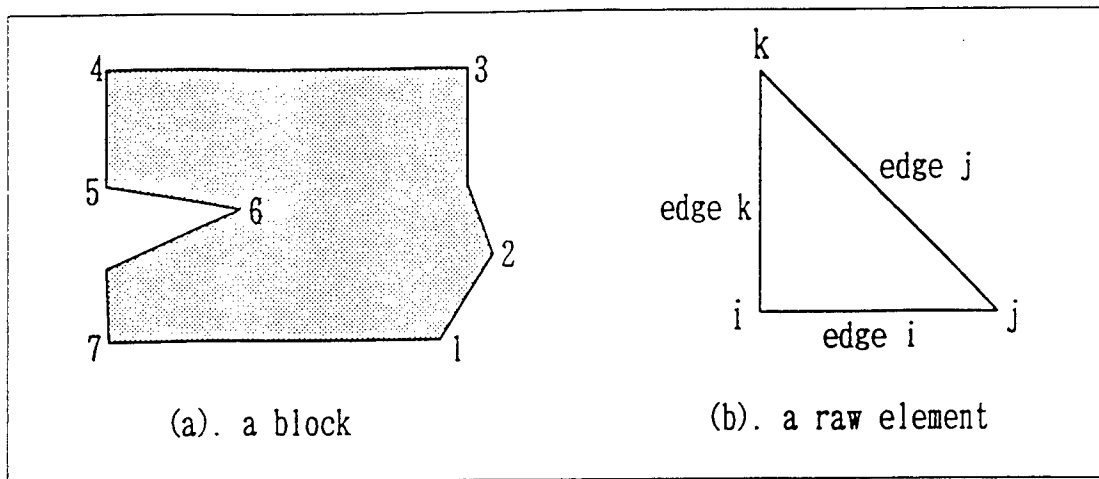


Fig.5. A block with ordered vertices and a raw element with three raw nodes and edges

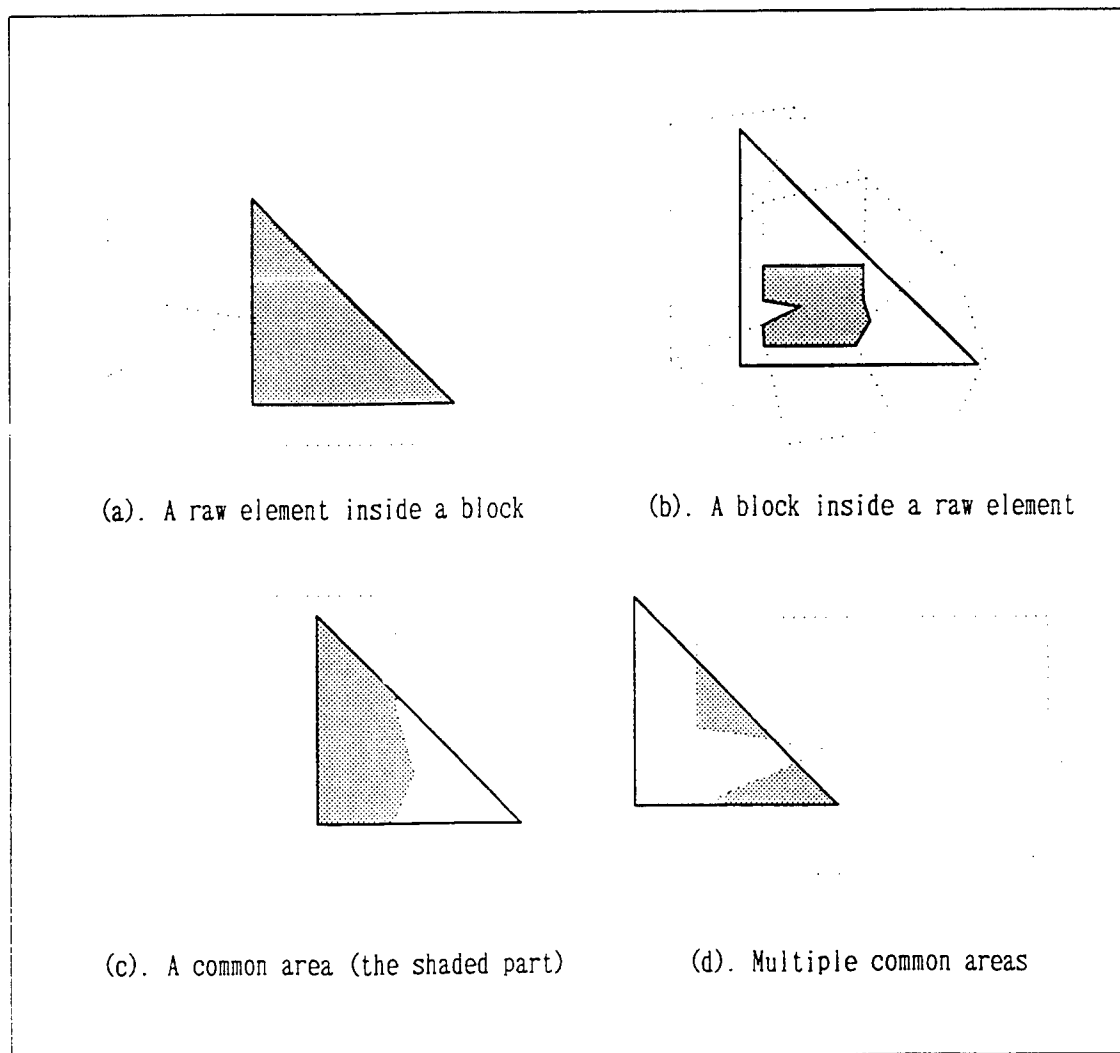


Fig.6. Various types of common areas between a raw element and a block

if any, inside points (the arrowed line in Fig.7(a)). We also define a special crossed line for a raw node inside the block as shown in Fig.7(b), where the arrowed line is the special crossed line defined for the raw node  $j$ , and it enters into the raw element from the edge  $i$ , exits from the edge  $j$ . The entering point and exiting point are the same for a special crossed line, i.e. the raw node itself.

The crossed lines for various types of common areas are shown in Fig.8. It can be found from the figure that all the common areas can be obtained if the crossed lines are connected in such a way that the exiting point of a crossed line is connected with the entering point of the other crossed line which is the nearest to it and lies in its left side. The vertices of the common area are the points in the connected crossed lines.

To specify a crossed line, we need to determine the entering point, the exiting point and, if any, inside points.

Inside points are those vertices of the block inside the raw element, which are easily detected.

Both entering and exiting points are the intersection points between a boundary line segment and an edge of the raw element. Whether an intersection point is an entering point or an exiting point can be judged as follows:

1. If a boundary line segment  $\overline{i, i+1}$  has only one intersection point with the three edges of the raw element, one of end points,  $i$  or  $i+1$ , should be inside the raw element. If the end point  $i+1$  is inside the raw element, the intersection point should be an entering point, otherwise, an exiting point.
2. If a boundary line segment  $\overline{i, i+1}$  has two intersection points with the three edges of the raw element, the one that is near in distance from the end point  $i$  is an entering point, and the other is an exiting point.

## 4.2 Mathematical Elements

An element is to be produced when a common area is found out. Producing an element means to determine the three element nodes for the mathematical element and to obtain the element vertices for the physical element.

The element vertices can be directly taken from the vertices of the common area. However, it is uncertain if an element node is directly taken from the corresponding raw node or from its copy. The copy of a raw node can be considered a new raw node which has the same coordinate as the original but a new node number next to the last raw node number.

Since a raw element may have common areas with more than one blocks, a raw node may

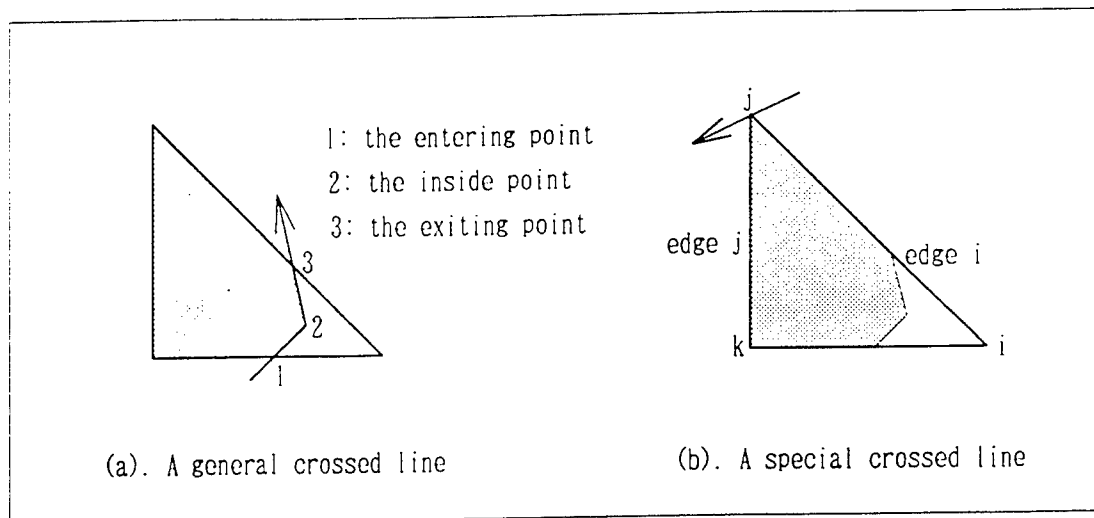


Fig.7. A general crossed line and a special crossed line

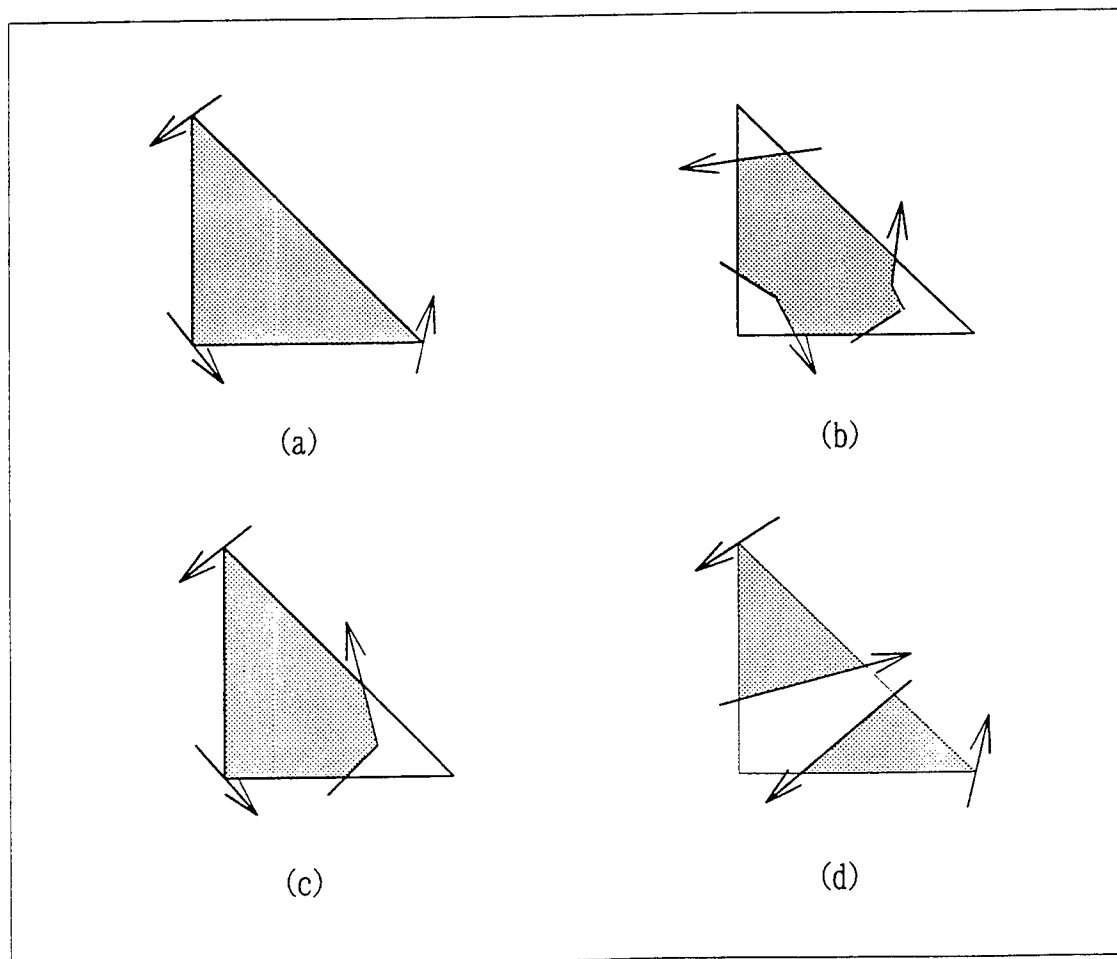


Fig.8. The crossed lines for various types of common areas

be related to several blocks. As we know, the element nodes for a physical block should totally be different from those for the other block. Therefore, if a raw node has already been used by a block, the other blocks can only use its copy. The copy for a block should be unique, but the copies for different blocks should be different.

In general, the element node derived from a raw node should be unique for all the elements related to the same block, that is, there is only one element node at a raw node point for a block, and it is shared by all the elements in that block.

However, there exists the special case when two adjacent elements in the same block are separated by fractures or boundaries. In this case, there may be two element nodes overlapped at a raw node point for two elements in the same block, that is, the copy of an element node should be used for one of the two elements. Which one should use the copy depends on the surrounding elements. First of all, we determine some element nodes based on the un-separated adjacent elements according to the rule that the element nodes should be the same along the common edge if there is no discontinuity between the two adjacent elements. Then, if some other element nodes still remained undetermined, they should be replaced by their copies.

### 4.3 An Example

Here we take the example shown in Fig.9 to explain the method more clearly.

The block system in the example consists of two physical blocks (Fig.9(a)), and block 2 contains a fracture.

The created cover is shown in Fig.9(b). The larger bold numbers denote raw elements and the smaller numbers denote raw nodes. For example, raw element 1 is represented by the three raw nodes 1, 2 and 4. There are 32 raw elements and 25 raw nodes in this example.

35 common areas are detected between 32 raw elements and 2 blocks. Therefore, 35 elements are produced in this example (Fig.9(c)), and the numbers in the figure denote the physical elements. Since some mathematical elements are overlapped each other, they are separately shown in Fig.9 (d), (e) and (f). In these figures, each triangle with thin lines represents a mathematical element, and the shaded part of a mathematical element is its corresponding physical element. The numbers in the figures denote the element node numbers.

Fig.9 (d) shows the mathematical elements related to block 1. For example, the element 26 has the element nodes 10, 16 and 26.

Fig.9 (e) shows the mathematical elements related to the right part and the part below the fracture of block 2. For example, the element 5 has the element nodes 7, 1 and 4.

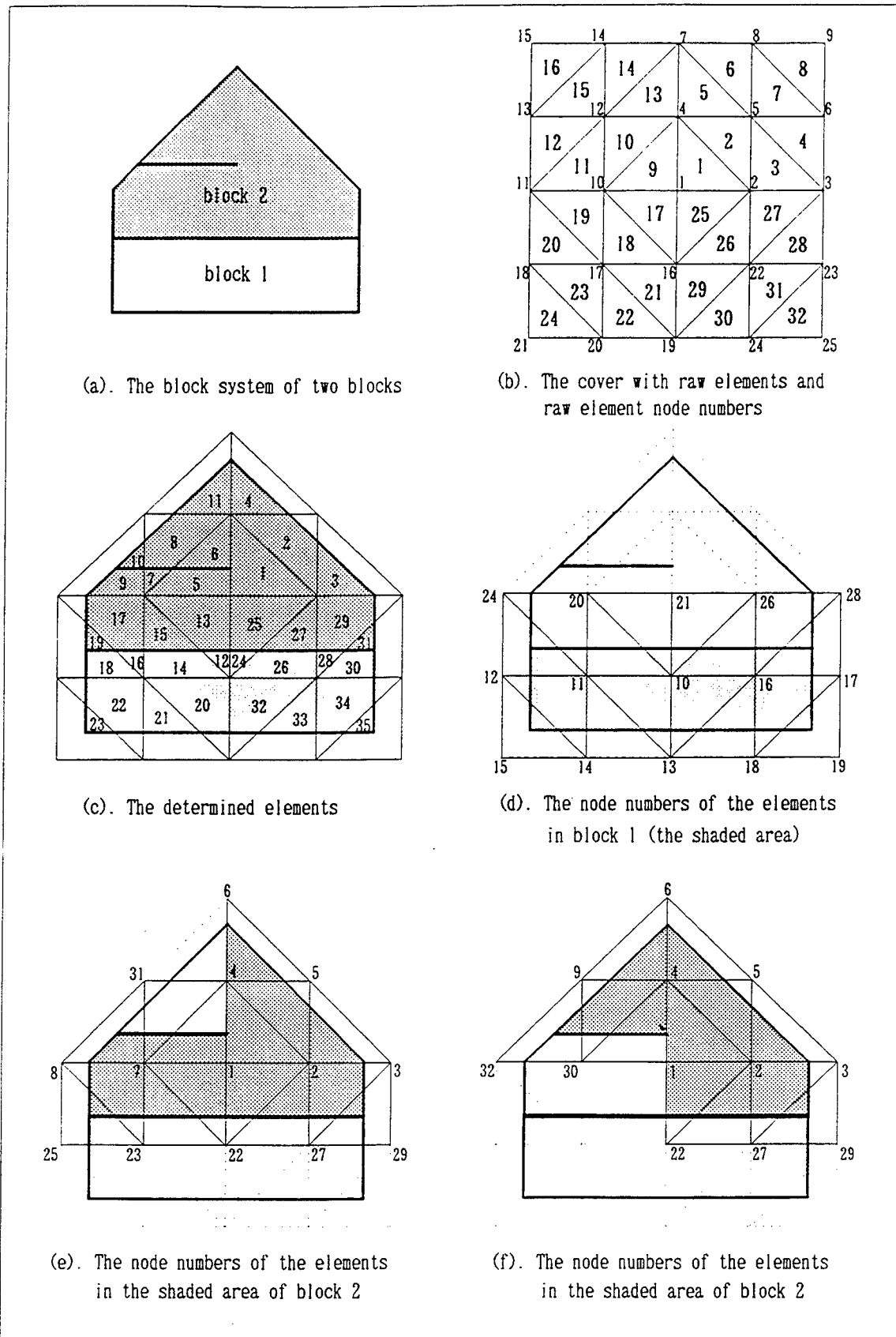


Fig.9. An example for making elements of MM by use of the method



Fig.9 (f) shows the mathematical elements related to the right part and the part above the fracture of block 2. For example, the element 6 has the element nodes 30, 1 and 4.

The following things should be emphasized in this example:

1. Element nodes are compressed

Since raw elements 8 and 16 are outside the block system completely, raw nodes 6, 8 and 9, as well as raw nodes 13, 14 and 15 are not used by any elements. As a result, element node numbers 6, 8, 9, 13, 14 and 15 should not be used by any elements because element nodes are derived from raw nodes. Obviously, unused element nodes should be deleted. That is why we need to compress the element nodes after all the elements are produced. By compressing, element nodes 7, 10, 11, 12 become 6, 7, 8, 9, and the element node numbers larger than 15 become smaller by 6. For example, element nodes 16, 22 and 32 of element 26 become 10, 16 and 26 by compressing. The element node numbers shown in Fig.9(d), (e) and (f) are the compressed numbers

2. Multiple elements may be derived from a raw element

For example, elements 26 and 27 are derived from raw element 26, elements 5 and 6 are derived from raw element 9.

3. Multiple element nodes may overlap at a raw node point

For example, there are 3 element nodes at raw node 10: element node 7 of element 7, element node 30 of element 8 and element node 20 of element 12.

4. The element nodes of the elements in block 1 are totally different from those in block 2

Comparing Fig.9(d) with Fig.9(e) and (f), it can be seen that the element nodes denoted in Fig.9(d) are totally different from those in Fig.9(e) and (f). Although both elements 26 and 27 are derived from the same raw element 26, the three element nodes 10, 16 and 26 of element 26 in block 1 are totally different from the three element nodes 22, 27 and 2 of the element 27 in block 2.

Here, we take element 26 as an example to explain how to determine the element nodes.

- (a) Since raw node 16 has been used as the element node of element 24 in the same block, it should also be used as the element node of element 26;
- (b) Since raw node 22 is not used by any element at that time, it can directly be used as the element node of element 26;
- (c) Since raw node 2 has already been used as the element node of elements 1, 2, 3 and 25 in block 2, the different block, the copy of raw node 2, which is numbered 32,

should be used as the element node of element 26.

(d) As a result, element 26 has three element nodes 16, 22 and 32, which become 10, 16 and 26 after compressing.

5. There is at least one different element node between the two elements divided by the fracture although they are in the same block and produced from the same raw element.

The number of different element nodes between this kind of two elements depends on the surrounding elements. For example, there is only one different element node between the elements 5 and 6 while there are two different element nodes between the elements 7 and 8, and three between the elements 9 and 10.

In the following, we take elements 5 and 6 as examples to see how to determine the element nodes when discontinuity is involved between two adjacent elements.

Because of the fracture in block 2, raw element 9 has 2 common areas with block 2. Therefore, elements 5 and 6 are produced from these two common areas. They are adjacent to element 1.

Since there is no any discontinuity from both elements to the element 1, the element nodes 1 and 4 along the common edge can be determined as those for the elements 5 and 6.

Since there is no any discontinuity between the elements 5 and 13, the element node 7 (which was numbered 10 before compressing) can be determined as the remained node of element 5. However, element node 7 can not be used as the remained node of element 6 since there is a discontinuity between element 6 and element 13. As a result, the copy of the element node 7, which has a new number 30 (which was numbered 36 before compressing), is used for the remained node of element 6.

## 5 About the Program

The program for the new method has been developed. It is coded with C language, X-Window and XView libraries on SUN WorkStation.

Fig.10 shows the menu panel and the working windows of the program. All the operations are nothing but pushing menu buttons or filling numbers in tables. The images of the input data are shown in the window immediately. Therefore, it is very easy to make a MM model by using the program.

The major procedures of making a MM model are as follows:

1. Input the physical block system.

The corresponding DDA model data, which is supposed to have already been made by

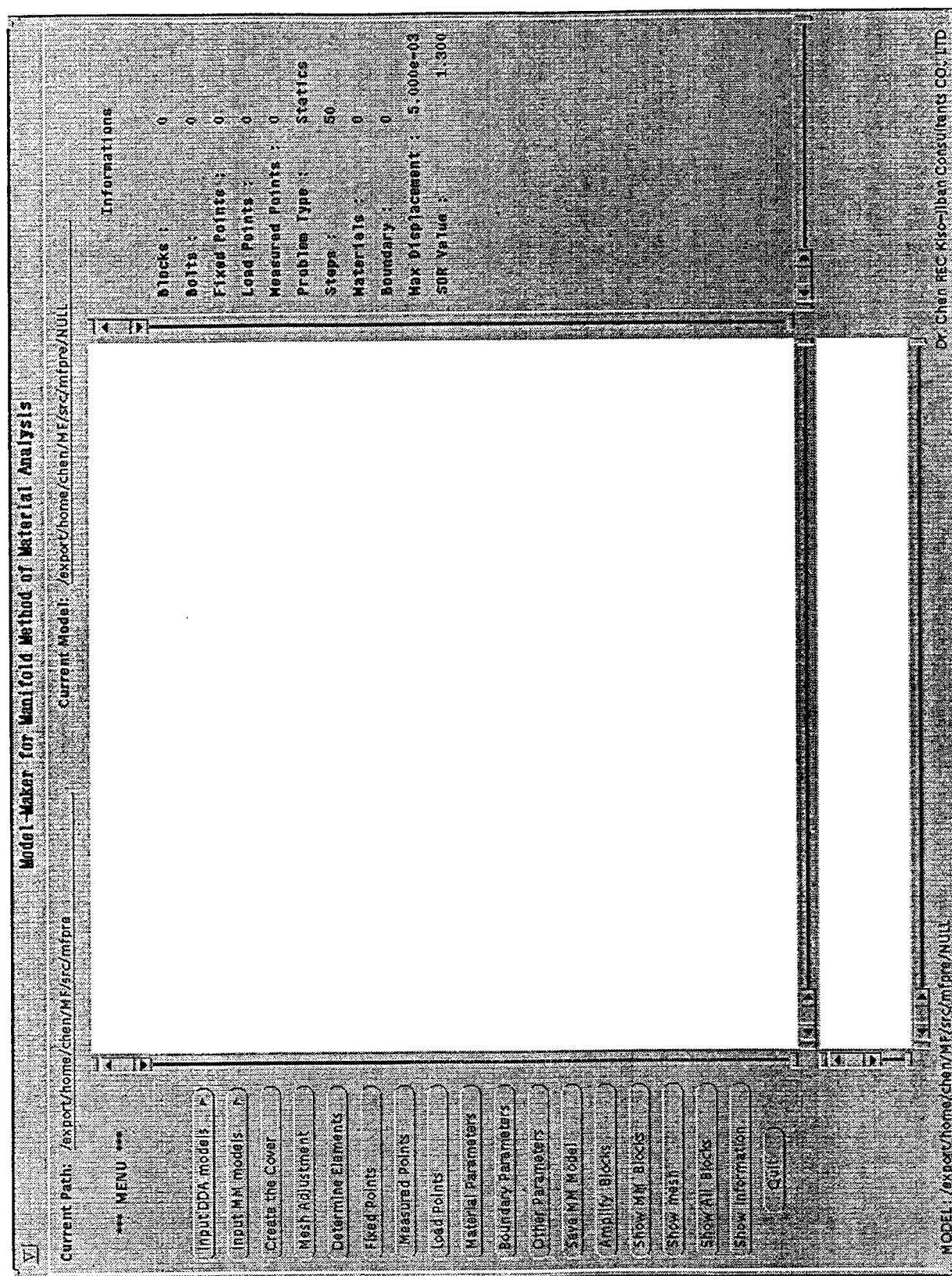


Fig. 10. The menu panel and work windows of Model—Maker for Manifold Method

DDAWorkTool, can be easily inputted from data files just by selecting the model name from the menu button [Input DDA models], which is a pull down menu and contains the names of all the DDA models in the *current directory*.

2. Create a cover over the block system.

After the block system is shown in the window, push the menu button [Create the Cover], and then, a table for inputting the parameters of the cover appears (Fig.11). Assigning the proper number to each item in the table and pushing the button [Create], the cover will be created automatically.

In the panel table shown in Fig.11, the items *Grids for Half Width* and *Grids for Half Height* refer to the numbers of half grids to be produced in horizontal and vertical directions respectively; the item *Over Cover* refers to the excess of the cover over the entire block system; the items *Center Shift for X* and *Center Shift for Y* refer to the excentricity of the axis center from the center of the block system.

3. Make all the elements and determine the boundary points of each block just by pushing the menu button [Determine Elements] (Fig.12).

## 6 Conclusions

The method for making MM models have been presented in this paper. It can create mathematical meshes automatically for any shape of physical meshes. We also propose to make physical meshes in the same way as making block systems by using DDAWorkTool, a powerful software developed for DDA method.

The concepts such as *Raw Element*, *Element*, *Mathematical Element* and *Physical Element* have been defined and used to describe a MM model with the help of the terms such as *Raw Node*, *Element Node*, *Element Vertex* and *boundary point*. Therefore, it becomes very clear what kind of data are needed in a MM model.

The program for the method has been developed and it has been shown to be very efficient by transferring a lot of DDA models into MM models. It will be put into practical use soon. We expect that the powerful MM method will get more and more widely practical applications by using the new program.

## References

Shi G. (1994): Manifold Method of Material Analysis, The Ninth Work Forum for the

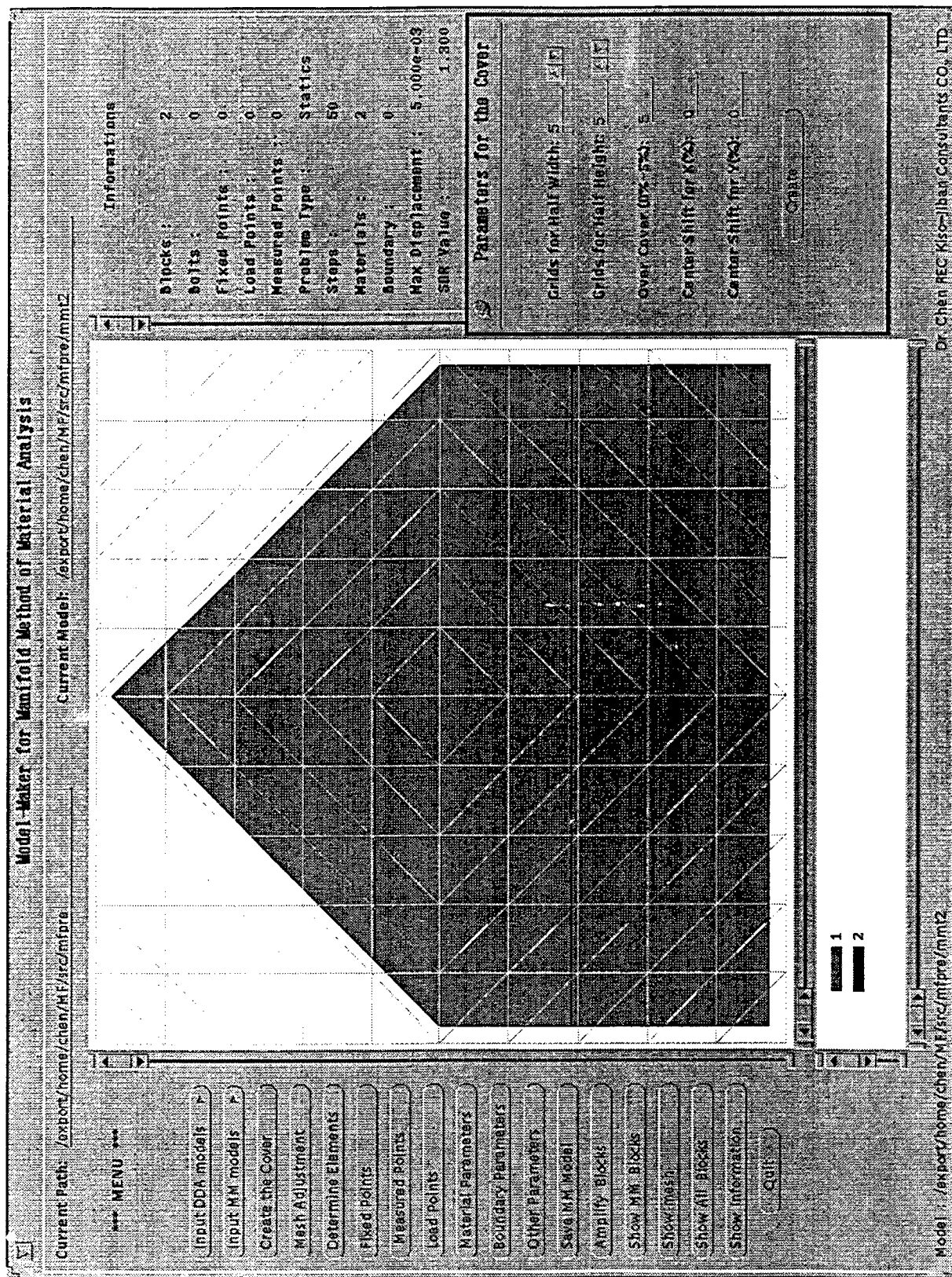


Fig. 11. The panel table for assigning the parameters of the cover to be created



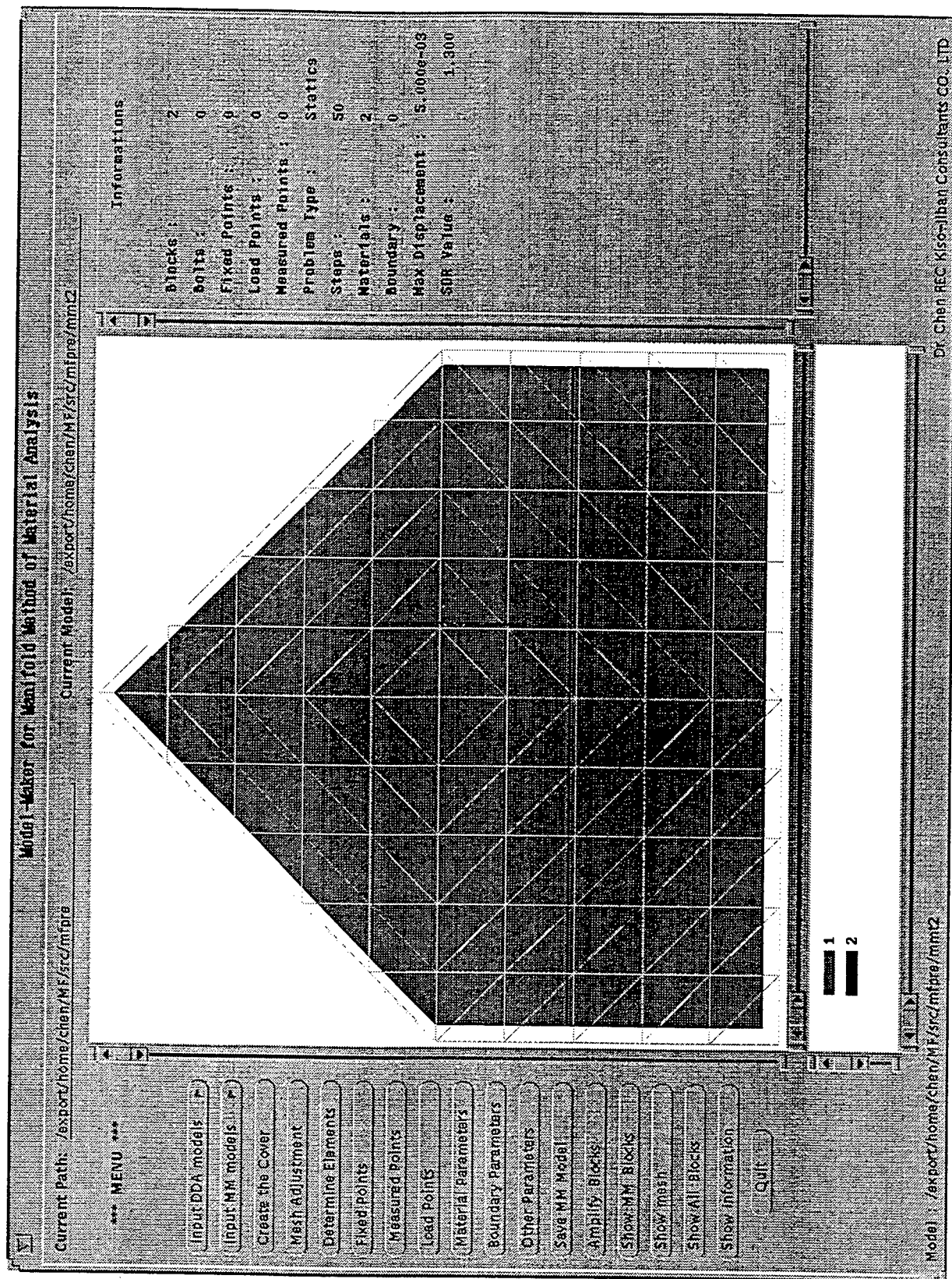


Fig. 12. All the elements are produced by pushing the button [Determine Elements]

Practical Application of DDA, Tokyo, Japan.

**Chen G.** , S. Miki and Y. Ohnishi (1995): A Comprehensive System Software for DDA (DDAWorkTool), The Fifth Work Forum for the Practical Application of Manifold Method, Tokyo, Japan. (In Japanese)

# Nonlinear Entrance Level Manifold Method

Chiao-Tung Chang and Paulo J. M. Monteiro

Department of Civil Engineering  
University of California at Berkeley  
Berkeley, CA 94720, U.S.A.

## Abstract

This paper presents a numerical model transitional from the Discontinuous Deformation Analysis (DDA) to the Manifold Method. The Manifold Method has two independent meshes: a mathematical and a physical mesh. In DDA which is a special case of the Manifold Method for a discontinuous block system, the physical and mathematical meshes are the same. The model presented here uses a finite element mesh for the mathematical covers in each DDA block and incorporates nonlinear material behavior. This formulation improves the physical mesh's deformation ability by placing a mathematical mesh of triangular elements in each individual material body. The nonlinear constitutive behavior of materials is incorporated in the formulation by using piecewise linear approximation similar to the DDA's step-by-step linear kinematics approach which has been successfully used in solving geometric nonlinearity problems. Therefore, continuous and discontinuous analyses can be performed to study the detailed mechanical response, the global stability and the failure modes of the finite element meshed multi-body system under static and dynamic loads.

## Introduction

The analysis of structural and material behavior varies with different mathematical tools. With the advent of digital computers, the analytical solutions obtained from simplified models no longer satisfied the engineer once computers allowed the conversion of a complex continuous problem to a discrete one. Finite Element Method (FEM) led to a revolution in mathematics, and made an important contribution in numerical analysis solving scientific and engineering problems in the early 1960s. Thus, leading computational mechanics into a new age. It is now a well developed and powerful



method for solving continuous deformation problems. For total discontinuous displacement, Shi derived the first entrance theory of block kinematics to regulate the movements of all the blocks and to find the locations of all contacts among the blocks. Using the minimization of total potential energy to reach equilibrium and adopting the implicit algorithm of FEM, Shi (1988) developed Discontinuous Deformation Analysis (DDA) to analyze the stability and stress distribution of a system of blocks containing pre-existing cracks or joints.

Since FEM and DDA adopt the same algorithm and energy theorem, Shi (1991) proposed the Manifold Method to bridge the gap between continuity and discontinuity. In this method the local functions defined on each cover are independent, and the global function of the manifold takes a percentage weight from the local functions on the overlapped regions of each cover. Thus, both the mathematical mesh and the physical mesh are independent. The mathematical mesh, chosen by the user, consists of overlapping finite covers which defines the displacement functions and derives the numerical interpolation from finite difference grids, finite element meshes, or series with convergence regions. The physical mesh, representing the material conditions, delimits the integration zone and includes the boundary of the material volume, joints, blocks and the dividing lines of different zones. Furthermore, Shi (1994) derived analytical solutions of simplex integration of n-dimensional general shaped domains, and was able to obtain integration of complex material domains from simple functions. Therefore, the global displacement functions of the manifold are able to represent large displacement and deformation of the material volume starting from fully continuous state, and allows the development of micro-crack zones which propagates into macrocracks, until the damage stage.

The displacement functions of DDA and the triangular element of FEM are complete first order polynomials. From the Manifold Method's point of view, the triangular element is composed of three constant covers. These three covers can be seen as three "nodes" of the element. Viewing from the displacement function of a triangular element, DDA's physical mesh of a block system overlays within the boundary of a big triangular element, common area of three mathematical covers. Shi transformed these nodal variables into six essential variables such as rigid body motion, axial and shear deformations, then placed them at each block's center of gravity to depict its trace of motion. After the transformation of variables, the multi-body system of the physical mesh is simply a system of blocks. Each block is a domain, and each domain is a cover. Blocks are in contact along their boundaries that are not overlapped with each other. Since the

mathematical mesh and the physical mesh are the same, in total discontinuity DDA is a special case of the Manifold Method.

Since a constant stress/strain field in each block is not a realistic assumption for a large block, one should select a mathematical mesh to improve the physical mesh or the block's deformation ability in order to enhance the precision of stress/strain distribution field. The model presented here used the triangular element of finite element mesh as its mathematical mesh. The roughness or refinement of the triangular element mesh in individual material body depends on the requirement of engineering accuracy. The more triangular elements are placed in each physical body, the more mathematical covers are overlapped together. The mathematical mesh region coincides with each physical body. Besides, the addition of nonlinear material behavior in each element using step-by-step linear approximation enables the proposed model to solve more realistic engineering problem.

The original Manifold Method computer program developed by Shi used arbitrary scaled equilateral triangular element mesh as its mathematical mesh. When two layers of mathematical and physical mesh merge together, more nodes or covers are generated along the boundaries of the physical mesh. The elements inside each physical body can have irregular forms that is more flexible than those in the proposed model.

## **Overlaying of Physical Mesh with Finite Element Mesh**

The main purpose of placing the mathematical covers of a finite element mesh in each material body is to improve its deformation ability. Not only the movements of the multi-body system will be depicted by DDA's block kinematics, but also the stress distributions within the material volume can be obtained. Once the finite element mesh of triangular elements is chosen, the complete first order polynomial displacement function are used to describe the element's behavior.

The geometry function of the material bodies is used as the contact boundaries, thus, so the shape of the physical body does not need to be triangular. By adding a finite element mesh as the mathematical mesh in individual body, more nodes are distributed along the contact boundaries of the block, and the contact detection from block system kinematics become more complicated in the discontinuous system. Consider a three-node element where the boundaries are drawn along the nodes in certain directions, forming a three-edge block with the same size as the element. This configuration is called a three-node "element block"—a block with nodal displacements as unknowns. If a three-node

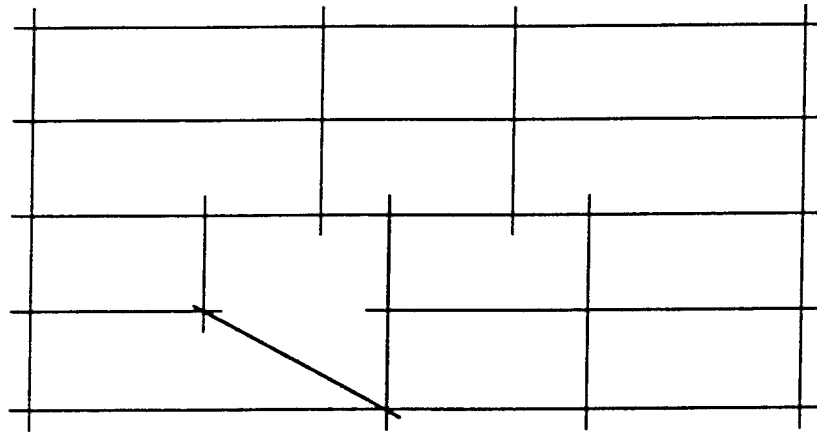


Figure 1.a. Input lines for mathematical mesh

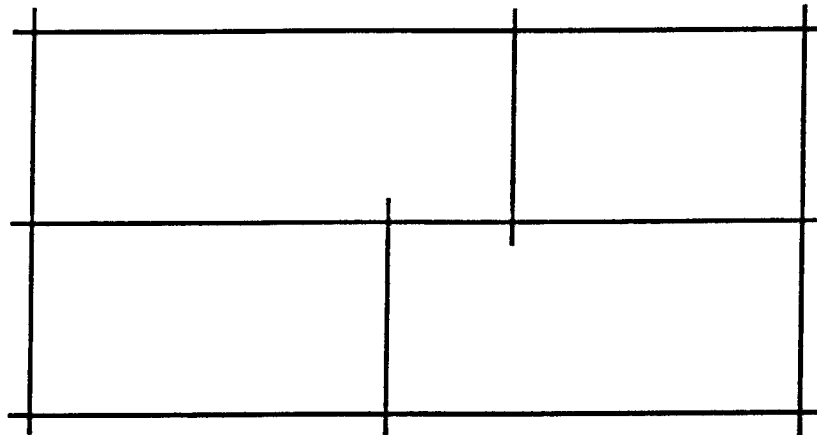


Figure 1.b. Input lines for physical mesh

18		19	19	20	31		21
14		15	15	16	30		17
14		15	15	16	30		17
26		25	25	28	29		27
9	10	10	11	24	12	12	13
5	6	6		23	7	7	8
5	6			23	7	7	8
1			2	22	3	3	4

Figure 1.c. Mesh of elements and blocks  
(same nodal numbers are shared between the elements, but different nodal numbers are used along the block boundaries)

element is extended to a n-node element mesh, an element-mesh block with n nodes is obtained. In general, a block can be as small as an element or as large as an element mesh. Different meshes can also be put into different blocks if conditions permit.

In the computer program, the mathematical meshes and the boundaries of the material bodies need to be input separately with line segments containing the coordinates of two end points (Figure 1.a, 1.b). Then, after the process of tree cutting and forming of the mathematical and physical meshes, both are merged with the same nodal numbers between the elements, but with different nodal numbers between the boundaries of the blocks (Figure 1.c). The basic element in this numerical model is triangular. For the convenience of putting the mesh in each block, four-node element meshes are generated first in the mesh program. Next, a condense five-node element—a quadrilateral element with four nodes on its vertices and one additional node inside it that forms four triangular elements—is used for the forward model computations.

Based on the idea of element-mesh blocks, the boundary of the mesh in standard FEM is just one block in DDA. Thus, FEM only has a mathematical mesh that is a special case in the Manifold Method for continuous problems. By choosing mathematical covers of the finite element mesh overlaid with physical mesh of the block system, it is possible to take advantage of the continuous properties in FEM and discontinuous characteristics of DDA, thereby simulating engineering problems more accurately.

### Simultaneous equilibrium equations

The simultaneous equilibrium equations derived by minimizing the total potential energy,  $\Pi$ , have the following form:

$$\begin{pmatrix} [K_{11}] & [K_{12}] & [K_{13}] & \cdots & [K_{1n}] \\ [K_{21}] & [K_{22}] & [K_{23}] & \cdots & [K_{2n}] \\ [K_{31}] & [K_{32}] & [K_{33}] & \cdots & [K_{3n}] \\ \vdots & \vdots & \vdots & \ddots & \vdots \\ [K_{n1}] & [K_{n2}] & [K_{n3}] & \cdots & [K_{nn}] \end{pmatrix} \begin{pmatrix} \{D_1\} \\ \{D_2\} \\ \{D_3\} \\ \vdots \\ \{D_n\} \end{pmatrix} = \begin{pmatrix} \{F_1\} \\ \{F_2\} \\ \{F_3\} \\ \vdots \\ \{F_n\} \end{pmatrix} \quad (1)$$

The nodal displacements are chosen as the unknown variables and each has two degree-of-freedom for the two-dimensional case. For the given i-th node,  $[K_{ij}]$  is  $2 \times 2$  submatrix representing the stiffness of displacement at the i-th node with respect to the load acting on the j-th node.  $\{D_i\}$  and  $\{F_i\}$  are  $2 \times 1$  submatrices for the corresponding unknown nodal displacement and nodal loading matrices.

## Displacement functions

For a triangular element, the displacement functions can be described by a complete first order polynomial

$$u = a_1 + b_1x + c_1y$$

$$v = a_2 + b_2x + c_2y$$

With  $(x_i, y_i)$  and  $(u_i, v_i)$  being the coordinates of nodes and related nodal displacements of the triangular element where  $i = 1, 2, 3$ ,

$$\begin{pmatrix} a_1 \\ b_1 \\ c_1 \end{pmatrix} = \begin{pmatrix} 1 & x_1 & y_1 \\ 1 & x_2 & y_2 \\ 1 & x_3 & y_3 \end{pmatrix}^{-1} \begin{pmatrix} u_1 \\ u_2 \\ u_3 \end{pmatrix}, \quad \begin{pmatrix} a_2 \\ b_2 \\ c_2 \end{pmatrix} = \begin{pmatrix} 1 & x_1 & y_1 \\ 1 & x_2 & y_2 \\ 1 & x_3 & y_3 \end{pmatrix}^{-1} \begin{pmatrix} v_1 \\ v_2 \\ v_3 \end{pmatrix}.$$

Set

$$\begin{pmatrix} f_{11} & f_{12} & f_{13} \\ f_{21} & f_{22} & f_{23} \\ f_{31} & f_{32} & f_{33} \end{pmatrix} = \begin{pmatrix} 1 & x_1 & y_1 \\ 1 & x_2 & y_2 \\ 1 & x_3 & y_3 \end{pmatrix}^{-1}, \quad (f_1 \ f_2 \ f_3) = (1 \ x \ y) \begin{pmatrix} f_{11} & f_{12} & f_{13} \\ f_{21} & f_{22} & f_{23} \\ f_{31} & f_{32} & f_{33} \end{pmatrix},$$

then

$$\begin{pmatrix} u \\ v \end{pmatrix} = \begin{pmatrix} f_1 & 0 & f_2 & 0 & f_3 & 0 \\ 0 & f_1 & 0 & f_2 & 0 & f_3 \end{pmatrix} \begin{pmatrix} u_1 \\ v_1 \\ u_2 \\ v_2 \\ u_3 \\ v_3 \end{pmatrix} = [\mathbf{T}]\{\mathbf{d}\}, \quad (2)$$

$$[\mathbf{T}] = (\mathbf{T}_1 \ \mathbf{T}_2 \ \mathbf{T}_3); \quad \{\mathbf{d}\} = \begin{pmatrix} \mathbf{d}_1 \\ \mathbf{d}_2 \\ \mathbf{d}_3 \end{pmatrix},$$

$$[\mathbf{T}_i] = \begin{pmatrix} f_i & 0 \\ 0 & f_i \end{pmatrix}; \quad \{\mathbf{d}_i\} = \begin{pmatrix} u_i \\ v_i \end{pmatrix}, \quad i = 1, 2, 3.$$

$[\mathbf{T}_i]$  and  $\{\mathbf{d}_i\}$  are the matrices of shape function and displacement variables per node.

### Inertia matrix

Because the inertia force plays a key role in rigid body motion, it is crucial to include it in dealing with the motions of a discontinuous multi-body system. Assuming the acceleration in each time step is constant, the  $2 \times 2$  nodal stiffness matrices and  $2 \times 1$  force matrices of element  $i$  can be described as

$$[\mathbf{K}_{i(r)i(s)}] = \frac{2M}{\Delta^2} \left[ \iint_A [\mathbf{T}_{i(r)}]^T [\mathbf{T}_{i(s)}] dx dy \right] \quad r, s = 1, 2, 3 \quad (3)$$

$$[\mathbf{F}_{i(r)}] = \frac{2M}{\Delta} \left[ \iint_A [\mathbf{T}_{i(r)}]^T [\mathbf{T}_{i(s)}] dx dy \right] \{V_{i(s)}(0)\} \quad \begin{cases} r = 1, 2, 3 \\ s = \text{tensor sum} \end{cases} \quad (4)$$

where

$$\{V_{i(s)}(0)\} = \frac{\partial}{\partial t} \begin{pmatrix} u_{i(s)}(0) \\ v_{i(s)}(0) \end{pmatrix}.$$

$M$  is the mass per unit area, and  $\Delta$  is time interval of current time step. The analytical solutions of the above integration that ensures the convergence of "open-close" iterations can be obtained (Chang 1994).

### Normal contact matrix

When two bodies are detected to be in contact, the requirement of no penetration must be satisfied according to DDA's block kinematics. The contact problem reduces to the relationship of angle-to-edge (point-to-line) case. When interpenetration pushes the point through the reference line, the distance between them should be zero after the installation of spring with stiffness  $p$  at the contact position. The nodal stiffness and force matrices of element  $i$  and  $j$  are described as

$$\begin{aligned} [\mathbf{K}_{i(r)i(s)}] &= p \{H_r\} \{H_s\}^T & r, s &= 1, 2, 3 \\ [\mathbf{K}_{i(r)j(s)}] &= p \{H_r\} \{G_s\}^T & r, s &= 1, 2, 3 \\ [\mathbf{K}_{j(r)i(s)}] &= p \{G_r\} \{H_s\}^T & r, s &= 1, 2, 3 \\ [\mathbf{K}_{j(r)j(s)}] &= p \{G_r\} \{G_s\}^T & r, s &= 1, 2, 3 \end{aligned} \quad (5)$$

$$\begin{aligned} \{F_{i(r)}\} &= -p \left( \frac{S_0}{L} \right) \{H_r\} & r &= 1, 2, 3 \\ \{F_{j(r)}\} &= -p \left( \frac{S_0}{L} \right) \{G_r\} & r &= 1, 2, 3 \end{aligned} \quad (6)$$

where

$$\text{for element } i \quad \begin{cases} i(1) = i_1 \\ i(2) = i_2 \\ i(3) = i_3 \end{cases} \quad \text{for element } j \quad \begin{cases} j(1) = j_1 \\ j(2) = j_2 \\ j(3) = j_3 \end{cases}$$

The detailed derivation of internal stress, external loading, displacement constraint, and contact matrices are described in Shyu (1993) and Chang (1994).

## Nonlinear Material Behavior

In structural mechanics, nonlinearity can be classified as material nonlinearity and geometric nonlinearity. Geometric nonlinearity is modeled in DDA using a discrete time system. The present work develops material nonlinearity formulation.

DDA uses a step-by-step linear approach. Each step starts with the deformed shape and positions from the previous step; the stresses from the previous step are considered as the initial stresses at the current step. After adopting the updated geometry, the contact positions, the velocities, and the stresses from the previous time step, the computation for the current step is independent from the data of the previous step. All the deformability constants, loading, initial stresses, and boundary conditions can be changed at the current step. Because the time interval of each time step is very small, the displacement, the deformations, and the changes of stresses are very small, so that the tangent modulus of the stress-strain relationship at the current step is very close to the secant modulus of the stress-strain curve. Thus, the arc-length method (Figure 2) can be used to calculate the piecewise linear modulus based on the updated values of stresses and strains for nonlinear constitutive behavior of materials.

The use of line segments to depict the nonlinear behavior of the material allows that the linear step-by-step approach can be employed in both material and geometric nonlinearity problems. It should be mentioned that solving nonlinear material problems using only one step may violate the infinitesimal displacement theory. When mathematical covers of finite element mesh and physical mesh of blocks are combined together to obtain the stress distributions, or to improve the deformation ability of the block, the use of piecewise linear stress-strain curve to solve material nonlinearity step by step allows the solutions of complex engineering problems.

The present work develops equations for nonlinear isotropic materials using principal strain as the criterion for the change of Young's modulus  $E$  and Poisson's ratio,  $\nu$ . The more line segments that are chosen to follow the stress-strain curve, the better

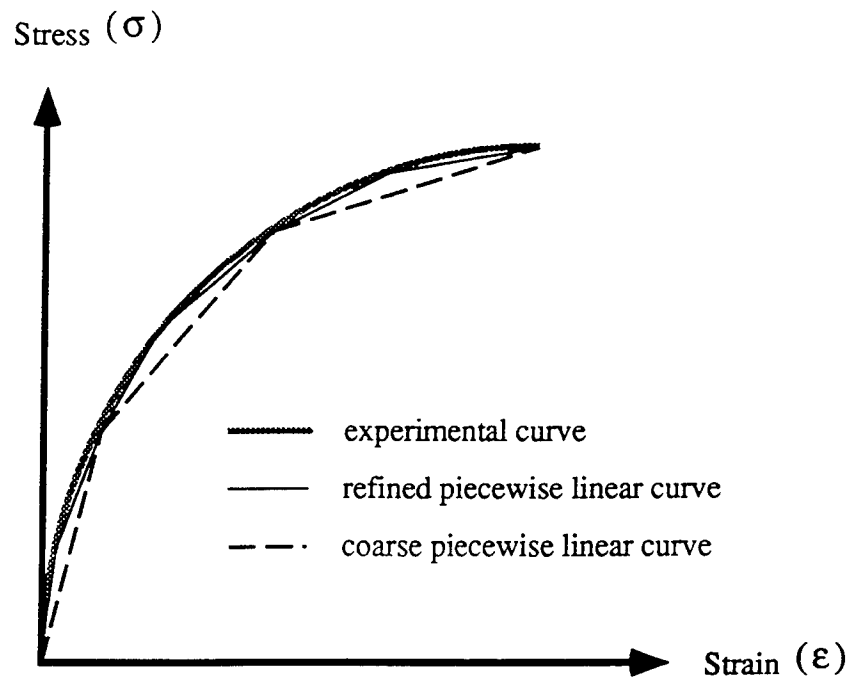


Figure 2. Arc-length method

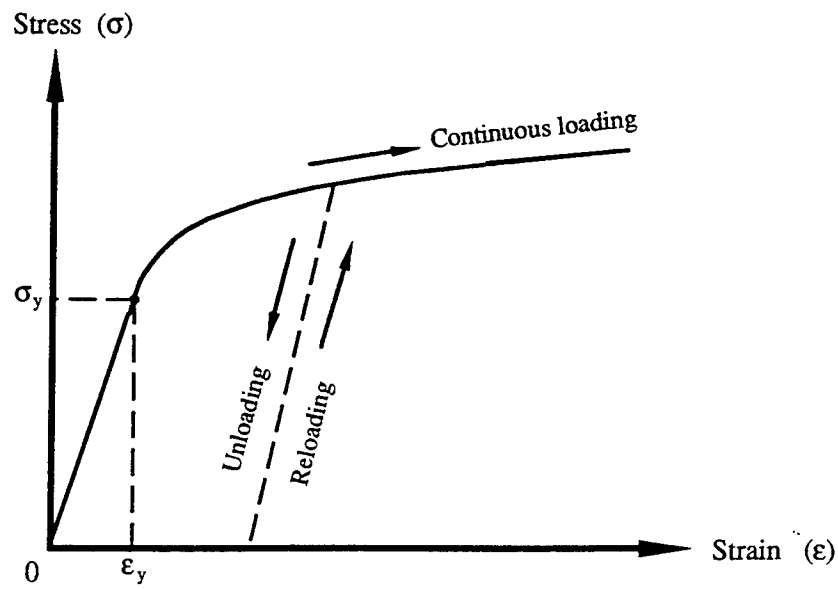


Figure 3. Nonlinear inelastic stress-strain modelling



approximation of nonlinear inelastic material behavior for each time step. Without the incorporation of a fracture criterion, the element meshed block of the system always remains as intact in the present model. The material is assumed to be strain hardening after yielding, because the strain-softening behavior observed in the experimental stress-strain curve reflects the global specimen instead of the individual blocks. The Bauschinger effect is considered in cyclic loading; the unloading and reloading paths after yielding are assumed to be the same in the stress-strain curve, as shown in Figure 3. The inclusion of nonlinear material behavior also provides another source of energy dissipation.

### Stiffness matrix

A linearly step-by-step approach to discretize the stress-strain curve can be used to simplify a material nonlinearity problem. For an isotropic inelastic material, the stress-strain relationship is assumed to be linear at each time step. After taking the derivatives of displacement variables from the elastic strain energy, three  $2 \times 2$  nodal stiffness of element  $i$  are formed.

$$[\mathbf{K}_{i(r)i(s)}] = [\mathbf{B}_{i(r)}]^T [\mathbf{E}_i] [\mathbf{B}_{i(s)}]; \quad r, s = 1, 2, 3$$

where

$$[\mathbf{E}_i] = \frac{E}{1-\nu^2} \begin{pmatrix} 1 & \nu & 0 \\ \nu & 1 & 0 \\ 0 & 0 & \frac{1-\nu}{2} \end{pmatrix}; \quad [\mathbf{B}_l] = \begin{pmatrix} f_{2l} & 0 \\ 0 & f_{3l} \\ f_{3l} & f_{2l} \end{pmatrix}, \quad l = 1, 2, 3;$$

$$i(l) = \begin{cases} i_1, & l = 1; & \text{first node} \\ i_2, & l = 2; & \text{second node} \\ i_3, & l = 3; & \text{third node} \end{cases}$$

### Applications

The following numerical simulations are presented to show the versatility of the model to study the stability and failure modes of the discontinuous structure systems, and the stress distribution analysis for nonlinear materials.

Figure 4-7 show the computations analyzing the compressive post-failure behavior of a marble specimen with preexisting cracks formed by Wood's metal (Chang

○ fixed pt  
 □ shaking pt  
  
 ..... element  
 — block  
  
 / plasticity  
 • unloading  
  
 step: 0 of 7000  
 g\_t: 0.000000  
 c\_t\_i: 0.000000

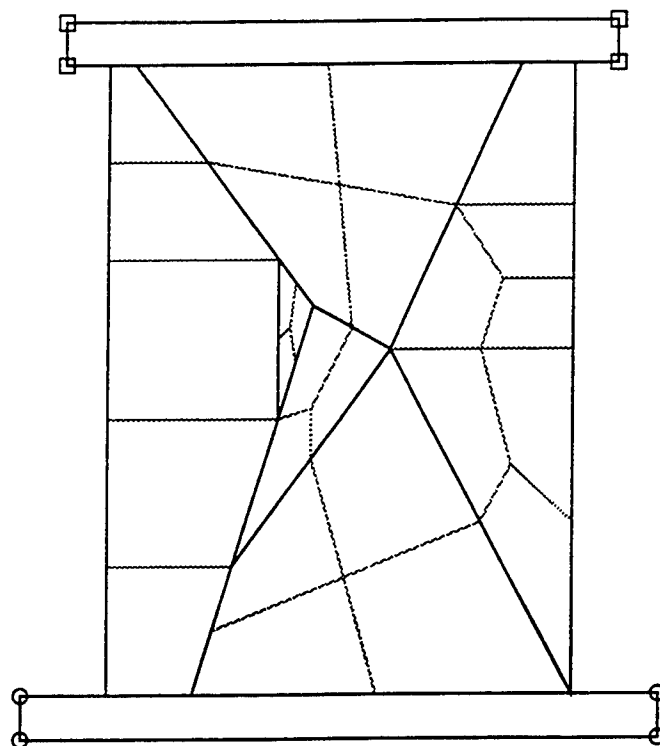


Figure 4. Original Configuration of the marble specimen

○ fixed pt  
 □ shaking pt  
  
 ..... element  
 — block  
  
 / plasticity  
 • unloading  
  
 step: 300 of 7000  
 g\_t: 0.299300  
 c\_t\_i: 0.001000

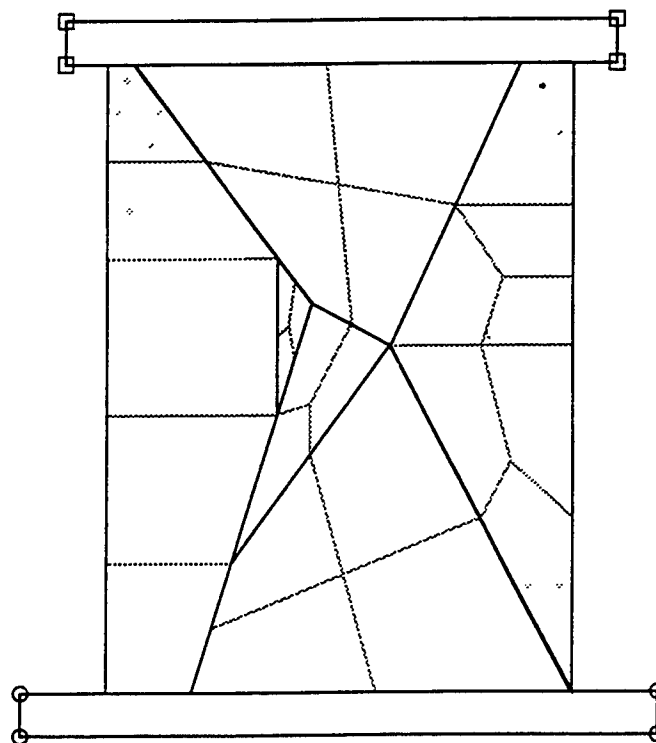


Figure 5. Configuration of the marble specimen, step=300

- fixed pt
- shaking pt

— element  
— block

- plasticity
- unloading

step: 4000 of 7000

g\_t: 1.413651

c\_t\_i: 0.000300

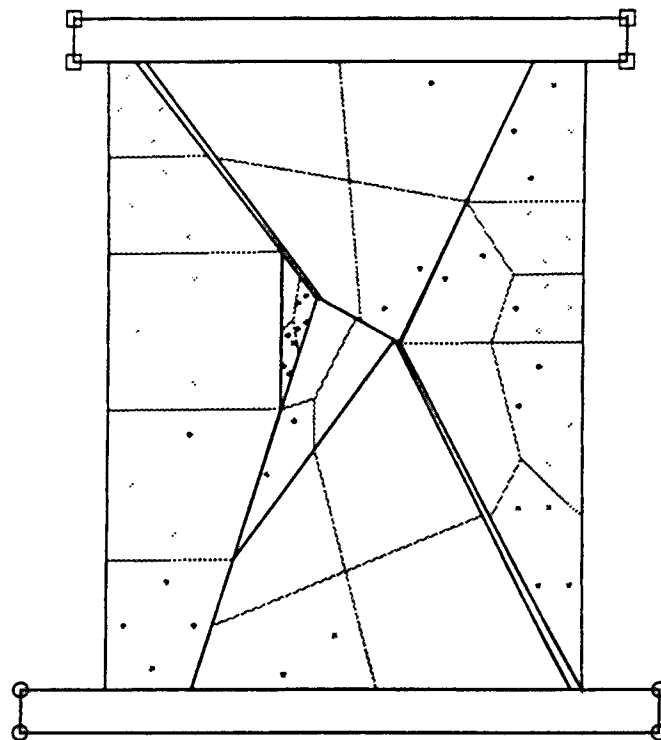


Figure 6. Configuration of the marble specimen, step=4000

- fixed pt
- shaking pt

..... element  
— block

- plasticity
- unloading

step: 7000 of 7000

g\_t: 2.398112

c\_t\_i: 0.001000

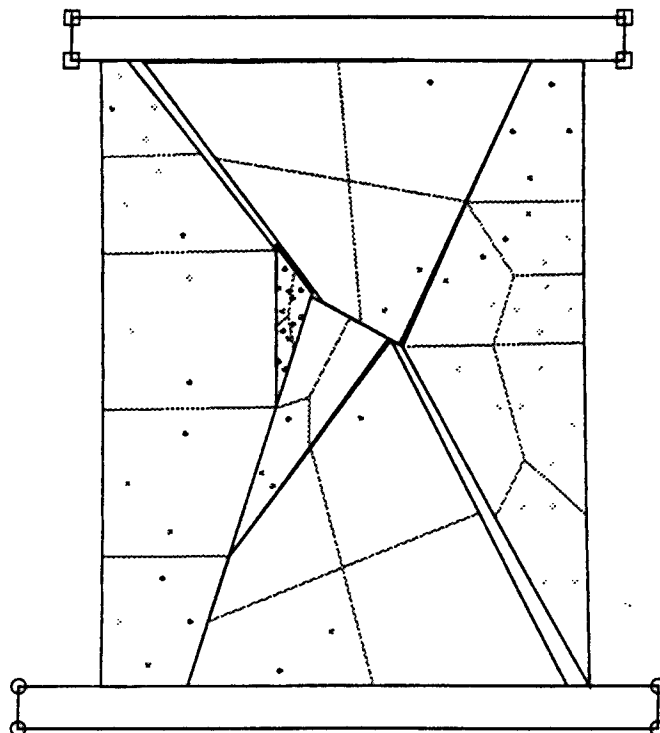


Figure 7. Configuration of the marble specimen, step=7000

○ fixed pt  
 ▽ loading pt

..... element  
 — block

step: 0 of 500  
 g\_t: 0.000000  
 c\_t\_i: 0.000000

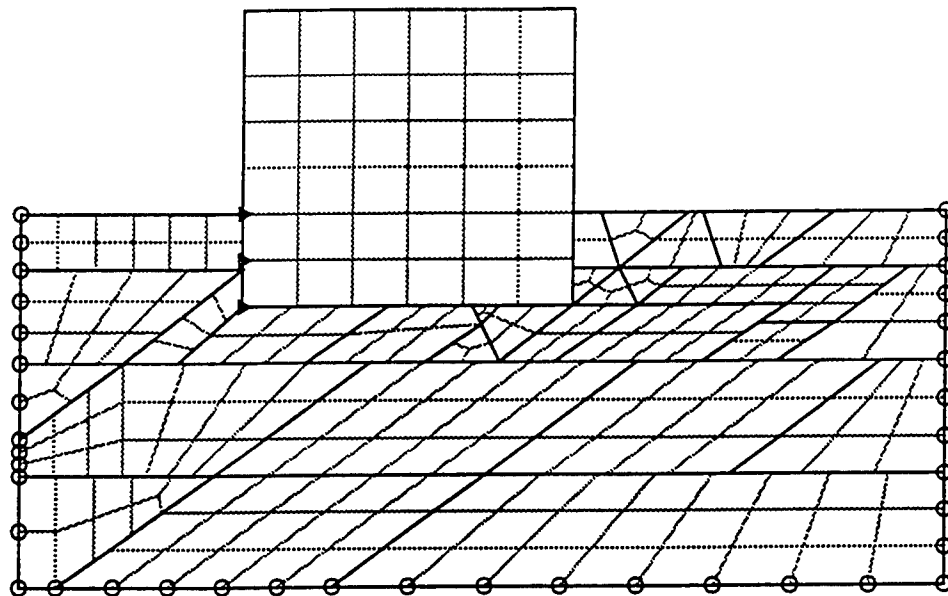


Figure 8. Original configuration of St. Francis Dam with bed rock

○ fixed pt  
 ▽ loading pt

..... element  
 — block

step: 300 of 500  
 g\_t: 1.454500  
 c\_t\_i: 0.005000

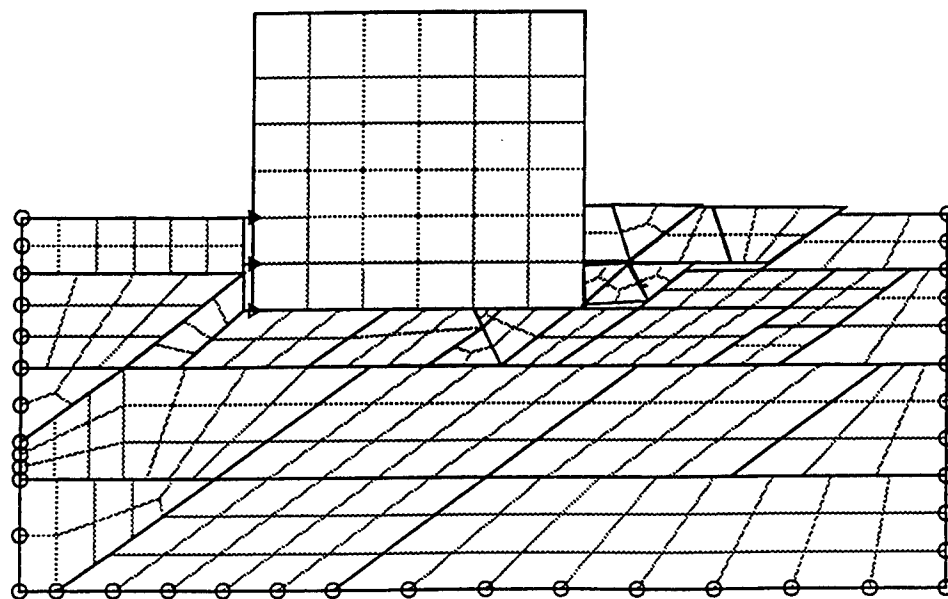


Figure 9. Configuration of St. Francis Dam with bed rock, step=300

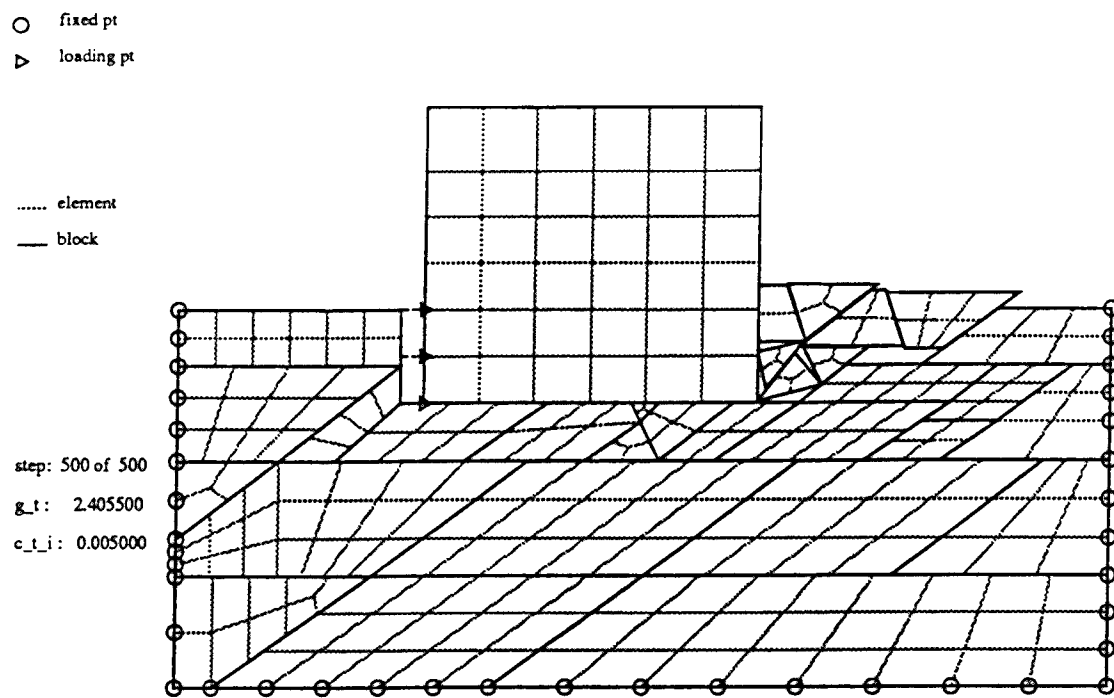


Figure 10. Configuration of St. Francis Dam with bed rock, step=500

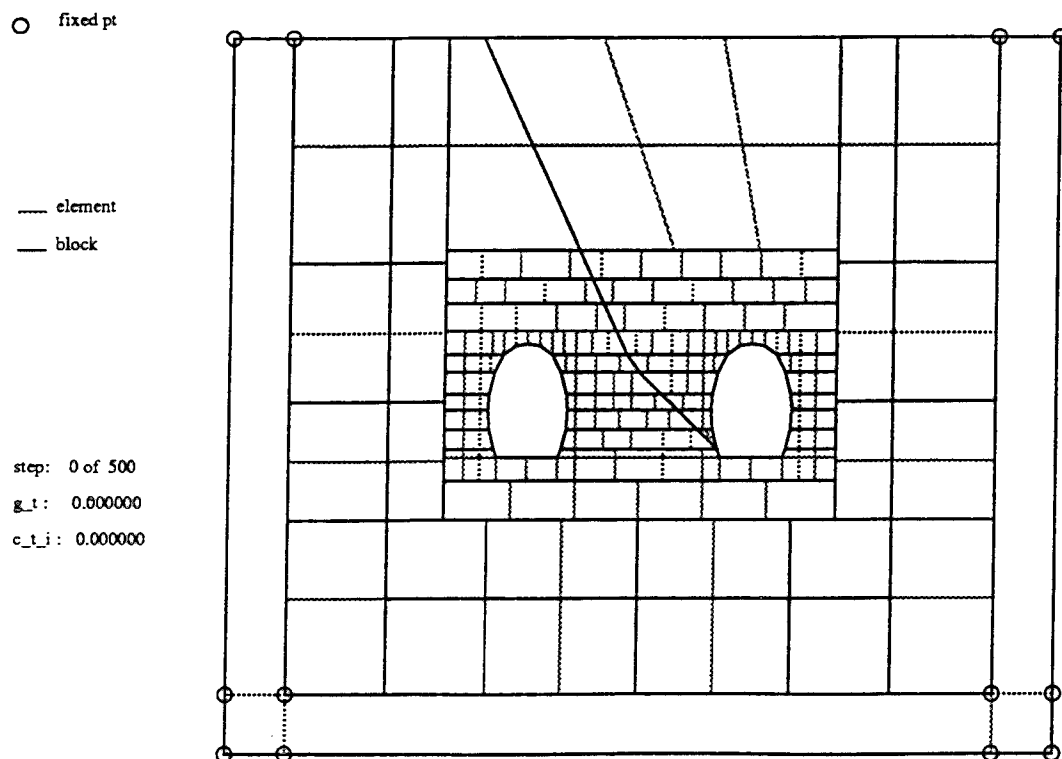


Figure 11. Reference configuration of rock caverns (no liner, no rock bolts)

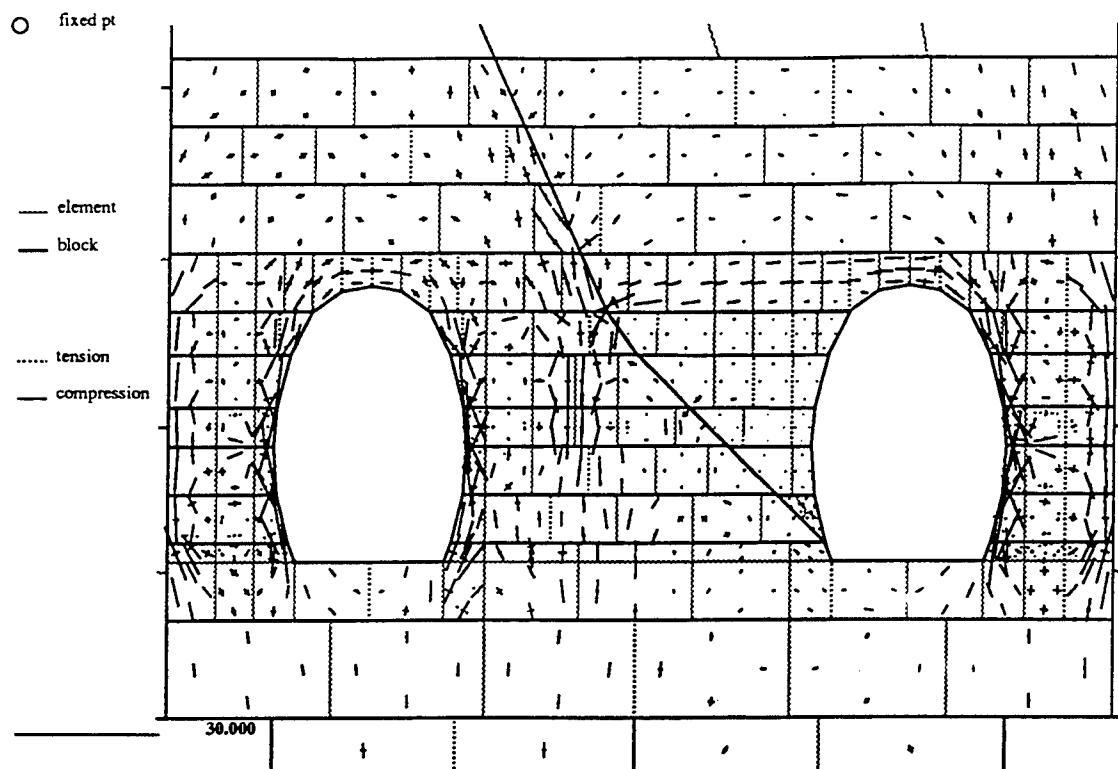


Figure 12. Principal stresses around two caverns (static excavation), step=500

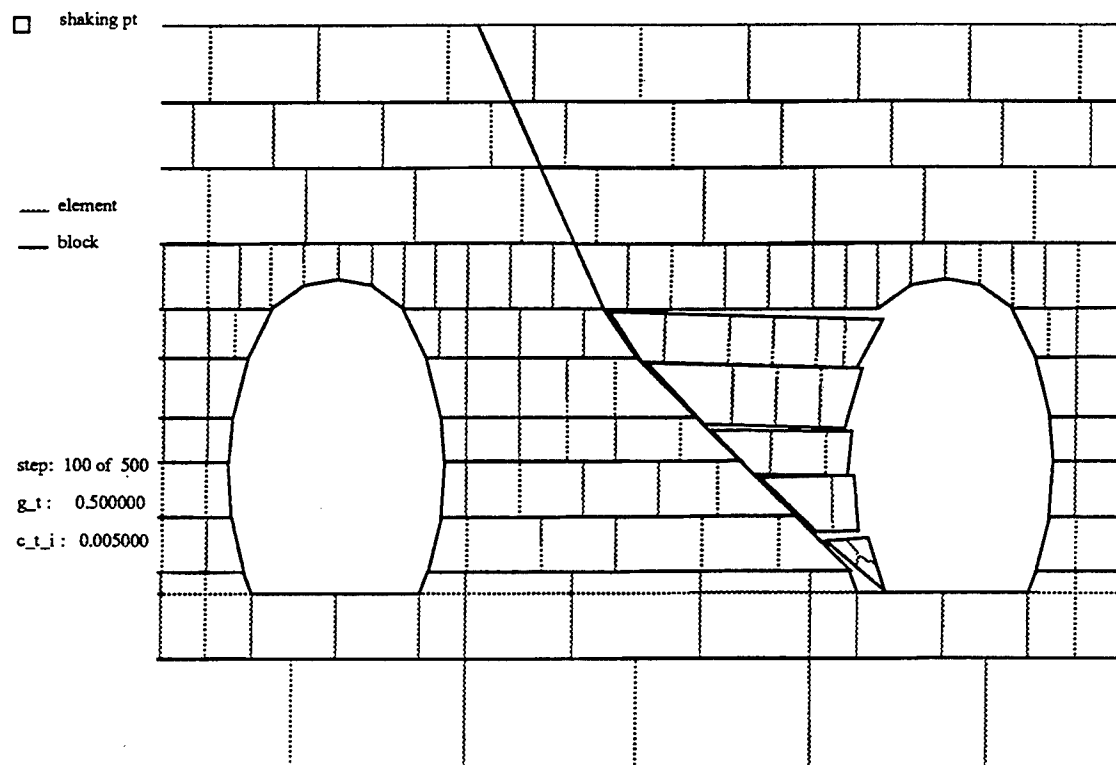


Figure 13. Magnification of two caverns during earthquake excitation, step=100

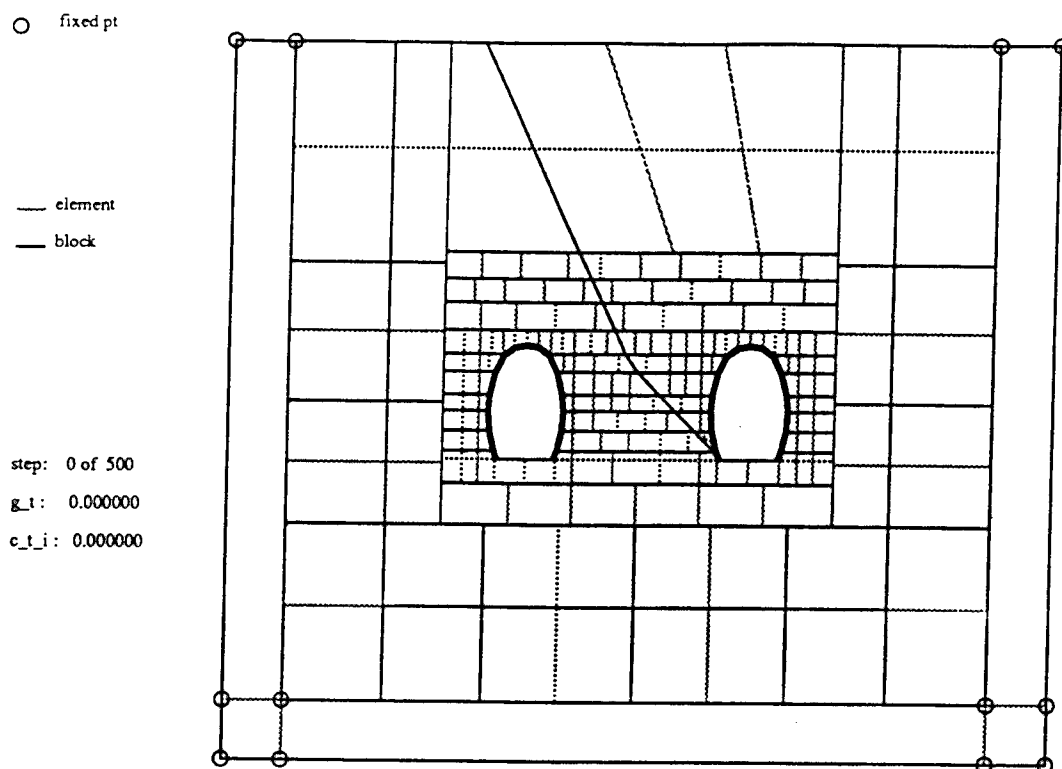


Figure 14. Original configuration of rock caverns with strong liner

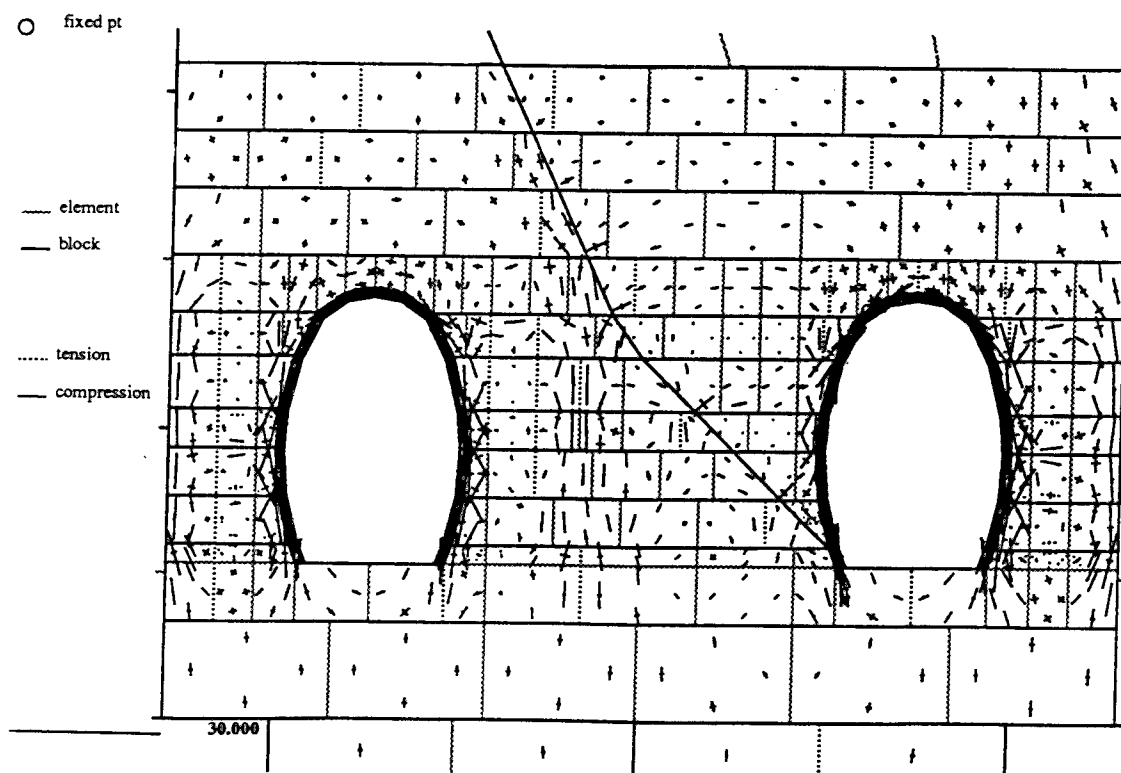


Figure 15. Principal stresses of two caverns (static excavation), step=500

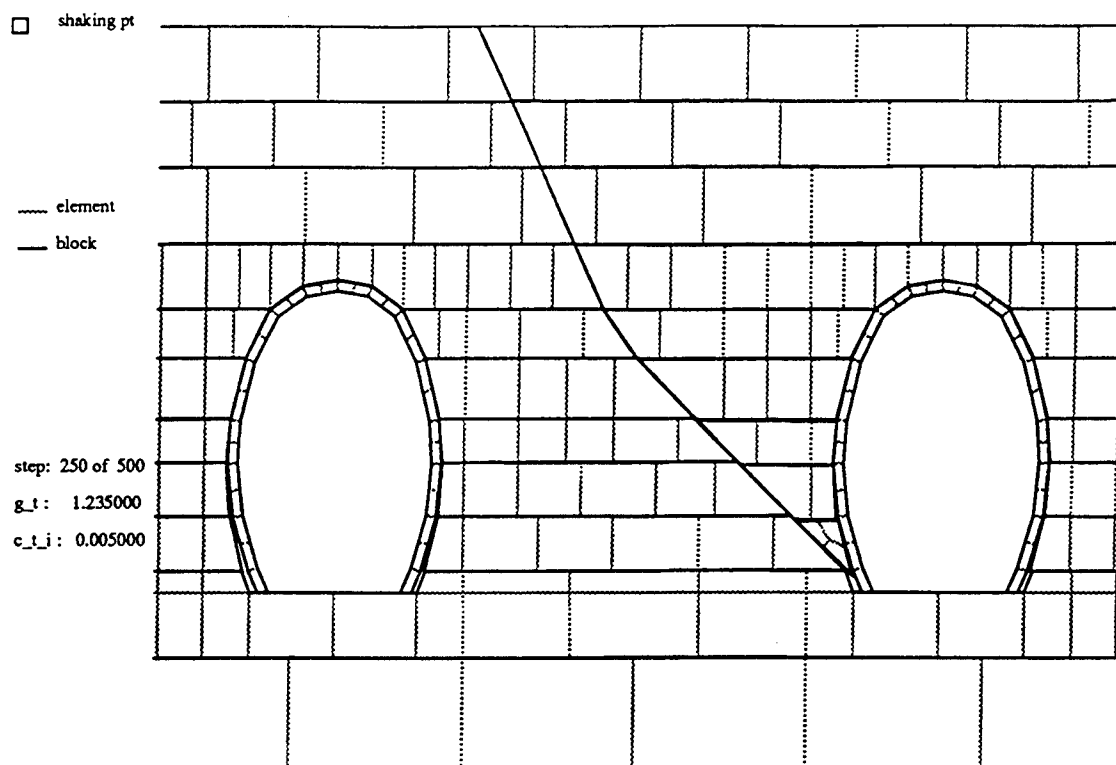


Figure 16. Rock caverns with strong liner under earthquake excitation, step=250

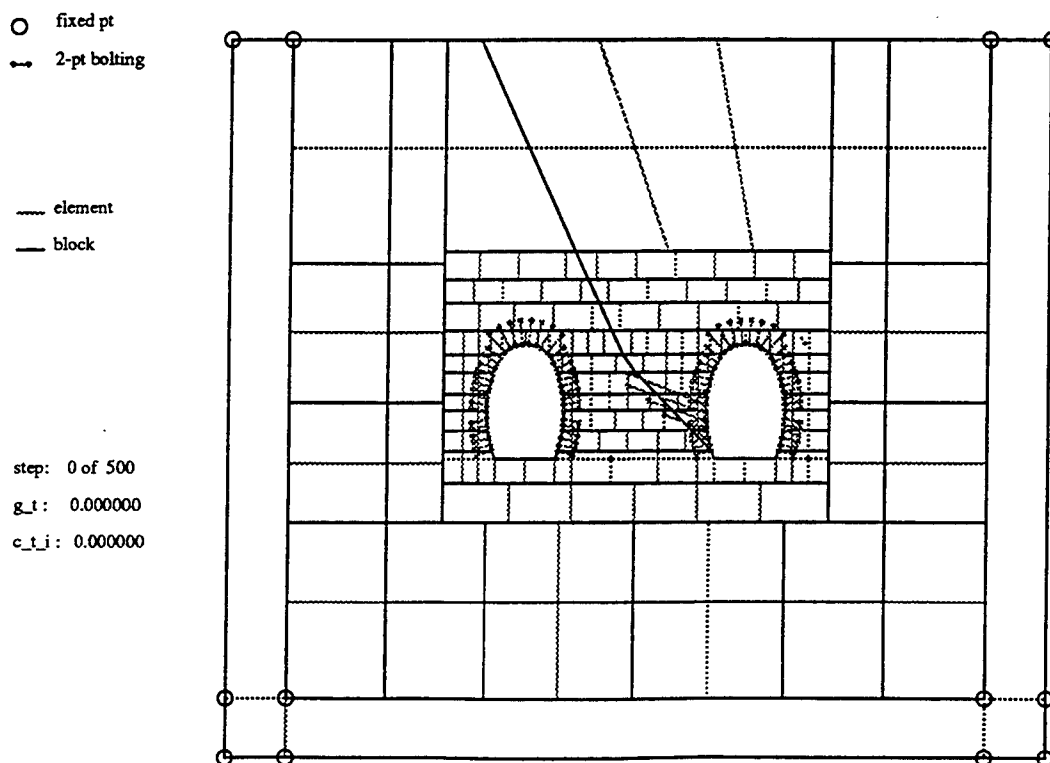


Figure 17. Original configuration of rock caverns with rock bolts



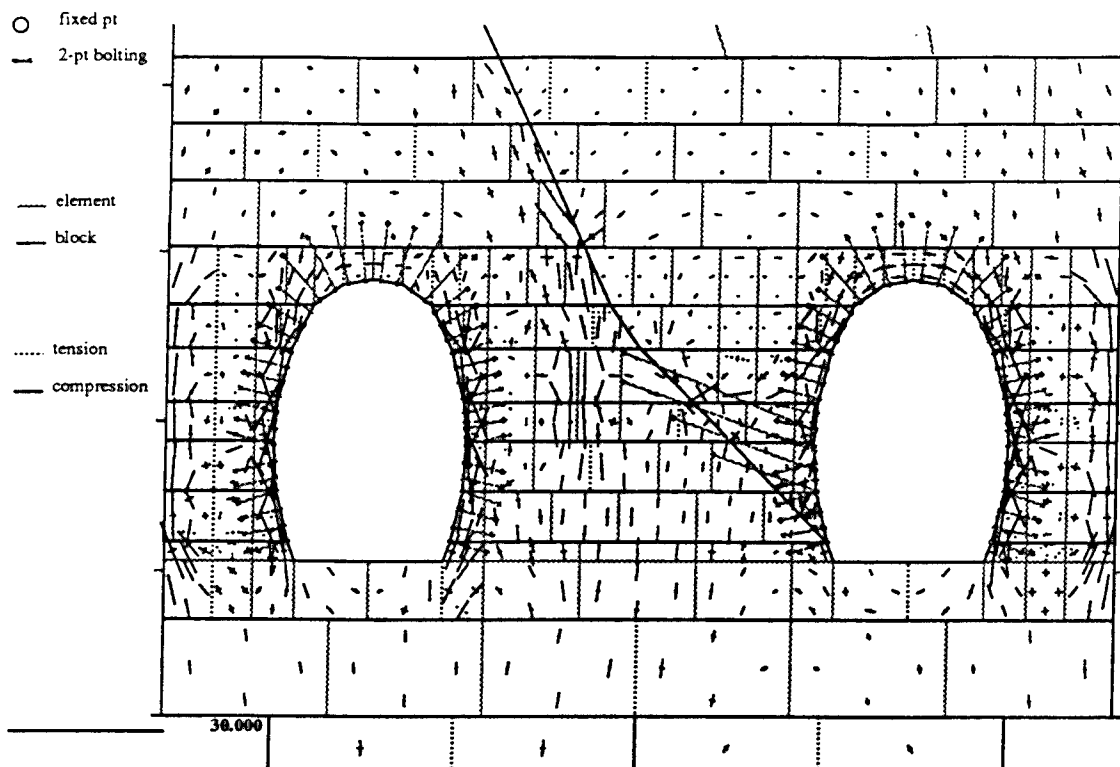


Figure 18. Principal stresses around two caverns (static excavation), step=500

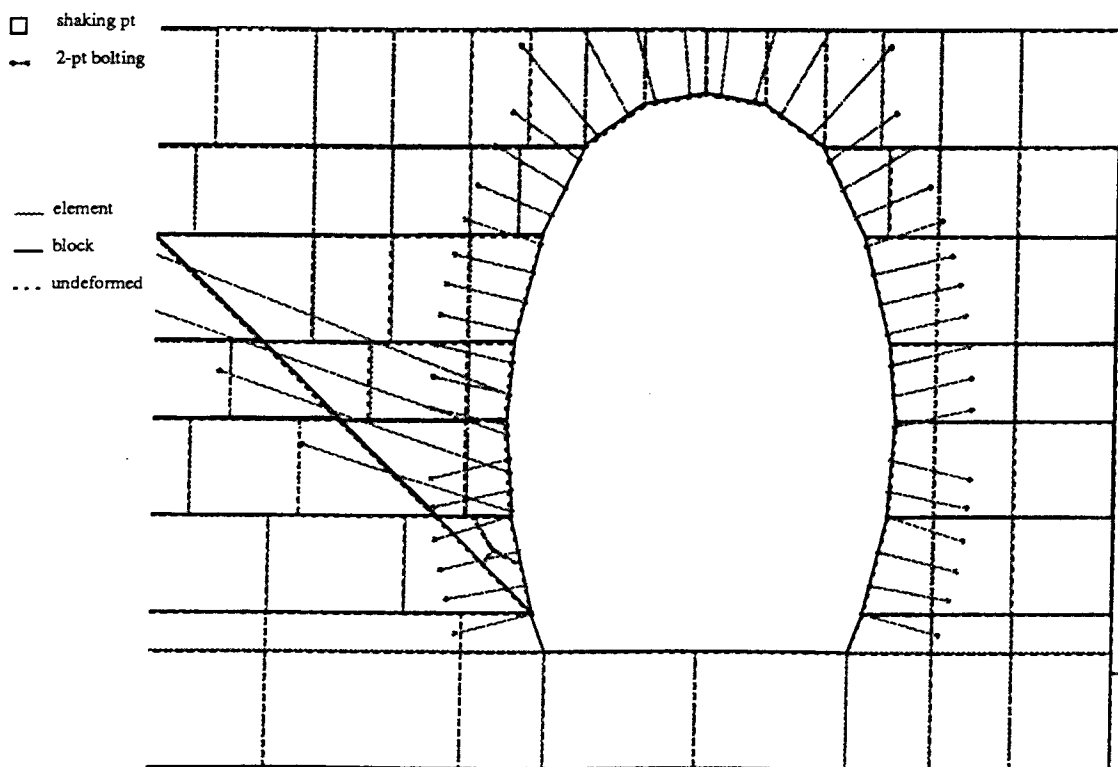


Figure 19. Magnification of right cavern under earthquake excitation, step=500

et al.). The propagation of plastic regions, the global stability and failure modes can be observed from the loading process.

The second application studies the initiation of block failures at the east abutment of the St. Francis Dam in failure reassessment (Rogers 1992; Rogers and McMahon 1993; Chang 1994). The modified rectangular dam is under the hydraulic pressure (horizontal stress), and the effective uniform vertical stress, the resultant of arching stress and vertical loads including the dead weight of the dam and full pore pressure, along the bottom of the dam. Figure 9-11 show the dynamic simulation process.

The last simulation analyzes the seismic response and global stability of large underground rock caverns with rock bolt and liner support (Chang 1994). Three cavern support designs were investigated: (1) reference case; (2) cavern supported by liner; (3) cavern support by rock bolts. Two stage computation — 500 time step static excavation, and 500 time step dynamic excitation were performed. Cavern 1 collapsed under seismic load (Figure 12-14); cavern 2 was stable (Figure 15-17), however the rocks around the cavern showed large deformation. Caverns 3 were safe due to rock intact stability and no noticeable movement of rocks were observed (Figure 18-20).

## Conclusions

By incorporating physical mesh of the multi-body block system overlaying mathematical covers of finite element mesh, and placing nonlinear material behavior into each triangular element, the proposed numerical model can solve large displacement and deformation problems for a continuous body or numerous discontinuous blocks with flexible moving boundary under static or dynamic loads, in addition to clarifying the stress distribution in the element block system. However, the boundaries of mathematical mesh of triangular elements are preset to be the same as physical boundaries. After mathematical mesh merges with physical mesh, the elements inside the physical bodies are regular forms that is less flexible than those in the Manifold Method. Therefore, the present model can be seen as an entrance level version of the Manifold Method.

## Acknowledgment

The authors would like to express our gratitude to Dr. Gen-hua Shi for his guidance and valuable suggestions in the development of the computer program.

## References

- Chang, C.-T. (1994). "Nonlinear dynamic discontinuous deformation analysis with finite element meshed block system." Ph.D. Dissertation, Department of Civil Eng., University of California at Berkeley.
- Chang, C.-T., Monteiro, P. J. M., Nemati, K. and Shyu, K. "Behavior of marble under compression," submitted to *ASCE Materials Journal*.
- Rogers, J. D. (1992). "Reassessment of the St. Francis dam failure." *Engineering Geology Practice in Southern California*, B.W. Pipkin and R. J. Proctor, ed., Southern California Section, Association of Engineering Geologists, 639-666.
- Rogers, J. D. and McMahon D. J. (1993). "Reassessment of the St. Francis dam failure." *10th Annual Conference of the Association of State Dam Safety Officials*.
- Shi, G. (1988). "Discontinuous deformation analysis—a new numerical model for the statics and dynamics of block systems." Ph.D. Dissertation, Department of Civil Eng., University of California at Berkeley.
- Shi, G. (1991). "Manifold method of material analysis." *Proc. 9th Army Conf. Appl. Math. Comp.*, June 18-21.
- Shi, G. (1994). "Modeling dynamic rock failure by discontinuous deformation analysis with simplex integrations." *Proc. 1st North American Rock Mech. Symp.*, 591-598.
- Shyu, K. (1993). "Nodal based discontinuous deformation analysis." Ph.D. Dissertation, Department of Civil Eng., University of California at Berkeley.
- Zienkiewicz, O. C. and Taylor, R. L. (1991). "The finite element method." 4th ed., vol. 1-2, McGraw-Hill, London.

# Manifold Method of Material Analysis

Dezhang Lin and Haihong Mo

Rock Mechanics Institute, University of Oklahoma, Norman, OK 73019, USA

## 1. INTRODUCTION

The manifold method is an approximate method of solving differential equations in material analysis. An approximate solution of the boundary-value problem is sought on a finite number of fixed intersecting subdomains (sectors, half-disks, disks), called basic covers, in the discrete form of integrals or differential operators based on the basis functions.

The approximate solution of a boundary-value problem, found by means of the manifold method, is convergent with respect to the discreteness parameter up to the boundary of the polygon (two-dimensional manifold) even if the defined boundary values of the solution are discontinuous within the polygon.

In the method of composite nets, the corresponding integral representation of the solution of the boundary-value problem is proximate with the account of interpolants of the derivatives of some orders which defined within a cover.

Numerical examples shows that the present implementation effectively computes stress concentrations and stress intensity factors at discontinuities with very irregular arrangement of nodes; the latter makes it very advantageous for modeling progressive discontinuity propagation.

The manifold method was recently developed to cope with coupled problems involving discontinua and continua. Since this method is in its infancy, a large number of issues need to be addressed and we will outline some of these issues and give some indications of how coupled problems can be addressed.

## 2. CONCEPTS OF MANIFOLDS

A set  $M$  is given the structure of a differentiable manifold if  $M$  is provided with a finite or countable collection of charts, so that every point is represented in at least one chart (see Bishop and Goldberg 1980).

A map is an open set  $U$  in the euclidean coordinate space  $q = (q_1, \dots, q_n)$ , together with a one-to-one mapping  $f: W \rightarrow U$  of a subset  $W \subset M$  of the set  $M$  onto  $U$  (see Fig.1).

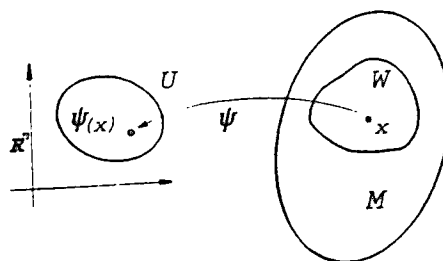


Figure 1: A map

Consider there are two maps  $f_i: W_i \rightarrow U_i$  and  $f_j: W_j \rightarrow U_j$ . If the set  $W_i$  and  $W_j$  intersect, then their intersection  $W_i \cap W_j$  has an image on both maps:

$$U_{ij} = f_i(W_i \cap W_j), \quad U_{ji} = f_j(W_j \cap W_i) \quad (1)$$

We assume that if points  $p_i$  and  $p_j$  in two charts  $U_i$  and  $U_j$  have the same image in  $M$ , then  $p_i$  and  $p_j$  have neighborhoods  $U_{ij} \subset U_i$  and  $U_{ji} \subset U_j$  with the same image in  $M$ . In this way we get a mapping  $f_j(f_i^{-1}(p_i)) : U_{ij} \rightarrow U_{ji}$  (see Fig.2).

Any point of  $M$  we can find a cover  $W$  and a diffeomorphism  $f$  of  $W$  with an open subset,  $U$ , of  $R^n$  given by setting the last  $n-k$  coordinates equal to zero. Suppose that we can cover  $M$  by a finite number of such covers,  $W_1, \dots, W_r$ . Each  $W_i$  comes with its own  $f_i$  and

$$f_i(W_i \cap M) = U_{ij} \cap R^k. \quad (2)$$

Let us call this subset  $U_{ij}$  is an open subset of  $R^k$ . On any overlap  $W_i \cap W_j$  we can consider the restriction of either  $f_i$  or  $f_j$ . So  $f_i(W_i \cap U_{ij})$  is an open subset of  $U_i$  and  $f_j(W_j \cap U_{ji})$  is an open subset of  $U_j$ .

This is a mapping of the region  $U_i$  of the euclidean space  $q$  onto the region  $U_j$  of the euclidean space  $q'$ , and it is given by  $n$  functions of  $n$  variables,  $q' = q'(q)$ , ( $q = q(q')$ ). The charts  $U_i$  and  $U_j$  are called compatible if these functions are differentiable. An atlas is a union of compatible maps. Two atlases are equivalent if their union is also an atlas.

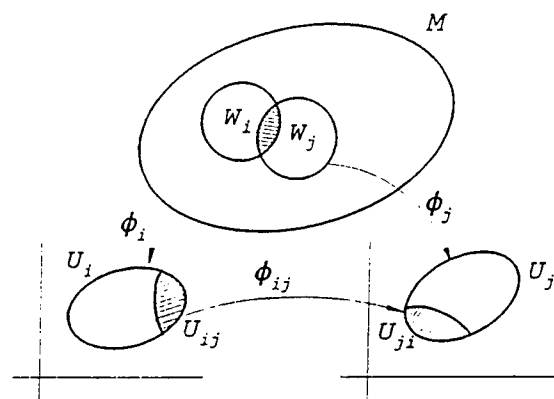


Figure 2: Compatible maps

A differentiable manifold is a class of equivalent atlases. We will consider only connected manifolds. Then the number  $n$  will be the same for all charts; it is called the dimension of the manifold. A neighborhood of a point on a manifold is the image under a mapping ( $p: U \rightarrow M$ ) of a neighborhood of the representation of this point in a chart  $U$ . We will assume that every two different points have non-intersecting neighborhoods.

In other word, instead of cutting  $M$  up into pieces, we write any form as a sum of small pieces each of which lives only on one coordinate patch on  $M$  which we can integrate by pulling it back to a subset of  $R^k$ . A repeated use of the change of variables formula easily shows that this definition of integral does not depend on the choice of the patch (see Arnold 1982).

Here are two examples:

- The sphere  $S^2 = (x, y, z) : x^2 + y^2 + z^2 = 1$  has the structure of a manifold, with maps, for example, consisting of two maps ( $U_i, f_i, i = 1, 2$ ) in stereographic projection (see Fig.3). Here we have

$$W_1 = S^2 - \{N\}, \quad U_1 = R_1^2, \quad (3)$$

$$W_2 = S^2 - \{S\}, \quad U_2 = R_2^2. \quad (4)$$

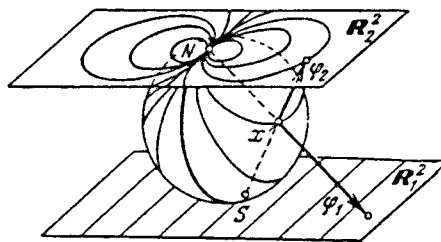


Figure 3: Maps of a sphere

- An map for the donut can be constructed by using angular coordinates. We can consider the four maps obtained (see Fig.4).

$$0 < \theta < 2\pi, \quad -\pi < \phi < \pi \quad (5)$$

$$0 < \phi < 2\pi, \quad -\pi < \theta < \pi \quad (6)$$

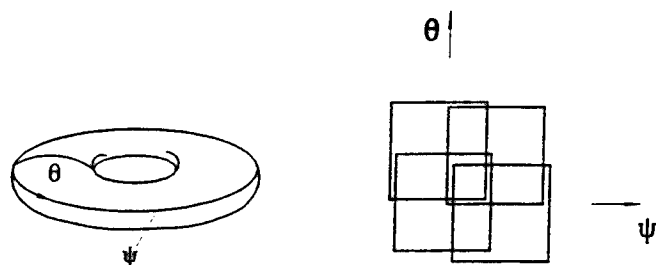


Figure 4: Map for a donut

### 3. MANIFOLD STRUCTURE

The set  $f(W)$  is not necessarily a smooth submanifold of  $M$ . It could have "self-intersections" or "folds" and could even be reduced to a point. However, even in the one-dimensional case, it is clear that it is inconvenient to restrict ourselves to contours of integration consisting of one piece: it is useful to be able to consider contours consisting of several pieces which can be traversed in either direction, perhaps more than once. The analogous concept in higher dimensions is called a chain.

A chain of dimension  $n$  on a manifold  $M$  consists of a finite collection of  $n$ -dimensional oriented simplices  $s_1, \dots, s_r$ , in  $M$  and integers  $m_1, \dots, m_r$ , called multiplicities (the multiplicities can be positive, negative, or zero).

A chain is denoted by

$$c_k = m_1 s_1 + \dots + m_r s_r. \quad (7)$$

The boundary of a polyhedron can be regarded as an example. Let  $K$  be a convex oriented  $k$ -dimensional polyhedron in  $k$ -dimensional euclidean space  $R^k$ . The boundary of  $K$  is the  $(k-1)$ -chain  $\partial K$  on  $R^k$  defined in the following way.

The cells  $s_i$  of the chain  $\partial K$  are the  $(k-1)$ -dimensional faces  $s_i$  of the polyhedron  $K$ , together with maps  $f_i : K_i \rightarrow R^k$  embedding the faces in  $R^k$  and orientations  $O_i$  defined below; the multiplicities are equal to 1:

$$\partial s = \sum s_i \quad s_i = (K_i, f_i, O). \quad (8)$$

Rule of orientation of the boundary. Let  $e_1, \dots, e_k$  be an oriented frame in  $R^k$ . Let  $K_i$  be one of the faces of  $K$ . We choose an interior point of  $K_i$  and there construct a vector  $n$  outwardly normal to the polyhedron  $K$ .

An orienting frame for the face  $K_i$  will be a frame  $f_1, \dots, f_k$ , on  $K_i$  such that the frame  $(n, f_1, \dots, f_k)$  is oriented correctly (i.e., the same way as the frame  $e_1, \dots, e_k$ ).

The boundary of a chain is defined in an analogous way. Let  $s = (K, f, O)$  be a  $k$ -dimensional cell in the manifold  $M$ . Its boundary  $\partial s$  is the  $(k-1)$ -chain:  $\partial s = \sum \sigma_i$  consisting of the cells  $\sigma_i = (K_i, f_i, O_i)$ , where the  $\Gamma_i$  are the  $(k-1)$ -dimensional faces of  $K$ ,  $O_i$  are orientations chosen by the rule above, and  $f_i$  are the restrictions of the mapping  $f : K \rightarrow M$  to the face  $\Gamma_i$ .

The boundary of a  $k$ -dimensional chain  $c_k$  in  $M$  is the sum of the boundaries of the cells of  $c_k$  with multiplicities:

$$\partial c_k = \partial(m_1 s_1 + \dots + m_r s_r) = m_1 \partial s_1 + \dots + m_r \partial s_r. \quad (9)$$

Obviously,  $\partial c_k$  is a  $(k-1)$ -chain on  $M$ .

Let  $\omega^k$  be a  $k$ -form on  $M$ , and  $c_k$  a  $k$ -chain on  $M$ ,  $c_k = \sum m_i s_i$ . The integral of the form  $\omega^k$  over the chain  $c_k$  is the sum of the integrals on cells, counting multiplicities:

$$\int_{c_k} \omega^k = \sum m_i \int_{s_i} \omega^k. \quad (10)$$



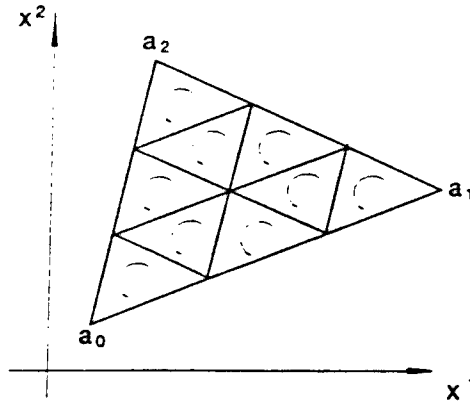


Figure 5: Simplicial subdivision of  $K$

For any polyhedron  $K$ , it can be partitioned into simplices:

$$K = \Sigma s_i, \quad \partial K = \Sigma \partial s_i \quad (11)$$

Let  $K$  be the simplex  $[p_0, p_1, p_2]$  in  $R^2$ , and let  $f: s \rightarrow R^2$  be a function whose components  $(f_1, f_2)$  have continuous derivatives on  $[p_0, p_1, p_2]$ . The integral within the simplex  $K$  is

$$\begin{aligned} \int_{[p_0, p_1, p_2]} D_{(1,2)}(f_1, f_2)(x) = & \left( \int_{[p_1, p_2]} + \int_{[p_2, p_0]} + \int_{[p_0, p_1]} \right) \\ & (f_1(x)D_1f_2(x)dx_1 - f_2(x)D_1f_1(x))dx_1 + \\ & (f_1(x)D_2f_2(x)dx_1 - f_2(x)D_2f_1(x))dx_2 \end{aligned} \quad (12)$$

where

$$D_{(1,2)}(f_1, f_2)(x) = \det[D_j f_i(x)], \quad i, j = 1, 2. \quad (13)$$

The integral on the left is an integral on the 2-dimensional simplex  $K$  in  $R^2$ . The integrals on the right in the above formulas are integrals on the one-dimensional simplexes  $[p_1, p_2]$ ,  $[p_2, p_0]$ ,  $[p_0, p_1]$  in  $R^2$ . Formula expresses the integral on a as an integral around the boundary of  $K$ . Observe that

$$\partial(p_0, p_1, p_2) = (p_1, p_2) + (p_2, p_0) + (p_0, p_1) \quad (14)$$

Figure 5 shows  $K$  as positively oriented in  $R^2$ , but the integral is a correct statement in all cases.

Let  $P_k, k = 1, 2, \dots$ , be a sequence of simplicial subdivisions of  $K$  which are positively oriented in  $R^2$ , and let  $c : (a_0, a_1, a_2)$  denote a simplex in  $P_k$ . If two simplexes  $s$  and  $s'$

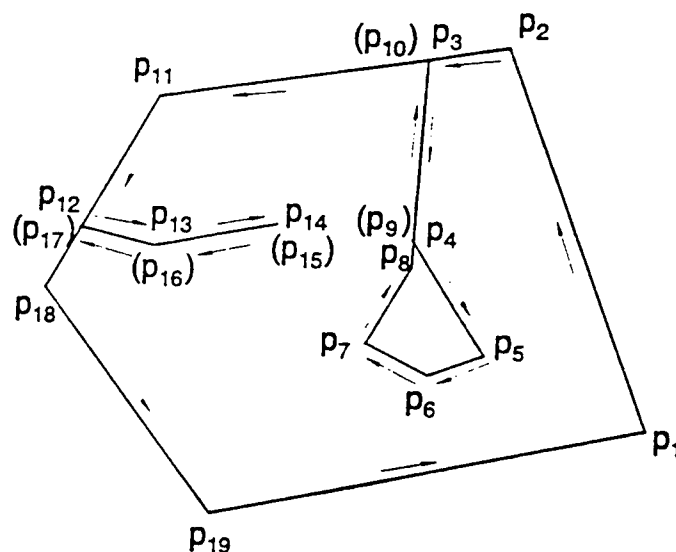


Figure 6: Division of a polyhedron and its boundary

have a one-dimensional side in common, then this side has opposite orientations because the simplexes in each  $P_k$  form an oriented Euclidean complex. Then two simplexes  $s$  and  $s'$ , with a one-dimensional side in common contribute two terms which cancel in the sum. The term remains after all cancellations have been made if and only if  $(a_1, a_2)$  is a side of only a single simplex  $c$ . After cancellations, if and only if  $(a_1, a_2)$  is a one-simplex in the boundary of the chain of all simplexes in  $P_k$ . There is no loss of generality in assuming that  $a_0$ , in the simplex  $c : (a_0, a_1, a_2)$ , is in the interior of  $s$ , and that the side of  $c$  in the boundary  $\partial K$  of  $K$  has vertices  $a_1$ , and  $a_2$ . Then the sum equals the sum of terms of the form shown in (14). Figure 4 indicates graphically the cancellation which occurs in the sum in (14) when the terms in the sum are represented in the form indicated in Figure 5 also indicates that the terms correspond to a counterclockwise, or positive, subdivision of the boundary of  $K$ .

#### 4. BOUNDARY VALUE PROBLEM OF A POLYGON

Before setting up a boundary-value problem we shall discuss the method of describing the boundary of a multiply-connected polygon  $K$ . Suppose a finite sequence of points  $p_1, p_2, \dots, p_k$ ,  $k > 2$ , is given in the two-dimensional complex plane  $z$ . We set  $p_0 = p_k$ .

Successively connecting the points  $p_1, p_2, \dots, p_k$  by line segments, we get a closed polygonal line  $\Gamma$ . We denote by  $c_j$  the segment whose endpoints are  $p_i$  and  $p_{j+1}$  and call it a side of the polygonal line  $\Gamma$ . The points  $p_1, p_2, \dots, p_k$ , are the vertices of the polygonal line  $\Gamma$  (see Figure 6).

Let  $p_i$  be a set of points of the complex plane  $z$  which belong to at least one side of the

polygonal line  $\Gamma$ . The closed polygonal line  $\Gamma$  is attainable from the inside (from the outside) if the following conditions are fulfilled:

- (a) there is a finite (infinite) domain  $K$  whose boundary coincides with  $p_K$ ;
- (b) the direction of traverse of the polygonal line  $\Gamma$  corresponding to the order of numbering of its vertices coincides with the generally accepted positive traverse of the boundary of the domain  $K$  for which the domain  $K$  is locally on the left of  $\Gamma$ .

Closed polygonal lines attainable from the inside or from the outside are called admissible polygonal lines.

An open finitely-connected bounded domain  $K$  in the complex plane  $z$  is a polygon if its boundary can be composed of a finite number of pairwise nonintersecting admissible closed polygonal lines one of which is attainable from the inside (the external boundary of the domain  $K$ ), and the others are attainable from the outside.

In the case when the boundary of the polygon  $K$  serves as only one polygonal line attainable from the inside, the polygon is simply connected.

The vertices, sides and angles of polygonal lines that form the boundary of the polygon  $K$  are the vertices, sides and angles of the polygon  $K$  itself. For the sake of convenience, we introduce the following unbroken numeration of the vertices and sides of the multiply connected polygon  $K$ . We preserve the numbers of the vertices and sides of the polygonal line attainable from the inside, i.e., the external boundary of the polygon  $K$ . Then we continue to number the vertices and, respectively, the sides of a certain closed polygonal line attainable from the outside, constituting a part of the boundary, by natural numbers. The new numeration is in the same order as the original numeration of the vertices and sides of the polygonal line. Then, by analogy, we continue to number the vertices and sides of the next polygonal line, attainable from the outside, constituting the boundary of the polygon  $K$ , and so on. The total number of vertices and sides of the polygon  $K$  will be denoted by  $n_b$ .

Let  $p_i$  be the set of all vertices of the polygon  $K$  for which the following conditions are fulfilled:

- (a) at a vertex lie the endpoints of two adjacent sides on which boundary conditions of the first kind are simultaneously specified;
- (b) the boundary values defined on these sides do not coincide at the vertex.

The solution of the boundary-value problem is a function  $u$  with the following properties:

- (1)  $u$  is bounded and satisfies partial differential equation on the polygon  $K$ .
- (2)  $u$  is continuous up to the boundary of the polygon  $K$ , except for the set  $p_i$  of its vertices at which the specified boundary values are discontinuous,
- (3) on the polygon  $K$  the function  $u$  has partial derivatives  $\partial u / \partial x$  and  $\partial u / \partial y$ , continuous up to its boundary, except for some of its vertices.

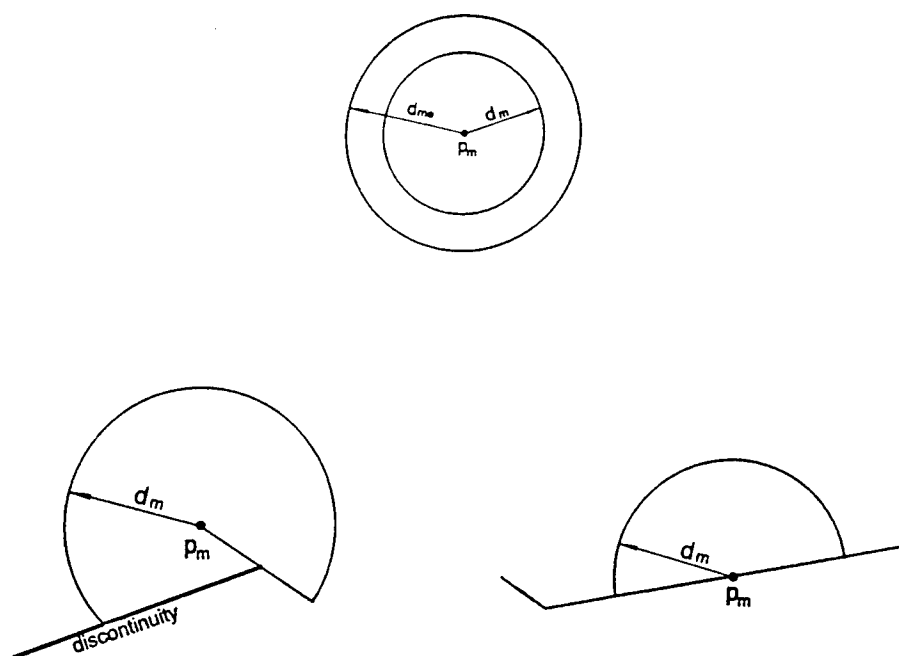


Figure 7: A cover and extended cover

## 5. FINITE COVERING OF A POLYGON

The first step in seeking an approximate solution of the boundary value problem by the method being considered is the construction of a covering of the polygon  $K$  by a finite number of overlapping sectors of disks, half-disks and disks which we shall call covers. An approximate solution of boundary value problem can be found on every cover as a certain elementary function.

Suppose we are given, generally speaking, a multiply-connected polygon  $K$  with vertices  $p_j, j = 1, 2, \dots, n_b$ . We choose a finite number of points  $p_q, q = n_b + 1, n_b + 2, \dots, L$ , lying inside (i.e., not at the endpoints) of some sides of the polygon  $K$  and also several points  $p_m, m = L + 1, L + 2, \dots, M$ , lying strictly within the polygon  $K, n_b < L < M$ . There may be several points chosen on some sides of the polygon and none on the other sides.

The covers (sectors of disks, half-disks, disks)  $C_b$  are called basic covers and the covers  $C_e$  are called extended covers. Every basic cover  $C_b$  is a part of the corresponding extended cover. Figures 7 shows a basic cover and its extended cover. A choice of covering is, evidently not unique. For instance, besides the covering of polygon shown in Figure 8, the covering depicted in Figure 9 is also permissible.

The closed basic covers of "smaller dimensions" form (with certain intersections) a covering of the closed polygon  $cls(K)$  and, all the more so, the closed extended blocks form the indicated covering.

The double covering of a polygon by basic and extended covers is necessary to find an approximate solution of the boundary-value problem by the manifold method. In what fol-

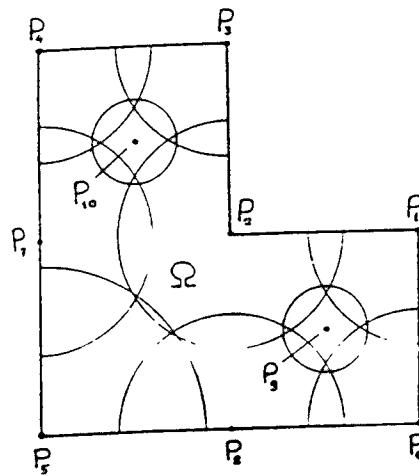


Figure 8: A covering of the polygon  $K$

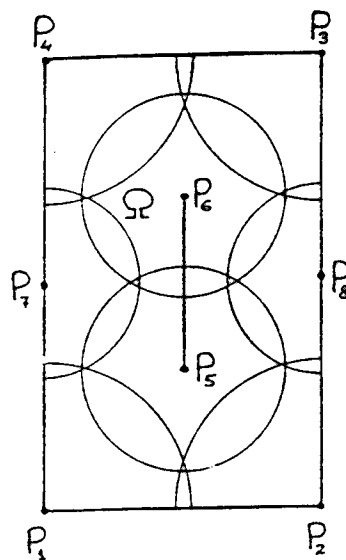


Figure 9: A covering of the polygon  $K$

lows, when speaking of a covering of the polygon  $K$ , we shall first of all bear in mind the existence of a covering by finite basic covers and finite extended covers. We shall obtain an approximate solution of boundary value problem on closed basic covers.

Here we construct integral representation of the solution of the boundary-value problem on basic covers, namely, sectors, half-disks, and disks. The solution is given on covers in terms of the shape functions (with basis functions) of the values of the solution itself within the boundary of the cover and also in terms of the specified boundary values of the required solution or of its normal derivative along the sides of the polygon  $K$  to which the corresponding polygon (block) is adjacent. These representations lie at the basis of the construction of an approximate manifold method for solving the boundary-value problem.

## 6. DISCRETE COORDINATE FUNCTIONS WITHIN A COVERING $C$

After constructing a finite covering of the polygon  $K$  by covers in accordance with the rules formulated, we define shape function which satisfy a local weighted least squares fitting within the cover. These shape functions explicitly appear in the representations of the solution of the boundary value problem on covers considered. Generally, piecewise continuous polynomial functions are involved which are defined to be zero outside of the specific cover assigned.

Let  $u$  be a function defined on a cover  $C$ . Then the approximation of the function  $u(\mathbf{x})$ ,  $u_h(\mathbf{x})$  in  $R^n$ , is given by  $u_I$  with  $n$  collocation points within the cover. Obviously,  $n$  may have to be large in order to capture in  $u_I = u(\mathbf{x}_I)$  all the important characteristics of  $u(\mathbf{x})$ .

$$u_h = \sum_{I=1}^{I=n} \lambda_I(\mathbf{x}) u_I \quad (15)$$

where the  $u_I$  are the elements in the linear independent basis that span a linear space  $C$  of  $\dim C = n$ .

Because we can not use an infinite number of basis functions are typical impossible. Some considerations are needed as to the choice of basis functions, in that some families of basis may be more successful in reducing approximation error. It is oftentimes useful to employ familiar functions such as the multidimensional polynomial, trigonometric functions, Legendre, Chebyshev in that these functions have nonzero value almost everywhere in the cover  $C$ . Generally, the classic piecewise continuous polynomial functions are involved which are defined to be zero outside of the cover assigned. In the examples presented here, for simplicity we use a set of classic polynomial, the normalized Legendre polynomials, although in general the method requires only the polynomial be orthonormal (see Nayroles 1992).

The approximation problem is to find the best approximation of  $u_h(\mathbf{x})$  using the basis function  $\phi = \{\phi_1, \phi_2, \dots, \phi_m\}$  on the cover  $C$ .

$$u_h = \sum_{j=1}^{j=m} \phi_j(\mathbf{x}) \mathbf{a} \quad (16)$$

The approximation of the function  $u_h$  at collocation point  $I$  is

$$u_h(\mathbf{x}_I) = \sum_{j=1}^{j=m} \phi_j(\mathbf{x}_I) \mathbf{a} \quad (17)$$

An inner product with respect to the weighting function  $W \geq 0$  is defined for functions  $\eta_i, \eta_j$  on  $C$

$$(\eta_i, \eta_j) = \int_C W \eta_i \eta_j dC \quad (18)$$

The vector  $\mathbf{a}$  can be easily obtained by minimizing a weighted  $L_2(C)$  norm within the cover  $C$ .

$$\min \int_C W(\mathbf{x}_I) (u_h(\mathbf{x}_I) - u_I)^2 dC \quad (19)$$

The shape function  $\lambda_I$  at point  $I$

$$\lambda_I = \mathbf{p}^t \mathbf{S}^{-1}(\mathbf{x}) \mathbf{T}(\mathbf{x}) \quad (20)$$

$$\mathbf{S}(\mathbf{x}) = \sum_I^n \mathbf{w}(\mathbf{x} - \mathbf{x}_I) \mathbf{p}(\mathbf{x}_I) \mathbf{p}^t(\mathbf{x}_I) \quad (21)$$

$$\mathbf{T}(\mathbf{x}) = [\mathbf{w}(\mathbf{x} - \mathbf{x}_I) \mathbf{p}(\mathbf{x}_I)] \quad (22)$$

Let  $\psi_j$  and  $\psi_k$  be in  $L_2(C)$ . Then  $\psi_j$  and  $\psi_k$  are orthogonal in  $C$  if

$$(\psi_j, \psi_k) = \int_C W(\mathbf{x}_I) \psi_j(\mathbf{x}_I) \psi_k(\mathbf{x}_I) dC = 0, \quad \text{if } j \neq k \quad (23)$$

A set of functions  $\psi_1, \psi_2, \dots, \psi_m$  in  $L_2(C)$  is an orthogonal set in  $C$  if  $(\psi_j, \psi_k) = 0$  for  $j \neq k$ .

The previous basis  $\{\phi_i\}$  of the cover  $C$  can be orthonormalized with respect to the inner-product by the Gram-Schmidt process as follows.

$$\begin{aligned} \psi_1 &= \phi_1 / \|\phi_1\| \\ \psi_2 &= [\phi_2 - (\phi_2, \psi_1) \psi_1] / \|\phi_2 - (\phi_2, \psi_1) \psi_1\| \\ \dots &= \dots \\ \dots &= \dots \\ \dots &= \dots \\ \psi_m &= [\phi_m - (\phi_m, \psi_1) \psi_1 - \dots - (\phi_m, \psi_{m-1}) \psi_{m-1}] \\ &\quad / \|\phi_m - (\phi_m, \psi_1) \psi_1 - \dots - (\phi_m, \psi_{m-1}) \psi_{m-1}\| \end{aligned} \quad (24)$$

From the above algorithm, the  $\{\psi_i; i = 1, 2, \dots, m\}$ , orthonormal with respect to weight function on the cover  $C$ , forms another basis of the  $L^2(C)$  Hilbert space (see Theodore 1993). If  $\psi_i$  is a polynomial of degree  $s$ , then the set is fully specified and unique. The first  $m$  of these polynomials form a subspace of this Hilbert space which is isomorphic with the

$R^m$  euclidean space. The elements of the basis vectors of this basis are defined for  $C$  due to the convenient properties that

$$(\psi_j, \psi_k) = \delta_{jk} \quad (25)$$

The weight function is made using the Gaussian distribution. Let  $p$  denote a positive real number. The weight function  $W(x, x_I)$  defined by

$$W(x, x_I) = \exp\left(-\left(\frac{\|x - x_I\|}{c}\right)^p\right) \quad \text{for } x \text{ within cover } C \quad (26)$$

This is useful, as correct choice of  $W(x, x_I)$  can effect a particular favorable distribution of the  $x_I$ .

## 7. INTEGRAL AND DIFFERENTIAL TYPE OF APPROXIMATION

The section is devoted to the discussion of several methods of numerical approximation that are based on manifold method discussed in the previous section. Many important engineering problems fall into the category of being operators, with supporting boundary conditions.

### • Generalized Fourier Series

In the first type of integral form an inner-product and norm is used to approximate such engineering problems by developing a generalized Fourier series. The resulting approximation is the approximation in that a least-squares ( $L_2$ ) error is minimized simultaneously for fitting both the problem's boundary conditions and satisfying the operator relationship (the governing equations) over the basic cover. Because the numerical technique involves a well-defined inner product, error evaluation is readily available using Bessells inequality. Minimization of the approximation error is subsequently achieved with respect to a weighting of the inner product components, and the addition of basis functions used in the approximation.

The general setting for solving a linear operator equation with boundary values by means of an inner product is as follows: Let  $C$  be a cover in  $R^m$  with boundary  $\Gamma$  and denote the closure of  $C$  by  $cl(C)$ ,  $dC$ . Consider the real Hilbert space  $L_2(cl(C))$ , which has inner product  $(f, g) = \int_C fgdC$ .

Then an inner product is given by

$$(f, g) = \int_K fgdC + \int_\Gamma fgd\Gamma \quad (27)$$

Choose a set of  $m$  linearly independent functions  $f_j$ , and  $S_m$  be the  $m$ -dimensional space spanned by the elements of  $f_j$ . Here, the elements of  $f_j$  will be assumed to be functions of dependent variables.

The generalized Fourier series approach can now be used to obtain the approximation  $\psi_j \in S_m$  of the function  $\psi_j$  using the defined innerproduct and corresponding norm.



The next step in developing generalized Fourier series is to construct a new set of functions which are the orthonormal representation of the  $f_j$ .

- Weak form

The calculus of variations provides an alternate method to the integral type of approximation.

Now consider the operator equation  $L$ :

$$Lu = f \text{ in } K \quad (28)$$

If  $u_0 \in C$ , where  $C$  is a basic cover, is such that

$$(Lu_0 - f, \phi_I) = 0 \text{ for every } I = 1, 2, \dots, \quad (29)$$

then we have  $Lu_0 - f = 0$  in  $H$ , that is,  $u_0$  is the solution of Eq.(28) in  $H$ . In other words, finding the solution of Eq. (28) is equivalent to finding the solution of Eq. (29). This equivalence forms the basis of the Galerkin method.

Consider the operator Eq. (28) and let the cover  $C$  be such that it contains all linear combinations of the form

$$u_h = \sum_I^n \phi_I u_I \text{ for every } I = 1, 2, \dots, n \quad (30)$$

where  $u_h$  is any irregular set of discretization points,  $n$  is number of discrete points within the cover and  $u_I$  are constants to be determined using Eq. (29):

$$(Lu_h - f, \phi_I) = 0, \quad I=1,2,\dots,n \quad (31)$$

This gives  $n$  equations for the  $n$  unknown constants.

If the operator  $L$  is linear, then Eq. (31) becomes

$$\sum_I^n (L\phi_I, \phi_K) u_I = (f, \phi_K), \quad K=1,2,\dots,n \quad (32)$$

Further, if  $L$  is symmetric, Eq. (31) becomes

$$\sum_I^n (\phi_I, L\phi_K) u_I = (f, \phi_K), \quad K=1,2,\dots,n \quad (33)$$

which is the same as the system obtained in the Ritz procedure.

It should be noted that the Galerkin method is applicable to a much larger class of operator equations than the positive-definite linear operator equations, which can be solved by the Ritz method. In the Galerkin method, the most general form of which is

given by Eq. (31), the operator  $L$  is not restricted to being positive definite, symmetric, or even linear. Due to this general nature of the Galerkin procedure, the questions of solvability, existence, and uniqueness of solutions, as one might suspect, are more difficult, in general.

Use of the weak form relaxes the continuity requirement of the coordinate functions, the essential boundary conditions of the coordinate functions is not imposed. On the other hand, the manifold method seeks solutions from the basic cover.

- Discrete Representation of Differential Operators

The solution of differential equations can be obtained based on the representation of the derivative operator in a discrete coordinate basis. This representation requires a suitable transformation from the representation of a function in a polynomial basis set, as discussed. It can be shown that when Gaussian quadrature rules based on these irregular points within a cover are used to evaluate the integrals appearing in Galerkin formulations of certain differential equations, then the resulting equations are equivalent to those determined by collocating the same points.

The linear differential equation is collocated in each cover. When the collocation equations resulting from the boundary conditions, continuity conditions, and differential equation are added together, they yield a linear equations, which is equal to the number of unknown expansion coefficients. Therefore, provided the coefficient matrix is nonsingular, this system of equations possesses an unique solution.

## 8. AN EXAMPLE FOR SOLVING ELASTIC PROBLEM ON A POLYGON

Let us consider tow-dimensional problem in a domain  $K$  with a known boundary  $\partial\Gamma$ .

$$\Delta \cdot \sigma + \mathbf{b} = 0 \quad \text{in } K \quad (34)$$

$$\sigma \cdot \mathbf{n} = \bar{\mathbf{t}} \quad \text{on } \Gamma_t \quad (35)$$

$$\mathbf{u} = \bar{\mathbf{u}} \quad \text{on } \Gamma_u \quad (36)$$

We assume that the domain has been covered by means of a set of finite covers and write the condition for equilibrium in the form of the virtual work equation:

$$\int_K \text{tr}(\sigma \cdot \text{def}(\delta \mathbf{v})) = \int_K \delta \mathbf{v} \cdot \mathbf{b} + \int_{\Gamma_t} \delta \mathbf{v} \cdot \bar{\mathbf{t}} + \int_{\Gamma_u} \delta \lambda \cdot (\mathbf{u} - \bar{\mathbf{u}}) + \int_{\Gamma_u} \delta \mathbf{v} \cdot \lambda \quad (37)$$

Clearly, the equivalence condition  $\lambda_I(\mathbf{x}_J) = \delta_{IJ}$  is not satisfied by all choices of basic functions. The interpolants  $\lambda_I$  are not only continuous but have continuous derivatives over the basic cover. In order to perform Gaussian quadrature the center of a cover will be located

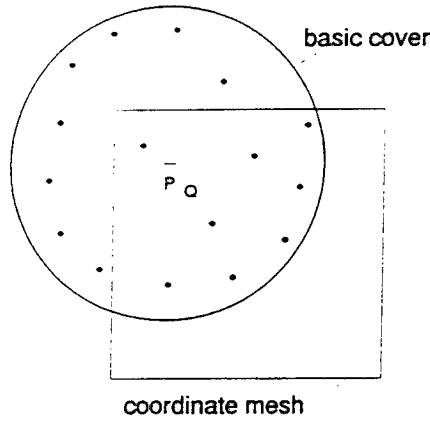


Figure 10: A cover for quadrature

at the quadrature points  $p_q$  (see Figure 10). Each point within the cover contributes nonzero entries to the integral equations.

We set up a system of linear algebraic equations for the approximate values  $u_I$  of the function  $u$  at the points  $p_I$ , by approximating the integral representations of the function  $u$  on covers by quadrature formulas. For a sufficiently large  $n$  this system is uniquely solvable.

An infinite plate with a central circular hole is subjected to a unidirectional tensile load in the  $y$  direction. One quadrant of a square plate, of side length  $2b$ , with a hole of radius  $a = 0.1b$  is divided into 121 regular patterns where Gaussian quadrature is performed. The distribution of 99 interpolants is shown in Fig (11). Use of small regular patterns around the edge of the hole facilitates the accurate modeling of circular shape of this boundary. The interpolants are polynomials which are fit to the nodal values by a least-squares approximation. The mesh is totally unnecessary in this method. The method used here requires only nodal data, no element connectivity is needed.

Plane strain condition is assumed with  $E = 1.0 \times 10^3$  and  $\mu = 0.3$ . The closed solution for the stress is

$$\sigma_{rr} = 1/2(1 - \frac{a^2}{r^2})(1 - (1 - \frac{3a^2}{r^2})\cos 2\theta) \quad (38)$$

$$\sigma_{\theta\theta} = 1/2(1 + \frac{a^2}{r^2} + (1 + \frac{3a^4}{r^4})\cos 2\theta) \quad (39)$$

$$\sigma_{r\theta} = 1/2(1 - \frac{a^2}{r^2})(1 + \frac{3a^4}{r^4})\sin 2\theta \quad (40)$$

Along the plane of symmetry  $\theta = 0$ , we have the tensile stress

$$\sigma_{\theta\theta} = 1/2(2 + \frac{a^2}{r^2} + \frac{3a^4}{r^4}) \quad (41)$$

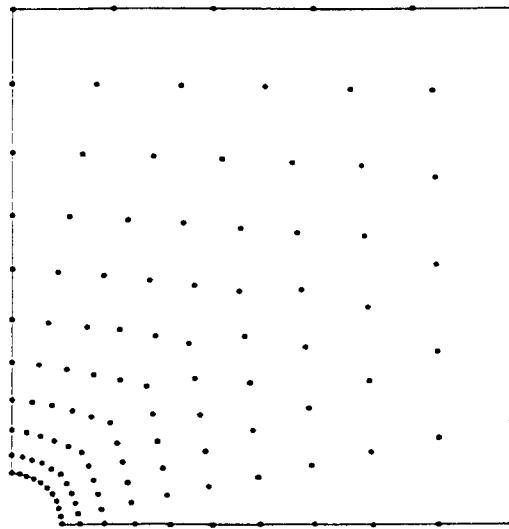


Figure 11: One quadrant of plate with a circular hole

An even better resolution of the stress concentration factor can be achieved by increasing the number of interpolants. As the width of the plate is reduced, so the exact solution for the stresses will deviate increasingly from the infinite plate solution. The larger the ratio  $a/b$ , the greater will be the effect of the finite boundaries on the stress concentration.

An evaluation of the modeling error can be made by comparing the calculated values and the exact values. The  $L^2$  displacement error norm and energy error norm can be defined as:

$$\left\{ \int_K (u_{app} - u_{exact})^T (u_{app} - u_{exact}) dK \right\}^{1/2} \quad (42)$$

$$\left\{ \int_K (\epsilon_{app} - \epsilon_{exact})^T D(\epsilon_{app} - \epsilon_{exact}) dK \right\}^{1/2} \quad (43)$$

Convergence rate in  $L^2$  norm of error in displacement for the plane strain case is less than  $10^{-5}$  and the convergence rate in energy norm is less than  $10^{-2}$ .

## 9. DISCUSSION

After constructing the required covering of an arbitrary polygon  $K$  by covers, the approximate solution of a boundary-value problem, found by means of the manifold method. No preliminary information is required concerning the connectivity of interpolants being covered. The approximate solutions may be obtained on the covers in the form of integration and differentiation.

The paper presents possibly the new and useful manifold method concepts that may serve the computer modelers in their attempt to bridge the gap between continuum analysis and discontinuum analysis.

#### ACKNOWLEDGEMENT

The author thanks Dr. Genhua Shi of WES, Department of the Army for helpful discussion. Funding was provided by Rock Mechanics Institute, University of Oklahoma and Education Department of the People's Republic of China.

#### REFERENCES

- Bishop, R. L. and Goldberg, S. (1980). "Tensor analysis on manifolds." Dover Publications, Inc.
- Arnold, V.I. (1982). "Mathematical methods of classical mechanics." Springer-Verlag.
- Nayroles, B. Touzot and Villon, P. (1992). "Generalizing the finite element method: Diffuse approximation and diffuse elements." Computational Mechanics, vol. 10, 307-318.
- Theodore V. Hromadka II. (1993). "The Best Approximation Method in Computational Mechanics." Springer-Verlag.

# Manifold Method with Four-node Isoparametric Finite Element Mesh

Kuokai Shyu

M. Reza Salami

Department of Civil Engineering,  
North Carolina Agricultural and Technical State University,  
Greensboro, NC 27411, U.S.A.

## Abstract

This paper presents a numerical model that incorporates four-node isoparametric finite element mesh to Gen-hua Shi's newly-developed two dimensional manifold method. Manifold method is a numerical method that pieces together finite element method and discontinuous deformation analysis. For manifold method, mathematical mesh (or finite covers) and physical mesh are independent. The mathematical mesh consists of overlapping covers, which are the interpolation points of the material volume. For each cover, a local displacement function is defined. These local displacement functions are connecting together to define a global displacement function for the entire material domain. On the other hand, the physical mesh which consists of boundaries of material volumes, joints, and blocks, defines the integration domain. Under the definition of finite covers, both finite element method and discontinuous deformation analysis are special cases of manifold method. The triangular element of finite element method is used to define finite covers of mathematical mesh in Shi's original work, and here, four-node isoparametric element is implemented to define the finite covers. The simulation of the large displacement and vibration characteristics of an automobile's leaf spring-dashpot suspension system is the numerical example.

## Introduction

For material analyses, the finite element method (FEM) is the widely-used numerical tool. However, conventional FEM was only limited to model continuum. Based on the phenomenon of complicated boundaries and discontinuous interfaces in real world, people tried to develop contact finite elements by using different kinds of contact constraint formulations (Simo *et al.*, 1985; Carpenter *et al.*, 1991; Huněk, 1993; Heegaard and Curnier, 1993). But the difficulty still exists because we need a complete block kinematics to describe motions and contact behaviors of a multi-body block system. Recently, Shi (1988) introduced

discontinuous deformation analysis (DDA), which included a complete block kinematics to obtain large displacement and deformation solutions for discontinuous multi-body system. The subsequent developments of DDA can be found in Shyu (1993); Ke (1993); Chang (1994).

Both FEM and DDA have very solid theoretical backgrounds, and each stands on the extreme case of modeling. From the numerical computation's point of view, conventional FEM is completely a continuous model while DDA is totally a discontinuous one. It is truly possible that there could be a method (model) which could link up both FEM and DDA. This means that there could be a method which could analyze a material volume from continuous state, through fracturing state, and to totally-damaged state. After all, Shi (1991) proposed another new method—manifold method, which could compute large displacement, deformation solutions, moving boundaries, flexible boundaries and free surfaces problems.

The basic meshes of manifold method are finite covers. Manifold method defines an independent local displacement function on each cover. These local displacement functions on finite covers are connected together through weighting functions to form a global displacement function for the entire material domain, i.e., these covers overlap each other and cover the entire material domain. Using finite cover system, manifold method totally separates the mathematical mesh and the physical mesh.

The mathematical mesh consists of overlapping covers, which are the interpolation points of the material volume. The mathematical mesh is chosen by the users, the fine or rough approximation of the mesh depends on engineering needs. For each cover, a local displacement function is defined. Conventional grids, finite element meshes or converged regions of series, can be defined as regions overlapped by finite covers in the mathematical mesh. On the other hand, the physical mesh which consists of real boundaries of material volumes, joints, and blocks, only defines the integration domain. The entire material system is formed by both the mathematical and physical meshes.

All the Regions of overlapped covers sharing a common finite cover form a cover space. If this cover space is completely cut through by physical mesh (joints, block boundaries), then this common finite cover is cut to two or more separately independent finite covers. Based on the finite cover concepts, manifold method is more flexible and general to include analytical method, FEM, DDA in a unified form, and to compute large displacements, deformations, moving boundaries and free surfaces of both continuous and discontinuous materials.

## Manifold Method with Finite Element Mesh

As mentioned above, the finite element mesh can be used as the mathematical mesh for manifold method. Under the definition of finite covers, the node of an element is just like a cover of manifold method and the element of FEM is just like a region overlapped by the covers of manifold method. Since a polynomial series can be defined on a cover, the nodal displacements of a node in finite element mesh are just zero order cover (constants) in manifold method. Therefore, after applying finite element mesh as the finite covers to the mathematical mesh of manifold method, the manifold method can perform the computations of FEM for continuous materials. And when the physical mesh is applied, the joint or discontinuous behaviors in the continuous domain can be computed as well.

For manifold method, the integration domains always have general shapes because the joints or physical boundaries are always complicated. Therefore, the computations of integration for manifold method are more difficult than those for FEM. However, the analytical solutions of integration have been found for many cases of manifold method (Shi, 1994). Based on finite cover system, manifold method computes the integrations of simple functions on complex domains (through the defined displacement function for each cover, and the defined weighting function for the overlapped region), while FEM computes the integrations of complex functions on simple domains (through isoparametric transformation to natural coordinates).

In Shi's original work of manifold method, the triangular finite element mesh is used as the mathematical mesh for manifold method. The number of elements for mathematical mesh depends on the accuracy needs of a specific problem. For each triangular element, there are three nodes, i.e., for each triangular region, there are three covers connected by a weighting function (shape function) to describe the displacement function of a triangular region. For each cover, the local displacement function is zero order constants (nodal displacements). And for each triangular region, the global displacement function is exactly a complete first order polynomial (displacement function for a triangular element in FEM).

Because the displacement function for a triangular region is precisely defined, joints of the physical mesh could randomly cut or cut through a cover space formed by triangular regions sharing the common finite cover. This makes possible the material region to be of any shape, because the material regions formed by the physical mesh only defines the integration domain. The displacement function for a material region is still exactly defined within the triangular region overlapped by three finite covers, even if these finite covers



are out of the boundaries of the material region. This means that the exact solutions of an integration for an irregularly-shaped material region can be obtained. If a joint does not cut through a cover space, then the cover space remains continuous for that common finite cover. On the other hand, if a joint completely cut through a cover space, then the cover space is discontinuous, and two separately independent cover spaces are generated.

As for the DDA case, the mathematical mesh of a large triangular region overlapped by three finite covers contains all the blocks inside the region. Each block completely cuts the three finite covers to include an individual three-cover mathematical mesh of its own. Each individual mathematical mesh does not overlap each other. The three-cover mathematical mesh defines an individual complete first order polynomial displacement function for each block. Then, DDA transforms the three-cover mathematical mesh to one-cover mathematical mesh, which defines the same displacement function for each block, namely

$$\begin{Bmatrix} u \\ v \end{Bmatrix} = \begin{bmatrix} 1 & 0 \\ 0 & 1 \\ -(y - y_0) & (x - x_0) \\ (x - x_0) & 0 \\ 0 & (y - y_0) \\ (y - y_0)/2 & (x - x_0)/2 \end{bmatrix}^T \begin{Bmatrix} u_0 \\ v_0 \\ r_0 \\ \epsilon_x \\ \epsilon_y \\ \gamma_{xy} \end{Bmatrix},$$

where  $(x_0, y_0)$  is the center of gravity of the block.

It is clear that the single mathematical cover is located at the center of gravity of the block and the weighting function is shown in the square brackets. The single mathematical cover contains six constants— $u_0, v_0, r_0, \epsilon_x, \epsilon_y, \gamma_{xy}$ .  $u_0, v_0, r_0$  are the rigid body translations and rotation of the center of gravity, and  $\epsilon_x, \epsilon_y, \gamma_{xy}$  are the normal and shear strains of the block.

Therefore, DDA is the totally discontinuous case of manifold method, and the mathematical mesh and the physical mesh of DDA are the same where all covers do not overlap.

In this way, when continuous mathematical mesh and discontinuous physical mesh are applied, joints in the material volume can open, slide; blocks can move according to the block kinematics, and the continuous area of the material volume remains continuous.

## Four-node Isoparametric Finite Element Mesh

In this paper, a four-node isoparametric finite element mesh is used as the mathematical mesh for manifold method. Each four-node element is corresponding to a quadrilateral

region overlapped by four finite covers. The nodal displacements of a node of four-node element are the zero order local displacement function terms defined for one finite cover of the quadrilateral region in manifold method. Since the overlapped region is quadrilateral, the weighting function for the quadrilateral region (or four-node element) can not be exactly defined, i.e., the global displacement function for a quadrilateral region can not be exactly described. For this reason, when using four-node isoparametric finite element mesh as the mathematical mesh for manifold method, the joints and block boundaries of physical mesh can only cut along the element boundaries, because it is difficult to obtain the global displacement function for an irregularly-shaped material region within the quadrilateral region.

When analyzing a material system, the simultaneous equilibrium equations are derived by minimizing total potential energy of the system. These equations have the form:  $[K]\{D\} = \{F\}$ , where  $[K]$  is the global coefficient matrix, and  $\{D\}$ ,  $\{F\}$  are the unknown and loading vectors.

The displacement field  $[u \ v]^T$  of a four-node element  $i$  (or quadrilateral region overlapped by four finite covers, see Figure 1) can be described as

$$\begin{Bmatrix} u \\ v \end{Bmatrix} = [\tilde{N}_i(x, y)]\{d_i\},$$

where

$$[\tilde{N}_i(x, y)] = \begin{bmatrix} \tilde{N}_1 & 0 & \tilde{N}_2 & 0 & \tilde{N}_3 & 0 & \tilde{N}_4 & 0 \\ 0 & \tilde{N}_1 & 0 & \tilde{N}_2 & 0 & \tilde{N}_3 & 0 & \tilde{N}_4 \end{bmatrix}$$

are the shape functions, and

$$\{d_i\} = [u_1 \ v_1 \ u_2 \ v_2 \ u_3 \ v_3 \ u_4 \ v_4]^T$$

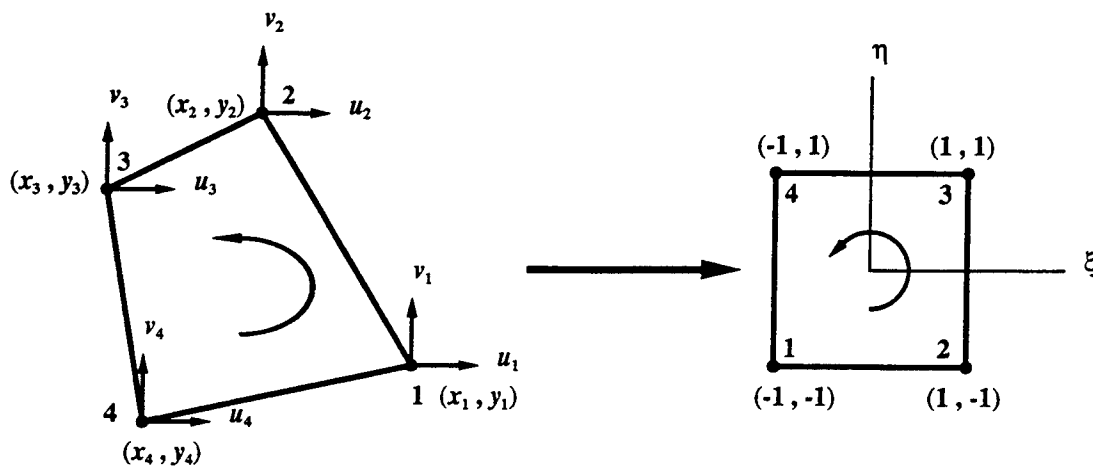


Figure 1. Four-node isoparametric element

are the nodal displacements. However,  $[\tilde{N}_i(x, y)]$  are difficult to define for general four-node elements. By isoparametric transformation, the shape functions  $[N_i]$  are defined in natural coordinates system  $(\xi, \eta)$ . The shape functions  $[N_i(\xi, \eta)]$  for the square element

$$N_k(\xi, \eta) = \frac{1}{4}(1 + \xi_k \xi)(1 + \eta_k \eta), \quad k = 1, 2, 3, 4$$

where  $(\xi_k, \eta_k)$  is the coordinates of the node of square element in natural coordinates. And

$$x = \sum_{k=1}^4 N_k(\xi, \eta) x_k; \quad y = \sum_{k=1}^4 N_k(\xi, \eta) y_k,$$

where  $(x_k, y_k)$  is the coordinates of the node of general four-node element.

### Elastic stiffness submatrix

For element  $i$ , strain field  $\{\epsilon_i\} = [B_i]\{d_i\}$  and stress field  $\{\sigma_i\} = [E_i][B_i]\{d_i\}$ , where

$$[B_i] = \begin{bmatrix} \frac{\partial \tilde{N}_1}{\partial x} & 0 & \frac{\partial \tilde{N}_2}{\partial x} & 0 & \frac{\partial \tilde{N}_3}{\partial x} & 0 & \frac{\partial \tilde{N}_4}{\partial x} & 0 \\ 0 & \frac{\partial \tilde{N}_1}{\partial y} & 0 & \frac{\partial \tilde{N}_2}{\partial y} & 0 & \frac{\partial \tilde{N}_3}{\partial y} & 0 & \frac{\partial \tilde{N}_4}{\partial y} \\ \frac{\partial \tilde{N}_1}{\partial y} & \frac{\partial \tilde{N}_1}{\partial x} & \frac{\partial \tilde{N}_2}{\partial y} & \frac{\partial \tilde{N}_2}{\partial x} & \frac{\partial \tilde{N}_3}{\partial y} & \frac{\partial \tilde{N}_3}{\partial x} & \frac{\partial \tilde{N}_4}{\partial y} & \frac{\partial \tilde{N}_4}{\partial x} \end{bmatrix},$$

and

$$[E_i] = \frac{E}{1 - \nu^2} \begin{bmatrix} 1 & \nu & 0 \\ \nu & 1 & 0 \\ 0 & 0 & \frac{1 - \nu}{2} \end{bmatrix}$$

for plane stress.  $E, \nu$  are Young's modulus and Poisson's ratio. For plane strain,  $E, \nu$  are replaced by  $E/(1 - \nu^2)$  and  $\nu/(1 - \nu)$ .

The derivatives

$$\left\{ \begin{array}{c} \frac{\partial \tilde{N}_k}{\partial x} \\ \frac{\partial \tilde{N}_k}{\partial y} \end{array} \right\} = [J_i]^{-1} \left\{ \begin{array}{c} \frac{\partial N_k}{\partial \xi} \\ \frac{\partial N_k}{\partial \eta} \end{array} \right\}, \quad k = 1, 2, 3, 4$$

where

$$[J_i] = \begin{bmatrix} \frac{\partial x}{\partial \xi} & \frac{\partial y}{\partial \xi} \\ \frac{\partial x}{\partial \eta} & \frac{\partial y}{\partial \eta} \end{bmatrix}$$

is the Jacobian matrix.

Then for element  $i$ , the local stiffness submatrix

$$t \left( \sum_{m=1}^2 \sum_{n=1}^2 [B_i(\xi_m, \eta_n)]^T [E_i] [B_i(\xi_m, \eta_n)] [J_i] W_m W_n \right) \quad (1)$$

is added to  $[K]$ .  $(\xi_m, \eta_n) = (\pm 1/\sqrt{3}, \pm 1/\sqrt{3})$ ,  $m, n = 1, 2$  are the Gauss integration points, and  $W_m, W_n = 1.0$  are the integration weights of Gaussian quadrature.  $t$  is the element thickness and  $||J_i||$  is the determinant of Jacobian matrix.

### Inertia submatrix

It is assumed that constant acceleration is over current time step and the initial element nodal displacements are zero (begins with updated configurations). Let  $M_i$  be the unit mass,  $\Delta$  be the time interval of current step, and  $\{v_i^0\}$  be the initial nodal velocities of element  $i$ . Then the local stiffness submatrix (consistent mass matrix)

$$\frac{2M_i}{\Delta^2} t \left( \iint_R [\tilde{N}_i(x, y)]^T [\tilde{N}_i(x, y)] dx dy \right) \quad (2)$$

is added to  $[K]$ , and

$$\frac{2M_i}{\Delta} t \left( \iint_R [\tilde{N}_i(x, y)]^T [\tilde{N}_i(x, y)] dx dy \right) \{v_i^0\} \quad (3)$$

is added to  $\{F\}$ . The analytical solutions of the integrations can be exactly evaluated (see [6]). For next time step, the initial nodal velocities will be the final velocities  $\{v_i\}$  at the end of current time step

$$\{v_i\} = \frac{2}{\Delta} \{d_i\} - \{v_i^0\}. \quad (4)$$

### Normal contact submatrix

When a close contact is detected between two blocks, the no-penetration requirement has to be fulfilled. All the contact conditions can be finally converted into the case of an angle  $P_5$  penetrating a contact edge  $\overline{P_6P_7}$  (see Figure 2). A spring (penalty) with stiffness  $p^n$  is introduced between the angle and the contact edge along normal direction of the

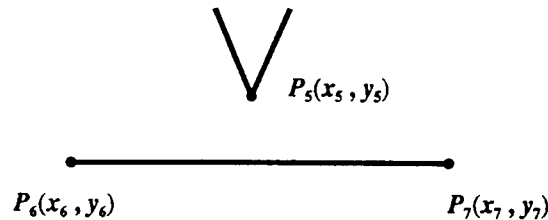


Figure 2. Normal contact of angle to edge

edge.  $P_5(x_5, y_5)$  is on element  $i$  and  $P_6(x_6, y_6), P_7(x_7, y_7)$  are on element  $j$ .  $P_5, P_6$  and  $P_7$  are assigned counterclockwise.  $(x_5, y_5), (x_6, y_6), (x_7, y_7)$  are mapped to  $(\xi_5, \eta_5), (\xi_6, \eta_6)$  and  $(\xi_7, \eta_7)$ . As spring is added, the distance from  $P_5$  to  $\overline{P_6P_7}$  should be zero after the displacement increments are applied (the second order terms are discarded as infinitesimals).

Denote

$$a^0 = \begin{vmatrix} 1 & x_5 & y_5 \\ 1 & x_6 & y_6 \\ 1 & x_7 & y_7 \end{vmatrix}$$

and

$$\begin{aligned} \{\mathbf{m}_i^n\}^T &= \frac{1}{L} \begin{Bmatrix} y_6 - y_7 \\ x_7 - x_6 \end{Bmatrix}^T [\mathbf{N}_i(\xi_5, \eta_5)]; \\ \{\mathbf{n}_j^n\}^T &= \frac{1}{L} \begin{Bmatrix} y_7 - y_5 \\ x_5 - x_7 \end{Bmatrix}^T [\mathbf{N}_j(\xi_6, \eta_6)] + \frac{1}{L} \begin{Bmatrix} y_5 - y_6 \\ x_6 - x_5 \end{Bmatrix}^T [\mathbf{N}_j(\xi_7, \eta_7)], \end{aligned}$$

where  $L = \sqrt{(x_7 - x_6)^2 + (y_7 - y_6)^2}$  is the length of the contact edge. Then the local stiffness submatrices

$$p^n \{\mathbf{m}_i^n\} \{\mathbf{m}_i^n\}^T \quad (5)$$

$$p^n \{\mathbf{m}_i^n\} \{\mathbf{n}_j^n\}^T \quad (6)$$

$$p^n \{\mathbf{n}_j^n\} \{\mathbf{m}_i^n\}^T \quad (7)$$

$$p^n \{\mathbf{n}_j^n\} \{\mathbf{n}_j^n\}^T \quad (8)$$

are added to  $[\mathbf{K}]$ , and the local force submatrices

$$-p^n \left( \frac{a^0}{L} \right) \{\mathbf{m}_i^n\} \quad (9)$$

$$-p^n \left( \frac{a^0}{L} \right) \{\mathbf{n}_j^n\} \quad (10)$$

are added to  $\{\mathbf{F}\}$ .

## Numerical Simulation

Before the simulation begins, the block system configuration is prepared by a pre-processor. Two kinds of meshes are input: the physical mesh and the mathematical mesh (see Figures 3 and 4). These two meshes will form a discontinuous block system and a continuous element system respectively. Due to the discontinuity of block boundary, the nodes along block boundaries are further separately numbered. Then the blocks and the elements

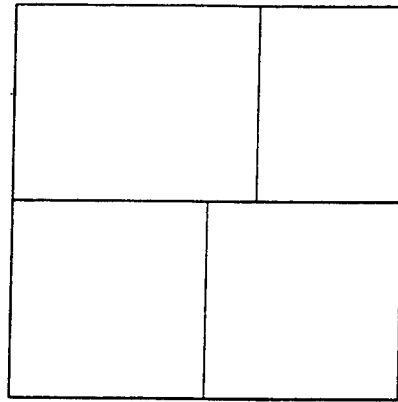


Figure 3. The physical mesh

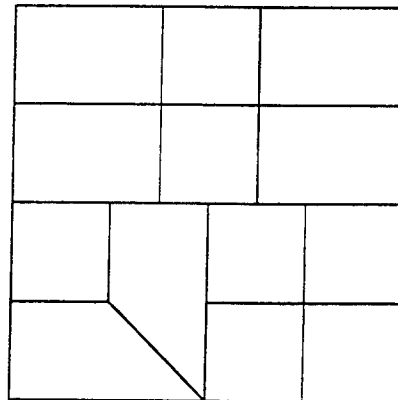


Figure 4. The mathematical mesh

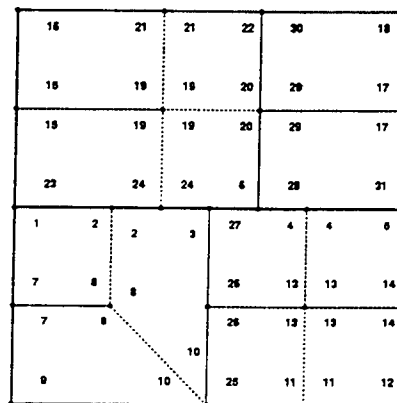


Figure 5. Block system with element meshes

are mapped together to produce a complete discontinuous block system with continuous element meshes inside (see Figure 5). Therefore, the block containing continuous element mesh can have a flexible boundary. The computer programs were written in ANSI C language and the computations were all performed on the Silicon Graphics workstation. Numerical simulation is performed to show the improvement and flexibility achieved when finite element mesh is associated with block kinematics to handle discontinuous contact problems under large displacements and deformations.

### Leaf spring-dashpot suspension system

The analysis of leaf spring is a laminated beam problem. It has the characteristics of large displacements and deformations, as well as complicated contact geometry and sliding conditions at discontinuous interfaces. The feature of flexible boundaries of the block is suitable for modeling large displacements and deformations of the leaf spring system.

The physical mesh and the mathematical mesh (see Figures 6 and 7) are input, and the block system is shown in Figure 8. Four oblique beams are piled up to form a leaf spring system. The top beam is 1.4 m long, beam depth is 0.8 cm. On top of the leaf spring is a large mass body with depth of 7 cm. The top beam is connected with the large mass body and is fixed at one end, shackled at the other end (bolt with stiffness  $EA = 200$  MN). Two bolts (stiffness  $EA = 60$  MN) connect the top and third beams to simulate the hoop clamps often seen in automobile's leaf spring system. Some other bolts (stiffness  $EA = 60, 200$  MN) are connected for the purpose of deforming the leaf spring system. The leaf spring is forced 10.5 cm downward at the center within 1.5 s to deform to a shape of an arc since most of the leaf spring systems are arc-shaped. The input data are the following:

plane strain, static condition,  
time steps: 2000,  
spring stiffness: 1000000 MN/m,  
time interval: 0.001 s,  
maximum displacement ratio: 0.002,  
friction angle:  $20^\circ$ ,  
element thickness: 0.1 m,  
unit mass:  $0.00785 \text{ Mkg/m}^3$ ,  
gravity:  $9.81 \text{ m/s}^2$ ,  
Young's modulus, Poisson's ratio: 200000 MPa, 0.28.



Figure 6. Physical mesh of the leaf spring

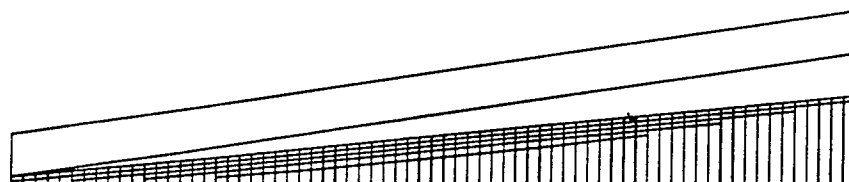


Figure 7. Mathematical mesh of the leaf spring



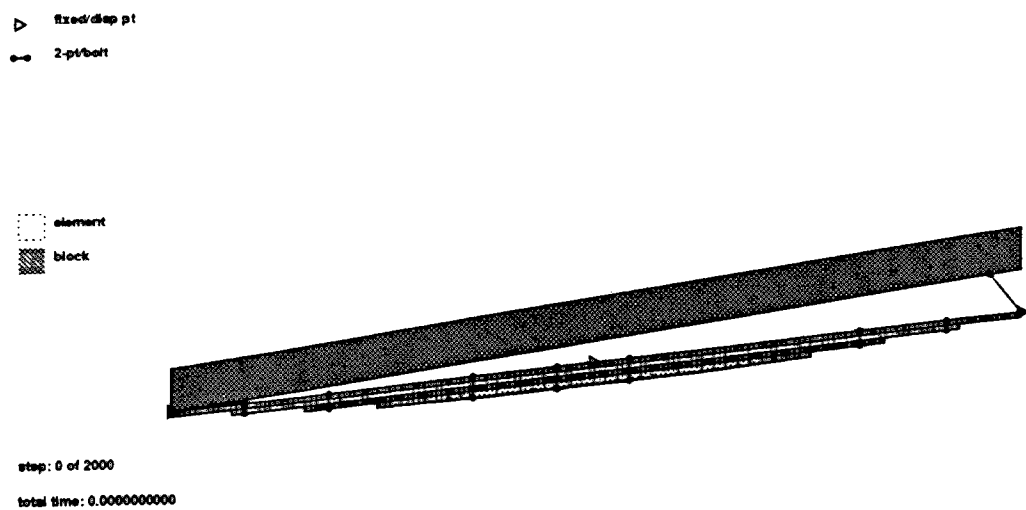


Figure 8. Block system with element meshes of the leaf spring

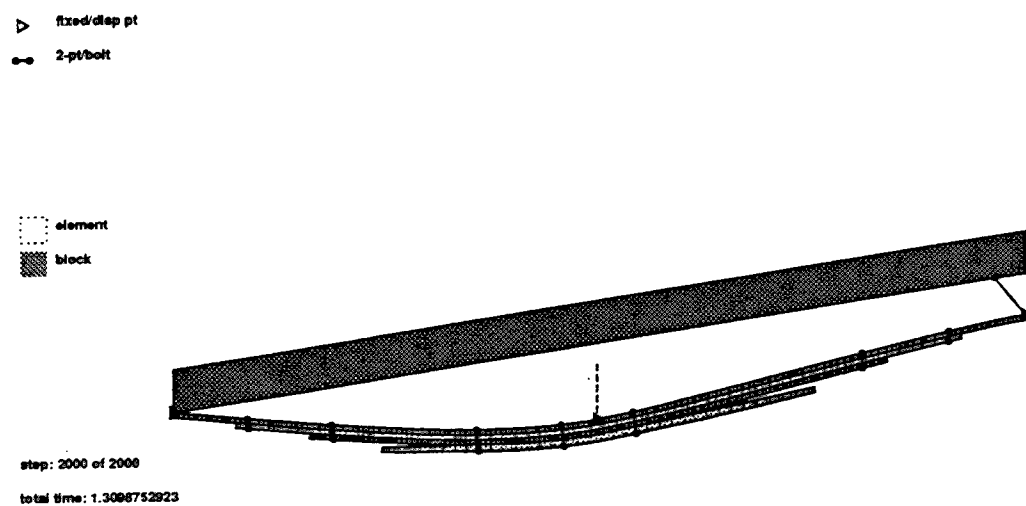


Figure 9. Deformed shape of the leaf spring

The solution of large displacement is the accumulations of the small displacement in each time step. Figure 9 shows the result at the end of calculation. This simulation demonstrates features of the numerical model which is capable of enhancing the deformation ability and refining the stress field of a block for discontinuous computation.

Suppose that the arc-shaped leaf spring will be mounted on a wheel to test the vibration behaviors of suspension system. The block system configuration from previous calculation is used and the stresses in beams as well as bolt forces are reset to zero. The orientations of the hoop clamps are corrected to be nearly perpendicular to the top beam. Six fixed points (or displacement-control points) are assigned near the center region to simulate the mounting of leaf spring to a wheel. A dashpot is connected between the large mass body and the bottom beam.

The following computations are intended to simulate the vibration response of an automobile under road excitation. The leaf spring carries two types of mass body: one is light mass (unit mass of  $0.00785 \text{ Mkg/m}^3$ ), the other is car mass (unit mass of  $0.05495 \text{ Mkg/m}^3$ ). The spring system is set to the equilibrium position under static loading of gravity force (see Figures 10 and 11).

The information of system stiffness of the leaf spring is required for dynamic computations. The loadings of  $\pm 0.02 \text{ MN}$ ,  $\pm 0.07 \text{ MN}$  are separately applied on top of the light and car masses to obtain system stiffness. Using static calculations, the loadings are applied within  $1.0 \text{ s}$  and time interval is  $1 \times 10^{-3} \text{ s}$ . Figures 12 and 13 show the load-displacement curves of static calculations for light and car masses. Therefore, the system stiffness is taken approximately as  $0.407 \text{ MN/m}$  for light mass case ( $1.815 \text{ MN/m}$  for car mass) for the following dynamic vibration computations.

A road excitation record is applied at the positions of mounting area. Dynamic calculations is required for vibration simulation. The damping coefficient is defined by  $\mu = 2\zeta\sqrt{mk}$ , where  $\zeta$  is damping ratio,  $m$  is total carrying mass, and  $k$  is system stiffness. Then the damping coefficient of dashpot is given by  $\mu \approx 0.0112\zeta$  for light mass case ( $\mu \approx 0.0625\zeta$  for car mass).

The response of the mass is recorded at the center on top of the mass body. The time step is  $7500$  and the time interval is  $4 \times 10^{-5} \text{ s}$ . For light mass case, a damping ratio of zero is used for dashpot to record the response of free vibrations. Figure 14 shows the response of free vibrations of the light mass.

▽ fixed pt  
 ● 2-pt/bolt  
 □ dashpot

□ element  
 ■ block

step: 400 of 400  
 total time: 3.9830000000

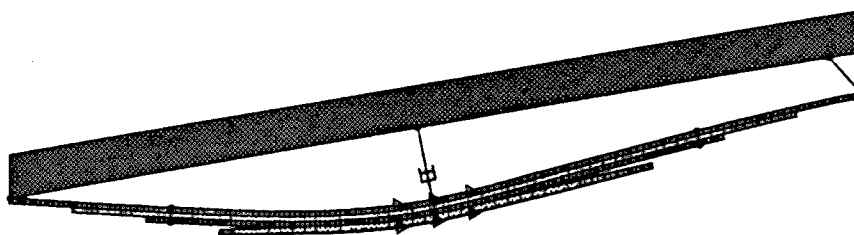


Figure 10. Equilibrium position of leaf spring, light mass

▽ fixed pt  
 ● 2-pt/bolt  
 □ dashpot

□ element  
 ■ block

step: 400 of 400  
 total time: 3.8838000000

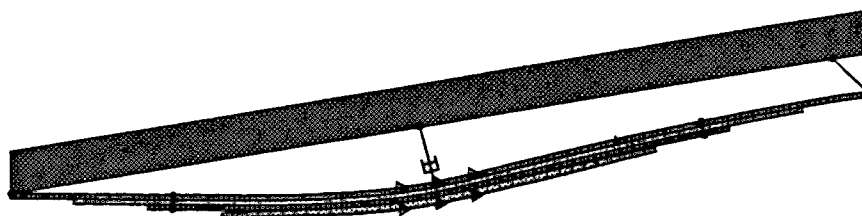


Figure 11. Equilibrium position of leaf spring, car mass

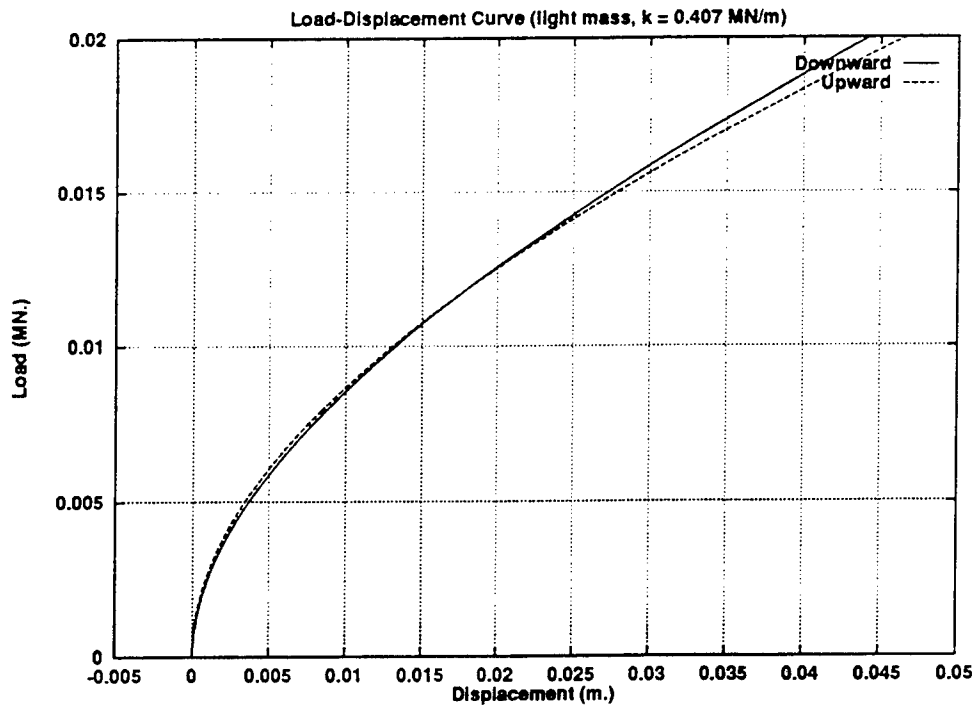


Figure 12. Load-displacement curves, static calculations

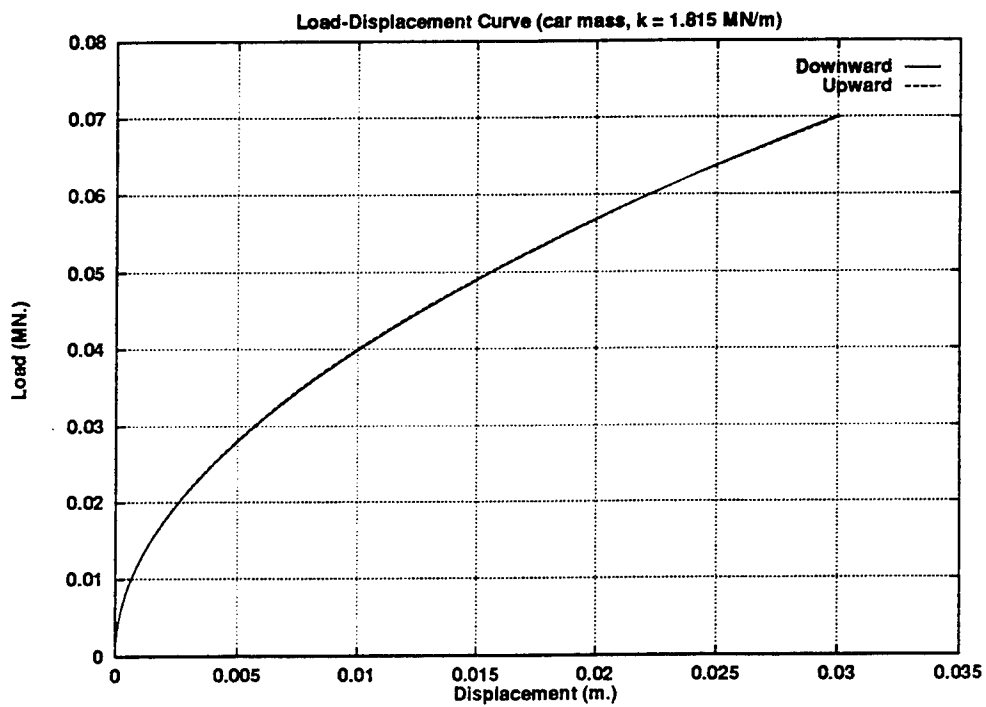


Figure 13. Load-displacement curves, static calculations

As another simulation, the car mass is carried to simulate the real automobile's leaf spring-dashpot suspension system. For the consideration of comfortable ride for commercial automobiles, damping coefficient for the dashpot is normally set close to critical damping (damping ratio of 1.0). A damping coefficient of 0.05625 MNs/m (damping ratio of 0.9) is assigned for the computation. Figure 15 shows the response of the car mass. The result gives the right response that there is no oscillation in the free vibration region.

## Conclusions

For manifold method, mathematical mesh (or finite covers) and physical mesh are independent. The mathematical mesh consists of overlapping covers, which are the interpolation points of the material volume; while the physical mesh which consists of boundaries of material volumes, joints, and blocks, defines the integration domain. For each cover, a local displacement function is defined. And for a specific region, covers overlap each other through a weighting function to define a global displacement function for that region. If the global displacement function can be precisely defined within a region, then the material region formed by the physical mesh can be of any shape and the joints can randomly cut or cut through the cover space because the manifold method computes the integrations of simple functions on complex domains.

When using finite element mesh as the mathematical mesh for manifold method, it is clear that manifold method is a numerical method that pieces together finite element method and discontinuous deformation analysis. Under the definition of finite covers, both finite element method and discontinuous deformation analysis are special cases of manifold method, and the nodal displacements are just the zero order terms of local displacement functions defined for finite covers.

When the triangular element mesh is used for mathematical mesh, the existence of "half element" is possible because the global displacement function for a triangular region is exactly the complete first order polynomial.

The four-node isoparametric finite element mesh is implemented as the mathematical mesh in this paper. However, the global displacement function of an element (or quadrilateral region in manifold method) can not be exactly defined, the joints of the physical mesh can only cut along the element boundaries.

In general, when using the concepts of finite covers, the manifold method is capable

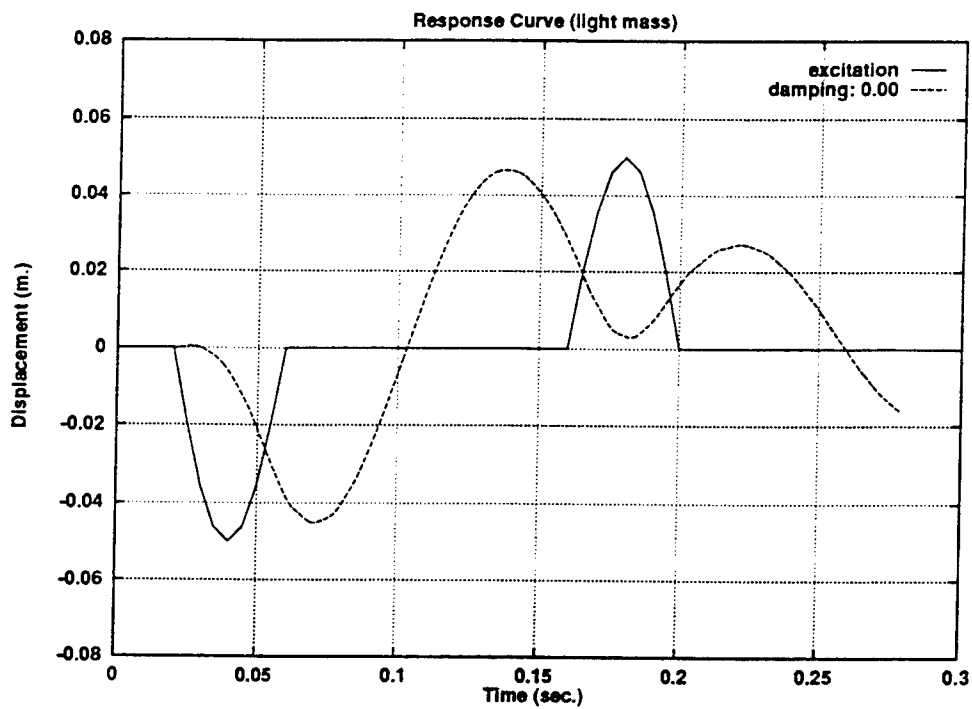


Figure 14. Response of the light mass

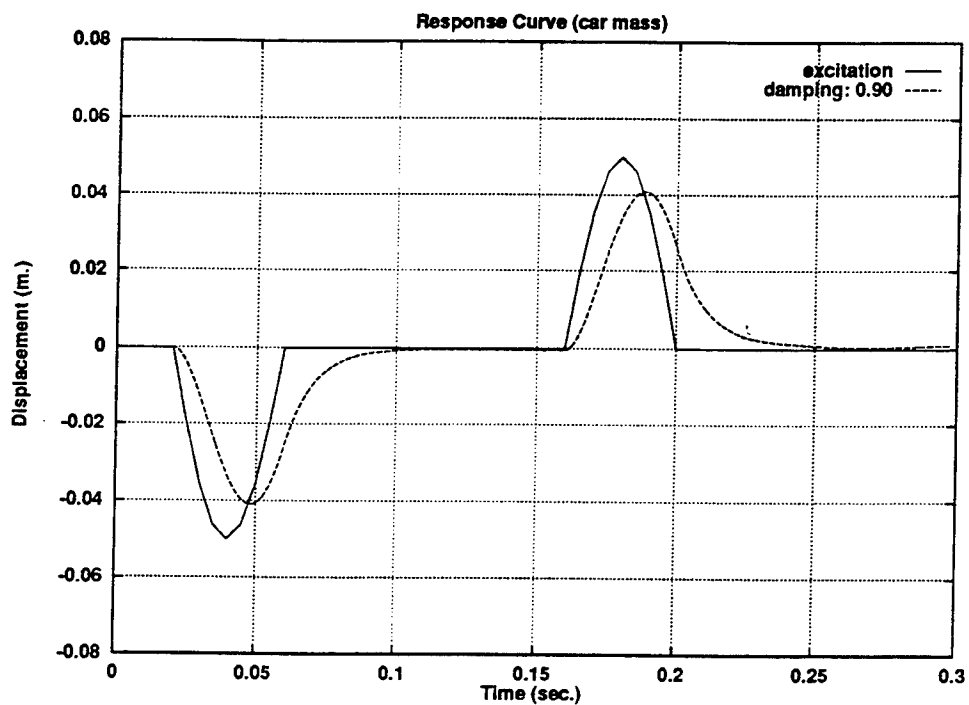


Figure 15. Response of the car mass

of computing material volume from continuous state, through fracturing state, to totally-damaged state. And it is able to analyze materials of free surfaces, flexible boundaries, moving boundaries, and even the case of different phases because the mathematical mesh can move with the physical mesh or can be fixed in space.

## Acknowledgement

The authors are grateful to Dr. Gen-hua Shi for the guidance in the development of the computer programs.

## References

- Carpenter, N. J. Taylor, R. L. and Katona, M. G. (1991), "Lagrange constraints for transient finite element surface contact", *Int. J. Numer. Meth. Engng.*, vol. 32, 103–128.
- Chang, C.-T. (1994), "Nonlinear dynamic discontinuous deformation analysis with finite element meshed block system", *Ph.D. Thesis*, Department of Civil Engineering, University of California at Berkeley.
- Heegaard, J.-H. and Curnier, A. (1993), "An augmented Lagrangian method for discrete large-slip contact problems", *Int. J. Numer. Meth. Engng.*, vol. 36, 569–593.
- Huněk, I. (1993), "On a penalty formulation for contact-impact problems", *Comput. Struct.*, vol. 48, 193–203.
- Ke, T. (1993), "Simulated testing of two dimensional heterogeneous and discontinuous rock masses using discontinuous deformation analysis", *Ph.D. Thesis*, Department of Civil Engineering, University of California at Berkeley.
- Shi, G. (1988), "Discontinuous deformation analysis—a new numerical model for the statics and dynamics of block systems", *Ph.D. Thesis*, Department of Civil Engineering, University of California at Berkeley.
- Shi, G. (1991), "Manifold method of material analysis", *Proc. 9th Army Conf. Appl. Math. Comp.*, June 18–21.
- Shi, G. (1994), "Modeling dynamic rock failure by discontinuous deformation analysis with simplex integrations", *Proc. 1st North Amer. Rock Mech. Symp (Austin, Texas)*, 591–598.
- Shyu, K. (1993), "Nodal-based discontinuous deformation analysis", *Ph.D. Thesis*, Department of Civil Engineering, University of California at Berkeley.
- Simo, J. C. Wriggers, P. and Taylor, R. L. (1985), "A perturbed Lagrangian formulation for the finite element solution of contact problems", *Comput. Meth. Appl. Mech. Engng.*, vol. 50, 163–180.

# Development of Second Order Displacement Function for DDA and Manifold Method

J.C. Chern, C.Y. Koo and S. Chen

Geotechnical Research Center  
Sinotech Engineering Consultants, Inc.  
Taipei, Taiwan

## Abstract

The developments of second order displacement function for DDA and manifold method were made by incorporating the complete second order terms to the first order displacement field. The formulations for the stiffness matrix and force matrix due to elastic stress, initial stress, point load, body force, inertia force, contact force and fixed point are presented. Several modifications to the first order DDA code to incorporate the second order displacement function and to improve the accuracy and efficiency of the calculation were implemented. The preliminary results from the validation tests show that with the improved deformation capability of the block, the second order DDA can better simulate the stress distribution and deformation of the block system and also release the restriction on block shape required for certain types of problem.

## 1. Introduction

Since the pioneering work on the analysis of discontinuous medium published by Gen-hua Shi in the late 1980's, discontinuous deformation analysis(DDA) and manifold method have become rapidly developing new numerical modeling techniques. These methods have rigorous scheme of block kinematics in dealing with the interactions between discrete blocks, and the equilibrium conditions are achieved by minimizing the total potential energy. Thus, they have found wide acceptance by researchers and engineers in analyzing various fields of problem.

In the present version of DDA method, it utilizes first order displacement function to describe the block movement and deformation. Therefore, constant stress or strain throughout the block is assumed and the capability of block deformation is limited. This may yield unreasonable results when the block deformation is large and geometry of the block is irregular. To overcome the limitations, two approaches have been attempted. They are:

- (1) adding artificial joints in the block (Ke, 1993); and
- (2) adding finite element meshes in the block (Shyu, 1993).

Manifold method which separates the mathematical mesh from the physical mesh can also improve the flexibility of deformation and achieve a better stress distribution throughout the block. High order displacement function is another approach to overcome



the limitations. Ideally, third order displacement function can have a better description of the block deformation. It also allows a second order stress and strain distribution for extreme value determination which is important in the analysis of stress concentration or fracturing of block. However, due to large computation capacity and CPU time required, this approach has not been attempted yet. At this stage, a second order displacement function was used as a practical compromise. This paper describes the formulation in DDA and manifold method using second order displacement function. Validation of second order DDA formulation and the coding are also presented.

## 2. Second Order Displacement Function for DDA Method

### 2.1 Displacement and deformation of block

The current version of DDA uses the first order displacement function to approximate the displacement field of the block. The displacement field is described as follows:

$$\begin{aligned} u &= a_1 + a_2x + a_3y \\ v &= b_1 + b_2x + b_3y \end{aligned} \quad (2-1)$$

The unknowns of the individual block can be represented by selecting the six displacement variables  $(u_0, v_0, r_0, \varepsilon_x, \varepsilon_y, r_{xy})$ , in which  $u_0, v_0$  are rigid body translation of a specific point  $(x_0, y_0)$  within the block;  $r_0$  is the rigid body rotation of the block with rotation center at  $(x_0, y_0)$ ;  $\varepsilon_x, \varepsilon_y$  and  $r_{xy}$  are the normal and shear strains of the block.

The second order displacement function used herein is extended from the first order function by adding the complete second order terms and is expressed as:

$$\begin{aligned} u &= a_1 + a_2x + a_3y + a_4x^2 + a_5xy + a_6y^2 \\ v &= b_1 + b_2x + b_3y + b_4x^2 + b_5xy + b_6y^2 \end{aligned} \quad (2-2)$$

The unknowns of the individual block can be represented by choosing the following twelve displacement variables,  $(u_0, v_0, r_0^c, \varepsilon_x^c, \varepsilon_y^c, r_{xy}^c, \varepsilon_{xx}, \varepsilon_{xy}, \varepsilon_{yx}, \varepsilon_{yy}, r_{xy,x}, r_{xy,y})$  in which  $u_0, v_0$  are rigid body translation of the block;  $r_0^c, \varepsilon_x^c, \varepsilon_y^c$  and  $r_{xy}^c$  are the constant terms of the rotation, normal and shear strains;  $\varepsilon_{xx}, \varepsilon_{xy}, \varepsilon_{yx}, \varepsilon_{yy}, r_{xy,x}, r_{xy,y}$  are the gradients of the normal and shear strains and they are expressed as follows:

$$\begin{aligned} u_0 &= a_1 + a_2x_0 + a_3y_0 + a_4x_0^2 + a_5x_0y_0 + a_6y_0^2 \\ v_0 &= b_1 + b_2x_0 + b_3y_0 + b_4x_0^2 + b_5x_0y_0 + b_6y_0^2 \\ r_0 &= \frac{1}{2} \left( \frac{\partial v}{\partial x} - \frac{\partial u}{\partial y} \right) = \frac{1}{2} [(b_2 - a_3) + (2b_4 - a_5)x_0 + (b_5 - 2a_6)y_0] \end{aligned} \quad (2-3)$$

The constant part of  $r_0$  is :

$$r_0^c = \frac{1}{2} (b_2 - a_3) \quad (2-4)$$

The normal and shear strains are:

$$\varepsilon_x = \frac{\partial u}{\partial x} = a_2 + 2a_4x + a_5y$$

$$\begin{aligned}\varepsilon_y &= \frac{\partial v}{\partial y} = b_3 + b_5 x + 2b_6 y \\ r_{xy} &= \frac{\partial v}{\partial x} + \frac{\partial u}{\partial y} = (b_2 + a_3) + (2b_4 + a_5)x + (2a_6 + b_5)y \quad (2-5)\end{aligned}$$

The constant terms of normal and shear strains are:

$$\varepsilon_x^c = a_2, \varepsilon_y^c = b_3, r_{xy}^c = b_2 + a_3 \quad (2-6)$$

The strain gradients  $\varepsilon_{x,x}, \varepsilon_{x,y}, \varepsilon_{y,x}, \varepsilon_{y,y}, r_{xy,x}, r_{xy,y}$  are defined as:

$$\begin{aligned}\varepsilon_{x,x} &= \frac{\partial \varepsilon_x}{\partial x} = 2a_4, \varepsilon_{x,y} = \frac{\partial \varepsilon_x}{\partial y} = a_5, \varepsilon_{y,x} = \frac{\partial \varepsilon_y}{\partial x} = b_5 \\ \varepsilon_{y,y} &= \frac{\partial \varepsilon_y}{\partial y} = 2b_6, r_{xy,x} = \frac{\partial r_{xy}}{\partial x} = 2b_4 + a_5, r_{xy,y} = \frac{\partial r_{xy}}{\partial y} = b_5 + 2a_6 \quad (2-7)\end{aligned}$$

Using equations (2-3), (2-4), (2-6) and (2-7), the coefficients of the displacement function can be solved and are equal to:

$$\begin{aligned}a_2 &= \varepsilon_x^c, a_3 = \frac{1}{2}(r_{xy}^c - 2r_0^c), a_4 = \frac{1}{2}\varepsilon_{x,x}, a_5 = \varepsilon_{x,y}, a_6 = \frac{1}{2}(r_{xy,y} - \varepsilon_{y,x}) \\ b_2 &= \frac{1}{2}(r_{xy}^c + 2r_0^c), b_3 = \varepsilon_y^c, b_4 = \frac{1}{2}(r_{xy,x} - \varepsilon_{x,y}), b_5 = \varepsilon_{y,x}, b_6 = \frac{1}{2}\varepsilon_{y,y} \quad (2-8)\end{aligned}$$

The displacement functions can be expressed as:

$$\begin{aligned}u &= u_0 - (y - y_0)r_0^c + (x - x_0)\varepsilon_x^c + \frac{1}{2}(y - y_0)r_{xy}^c + \frac{1}{2}(x^2 - x_0^2)\varepsilon_{x,x} + (xy - x_0y_0)\varepsilon_{x,y} \\ &\quad - \frac{1}{2}(y^2 - y_0^2)\varepsilon_{y,x} + \frac{1}{2}(y^2 - y_0^2)r_{xy,y} \\ v &= v_0 + (x - x_0)r_0^c + (y - y_0)\varepsilon_y^c + \frac{1}{2}(x - x_0)r_{xy}^c - \frac{1}{2}(x^2 - x_0^2)\varepsilon_{x,y} + (xy - x_0y_0)\varepsilon_{y,x} \\ &\quad + \frac{1}{2}(y^2 - y_0^2)\varepsilon_{y,y} + \frac{1}{2}(x^2 - x_0^2)r_{xy,x}\end{aligned}$$

And the displacement functions can be written in matrix form as:

$$\begin{bmatrix} u \\ v \end{bmatrix}_{2 \times 1} = [T]_{2 \times 12} [D]_{12 \times 1} \quad (2-9)$$

in which  $[T]$  may be expressed as  $[T_1 \ T_2 \ T_3]$  and

$$\begin{aligned}T_1 &= \begin{bmatrix} 1 & 0 & -(y - y_0) & (x - x_0) & 0 & \frac{1}{2}(y - y_0) \\ 0 & 1 & (x - x_0) & 0 & (y - y_0) & \frac{1}{2}(x - x_0) \end{bmatrix} \\ T_2 &= \begin{bmatrix} \frac{1}{2}(x^2 - x_0^2) & (xy - x_0y_0) & -\frac{1}{2}(y^2 - y_0^2) \\ 0 & -\frac{1}{2}(x^2 - x_0^2) & (xy - x_0y_0) \end{bmatrix} \\ T_3 &= \begin{bmatrix} 0 & 0 & \frac{1}{2}(y^2 - y_0^2) \\ \frac{1}{2}(y^2 - y_0^2) & \frac{1}{2}(x^2 - x_0^2) & 0 \end{bmatrix}\end{aligned}$$

and the displacement variable matrix  $[D]^T$  is :

$$[u_o, v_o, r_o^c, \epsilon_x^c, \epsilon_y^c, r_{xy}^c, \epsilon_{x,x}, \epsilon_{x,y}, \epsilon_{y,x}, \epsilon_{y,y}, r_{xy,x}, r_{xy,y}]$$

## 2.2 Elastic stiffness matrix

For linear elastic material, the elastic strain energy  $\Pi_e$  produced by the stresses in the block is:

$$\begin{aligned}\Pi_e &= \iint \frac{1}{2} (\sigma_x \epsilon_x + \sigma_y \epsilon_y + \tau_{xy} r_{xy}) dx dy \\ &= \iint \frac{1}{2} [\epsilon][\sigma] dx dy\end{aligned}\quad (2-10)$$

For plane stress condition, the stress-strain relationship is given by:

$$\begin{bmatrix} \sigma_x \\ \sigma_y \\ \tau_{xy} \end{bmatrix} = \frac{E}{1-\nu^2} \begin{bmatrix} 1 & \nu & 0 \\ \nu & 1 & 0 \\ 0 & 0 & \frac{1-\nu}{2} \end{bmatrix} \begin{bmatrix} \epsilon_x \\ \epsilon_y \\ r_{xy} \end{bmatrix} = [E_i] \begin{bmatrix} \epsilon_x \\ \epsilon_y \\ r_{xy} \end{bmatrix}\quad (2-11)$$

where E and  $\nu$  are Young's modulus and Poisson's ratio. The strains can be approximated by

$$\begin{aligned}\epsilon_x &= \epsilon_x^c + \epsilon_{x,x}x + \epsilon_{x,y}y \\ \epsilon_y &= \epsilon_y^c + \epsilon_{y,x}x + \epsilon_{y,y}y \\ r_{xy} &= r_{xy}^c + r_{xy,x}x + r_{xy,y}y\end{aligned}\quad (2-12)$$

and can be written in matrix form as follows:

$$[\epsilon_x \quad \epsilon_y \quad r_{xy}] = [D]^T \begin{bmatrix} 0 & 0 & 0 \\ 0 & 0 & 0 \\ 0 & 0 & 0 \\ 1 & 0 & 0 \\ 0 & 1 & 0 \\ 0 & 0 & 1 \\ x & 0 & 0 \\ y & 0 & 0 \\ 0 & x & 0 \\ 0 & y & 0 \\ 0 & 0 & x \\ 0 & 0 & y \end{bmatrix} = [D]^T [N]^T$$

Therefore, the elastic strain energy of the i-th block can be written in matrix form as:

$$\Pi_e = \frac{1}{2} \iint [D_i]^T [N_i]^T [E_i] [N_i] [D_i] dx dy \quad (2-13)$$

By minimizing the strain energy, it leads to the stiffness matrix:

$$K_{rs} = \frac{\partial^2 \Pi_e}{\partial d_{ri} \partial d_{sj}} = \iint [N_i]^T [E_i] [N_i] dx dy \quad (2-14)$$

where the integration  $\iint [N_i]_{12 \times 3}^T [E_i]_{3 \times 3} [N_i]_{3 \times 12} dx dy$  can be expressed in the following form:

$$\frac{E}{1-\nu^2} \begin{bmatrix} 0 & 0 & 0 & 0 & 0 & 0 & 0 & 0 & 0 & 0 & 0 & 0 \\ 0 & 0 & 0 & 0 & 0 & 0 & 0 & 0 & 0 & 0 & 0 & 0 \\ 0 & 0 & 0 & 0 & 0 & 0 & 0 & 0 & 0 & 0 & 0 & 0 \\ S & S\nu & 0 & S_x & S_y & S_{xx}\nu & S_{xy}\nu & 0 & 0 & 0 & 0 \\ S & 0 & 0 & S_x\nu & S_y\nu & S_{xx} & S_{xy} & 0 & 0 & 0 & 0 \\ \frac{(1-\nu)}{2}S & 0 & 0 & 0 & 0 & 0 & 0 & S_x \frac{(1-\nu)}{2} & S_y \frac{(1-\nu)}{2} & 0 & 0 \\ S_{xx} & S_{xy} & S_{xx}\nu & S_{xy}\nu & 0 & 0 & 0 & 0 & 0 & 0 & 0 \\ S_{yy} & S_{xy}\nu & S_{yy}\nu & 0 & 0 & 0 & 0 & 0 & 0 & 0 & 0 \\ S_{xx} & S_{xy} & 0 & 0 & 0 & 0 & 0 & 0 & 0 & 0 & 0 \\ S_{yy} & 0 & 0 & 0 & 0 & 0 & 0 & 0 & 0 & 0 & 0 \\ \text{Symmetric} & & & & & & & S_{xx} \frac{(1-\nu)}{2} & S_{xy} \frac{(1-\nu)}{2} & S_{xy} \frac{(1-\nu)}{2} & S_{yy} \frac{(1-\nu)}{2} \end{bmatrix}$$

in which  $S$ ,  $S_x$ ,  $S_y$ ,  $S_{xx}$ ,  $S_{xy}$  and  $S_{yy}$  are the two dimensional Simplex integrations as defined by Shi(1989).

### 2.3 Initial stress matrix

For the i-th block, the potential energy of the initial stresses  $(\sigma_x^0, \sigma_y^0, \tau_{xy}^0)$  is:

$$\begin{aligned} \Pi_{\sigma^0} &= -\iint (\epsilon_x \sigma_x^0 + \epsilon_y \sigma_y^0 + r_{xy} \tau_{xy}^0) dx dy = -\iint [\epsilon]^T [\sigma^0] dx dy \\ &= -\iint [D_i]^T [N_i]^T [E_i] \begin{bmatrix} \epsilon_x^0 \\ \epsilon_y^0 \\ r_{xy}^0 \end{bmatrix} dx dy \end{aligned} \quad (2-15)$$

in which

$$\begin{aligned} \epsilon_x^0 &= \epsilon_x^{c0} + \epsilon_{x,x}^0 x + \epsilon_{x,y}^0 y \\ \epsilon_y^0 &= \epsilon_y^{c0} + \epsilon_{y,x}^0 x + \epsilon_{y,y}^0 y \\ r_{xy}^0 &= r_{xy}^{c0} + r_{xy,x}^0 x + r_{xy,y}^0 y \end{aligned}$$

Therefore,

$$\Pi_{\sigma^0} = -\iint [D_i]^T [N_i]^T [E_i] [N_i] [D_i^0] dx dy \quad (2-16)$$

By minimizing the potential energy, it leads to the force matrix of the initial stress of the i-th block as follows:

$$\begin{aligned} f_r &= -\frac{\partial \Pi_{\sigma^0}}{\partial d_{ri}} = \iint [N_i]^T [E_i] [N_i] dx dy \cdot [D_i^0] \\ &= [NN_i]_{12 \times 12} \cdot [D_i^0]_{12 \times 1}, \quad r = 1, \dots, 12 \end{aligned} \quad (2-17)$$

where

$$[NN_i] = \iint [N_i]_{12 \times 3}^T [E_i]_{3 \times 3} [N_i]_{3 \times 12} dx dy$$

and

$$[D_i^0]_{1 \times 12}^T = [u_0^0 \quad v_0^0 \quad r_0^0 \quad \epsilon_x^0 \quad \epsilon_y^0 \quad r_{xy}^0 \quad \epsilon_{x,x}^0 \quad \epsilon_{x,y}^0 \quad \epsilon_{y,x}^0 \quad \epsilon_{y,y}^0 \quad r_{xy,x}^0 \quad r_{xy,y}^0]$$

## 2.4 Point load force matrix

The potential energy of the i-th block due to point loads  $(F_x, F_y)$  is:

$$\begin{aligned} \Pi_p &= -(F_x u + F_y v) = -[u \quad v] \begin{bmatrix} F_x \\ F_y \end{bmatrix} \\ &= -[D_i]^T [T_i]^T \begin{bmatrix} F_x \\ F_y \end{bmatrix} \end{aligned} \quad (2-18)$$

By minimizing the potential energy, the force matrix due to point load is obtained as:

$$f_r = \frac{\partial \Pi_p}{\partial d_{ri}} = [T_i]^T \begin{bmatrix} F_x \\ F_y \end{bmatrix}, \quad r = 1, \dots, 12 \quad (2-19)$$

## 2.5 Body force matrix

Assuming that  $(f_x, f_y)$  is the constant body force of the i-th block, the potential energy due to the body force is:

$$\begin{aligned} \Pi_B &= -\iint (f_x u + f_y v) dx dy \\ &= -\iint [u \quad v] \begin{bmatrix} f_x \\ f_y \end{bmatrix} dx dy = -[D_i]^T \iint [T_i]^T dx dy \begin{bmatrix} f_x \\ f_y \end{bmatrix} \end{aligned} \quad (2-20)$$

The integration can be written as:

$$\iint [T_i]^T dx dy = \begin{bmatrix} S & 0 \\ 0 & S \\ 0 & 0 \\ 0 & 0 \\ 0 & 0 \\ 0 & 0 \\ \frac{1}{2} \left( S_{xx} - \frac{S_x^2}{S} \right) & 0 \\ S_{xy} - \frac{S_x S_y}{S} & -\frac{1}{2} \left( S_{xx} - \frac{S_x^2}{S} \right) \\ -\frac{1}{2} \left( S_{yy} - \frac{S_y^2}{S} \right) & \left( S_{xy} - \frac{S_x S_y}{S} \right) \\ 0 & \frac{1}{2} \left( S_{yy} - \frac{S_y^2}{S} \right) \\ 0 & \frac{1}{2} \left( S_{xx} - \frac{S_x^2}{S} \right) \\ \frac{1}{2} \left( S_{yy} - \frac{S_y^2}{S} \right) & 0 \end{bmatrix}$$

where  $S$ ,  $S_x$ ,  $S_y$ ,  $S_{xx}$ ,  $S_{xy}$  and  $S_{yy}$  are the Simplex integrations.

By minimizing the potential energy, the body force matrix is

$$f_r = \frac{\partial \Pi_B}{\partial d_{ri}} = - \iint [T_i]^T dx dy \begin{bmatrix} f_x \\ f_y \end{bmatrix}, \quad r = 1, \dots, 12$$

which will be added into the global force matrix.

## 2.6 Inertia force matrix

The potential energy for the  $i$ -th block due to inertia forces  $(F_x, F_y)$  of unit area is:

$$\Pi_i = - \iint [u \quad v] \begin{bmatrix} F_x \\ F_y \end{bmatrix} dx dy \quad (2-21)$$

The initial forces per unit area are

$$\begin{bmatrix} F_x \\ F_y \end{bmatrix} = -M \begin{bmatrix} \frac{\partial^2 u(t)}{\partial t^2} \\ \frac{\partial^2 v(t)}{\partial t^2} \end{bmatrix} \quad (2-22)$$

according to Newton's Second Law of Motion.  $M$  is the mass per unit area. From equations (2-9) and (2-22), the potential energy can be expressed as:

$$\begin{aligned} \Pi_i &= \iint M [u \quad v] \begin{bmatrix} \frac{\partial^2 u(t)}{\partial t^2} \\ \frac{\partial^2 v(t)}{\partial t^2} \end{bmatrix} dx dy \\ &= \iint M [D_i]^T [T_i]^T [T_i] \frac{\partial^2 D_i(t)}{\partial t^2} dx dy \end{aligned} \quad (2-23)$$

Neglecting the higher order term of Taylor's series expansion,

$$\frac{\partial^2 D_i(t)}{\partial t^2} = \frac{2}{\Delta^2} [D_i] - \frac{2}{\Delta} \frac{\partial D_i(t)}{\partial t}$$

where  $\Delta$  is the time increment, therefore, the potential energy due to inertia force is

$$\Pi_i = [D_i]^T \iint [T_i]^T [T_i] dx dy \left( \frac{2M}{\Delta^2} [D_i] - \frac{2M}{\Delta} [V_0] \right)$$

Minimizing the potential energy, we obtained

$$K_{rs} = \frac{2M}{\Delta^2} \iint [T_i]_{12 \times 2}^T [T_i]_{2 \times 12} dx dy, \quad r, s = 1, \dots, 12 \quad (2-24)$$

which will be added into stiffness matrix, and another term

$$f_r = \frac{2M}{\Delta} \iint [T_i]_{12 \times 2}^T [T_i]_{2 \times 12} dx dy [V_0], \quad r = 1, \dots, 12 \quad (2-25)$$

will be added into the force matrix. The integration  $\iint [T_i]^T [T_i] dx dy$  is a  $12 \times 12$  matrix and is in the following form:

$$\begin{bmatrix}
S & 0 & 0 & 0 & 0 & 0 & \frac{1}{2}S_1 & S_3 & -\frac{1}{2}S_2 & 0 & 0 & \frac{1}{2}S_2 \\
S & 0 & 0 & 0 & 0 & 0 & 0 & -\frac{1}{2}S_1 & S_3 & \frac{1}{2}S_2 & \frac{1}{2}S_1 & 0 \\
S_1 + S_2 & -S_3 & S_3 & \frac{1}{2}S_1 - \frac{1}{2}S_2 & -\frac{1}{2}S_7 & -S_{12} - \frac{1}{2}S_8 & \frac{1}{2}S_9 + S_{11} & \frac{1}{2}S_{10} & \frac{1}{2}S_8 & -\frac{1}{2}S_9 & & \\
& S_1 & 0 & \frac{1}{2}S_3 & \frac{1}{2}S_8 & S_{11} & -\frac{1}{2}S_{10} & 0 & 0 & \frac{1}{2}S_{10} & & \\
& & S_2 & \frac{1}{2}S_3 & 0 & -\frac{1}{2}S_7 & S_{12} & \frac{1}{2}S_9 & \frac{1}{2}S_7 & 0 & & \\
& & & \frac{1}{4}S_1 + \frac{1}{4}S_2 & \frac{1}{4}S_7 & \frac{1}{2}S_{12} - \frac{1}{4}S_8 & -\frac{1}{4}S_9 + \frac{1}{2}S_{11} & \frac{1}{4}S_{10} & \frac{1}{4}S_8 & \frac{1}{4}S_9 & & \\
& & & & \frac{1}{4}S_{13} & \frac{1}{2}S_{16} & -\frac{1}{4}S_{15} & 0 & 0 & \frac{1}{4}S_{15} & & \\
& & & & & S_{18} + \frac{1}{4}S_{13} & -\frac{1}{2}S_{17} - \frac{1}{2}S_{16} & -\frac{1}{4}S_{15} & -\frac{1}{4}S_{13} & \frac{1}{2}S_{17} & & \\
& & & & & & \frac{1}{4}S_{14} + S_{18} & \frac{1}{2}S_{17} & \frac{1}{2}S_{16} & -\frac{1}{4}S_{14} & & \\
& & & & & & & \frac{1}{4}S_{14} & \frac{1}{4}S_{15} & 0 & & \\
& & & & & & & & \frac{1}{4}S_{13} & 0 & & \\
& & & & & & & & & \frac{1}{4}S_{14} & & \\
\end{bmatrix}$$

*Symmetric*

in which  $S, S_1, \dots, S_{18}$  are functions of Simplex integration. The high order Simplex integrations are as follows:

$$S_{xxx} = \iint x^3 dx dy = \sum_{i=1}^M \frac{1}{20} (x_i^3 + x_i^2 x_{i+1} + x_i x_{i+1}^2 + x_{i+1}^3) J_0$$

$$S_{yyy} = \iint y^3 dx dy = \sum_{i=1}^M \frac{1}{30} (y_i^3 + y_i^2 y_{i+1} + y_i y_{i+1}^2 + y_{i+1}^3) J_0$$

$$S_{xxxx} = \iint x^4 dx dy = \sum_{i=1}^M \frac{1}{30} (x_i^4 + x_i^3 x_{i+1} + x_i^2 x_{i+1}^2 + x_i x_{i+1}^3 + x_{i+1}^4) J_0$$

$$S_{yyyy} = \iint y^4 dx dy = \sum_{i=1}^M \frac{1}{30} (y_i^4 + y_i^3 y_{i+1} + y_i^2 y_{i+1}^2 + y_i y_{i+1}^3 + y_{i+1}^4) J_0$$

$$S_{xxy} = \iint x^2 y dx dy = \sum_{i=1}^M \frac{1}{60} (3x_i^2 y_i + 2x_i x_{i+1} y_i + x_{i+1}^2 y_i + x_i^2 y_{i+1} + 2x_i x_{i+1} y_{i+1} + 3x_{i+1}^2 y_{i+1}) J_0$$

$$S_{xyy} = \iint xy^2 dx dy = \sum_{i=1}^M \frac{1}{60} (3y_i^2 x_i + 2y_i y_{i+1} x_i + y_{i+1}^2 x_i + y_i^2 x_{i+1} + 2y_i y_{i+1} x_{i+1} + 3y_{i+1}^2 x_{i+1}) J_0$$

$$S_{xxxy} = \iint x^3 y dx dy = \sum_{i=1}^M \frac{1}{120} (4x_i^3 y_i + 3x_i^2 x_{i+1} y_i + 2x_i x_{i+1}^2 y_i + x_{i+1}^3 y_i + x_i^3 y_{i+1} + 2x_i^2 x_{i+1} y_{i+1} + 3x_i x_{i+1}^2 y_{i+1} + 4x_{i+1}^3 y_{i+1}) J_0$$

$$S_{xyyy} = \iint xy^3 dx dy = \sum_{i=1}^M \frac{1}{120} (4y_i^3 x_i + 3y_i^2 y_{i+1} x_i + 2y_i y_{i+1}^2 x_i + y_{i+1}^3 x_i + y_i^3 x_{i+1} + 2y_i^2 y_{i+1} x_{i+1} + 3y_i y_{i+1}^2 x_{i+1} + 4y_{i+1}^3 x_{i+1}) J_0$$

$$S_{xxyy} = \iint x^2 y^2 dx dy = \sum_{i=1}^M \frac{1}{180} (6x_i^2 y_i^2 + 3x_i^2 y_i y_{i+1} + x_i^2 y_{i+1}^2 + 3x_i x_{i+1} y_i^2 + 4x_i x_{i+1} y_i y_{i+1} + 3x_i x_{i+1} y_{i+1}^2 + x_{i+1}^2 y_i^2 + 3x_{i+1}^2 y_i y_{i+1} + 6x_{i+1}^2 y_{i+1}^2) J_0$$

## 2.7 Fixed point matrix

The constraint at the fixed point on the block boundary may be simulated by using two stiff springs acting on the fixed points. The potential energy due to the springs at the  $i$ -th block is equal to :

$$\begin{aligned}\Pi_f &= -\frac{1}{2} \begin{bmatrix} u & v \end{bmatrix} \begin{bmatrix} f_x \\ f_y \end{bmatrix} \\ &= -\frac{1}{2} \begin{bmatrix} u & v \end{bmatrix} \begin{bmatrix} -pu \\ -pv \end{bmatrix} \\ &= \frac{p}{2} [D_i]^T [T_i]^T [T_i] [D_i] \end{aligned} \quad (2-26)$$

where  $p$  is the spring constant at the fixed point. The stiffness matrix due to fixed point can be obtained as follows:

$$K_{rs} = \frac{\partial^2 \Pi_f}{\partial d_{ri} \partial d_{si}} = p [T_i]_{12 \times 2}^T [T_i]_{2 \times 12} \quad , \quad r, s = 1, \dots, 12 \quad (2-27)$$

## 2.8 Normal and shear contact matrices

The formulations for normal and shear contact matrices are exactly the same as those given by Shi(1989) with exception of using extended  $[T]$  and  $[D]$  matrices. The sub-matrices due to the interaction between blocks are mainly induced by the contact forces which are determined by the quantity of penetration, relative movement between blocks and stiffness of contact spring. They are :

$$p[e_i]_{12 \times 1} [e_i]_{1 \times 12}^T, p[e_i]_{12 \times 1} [g_j]_{1 \times 12}^T, p[g_j]_{12 \times 1} [e_i]_{1 \times 12}^T, p[g_j]_{12 \times 1} [g_j]_{1 \times 12}^T$$

which are added to the stiffness matrix  $[K_{ii}]$ ,  $[K_{ij}]$ ,  $[K_{ji}]$ ,  $[K_{jj}]$ ; and

$$-\frac{pS_0}{l} [e_i]_{12 \times 1}, -\frac{pS_0}{l} [g_j]_{12 \times 1}$$

are added to the force matrix  $[F_i]$ ;  $[F_j]$ .

In these sub-matrices,  $p$  is the stiffness of contact spring,  $l$  is the length of contact edge, and  $[e_i]$ ,  $[g_j]$  have the following forms:

$$\begin{aligned}[e_i]_{12 \times 1} &= \frac{1}{l} [T_i(x_1, y_1)]^T \begin{bmatrix} y_2 - y_3 \\ x_3 - x_2 \end{bmatrix} \\ [g_j]_{12 \times 1} &= [T_j(x_2, y_2)]^T \begin{bmatrix} y_3 - y_1 \\ x_1 - x_3 \end{bmatrix} + [T_j(x_3, y_3)]^T \begin{bmatrix} y_1 - y_2 \\ x_2 - x_1 \end{bmatrix} \end{aligned}$$

and



$$S_0 = \begin{bmatrix} 1 & x_1 & y_1 \\ 1 & x_2 & y_2 \\ 1 & x_3 & y_3 \end{bmatrix}$$

The stiffness matrices and force matrices at the individual block derived above are assembled into global stiffness and force matrix for the block system. Simultaneous equations were formed for solving the unknowns  $[D]$  for all blocks.

### 3. Development of Second Order Displacement Function for Manifold Method

#### 3.1 Second order displacement function

Complete second order displacement functions were used to approximate the movement and deformation of the manifold covered by the mathematical mesh.

$$\begin{aligned} u &= a_1 + a_2x + a_3y + a_4x^2 + a_5xy + a_6y^2 \\ v &= b_1 + b_2x + b_3y + b_4x^2 + b_5xy + b_6y^2 \end{aligned} \quad (3-1)$$

For six vertices element with nodal coordinates  $(x_i, y_i)$ ,  $i = 1, \dots, 6$ , the nodal displacements are:

$$\begin{bmatrix} u_1 \\ u_2 \\ u_3 \\ u_4 \\ u_5 \\ u_6 \end{bmatrix} = \begin{bmatrix} 1 & x_1 & y_1 & x_1^2 & x_1y_1 & y_1^2 \\ 1 & x_2 & y_2 & x_2^2 & x_2y_2 & y_2^2 \\ 1 & x_3 & y_3 & x_3^2 & x_3y_3 & y_3^2 \\ 1 & x_4 & y_4 & x_4^2 & x_4y_4 & y_4^2 \\ 1 & x_5 & y_5 & x_5^2 & x_5y_5 & y_5^2 \\ 1 & x_6 & y_6 & x_6^2 & x_6y_6 & y_6^2 \end{bmatrix} \begin{bmatrix} a_1 \\ a_2 \\ a_3 \\ a_4 \\ a_5 \\ a_6 \end{bmatrix} = [S]_{6 \times 6} [A_1]_{6 \times 1}$$

Similarly

$$\begin{bmatrix} v_1 \\ v_2 \\ v_3 \\ v_4 \\ v_5 \\ v_6 \end{bmatrix} = [S]_{6 \times 6} \begin{bmatrix} b_1 \\ b_2 \\ b_3 \\ b_4 \\ b_5 \\ b_6 \end{bmatrix} = [S]_{6 \times 6} [A_2]_{6 \times 1}$$

So the coefficients can be obtained as

$$[A_1] = [S]^{-1} \begin{bmatrix} u_1 \\ u_2 \\ u_3 \\ u_4 \\ u_5 \\ u_6 \end{bmatrix} \quad \text{and} \quad [A_2] = [S]^{-1} \begin{bmatrix} v_1 \\ v_2 \\ v_3 \\ v_4 \\ v_5 \\ v_6 \end{bmatrix} \quad (3-2)$$

Therefore, the displacements at any point within the mesh are

$$u = \begin{bmatrix} 1 & x & y & x^2 & xy & y^2 \end{bmatrix} [S]^{-1} \begin{bmatrix} u_1 \\ u_2 \\ u_3 \\ u_4 \\ u_5 \\ u_6 \end{bmatrix}; \quad v = \begin{bmatrix} 1 & x & y & x^2 & xy & y^2 \end{bmatrix} [S]^{-1} \begin{bmatrix} v_1 \\ v_2 \\ v_3 \\ v_4 \\ v_5 \\ v_6 \end{bmatrix} \quad (3-3)$$

Let

$$[f_1 \ f_2 \ f_3 \ f_4 \ f_5 \ f_6] = \begin{bmatrix} 1 & x & y & x^2 & xy & y^2 \end{bmatrix} [S]^{-1} \quad (3-3)$$

where

$$[S]^{-1} = \begin{bmatrix} 1 & x_1 & y_1 & x_1^2 & x_1 y_1 & y_1^2 \\ 1 & x_2 & y_2 & x_2^2 & x_2 y_2 & y_2^2 \\ 1 & x_3 & y_3 & x_3^2 & x_3 y_3 & y_3^2 \\ 1 & x_4 & y_4 & x_4^2 & x_4 y_4 & y_4^2 \\ 1 & x_5 & y_5 & x_5^2 & x_5 y_5 & y_5^2 \\ 1 & x_6 & y_6 & x_6^2 & x_6 y_6 & y_6^2 \end{bmatrix}^{-1} = \begin{bmatrix} f_{11} & f_{12} & \cdots & f_{15} & f_{16} \\ f_{21} & f_{22} & \cdots & f_{25} & f_{26} \\ \vdots & \vdots & \ddots & \vdots & \vdots \\ f_{51} & f_{52} & \cdots & f_{55} & f_{56} \\ f_{61} & f_{62} & \cdots & f_{65} & f_{66} \end{bmatrix} \quad (3-4)$$

Equation (3-3) can be rewritten into

$$[f_1 \ f_2 \ f_3 \ f_4 \ f_5 \ f_6] = \begin{bmatrix} f_{11} + f_{21}x + f_{31}y + f_{41}x^2 + f_{51}xy + f_{61}y^2 \\ f_{12} + f_{22}x + f_{32}y + f_{42}x^2 + f_{52}xy + f_{62}y^2 \\ f_{13} + f_{23}x + f_{33}y + f_{43}x^2 + f_{53}xy + f_{63}y^2 \\ f_{14} + f_{24}x + f_{34}y + f_{44}x^2 + f_{54}xy + f_{64}y^2 \\ f_{15} + f_{25}x + f_{35}y + f_{45}x^2 + f_{55}xy + f_{65}y^2 \\ f_{16} + f_{26}x + f_{36}y + f_{46}x^2 + f_{56}xy + f_{66}y^2 \end{bmatrix}^T \quad (3-5)$$

Therefore displacement field can be written in matrix form as:

$$\begin{bmatrix} u \\ v \end{bmatrix} = [T_e]_{2 \times 12} [D_e]_{12 \times 1} \quad (3-6)$$

where

$$[T] = \begin{bmatrix} f_1 & 0 & f_2 & 0 & f_3 & 0 & f_4 & 0 & f_5 & 0 & f_6 & 0 \\ 0 & f_1 & 0 & f_2 & 0 & f_3 & 0 & f_4 & 0 & f_5 & 0 & f_6 \end{bmatrix}$$

and

$$[D] = [u_1 \ v_1 \ u_2 \ v_2 \ u_3 \ v_3 \ u_4 \ v_4 \ u_5 \ v_5 \ u_6 \ v_6]^T$$

### 3.2 Elastic stiffness matrix

The strain energy in the element is:

$$\Pi_E = \iint \frac{1}{2} (\sigma_x \varepsilon_x + \sigma_y \varepsilon_y + \tau_{xy} \gamma_{xy}) dx dy \quad (3-7)$$

For linear elastic material, the stress-strain relationship in plane stress condition is given by the following equation.

$$\begin{bmatrix} \sigma_x \\ \sigma_y \\ \tau_{xy} \end{bmatrix} = \frac{E}{1-\nu^2} \begin{bmatrix} 1 & \nu & 0 \\ \nu & 1 & 0 \\ 0 & 0 & \frac{1-\nu}{2} \end{bmatrix} \begin{bmatrix} \epsilon_x \\ \epsilon_y \\ r_{xy} \end{bmatrix} = [E_e] \begin{bmatrix} \epsilon_x \\ \epsilon_y \\ r_{xy} \end{bmatrix} \quad (3-8)$$

From Eqn. (3-5) and definition of strains,

$$\begin{bmatrix} \epsilon_x \\ \epsilon_y \\ r_{xy} \end{bmatrix} = \begin{bmatrix} \frac{\partial u}{\partial x} \\ \frac{\partial v}{\partial y} \\ \frac{\partial u}{\partial y} + \frac{\partial v}{\partial x} \end{bmatrix} \quad (3-9)$$

$$\begin{aligned} &= \begin{bmatrix} \frac{\partial f_1}{\partial x} & 0 & \frac{\partial f_2}{\partial x} & 0 & \frac{\partial f_3}{\partial x} & 0 & \frac{\partial f_4}{\partial x} & 0 & \frac{\partial f_5}{\partial x} & 0 & \frac{\partial f_6}{\partial x} & 0 \\ 0 & \frac{\partial f_1}{\partial y} & 0 & \frac{\partial f_2}{\partial y} & 0 & \frac{\partial f_3}{\partial y} & 0 & \frac{\partial f_4}{\partial y} & 0 & \frac{\partial f_5}{\partial y} & 0 & \frac{\partial f_6}{\partial y} \\ \frac{\partial f_1}{\partial y} & \frac{\partial f_1}{\partial x} & \frac{\partial f_2}{\partial y} & \frac{\partial f_2}{\partial x} & \frac{\partial f_3}{\partial y} & \frac{\partial f_3}{\partial x} & \frac{\partial f_4}{\partial y} & \frac{\partial f_4}{\partial x} & \frac{\partial f_5}{\partial y} & \frac{\partial f_5}{\partial x} & \frac{\partial f_6}{\partial y} & \frac{\partial f_6}{\partial x} \end{bmatrix} [D_e] \\ &= [B_e]_{3 \times 12} [D_e]_{12 \times 1} \end{aligned} \quad (3-10)$$

where

$$\frac{\partial f_i}{\partial x} = f_{2i} + 2f_{4i}x + f_{5i}y ; \quad \frac{\partial f_i}{\partial y} = f_{3i} + f_{5i}x + 2f_{6i}y , \quad i = 1, \dots, 6$$

The strain energy of the element can be expressed as

$$\Pi_E = \frac{1}{2} \iint w(x, y) [D_e]_{1 \times 12}^T [B_e]_{12 \times 3}^T [E_e]_{3 \times 3} [B_e]_{3 \times 12} [D_e]_{12 \times 1} dx dy \quad (3-11)$$

in which  $w(x, y)$  is the weighting function to compute the integration over the common area between mathematical mesh and physical mesh. Minimizing the potential energy, the stiffness matrix of the element is

$$K_{rs} = \frac{\partial^2 \Pi_E}{\partial d_{re} \partial d_{se}} = \iint w(x, y) [B_e]_{12 \times 3}^T [E_e]_{3 \times 3} [B_e]_{3 \times 12} dx dy \quad r, s = 1, \dots, 12 \quad (3-12)$$

where the integration  $\iint w(x, y) [B_e]_{12 \times 3}^T [E_e]_{3 \times 3} [B_e]_{3 \times 12} dx dy$  is a  $12 \times 12$  matrix and it contains 144 complex integrations which may be carried out by using the integration program.

### 3.3 Initial stress matrix

For element  $e$ , the potential energy of the initial stresses  $(\sigma_x^0, \sigma_y^0, \tau_{xy}^0)$  is :

$$\Pi_{\sigma^0} = - \iint (\epsilon_x \sigma_x^0 + \epsilon_y \sigma_y^0 + r_{xy} \tau_{xy}^0) dx dy = - \iint [\epsilon]^T [\sigma^0] dx dy$$

$$= - \iint w(x, y) [D_e]^T [B_e]^T [E_e] \begin{bmatrix} \epsilon_x^0 \\ \epsilon_y^0 \\ r_{xy}^0 \end{bmatrix} dx dy \quad (3-13)$$

where

$$\begin{bmatrix} \epsilon_x^0 \\ \epsilon_y^0 \\ r_{xy}^0 \end{bmatrix} = [B_e]_{3 \times 12} [D_e^0]_{12 \times 1}$$

Therefore, the potential energy of initial stresses  $\Pi_{\sigma^0}$  can be expressed as

$$\Pi_{\sigma^0} = - \iint [D_e]^T [B_e]^T [E_e] [B_e] [D_e^0] dx dy \quad (3-14)$$

Minimizing the potential energy, it leads to the force matrix of the element.

$$f_r = - \frac{\partial \Pi_{\sigma^0}}{\partial d_{re}} = \iint w(x, y) [B_e]_{12 \times 3}^T [E_e]_{3 \times 3} [B_e]_{3 \times 12} dx dy \cdot [D_e^0] \quad (3-15)$$

### 3.4 Point load matrix

The potential energy of point loads  $(F_x, F_y)$  acting at coordinates  $(x, y)$  of element  $e$  is

$$\begin{aligned} \Pi_p &= -(F_x u + F_y v) \\ &= -[D_e]^T [T_e]^T \begin{bmatrix} F_x \\ F_y \end{bmatrix} \end{aligned} \quad (3-16)$$

Minimizing the potential energy, it yields the force matrix due to point loads

$$f_r = \frac{\partial \Pi_p}{\partial d_{re}} = [T_e]^T \begin{bmatrix} F_x \\ F_y \end{bmatrix}, \quad r = 1, \dots, 12 \quad (3-17)$$

### 3.5 Body force matrix

The potential energy due to body forces  $(f_x, f_y)$  of element  $e$  is:

$$\begin{aligned} \Pi_B &= - \iint (f_x u + f_y v) dx dy \\ &= -[D_e]^T \iint w(x, y) [T_e]^T dx dy \begin{bmatrix} f_x \\ f_y \end{bmatrix} \end{aligned} \quad (3-18)$$

Minimizing the potential energy, it leads to the force matrix due to body forces:

$$f_r = \frac{\partial \Pi_B}{\partial d_{re}} = \iint w(x, y) [T_e]^T \begin{bmatrix} f_x \\ f_y \end{bmatrix} dx dy, \quad r = 1, \dots, 12 \quad (3-19)$$

### 3.6 Fixed point matrix

As a boundary condition, the constraint at the fixed point can be simulated by using stiff spring. The spring forces in element  $e$  are:

$$\begin{bmatrix} f_x \\ f_y \end{bmatrix} = \begin{bmatrix} -pu \\ -pv \end{bmatrix} \quad (3-20)$$

where  $p$  is the spring constant. The potential energy caused by the force acting on the fixed point is :

$$\begin{aligned} \Pi_f &= -\frac{1}{2} \begin{bmatrix} u & v \end{bmatrix} \begin{bmatrix} f_x \\ f_y \end{bmatrix} \\ &= \frac{p}{2} [D_e]^T [T_e]^T [T_e] [D_e] \end{aligned} \quad (3-21)$$

Minimizing the potential energy, it leads to stiffness matrix

$$K_{rs} = \frac{\partial^2 \Pi_f}{\partial d_{re} \partial d_{se}} = p [T_e]^T [T_e] \quad , \quad r, s = 1, \dots, 12 \quad (3-22)$$

### 3.7 Inertia force matrix

The inertia forces of mass per unit area are:

$$\begin{bmatrix} F_x \\ F_y \end{bmatrix} = -M \begin{bmatrix} \frac{\partial^2 u(t)}{\partial t^2} \\ \frac{\partial^2 v(t)}{\partial t^2} \end{bmatrix} \quad (3-23)$$

The potential energy due to inertia forces of the element  $e$  is:

$$\begin{aligned} \Pi_I &= \iint w(x, y) M \begin{bmatrix} u & v \end{bmatrix} \begin{bmatrix} \frac{\partial^2 u(t)}{\partial t^2} \\ \frac{\partial^2 v(t)}{\partial t^2} \end{bmatrix} dx dy \\ &= \iint M w(x, y) [D_e]^T [T_e]^T [T_e] \frac{\partial^2 D_e(t)}{\partial t^2} dx dy \end{aligned} \quad (3-24)$$

Rewriting  $D_e(t)$  in Taylor's series expansion and neglecting the higher order term of Taylor's series expansion,

$$\frac{\partial^2 D_e(t)}{\partial t^2} = \frac{2}{\Delta^2} [D_e] - \frac{2}{\Delta} \frac{\partial D_e(t)}{\partial t}$$

where  $\Delta$  is the time increment, therefore, the potential energy due to inertia forces is

$$\Pi_I = [D_e]^T \iint w(x, y) [T_e]^T [T_e] dx dy \left( \frac{2M}{\Delta^2} [D_e] - \frac{2M}{\Delta} [V_0] \right)$$

Minimizing the potential energy, it leads to stiffness matrix

$$K_{rs} = \frac{2M}{\Delta^2} \iint w(x, y) [T_e]^T [T_e] dx dy \quad , \quad r, s = 1, \dots, 12 \quad (3-25)$$

and another term  $f_r$  is the force matrix.

$$f_r = \frac{2M}{\Delta} \iint w(x, y) [T_e]^T [T_e] dx dy [V_0] \quad , \quad r = 1, \dots, 12 \quad (3-26)$$

The integration  $\iint [T_e]^T [T_e] dx dy$  is a 12x12 matrix and it contains 144 complex integrations which can be carried out by using the integration program.

### 3.8 Normal and shear contact matrices

The formulations for normal and shear contact matrices are almost the same as those given by the first order manifold method with the exception of using extended  $[T_e]$  and  $[D_e]$  matrices. The sub-matrices due to the interaction between elements are mainly induced by the contact forces which are determined by the quantity of penetration, relative movement between elements and stiffness of contact spring. They are :

$$p[H_{ei}]_{12 \times 1}[H_{ei}]_{1 \times 12}^T, p[H_{ei}]_{12 \times 1}[G_{ej}]_{1 \times 12}^T, p[G_{ej}]_{12 \times 1}[H_{ei}]_{1 \times 12}^T, p[G_{ej}]_{12 \times 1}[G_{ej}]_{1 \times 12}^T$$

which are added to the stiffness matrix  $[K_{ii}]$ ,  $[K_{ij}]$ ,  $[K_{ji}]$ ,  $[K_{jj}]$ ; and

$$-\frac{pS_0}{l}[H_{ei}]_{12 \times 1}, -\frac{pS_0}{l}[G_{ej}]_{12 \times 1}$$

are added to the force matrix  $[F_i]$  and  $[F_j]$ .

In these sub-matrices,  $p$  is the stiffness of contact spring,  $l$  is the length of contact edge, and  $[H_{ei}]$ ,  $[G_{ej}]$  in normal contact matrices have the following forms:

$$\begin{aligned} [H_{ei}]_{12 \times 1} &= [T_{ei}(x_1, y_1)]^T \begin{bmatrix} y_2 - y_3 \\ x_3 - x_2 \end{bmatrix} \\ [G_{ei}]_{12 \times 1} &= [T_{ej}(x_2, y_2)]^T \begin{bmatrix} y_3 - y_1 \\ x_1 - x_3 \end{bmatrix} + [T_{ej}(x_3, y_3)]^T \begin{bmatrix} y_1 - y_2 \\ x_2 - x_1 \end{bmatrix} \end{aligned}$$

and

$$S_0 = \begin{vmatrix} 1 & x_1 & y_1 \\ 1 & x_2 & y_2 \\ 1 & x_3 & y_3 \end{vmatrix}$$

and  $[H_{ei}]$ ,  $[G_{ej}]$  have the following forms in shear contact matrices:

$$\begin{aligned} [H_{ei}]_{12 \times 1} &= [T_{ei}(x_1, y_1)]^T \begin{bmatrix} x_3 - x_2 \\ y_2 - y_3 \end{bmatrix} \\ [G_{ei}]_{12 \times 1} &= [T_{ej}(x_2, y_2)]^T \begin{bmatrix} -x_1 + 2(1-w)x_2 + (2w-1)x_3 \\ -y_1 + 2(1-w)y_2 + (2w-1)y_3 \end{bmatrix} \\ &\quad + [T_{ej}(x_3, y_3)]^T \begin{bmatrix} x_1 + (2w-1)x_2 - 2wx_3 \\ y_1 + (2w-1)y_2 - 2wy_3 \end{bmatrix} \end{aligned}$$

where  $0 \leq w \leq 1$ ; and  $S_0$  can be expressed as follow

$$S_0 = [x_1 - (1-w)x_2 - wx_3 \quad y_1 - (1-w)y_2 - wy_3] \begin{bmatrix} x_3 - x_2 \\ y_3 - y_2 \end{bmatrix}$$

The stiffness matrices and force matrices at the individual element derived above are assembled into global stiffness and force matrices for the system. Simultaneous equations were formed for solving the unknowns  $[D]$  for all elements.

## 4. Validation of Second Order DDA Code

### 4.1 Modification of DDA code

DDA code version(1993) developed by Dr. Gen-hua Shi was used as the basic program for modification. The main features of the modified version of DDA program include :

- (1) incorporate the second order displacement function;
- (2) revise the variable contact spring constant to fixed value;
- (3) change the solver of simultaneous equation from successive over-relaxation (S.O.R.) technique to preconditioned biconjugate gradient(PBCG) method; and
- (4) change the convergence criteria from iteration number of 200 or relative criterion of  $10^{-8}$  to an absolute criterion of  $10^{-8}$ .

This modified version of the program was used for validation analysis to check the correctness of formulation and coding. The results are presented in the following section.

### 4.2 Results of validation

#### (1) Patch test

A displacement functions assumed for the block shown in Figure 1 are as follows:

$$u = 0.01x - 0.01y + 0.001x^2 + 0.0001xy - 0.001y^2$$

$$v = -0.01x + 0.01y - 0.001x^2 - 0.0001xy + 0.001y^2$$

The prescribed displacements at the 12 vertices, which are consistent with the displacement function, were applied to the block and are shown in Table 1. The displacements at 4 locations within the block were calculated by the code and compared with those obtained by the displacement function. The results are shown in Table 2.

Table 1 Prescribed displacements at the vertices

Vertices coord.	Prescribed displacements	
	$u$	$v$
A(0,0)	0	0
B(1,0)	0.011	-0.011
C(3,0)	0.039	-0.039
D(4.5,0)	0.06525	-0.06525
E(4,1)	0.0454	-0.0454
F(3.5,2)	0.02395	-0.02395
G(3,3)	0.0009	-0.0009
H(2,3)	-0.0144	0.0144
I(1,3)	-0.0277	0.0277

J(0,3)	-0.039	0.039
K(0,2)	-0.024	0.024
L(0,1)	-0.011	0.011

Table 2 Patch test results

Measuring points coord.	Exact solutions		SDDA	
	$u$	$v$	$u$	$v$
M(1,1)	0.0001	-0.0001	0.000095	-0.000095
N(1,2)	-0.0128	0.0128	-0.012806	0.012806
O(3,2)	0.0156	-0.0156	0.015598	-0.015598
P(3,1)	0.0283	-0.0283	0.028296	-0.028296

From the preliminary tests, it may be concluded that the second order formulation and coding are correct. But there are still many functions, such as point load, body force, inertia force, etc. to be validated.

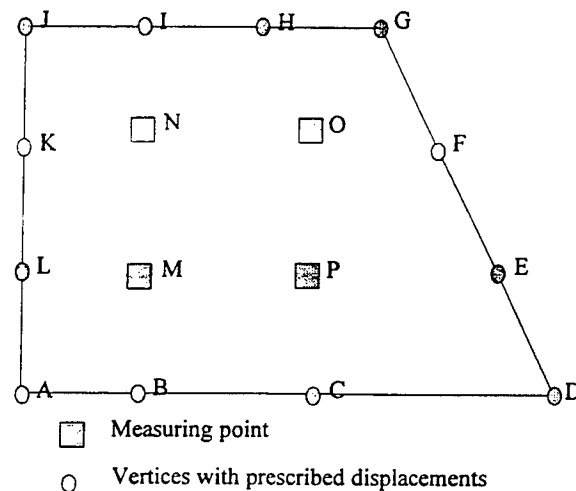


Figure 1. Block configuration for patch test

## (2) Cantilever beam

An 8 m long x 1 m deep cantilever beam with unit thickness subjected to 1 ton concentrated load at the end of the beam was used for validation. The material properties of the beam were assumed to be  $E=10^5 T/m^2$  and  $\nu=0.2$ . The problem was solved by dividing the beam into 1, 4, 8, 16, 32 and 64 blocks. The results for the deformation along the beam axis are shown in Figure 2. And stress components  $\sigma_x$  at the centroid of each block for the case of 64 blocks are shown in Figure 3. It may be seen that 64 blocks can obtain good approximation as compared with analytical solution. This example also illustrates that the second order DDA can release the restriction of block shape requirement for certain types of problem, such as beams. It also requires a smaller number of blocks to achieve the same degree of accuracy as the first order code.



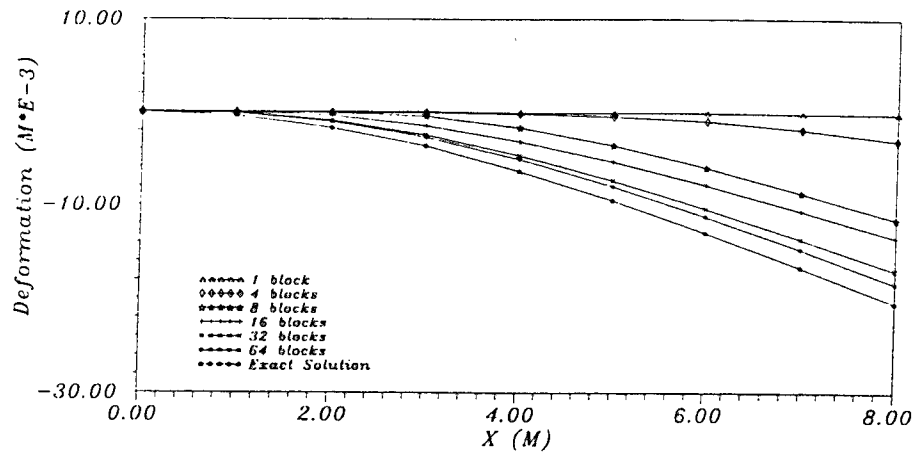


Figure 2. Results for the deformation of cantilever beam

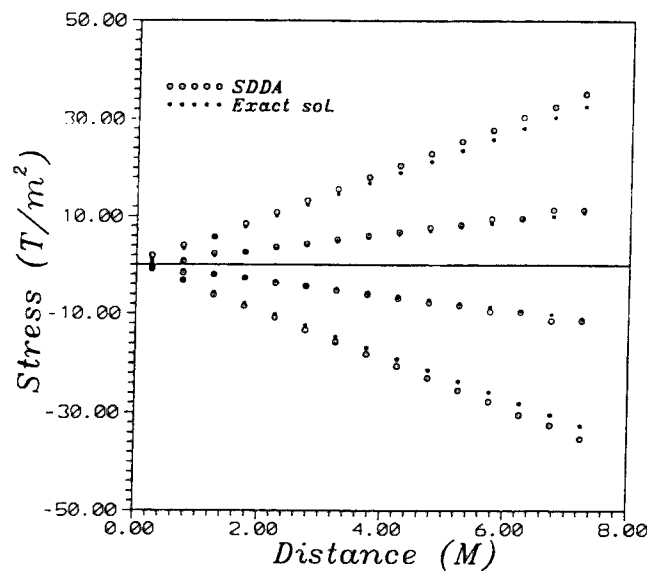


Figure 3. Results for the distribution of  $\sigma_x$  at the centroid of blocks

### (3) Kirsch solution

This problem used a uniformly loaded linear elastic plate with a central circular opening to study the effect of stress concentration. To simplify the calculation, a slice of the plate as shown in Figure 4 was used. The problem was analyzed by using 8 blocks together with 2 rigid blocks to provide the frictionless lateral boundaries which simulate the condition of zero circumferential displacement. The results of stress concentration factors for radial stress, circumferential stress and shear stress at the block centroid together with the analytical solutions are shown in Figure 5. Very good agreement in results may be seen even for the very crude blocks adopted.

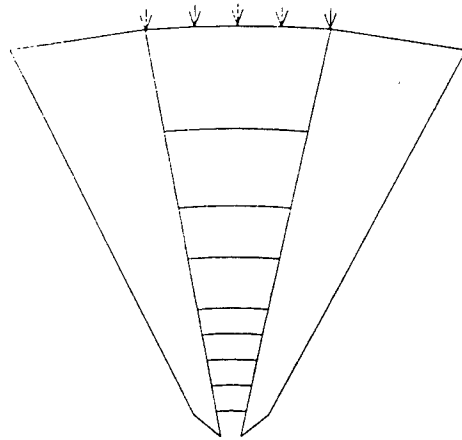


Figure 4. Block system for simulating the Kirsch solution

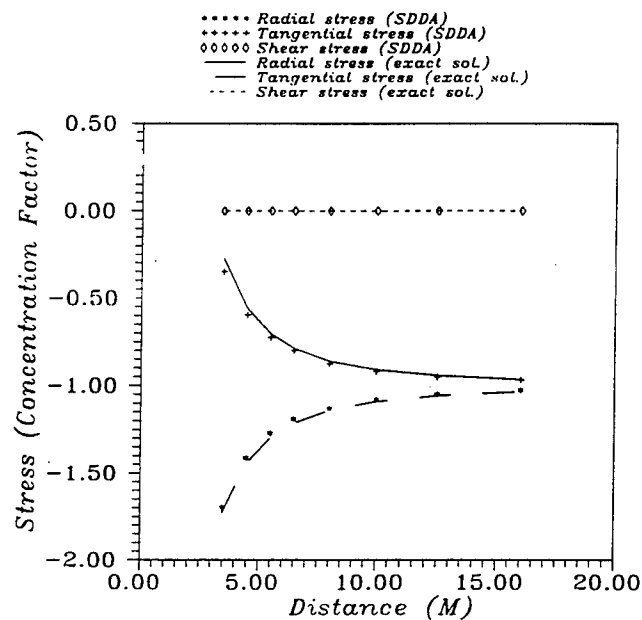


Figure 5. Comparison of results calculated by second order DDA and exact solutions

## 5. Discussions and Conclusions

In this paper, second order displacement function formulations for DDA and manifold method are presented. Modifications to the original DDA code were made. Validation test results showed that it can obtained results in good agreement with the analytical results. From these studies, it appears that the major improvements in adopting the second order displacement function in DDA method are :

- (1) with improved deformation mode, second order DDA can release the requirement for block shape in certain types of problem, such as beam;
- (2) reduce the block number required for calculation, especially in the case with large deformation or stress concentration; and
- (3) improve the efficiency of calculation and obtain a better stress and strain distributions in blocks.

From the limited experience in using DDA to solve the engineering problems, it appears that the second order DDA with improved solving technique can model many types of problem more accurately and efficiently in comparison with the original version of DDA. The most severe limitation in using DDA to solve practical problem is the memory capacity of the computing facility and the computing time required. However, with the rapid development in computer hardware, DDA can be a powerful tool in solving the engineering problems.

## Acknowledgments

The authors are deeply indebted to the original developer of DDA and manifold method, Dr. Gen-hua Shi, for his continued guidance, assistance and encouragement during the course of these studies. Thanks are also due to Dr. Jeen-shang Lin of University of Pittsburgh for his valuable suggestions and comments in the development of second order DDA formulation. Acknowledgment is also extended to Sinotech Engineering Consultants, Inc. for funding this research project.

## References

1. Chen, S. (1993). "Slope Stability Assessment Based Upon Discontinuous Deformation Analysis" Ph.D. Dissertation, Dept. of Civil Engineering, University of Pittsburgh
2. Chern, J.C., Chen, S. and Koo, C. Y. (1995). "Application of DDA in Stability Assessment of Tunnel near Slope", Invited paper for International Journal for Numerical & Analytical Methods in Geomechanics. (in press)
3. Ke, Te-chih (1993). "Simulated Testing of Two Dimensional Heterogeneous and Discontinuous Rock Masses Using Discontinuous Deformation Analysis," Ph.D. Dissertation, Dept. of Civil Engineering, University of California, Berkeley.
4. Lin, J.S. and Chen, S. (1994). "Determination of Safety of Factor for slope stability analysis by using DDA" Rock Engineering Symposium in Taiwan, pp.269~277.
5. Shi, G.H. (1988). "Discontinuous Deformation Analysis: A New Numerical Model for the Static and Dynamics of Block Systems," Ph.D. Dissertation, Dept. of Civil Engineering, University of California, Berkeley.
6. Shi, G.H. (1994). "Discontinuous Deformation Analysis with Simplex Integrations", Geotechnical Lab., U.S. Army Engineer Waterways Experiment Station, Vicksburg.
7. Shi, G.H. (1994). "Manifold Method of Material Analysis", Geotechnical Lab., U.S. Army Engineer Waterways Experiment Station, Vicksburg.
8. Shyu, K. K. (1993). "Nodal-based Discontinuous Deformation Analysis" Ph.D. Dissertation, Dept. of Civil Engineering, University of California, Berkeley.
9. "The Application of Discontinuous Deformation Analysis in Rock Mechanics" Report to the Research Foundation of Sinotech Engineering Consultants, Inc., Taipei. Taiwan. (in press , in Chinese) •
10. William, H.P., Saul, A.T., William T.V. and Brian, P.F. (1992). "Numerical Recipes", Cambridge University Press, New York.

# Applications of DDA Augmented Lagrangian Method and Fracturing Algorithms in the Manifold Method

C. T. Lin<sup>+</sup> and B. Amadei<sup>++</sup>

<sup>+</sup> Land and Mineral Resources Division, Energy and Resources Laboratories,  
Industrial Technology Research Institute, Hsinchu, Taiwan, RACE

<sup>++</sup> Department of Civil Engineering, University of Colorado at Boulder, Colorado, U.S.A.

## Abstract

Beginning with the original work of Dr. Shi [1], called the *Manifold method*, two extensions to the method are explored in this paper. The extensions consist of improving the contact algorithms and adding block fracturing capabilities. Discontinuous contacts between blocks are to be modeled using an Augmented Lagrangian Method instead of the penalty method originally proposed by Dr. Shi [1]. This allows the discontinuous contacts to be enforced more precisely and contact forces to be determined more accurately. Two fracturing algorithms, which have been implemented in the DDA method by Lin [2], are introduced into the manifold method. Using a three-parameter (cohesion, friction, tensile strength) Mohr-Coulomb criterion, one algorithm allows intact rocks to be broken into smaller blocks. Fracturing can be in shear or tension. The second algorithm allows fractures to propagate inside the blocks either in Mode I (tensile fracturing) or Mode II (shear fracturing). These two extensions are proposed to be implemented into the original program of the manifold method. With the two extensions, the manifold method will be more applicable to a greater range of rock mechanics problems and other engineering problems involving blocky systems. Two numerical examples implemented in the DDA method are presented to examine the two extensions with regard to masonry wall and slope stability problems with plane stress condition. The examples using the proposed extensions implemented into the manifold method will be presented in the near future.

## The Augmented Lagrangian Method

The penalty method, which was originally used in the DDA and manifold methods, of enforcing contact constraints has proved effective in many areas of numerical modeling and is discussed by Campbell [3], Felippa [4, 5], and Zienkiewicz et al. [6]. The advantages of such a method are: (1) the number of governing equations is not increased because of the contacts and (2) the solution is easily obtained by simply adding contact components to the stiffness matrix. However, the method has three major disadvantages. First, the accuracy of the contact solution depends highly on the choice of the penalty number and the optimal number cannot be explicitly found beforehand. Secondly, the penalty approach satisfies the contact constraints only approximately. Finally, the contact forces must be calculated using auxiliary calculations. All three limitations

can be overcome by using An **Augmented Lagrangian Method**.

The classical Lagrange Multiplier Method was one of the first methods to solve block contact problems when contact forces are explicitly obtained. However, as shown by Lin [2], the method increases the number of governing equations and extra computational effort is needed to solve the increased number of equations. A modified Lagrange Multiplier (Augmented Lagrangian Method) can be used, instead, to retain the simplicity of the penalty method and minimize the disadvantages of the penalty method and the classical Lagrange Multiplier Method.

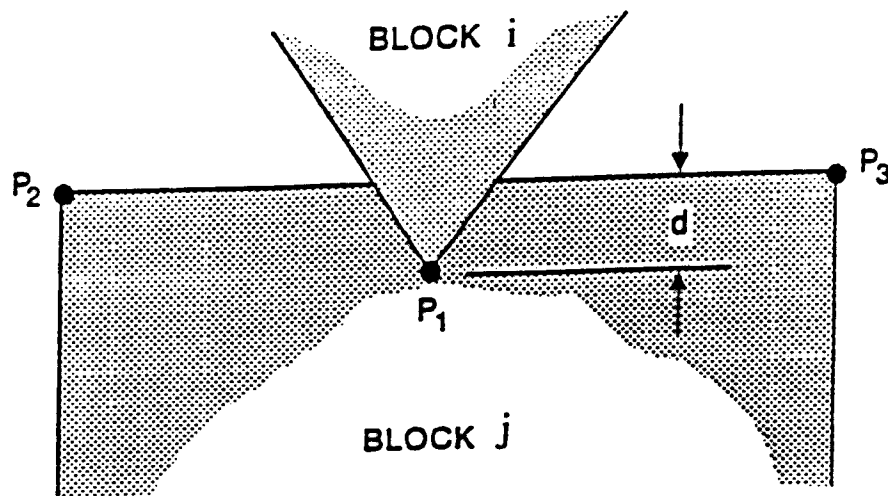


Figure 1. Interaction between two contacting blocks.

Consider two blocks  $i$  and  $j$  as shown in Figure 1, where point  $P_1$  of block  $i$  penetrates a depth,  $d$ , into edge  $P_2P_3$  of block  $j$ . Let  $(x_m, y_m)$  and  $(u_m, v_m)$  be, respectively, the coordinates and the displacement increments at points  $P_m$  ( $m=1,2,3$ ). Using the penalty method is equivalent to placing a spring between point  $P_1$  and the edge  $P_2P_3$ , perpendicular to  $P_2P_3$ . The strain energy of the contact spring is equal to  $pd^2/2$  where  $p$  is a large positive penalty number which is also the spring stiffness. On the other hand, using the Lagrange Multiplier Method, the strain energy of the contact is equal to  $\lambda d$  where  $\lambda$  is the unknown contact force due to the penetration of point  $P_1$  into the edge  $P_2P_3$ .

The essential concept behind the Augmented Lagrangian Method is to use both a penalty number,  $p$  (representing the stiffness of the contact spring) and a Lagrange multiplier,  $\lambda^*$  (representing the contact force  $\lambda$ ), for each block-to-block contact to iteratively calculate the contact force [7]. An iterative method is used to calculate the Lagrange multiplier until the distance,  $d$ , of penetration of one block into the other is below a minimum specified tolerance and the residual forces between block contacts is also below another minimum specified tolerance.

Consider, again, two blocks  $i$  and  $j$  as shown in Figure 1. When using the Augmented Lagrangian Method, the contact force at the contact point can be accurately approximated by

iteratively calculating the Lagrange multiplier  $\lambda^*$ . A first order updated value for  $\lambda^*$  can be written as follows

$$\lambda \approx \lambda_{k+1}^* = \lambda_k^* + pd \quad (1)$$

where the penalty number,  $p$ , can be variable and does not have to be a very large number as in the penalty method. In Equation (1),  $\lambda_k^*$  is the Lagrange multiplier at the  $k^{\text{th}}$  iteration and  $\lambda_{k+1}^*$  is the updated Lagrange multiplier. At the  $k^{\text{th}}$  iteration, the strain energy,  $\Pi_s$ , resulting from the contact force becomes

$$\Pi_s = \lambda_k^* d + \frac{1}{2}pd^2 \quad (2)$$

Equation (2) consists of two components. The first component is the strain energy resulting from the iterative Lagrange Multiplier  $\lambda_k^*$ , and the penalty constraint creates the second. The contribution of the second component to the  $6n \times 6n$  global stiffness matrix  $\mathbf{K}$  was already covered by Shi [8], so only the contribution of the first component of Equation (2) to matrix  $\mathbf{K}$  is derived below.

After the displacement increments  $(u_i, v_i)$  are calculated, the perpendicular distance  $d$  between point  $P_1 (x_1, y_1)$  and the reference edge  $P_2P_3$  can be calculated as follows

$$d = \frac{\Delta}{l} = \frac{1}{l} \begin{vmatrix} 1 & x_1+u_1 & y_1+v_1 \\ 1 & x_2+u_2 & y_2+v_2 \\ 1 & x_3+u_3 & y_3+v_3 \end{vmatrix} \quad (3)$$

where  $l$  is the length of  $P_2P_3$  and  $\Delta$  is such that

$$\Delta = \begin{vmatrix} 1 & x_1 & y_1 \\ 1 & x_2 & y_2 \\ 1 & x_3 & y_3 \end{vmatrix} + \begin{vmatrix} 1 & u_1 & y_1 \\ 1 & u_2 & y_2 \\ 1 & u_3 & y_3 \end{vmatrix} + \begin{vmatrix} 1 & x_1 & v_1 \\ 1 & x_2 & v_2 \\ 1 & x_3 & v_3 \end{vmatrix} + \begin{vmatrix} 1 & u_1 & v_1 \\ 1 & u_2 & v_2 \\ 1 & u_3 & v_3 \end{vmatrix} \quad (4)$$

The last term in Equation (4) can be neglected since it is an infinitesimal second order function of the displacements. Denoting the first term by  $S_0$ , Equation (4) can then be approximated as:

$$\Delta \approx S_0 + \begin{vmatrix} 1 & u_1 & y_1 \\ 1 & u_2 & y_2 \\ 1 & u_3 & y_3 \end{vmatrix} + \begin{vmatrix} 1 & x_1 & v_1 \\ 1 & x_2 & v_2 \\ 1 & x_3 & v_3 \end{vmatrix} \quad (5)$$

Combining Equations (3) and (5) gives

$$d = \frac{S_0}{l} + E D_i + G D_j \quad (6)$$

where  $E$  and  $G$  are  $1 \times 6$  matrices with components  $e_r$  and  $g_r$  ( $r=1-6$ ) defined as

$$\begin{aligned} e_r &= \frac{1}{l} [(y_2 - y_3)t_{1r}(x_1, y_1) + \\ &\quad (x_3 - x_2)t_{2r}(x_1, y_1)] \\ g_r &= \frac{1}{l} [(y_3 - y_1)t_{1r}(x_2, y_2) + \\ &\quad (x_1 - x_3)t_{2r}(x_2, y_2)] + \\ &\quad \frac{1}{l} [(y_1 - y_2)t_{1r}(x_3, y_3) + \\ &\quad (x_2 - x_1)t_{2r}(x_3, y_3)] \end{aligned} \quad (7)$$

In (7),  $t_{1r}(x_1, y_1)$  and  $t_{2r}(x_1, y_1)$  are the components of matrix  $T_i$  defined by Shi [8] for block  $i$  with the center of rotation  $(x_{i0}, y_{i0})$ ; and,  $t_{1r}(x_2, y_2)$ ,  $t_{2r}(x_2, y_2)$ ,  $t_{1r}(x_3, y_3)$ , and  $t_{2r}(x_3, y_3)$  are the components of matrix  $T_j$  for block  $j$  with the center of rotation  $(x_{j0}, y_{j0})$ .

Denoting this first component as  $\Pi_{s1}$  and using the definition of  $d$  in Equation (2) gives

$$\Pi_{s1} = \lambda_k^* \left( \frac{S_0}{l} + E D_i + G D_j \right). \quad (8)$$

The first derivatives of  $\Pi_{s1}$  with respect to  $d_i$  and  $d_j$  at 0 are equal to

$$f_{ri} = -\frac{\partial \Pi_{s1}(0)}{\partial d_{ri}} = -\lambda_k^* e_r, \quad r=1-6, \quad (9)$$

and

$$f_{rj} = -\frac{\partial \Pi_{s1}(0)}{\partial d_{rj}} = -\lambda_k^* g_r, \quad r=1-6, \quad (10)$$

which form two  $6 \times 1$  matrices  $-\lambda_k^* E^T$  and  $-\lambda_k^* G^T$  that are added to sub-matrices  $F_i$  and  $F_j$ , respectively. Note that the  $\lambda_k^*$  values are known and calculated from the previous iteration. They are distinct from the  $\lambda$  values which are unknowns in the classical Lagrange Multiplier Method.

Equations (9) and (10) were derived for the first component of the strain energy,  $\Pi_s$ , in (2). The second component in Equation (2) is associated with the penalty method and its

contribution to the simultaneous equilibrium equations was already derived by Shi [8]. For the Augmented Lagrangian Method, the combined contributions of the first and second components of  $\Pi_s$  to the simultaneous equilibrium equations  $\mathbf{K} \mathbf{D} = \mathbf{F}$  can be summarized as follows:

$$p e_r e_r \rightarrow K_{ii}, r=1-6, \quad (11)$$

is added to sub-matrix  $K_{ii}$  in the simultaneous equilibrium equations;

$$p e_r g_r \rightarrow K_{ij}, r=1-6, \quad (12)$$

is added to sub-matrix  $K_{ij}$  in the simultaneous equilibrium equations;

$$p g_r e_r \rightarrow K_{ji}, r=1-6, \quad (13)$$

is added to sub-matrix  $K_{ji}$  in the simultaneous equilibrium equations;

$$p g_r g_r \rightarrow K_{jj}, r=1-6, \quad (14)$$

is added to sub-matrix  $K_{jj}$  in the simultaneous equilibrium equations;

$$-(\lambda_k^* + \frac{pS_0}{l})e_r \rightarrow F_i, r=1-6, \quad (15)$$

is added to sub-matrix  $F_i$  in the simultaneous equilibrium equations; and

$$-(\lambda_k^* + \frac{pS_0}{l})g_r \rightarrow F_j, r=1-6, \quad (16)$$

is added to sub-matrix  $F_j$  in the simultaneous equilibrium equations.

The feature of calculating the contact force  $\lambda$  from the Lagrange Multiplier Method is retained here by using the iterative algorithm. However, since a value of  $\lambda_k$  is known at each iteration, there is no increase in the size of the system of simultaneous equilibrium equations. In addition, the simplicity of the penalty method is retained and the disadvantages are minimized. From a physical point of view, again, the Lagrange multiplier,  $\lambda$ , represents the contact force along a point of contact between two blocks and the penalty number,  $p$ , represents the stiffness of the contact spring. The final exact contact forces can always be obtained by the iterative method even with small initial values of the penalty number.

However, if the initial penalty number is too small, many iterations are required, making the method less efficient. Hence, the penalty number  $p$  governs the rate of convergence of the iterative effort. This is because the penalty number represents the stiffness of the contact spring and a stronger spring pushes the interpenetration distance  $d$  to a required minimum much faster than a weaker spring does. In general, it is necessary to increase the penalty number after a certain number of iterations within any time step. This variable penalty number approach



represents a major improvement over the penalty method used by Shi [8]. Shi recommended that the penalty number be within 10 to 1000 times the Young's Modulus of the block material in order to prevent the blocks from penetrating one another excessively. This constraint no longer applies when using the variable penalty number approach in the Augmented Lagrangian Method.

The Augmented Lagrangian Method was implemented in the original DDA program with a variable penalty number function. Except for substituting the Augmented Lagrangian Method for the penalty method, all other features of the DDA program developed by Shi were retained. The most important feature of the new program is that any initial penalty number can now be selected by the user. Then, at each time step, and for each iteration within that time step, the optimal penalty number is found for all contacts by the program itself in order to satisfy the requirements of minimum distance of contact interpenetration and minimum residual forces between block contacts. All the features with the Augmented Lagrangian Method will be also implemented in the manifold method.

### Residual forces in the augmented Lagrangian method

The Augmented Lagrangian Method is an iterative method to obtain exact solutions for contact forces. The precision of the solution depends on residual forces that are produced during the iterative calculations of the contact forces. From a physical point of view, the residual forces are the unbalanced forces between external forces and internal forces. The external forces include all surface tractions, body forces and contact forces. As the contact forces are gradually approached by Lagrangian multipliers  $\lambda^*$ , the unbalanced (residual) forces should converge to zero.

The criterion for convergence is based on the  $L_2$  norm of the residual forces, that is

$$\frac{\|KD_{k+1} - KD_k\|}{\|KD_1\|} \leq \epsilon \quad (17)$$

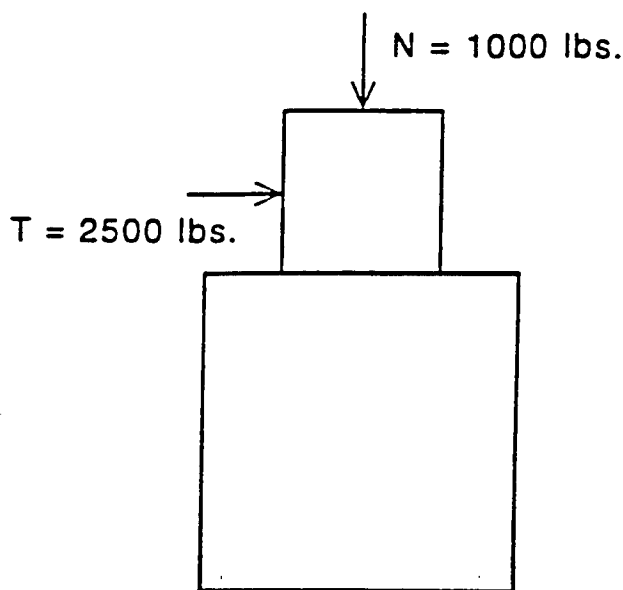
where the tolerance,  $\epsilon$ , is a positive number that is specified by the user. For a good approximation to the exact solution, this values should be close to zero. In the DDA examples presented below, values of  $\epsilon$  ranging between 0 (corresponding to no contact) and 0.1 were found to give excellent results.

### Illustrative example

As an illustrative example, consider the two-block system shown in Figure 2(a). The bottom block is fixed and the top block is subject to a vertical load of 1,000 lbs (4.4 kN) and a horizontal load of 2,500 lbs (11.0 kN). The interface between the two blocks has zero cohesion and a friction angle of  $30^\circ$ . The intact material in the blocks has a Young's modulus of  $10^8$  psf (4,781 MPa), a Poisson's ratio of 0.25 and a unit weight of 130 pcf (0.02 MN/m<sup>3</sup>). Both the penalty method of Shi [8] and the Augmented Lagrangian Method with variable penalty number were used to solve the same problem with a low initial value of the penalty number equal to  $10^4$  lbs/ft (0.15 MN/m).

The deformation of the block system, using the Augmented Lagrangian Method to enforce the contact interface, is shown in Figures 2(b) after 30, 60, 90, and 315 time steps of 0.01 seconds. It is clear that no block interpenetration occurs here even though the initial penalty

number is low. On the other hand, the deformation of the block system, using the classical penalty method, shown in 2(c) after 30, 60, and 90 time steps of 0.01 seconds, indicates that a small penalty number is unable to enforce the interpenetration constraint.



a. STEP 0

Figure 2(a). Initial configuration.

#### Remarks

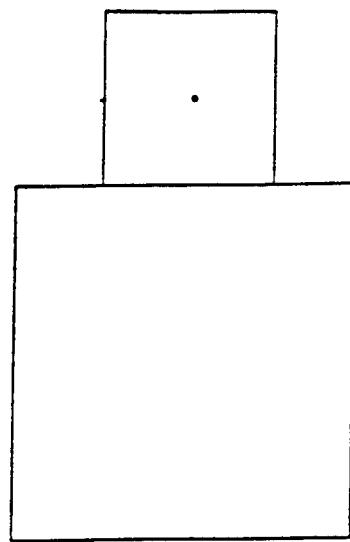
Using the Augmented Lagrangian Method to enforce contact restraints retains the simplicity of the penalty method and reduces the disadvantages of the penalty and classical Lagrange Multiplier methods. Moreover, the accuracy of the contact forces is controlled by the residual forces. If sliding does not take place along a block-to-block (i.e. Coulomb friction is not mobilized), two springs with same stiffness added at a right angle to each other are required in the DDA or manifold method. In this case, the spring forces and stiffnesses are determined using the same methodology as described above. Another situation where two springs are necessary is in the sub-block analysis which was first presented by Lin [2].

### Block Fracturing

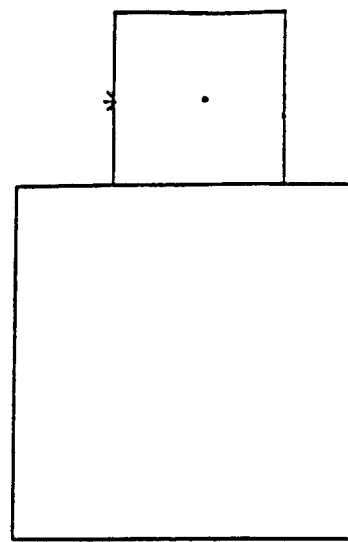
This capability allows intact blocks to be broken into smaller blocks, and allows for Mode I, Mode II or mixed Modes I and II fracture propagation within sub-blocks in the DDA method and mathematical meshes in the manifold method.

#### Fracturing criterion

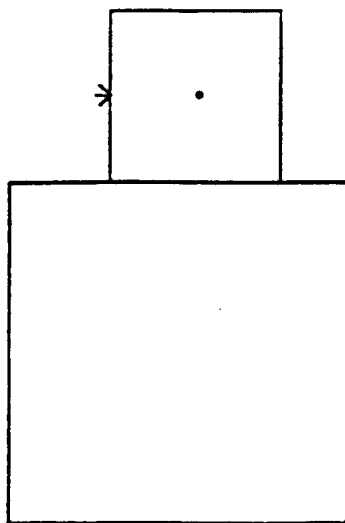
The criterion selected in this research for block fracturing is a Mohr-Coulomb criterion with three parameters :  $s_0$  is the inherent shear strength of the block material,  $\phi$  is its friction angle, and  $T_0$  represents its tensile strength. It is assumed that tensile normal stresses are positive, and the major and minor principal stresses are denoted as  $\sigma_1$  and  $\sigma_3$  (with  $\sigma_1 \geq \sigma_3$ ), respectively.



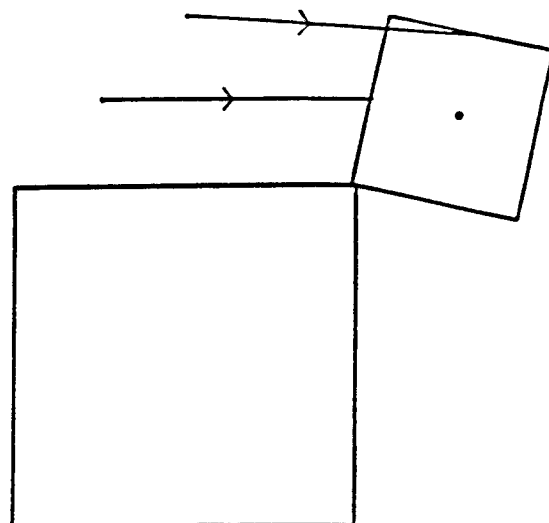
STEP 30



STEP 60

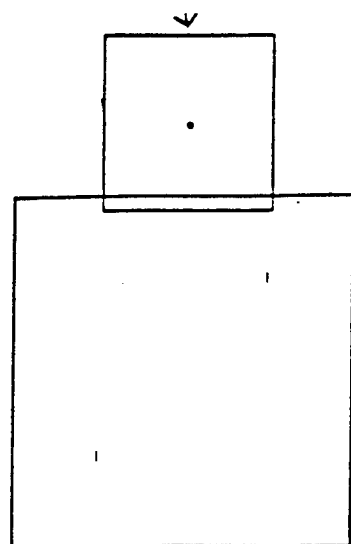


STEP 90

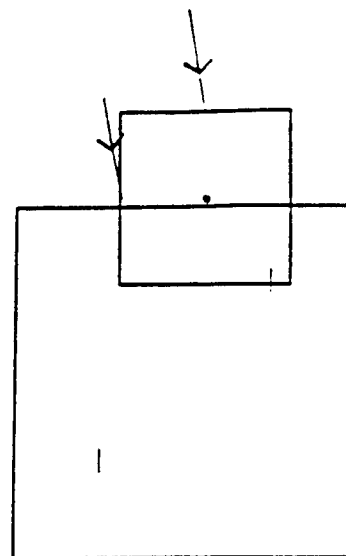


STEP 315

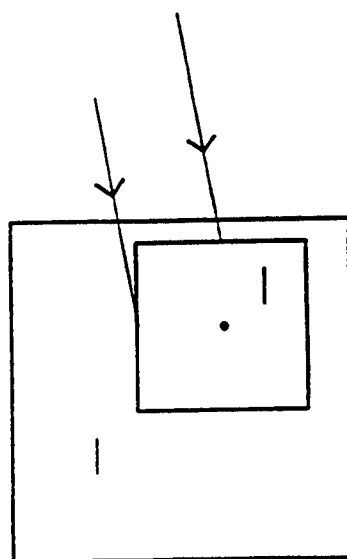
Figure 2(b). Deformation of the block system after 30, 60, 90 and 315 time steps of 0.01 seconds with the Augmented Lagrangian Method.



STEP 30



STEP 60



STEP 90

Figure 2(c). Deformation of the block system after 30, 60, 90 and 315 time steps of 0.01 seconds with the penalty method.

A critical value of the minor principal stress is defined as

$$\sigma_{3c} = -C_o + T_o \tan^2\left(\frac{\pi}{4} + \frac{\phi}{2}\right) \quad (18)$$

where  $C_o = 2s_o \tan(\pi/4 + \phi/2)$  is the unconfined compressive strength of the block material. According to the Mohr-Coulomb fracturing criterion, shear failure occurs when

$$\sigma_3 < \sigma_{3c} \quad \wedge \quad \sigma_3 \leq -C_o + \sigma_1 \tan^2\left(\frac{\pi}{4} + \frac{\phi}{2}\right) \quad (19)$$

(where ' $\wedge$ '='and') and tensile failure occurs when

$$\sigma_3 \geq \sigma_{3c} \quad \wedge \quad \sigma_1 \geq T_o \quad (20)$$

The immediate advantage of this criterion is that different types of fracture (in tension or shear) are well defined by the transitional normal stress  $\sigma_{3c}$ . Tensile failure is more likely to occur in strong brittle rocks under tension. On the other hand, shear failure is more likely to occur in soil or in weak rocks.

### Intact block fracture

The three-parameter Mohr-Coulomb criterion was added to the DDA program and is graphically shown in the theoretical and physical plots in Figures 3(a) and 3(b). For each block of the system, the major and minor in-plane principal stresses  $\sigma_1$  and  $\sigma_3$  are determined at the block's centroid. These two stress components are then compared to the third principal stress which is equal to 0 for a state of plane stress. The largest of the three principal stresses is taken as  $\sigma_1$  and the smallest as  $\sigma_3$ . In the program, the user divides the blocks into two groups : those that are allowed to break (breakable blocks) and those that are not (intact blocks). Fracturing of the blocks in the first group is determined in the program by comparing  $\sigma_1$  and  $\sigma_3$  with the following expressions of the three-parameter Mohr-Coulomb criterion

$$\sigma_1 \geq T_o \quad \text{if} \quad \sigma_1 > \sigma_3 > 0 \quad (21a)$$

$$\sigma_1 \geq T_o \quad \text{if} \quad \sigma_1 > 0 > \sigma_3 > \sigma_{3c} \quad (21b)$$

$$\sigma_3 \leq -C_o + \sigma_1 \tan^2\left(\frac{\pi}{4} + \frac{\phi}{2}\right) \quad \text{if} \quad \sigma_1 > 0 > \sigma_{3c} > \sigma_3 \quad (21c)$$

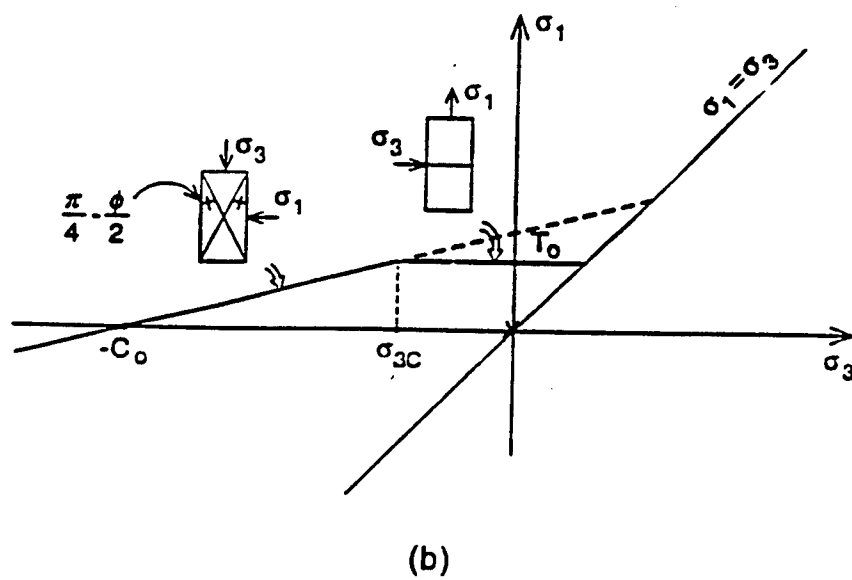
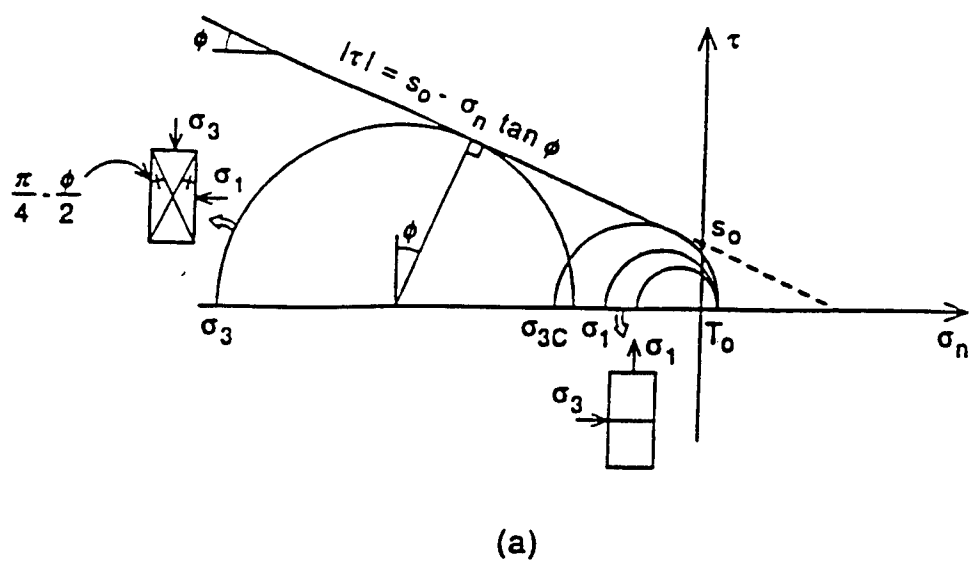


Figure 3. The Mohr-Coulomb criterion with three parameters.

$$\sigma_3 \leq -C_0 \quad \text{if} \quad 0 > \sigma_1 > \sigma_3 \quad (21d)$$

If condition (21c) is satisfied within a breakable block, shear failure is assumed to occur with two failure planes passing through the block's centroid and inclined at  $\pm (\pi/4 - \phi/2)$  with respect to  $\sigma_3$ , as shown in Figure 3(b). Then, the block is divided into four blocks and the analysis is resumed with a new block configuration. If, on the other hand, either condition (21a) or (21b) is satisfied within a breakable block, tensile failure occurs with a failure plane passing through the block's centroid and oriented at right angles to  $\sigma_1$  as shown in Figure 3(a). In this case, the block is divided into two blocks and the analysis is resumed. This process is repeated for all breakable blocks in the system. In this formulation, no energy dissipation is assumed to occur during shear or tensile failure. Upon breaking, the new blocks are assumed to have the same velocities as the original block. Also, the new fractures have Coulomb friction and cohesion. Note that condition (21d) is not considered in this thesis since, in that case, shear failure occurs on two planes in a direction parallel to  $\sigma_1$ .

### Sub-block fracture

Consider a large block divided into several sub-blocks, as shown in Figure 4, that can be triangular mathematical meshes in the manifold method. The sub-block contacts satisfy the displacement compatibility conditions along block-to-block contacts. A crack has been initiated. Fracturing takes place at the crack tip (point A in Figure 4) and the direction of crack propagation depends on the state of stress in the sub-block in direct contact with the crack tip (shaded sub-block in Figure 4). Mode I (tensile), Mode II (shear), or mixed Mode I and Mode II fracture propagation is allowed as specified by the user. In each case, propagation results in the sub-block in contact with the crack tip to be divided into two new sub-blocks and the process is repeated at the next time step. In contrast to the independent fracturing of whole blocks, sub-block fracturing allows continuous crack propagation. All new crack surfaces have Coulomb friction and cohesion.

### Mode I fracture (tensile failure)

With this type of fracture mode, the crack will propagate through the sub-block just ahead of the crack tip if the principal stresses  $\sigma_1$  and  $\sigma_3$  in that sub-block satisfy condition (20). The direction of crack propagation will be perpendicular to  $\sigma_1$ .

A typical example of this type of fracture is shown in Figure 5. The crack is initiated at point 1. Point O is the centroid of the sub-block. When the state of stress of the sub-block (or at point O) satisfies condition (20), the crack propagates from point 1 to point 2 in a direction perpendicular to  $\sigma_1$ .

### Mode II fracture (shear failure)

The crack will propagate through the sub-block just ahead of the crack tip if the principal stresses  $\sigma_1$  and  $\sigma_3$  in that sub-block satisfies (19). Now, the direction of propagation is inclined at  $+(\pi/4 - \phi/2)$  or  $-(\pi/4 - \phi/2)$  with respect to  $\sigma_3$ . One of those two directions is specified by the user.

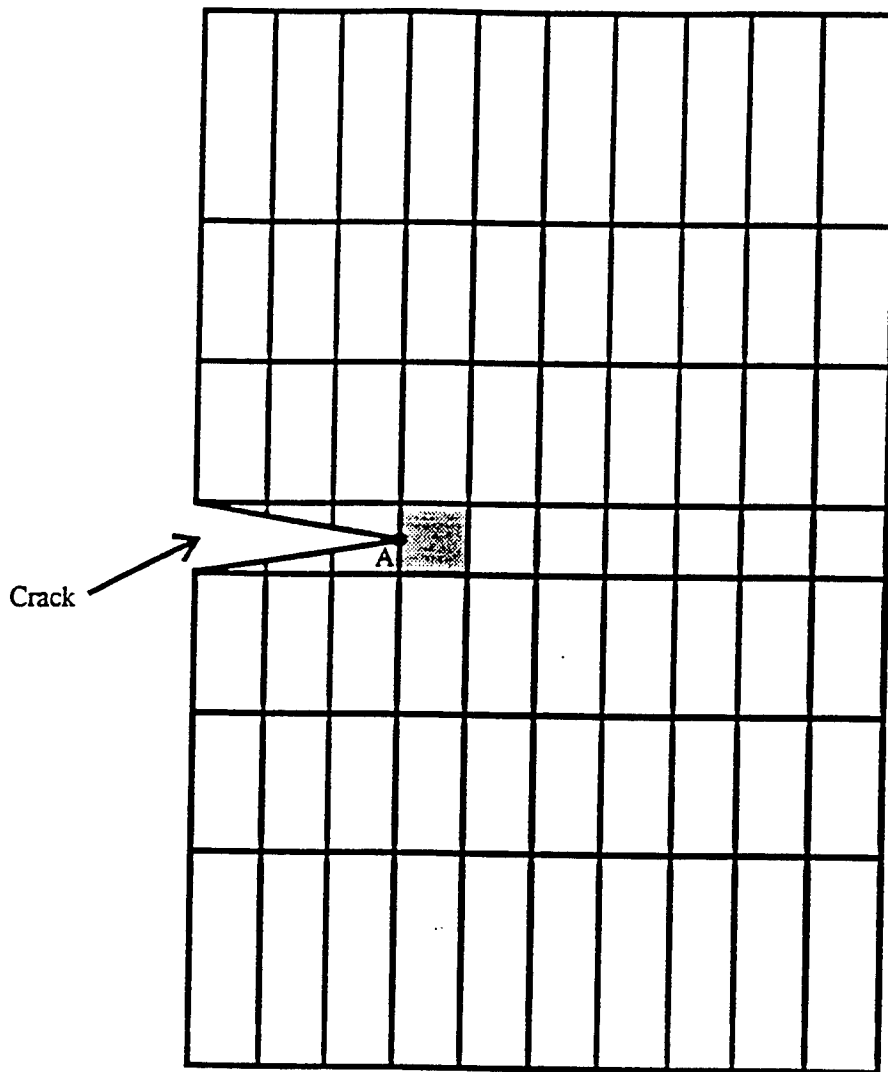
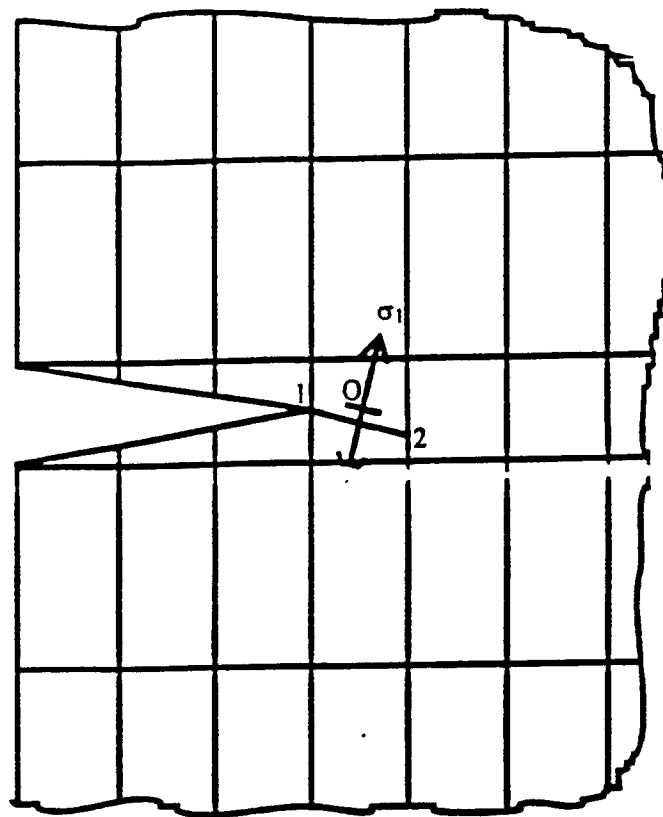


Figure 4. A large block consists of several sub-blocks and a initial crack with crack tip at point A. The sub-block in contact with the crack tip is shaded.





- \* O : represents centroid of the sub-block.
- \*\* 1-2 : represents the Mode I cracking plane.
- \*\*\*  $\sigma_1$  : represents the major principal stress.

Figure 5. Model I sub-block fracturing.

A typical example of this type of fracture is shown in Figures 6(a) and 6(b). In Figure 6(a), the crack is initiated at point 1. Point O is the centroid of the sub-block. When the state of stress in the sub-block ahead of the crack front satisfies (19), the crack propagates from point 1 to 2 in a direction inclined at  $+(\pi/4 - \phi/2)$  with respect to  $\sigma_3$ . Similarly, Figure 6(b) shows another possible shear cracking plane, with the direction of propagation from point 1 to 2 inclined at  $-(\pi/4 - \phi/2)$  with respect to  $\sigma_3$ .

### Mixed mode fracture

Here, the crack will propagate through the sub-block ahead of the crack front if the principal stresses  $\sigma_1$  and  $\sigma_3$  in the sub-block satisfy either Equation (19) or (20). The direction of propagation is perpendicular to  $\sigma_1$  if  $\sigma_1$  and  $\sigma_3$  satisfy condition (20). On the other hand, the direction of propagation is inclined at  $+(\pi/4 - \phi/2)$  or  $-(\pi/4 - \phi/2)$  with respect to  $\sigma_3$  if  $\sigma_1$  and  $\sigma_3$  satisfy condition (19). In the latter case, one of the shear fracturing directions must be specified by the user.

The advantage of the mixed mode option is that either tensile or shear fracture is determined by the state of stress in the sub-block ahead of the crack front at the time of fracture.

### Energy balance during fracturing

Although classical fracture mechanics stipulates that some strain energy is released during fracture [9], the current research does not include an energy loss criterion. Therefore, an alternative kinematic condition has to be satisfied and enforced in the model.

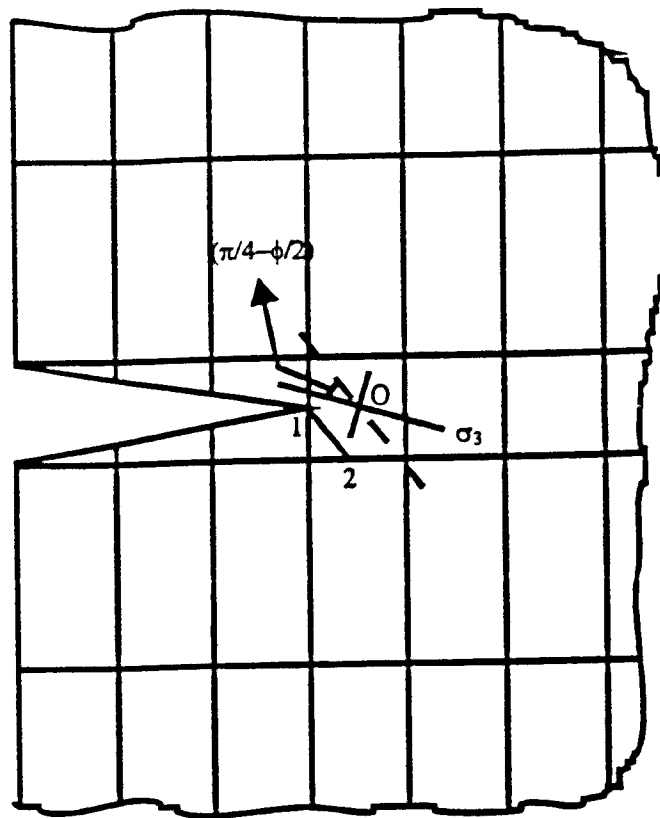
Consider a block (or sub-block)  $i$  that is to be fractured at a certain time step when the state of stress in the block satisfies the fracturing criterion. A fracture plane is introduced and two new blocks are formed. One is denoted as block  $i1$  and the other as block  $i2$ . At the end of the time step, the new block velocities  $\partial D_{i1}(t)/\partial t$  and  $\partial D_{i2}(t)/\partial t$  are assumed to satisfy the following equation

$$\frac{\partial D_i(t)}{\partial t} = \frac{\partial D_{i1}(t)}{\partial t} = \frac{\partial D_{i2}(t)}{\partial t} \quad (22)$$

where  $\partial D_i(t)/\partial t$  is the velocity of the original block. Since velocities are conserved, there is no energy loss associated with fracturing.

### Remarks

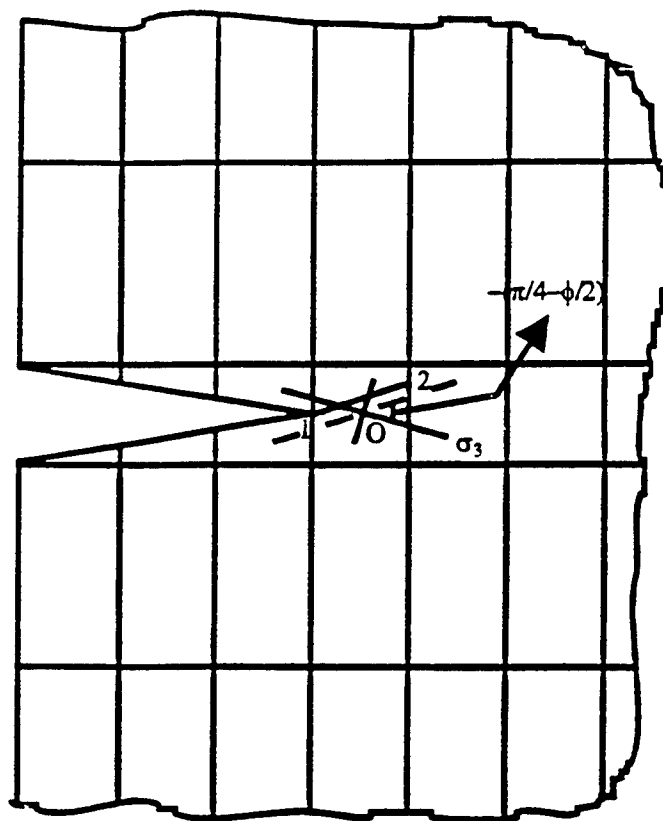
Since the DDA or manifold method assumes discontinuity of element joints, the newly created discontinuous element joints resulting from block fracturing can be naturally handled by the methods. They are also given Coulomb friction and cohesion. With the same concept in the cases of applying the intact block and sub-block fracturing capabilities in the DDA method described above, the addition of the block fracturing algorithms in the manifold method will make the method a powerful tool for modeling fracture propagation in already fractured rock masses or other blocky systems.



- \* O : represents centroid of the sub-block.
- \*\* 1-2 : represents the Mode II cracking plane.
- \*\*\*  $\sigma_3$  : represents the minor principal stress.

(a)

Figure 6(a). Mode II sub-block fracturing.



- \* O : represents centroid of the sub-block.
- \*\* 1-2 : represents the Mode II cracking plane.
- \*\*\*  $\sigma_3$  : represents the minor principal stress.

(b)

Figure6(b). Mode II sub-block fracturing.

## Numerical Examples

### Modeling masonry structures

Masonry structures are blocky systems that are of great interest to civil engineers. Masonry structures, and in particular unreinforced masonry structures such as stone and brick walls, arches and vaults, constitute a sizable portion of existing buildings (some of them with historical value) all over the world. Many of these structures suffer from numerous deficiencies related to the construction material, construction techniques or to continuous deterioration due to aging. Also, older stone masonry structures can be quite complex in their geometry and composition. Being able to analytically model unreinforced masonry structures and their behavior under vertical and horizontal loads is very important when assessing their short and long term stability and the needs for repair and retrofitting.

Masonry structures are discontinua at the engineering scale. They consist essentially of intact units e.g. masonry blocks (stone, clay units) separated by discontinuities (mortar joints). The discontinuities can be inherent or induced by loading. There is enough laboratory and field evidence to show that these discontinuities have a strong non-linear effect and dominate the deformation and strength behavior of masonry structures. In general, continuum models are inadequate in predicting the response of such systems to loading and unloading. This has led many structural engineers to use analysis and design methods that rely heavily on empirical rules.

The numerical models used for the structural analysis of masonry structures have been mostly based on the FEM method, in which the masonry is treated as a continuum, an equivalent continuum or a discontinuum with discrete interfaces [10, 11]. Both discrete and smeared crack models have been used [12, 13, 14, 15, 16]. Also, some attempt has been made in using discrete element methods for masonry structures [17, 18]. Applications of rigid block solutions (similar to DEM methods) to masonry arches were presented by Melbourne and Gilbert [19] and Melbourne et al. [20]. A review of the different numerical approaches used in structural masonry can be found in Middleton and Pande [21].

In general, none of the past approaches has adequately modeled the occurrence and propagation of the brittle cracking and sliding which characterizes the behavior of unreinforced masonry structures. The example presented below is designed to show how the new DDA model can capture this behavior.

#### Example 1

A racking test involving an unreinforced masonry wall section with the geometry of Figure 7 subjected to a vertical load and a horizontal shear load, is considered in this section [22]. This experiment, basically, is designed to simulate the response of a shear wall in a building to in-plane loads [23, 24, 25].

Consider now a 28.67 in. x 39.4 in. (72.8 cm x 100 cm) unreinforced masonry wall, as shown in Figure 7.1.1, which consists of 10 layers of bricks with 3.5 units per layer. The bricks are 8.19 in. x 3.94 in. (20.8 cm x 10 cm) in size. The shear wall sits on a fixed base and has a 35.74 in. x 3.54 in. (90.7 cm x 9 cm) beam on top. A horizontal point load of 450 kips (2 MN) is applied from left to right and a vertical downward load  $P$  placed on top of the wall. The wall and the beam are assumed to have a Young's Modulus  $E=1.84 \times 10^8$  psf (8,800 MPa) and a Poisson's ratio  $\nu=0.16$ . The bricks have a unit weight  $\gamma=150$  pcf ( $2.36 \times 10^{-2}$  MN/m<sup>3</sup>), an inherent



shear strength (cohesion)  $s_0=73$  ksf (3.5 MPa), a tensile strength  $T_0=72$  ksf (3.45 MPa), and a internal friction angle  $\phi=30$  degrees. Two kinds of brick joints were considered in this example. In the first case, the brick joints have a uniform joint friction angle of  $32.6^\circ$  and a cohesion of 27.4 kips/ft (0.40 MN/m). In the second case, the brick joints have a uniform joint friction angle of 32.6 degrees and zero cohesion. The beam and the fixed base are represented by one DDA block each. Also, each brick is represented by one DDA block. No sub-blocks are used in this example.

Either shear or tensile fracturing of each breakable block is allowed in this example, depending on the values of the major and minor principal stresses, as described above. When shear fracturing occurs, the fracturing plane passes through the centroid of the block and is inclined at  $+(\pi/4-\phi/2)$  with respect to the minimum principal stress  $\sigma_3$ . When tensile fracturing occurs, the fracturing plane passes through the centroid of the block and is perpendicular to the major principal stress  $\sigma_1$ .

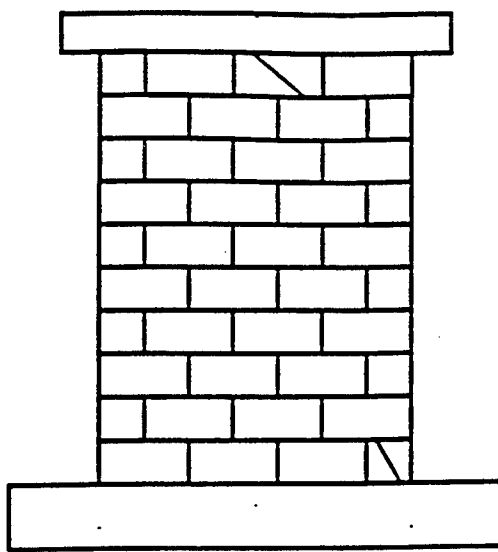
For the case of cohesive joints, the DDA program was run with the following specifications:

Initial Penalty Number	Time Step (seconds)	Max. No. of Iterations per Time Step	Residual Force Ratio ( $\epsilon$ ) (Eq. (17))
$1.84 \times 10^8$ lbs/ft ( $2.69 \times 10^3$ MN/m)	$1 \times 10^{-4}$	16	$\leq 0.1$

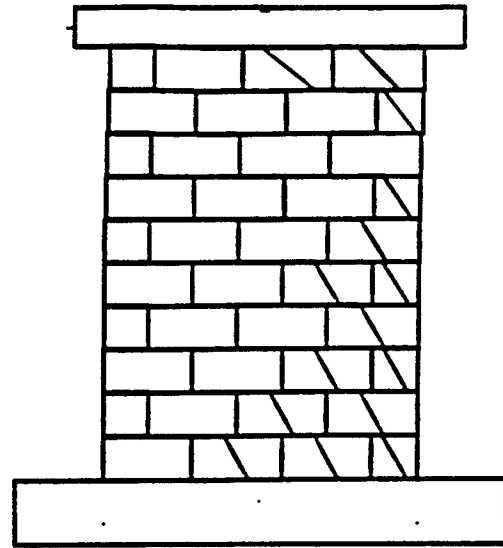
Figures 8(a)-(d) show the deformed and fractured shear wall with cohesive joints after 10, 30, 90, and 100 time steps, respectively. In this example, the vertical load  $P$  is equal to 808 kips (3.6 MN). It is clear that the wall starts cracking near its right toe. Then more diagonal cracks develop from that area and propagate towards the top left hand side of the wall. It can also be seen that although the wall was initially intact, fracturing occurs across the brick units with some offset along the brick joints. Note here that fracturing of the wall proceeds without user intervention; fracture orientation, new element generation and new interactions being automatically calculated within the program. This analysis would be extremely difficult using conventional finite element or boundary element methods.

Figures 9(a)-(d) show the results of another numerical run where the bricks are now assumed to be frictionless and to have a cohesion of 27.4 kips/ft (0.4 MN/m). All other mechanical properties and the computer run specifications are the same as before. The vertical load  $P$  is equal to 493 kips (2.2 MN). Figures 9(a)-(d) show that diagonal wall fracturing is more defined here than in Figures 8(a)-(d).

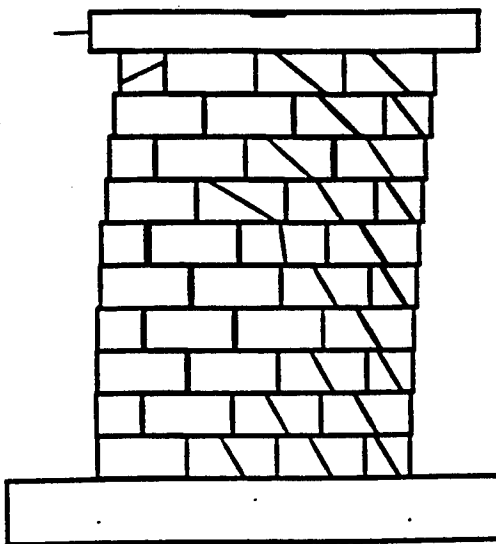
For the case of cohesionless joints and bricks with internal friction and cohesion, the DDA program was run with the following specifications:



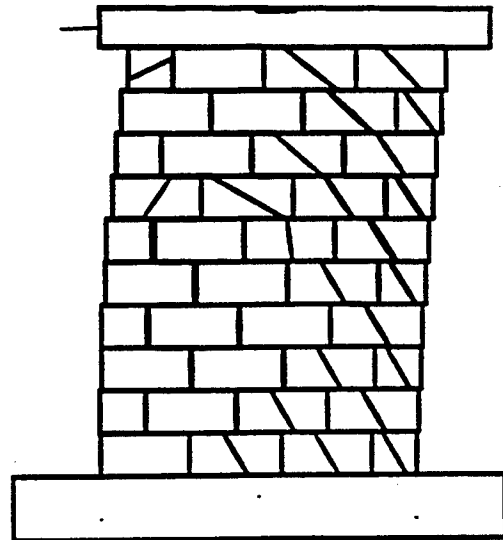
(a)



(b)



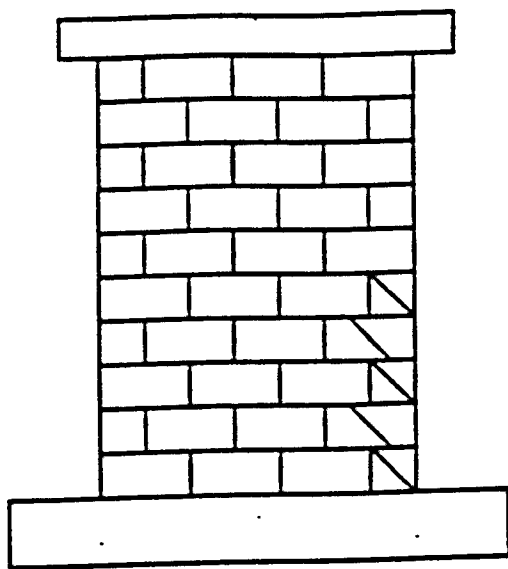
(c)



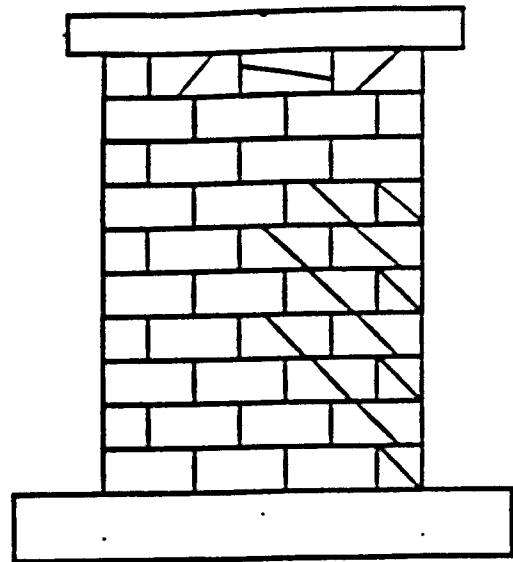
(d)

Figure 8. Deformed and fractured shear wall with cohesive joints after 10, 30, 90, and 100 time steps of  $10^{-4}$  seconds in (a)-(d). Bricks have an internal angle of  $30^\circ$ .

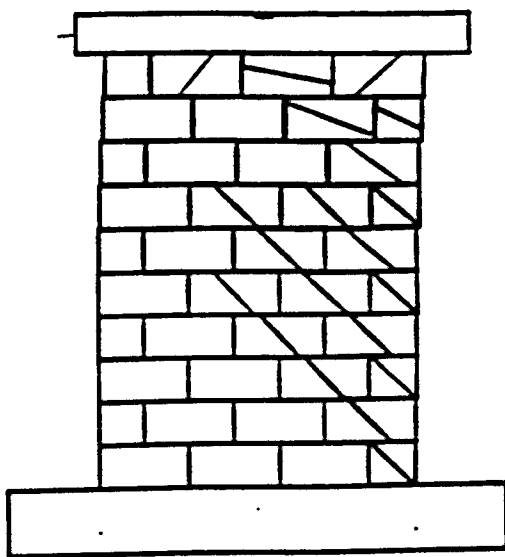




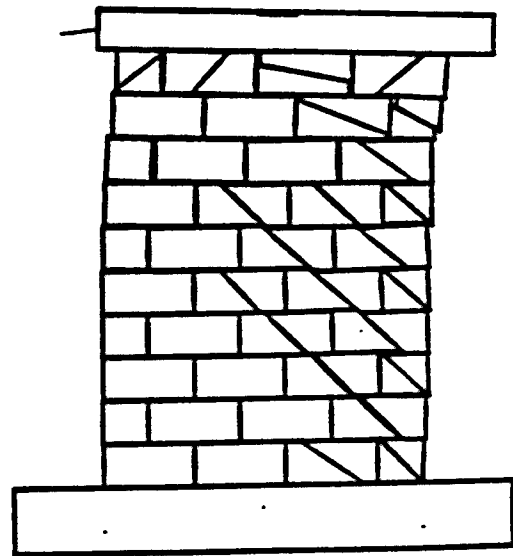
(a)



(b)



(c)



(d)

Figure 9. Deformed and fractured shear wall with cohesionless joints after 10, 22, 46, and 70 time steps of  $10^{-4}$  seconds in (a)-(d). Bricks are assumed to be frictionless.

Initial Penalty Number	Time Step (seconds)	Max. No. Iterations per Time Step	Residual Force Ratio ( $\epsilon$ ) (Eq. (17))
$1.84 \times 10^8$ lbs/ft ( $2.69 \times 10^3$ MN/m)	$1 \times 10^{-4}$	4	$\leq 0.1$

Figures 10(a)-(d) show the deformed and fractured shear wall with cohesionless joints after 10, 15, 30, and 50 time steps, respectively. It is clear here that cracking of the wall starts again at its right toe. More cracks develop from that area, and propagate upwards but not diagonally.

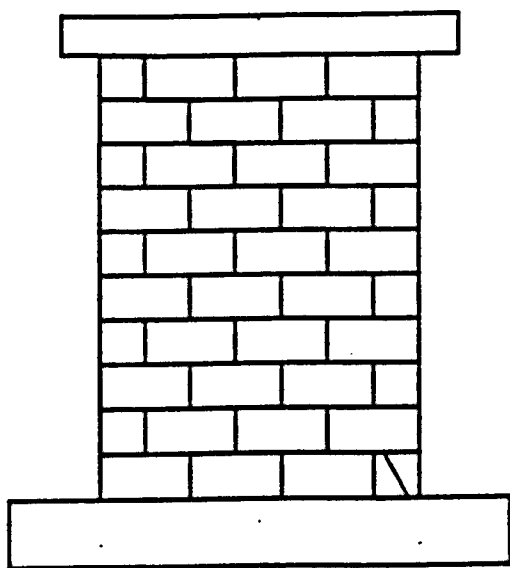
The use of the DDA method to study the fracture behavior of unreinforced masonry shear walls is still at the exploratory stage. The purpose of the above examples was to show how the DDA formulation could help in providing a better understanding of the behavior of unreinforced masonry structures at the field scale. The fracture modes shown in Figures 8, 9 and 10 are consistent with those observed in laboratory tests on masonry walls [14]. The numerical results also show that joint cohesion and brick internal friction have a significant effect on the deformation and fracturing of unreinforced masonry shear walls.

## Example 2

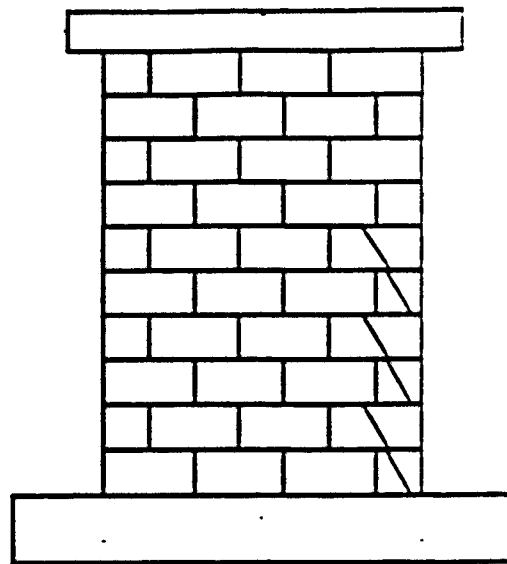
Consider now another 64 in. x 64 in. (162.6 cm x 162.6 cm) unreinforced masonry wall, as shown in Figure 11, which consists of 8 layers of bricks with 4 units per layer. The bricks are 16 in. x 8 in. (40.6 cm x 20.3 cm) in size. The shear wall sits on a fixed base and has a 80 in. x 8 in. (203.2 cm x 20.3 cm) beam on top. In order to avoid any rotation of the beam, a fixed top is placed on top of the wall, as shown in Figure 11. A horizontal point load of 45 kips (0.2 MN) is applied from left to right on the beam and a total vertical downward load of 78 kips (0.35 MN) is placed on top of the beam. The wall and the beam have a Young's Modulus  $E = 7.2 \times 10^8$  psf (34,470 MPa) and a Poisson's ratio  $\nu = 0.16$ . The bricks have a unit weight  $\gamma = 150$  pcf ( $2.36 \times 10^{-2}$  MN/m<sup>3</sup>), a compressive yield stress  $f_0 = 1.44 \times 10^5$  psf (6.89 MPa), and a compressive strength  $f_m = 2.88 \times 10^5$  psf (13.8 MPa). The brick joints have a uniform joint friction angle of  $38.3^\circ$  and a cohesion of 3.07 kips/ft (0.045 MN/m). All the material properties were obtained from the paper by Lotfi and Shing [14] for the purpose of comparison.

The beam, the fixed base and the fixed top are represented by one DDA block each. Also, each brick is represented by one DDA block. No sub-blocks are used in this example. All the bricks are non-breakable.

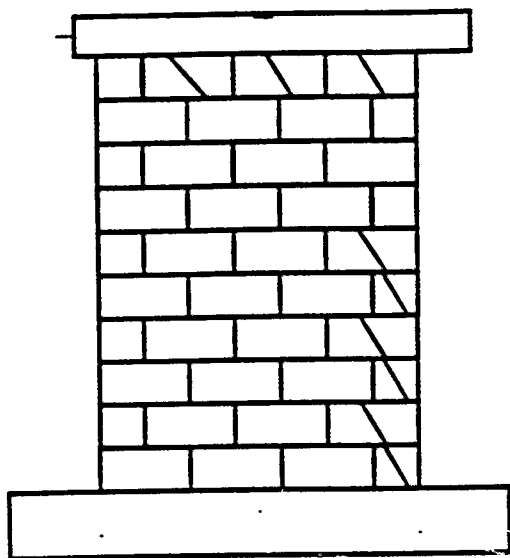
The DDA program was run with the following specifications:



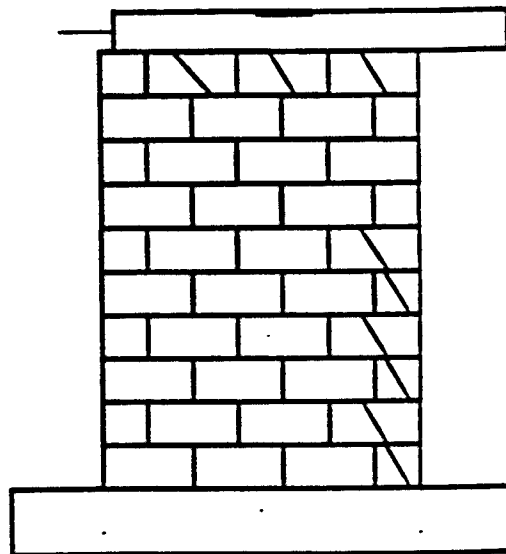
(a)



(b)



(c)



(d)

Figure 10. Deformed and fractured shear wall with cohesionless joints after 10, 15, 30, and 50 time steps of  $10^{-4}$  seconds in (a)-(d).

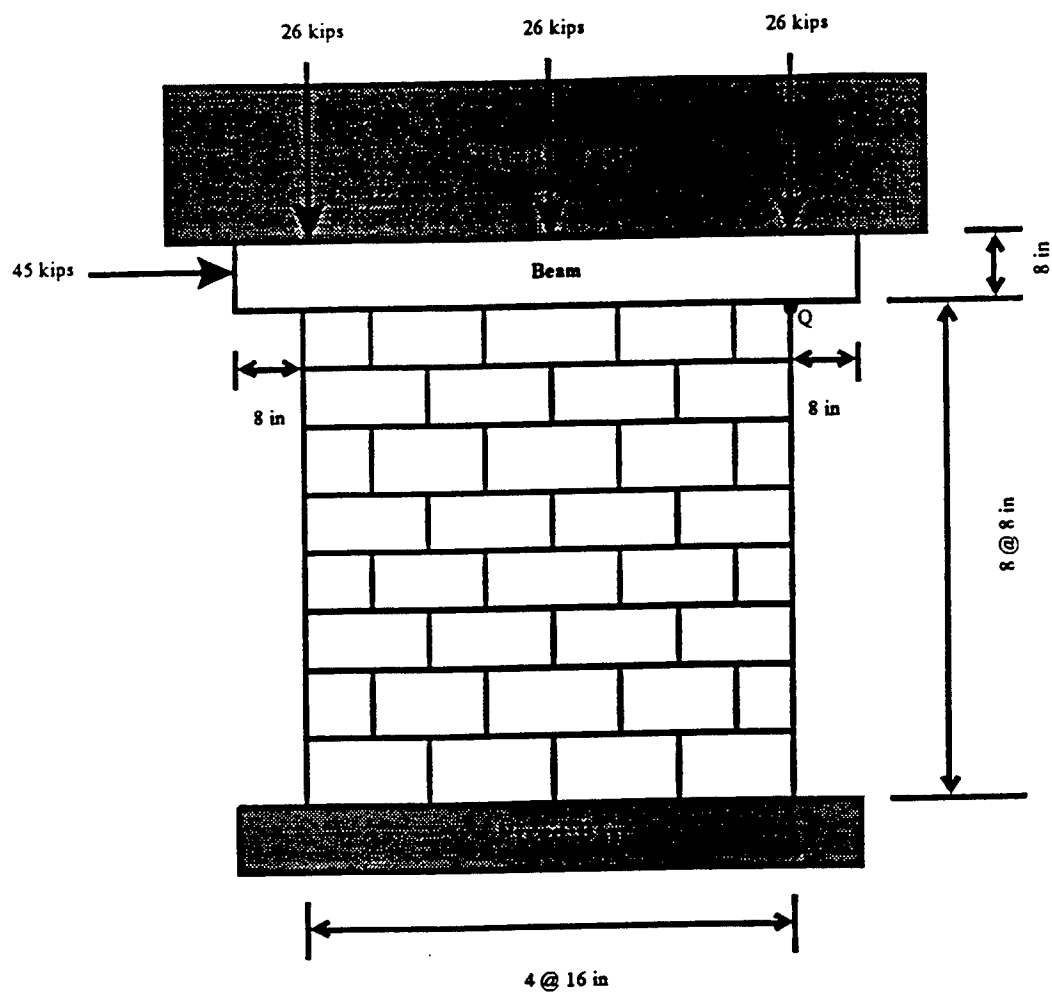


Figure 11. Initial configuration of a shear wall with a total vertical load of 78 kips(0.35 MN) and a horizontal load of 45 kips (0.20 MN).

Initial Penalty Number	Time Step (seconds)	Max. No. Iterations per Time Step	Residual Force Ratio ( $\epsilon$ ) (Eq. (17))
$7.2 \times 10^{10}$ lbs/ft ( $1.05 \times 10^3$ MN/m)	$1 \times 10^{-4}$	2	$\leq 0.1$

Figure 12(a) shows the distribution of the minor principal stress  $\sigma_3$  over the wall after 100 time steps. It is clear that the crushing areas of the masonry wall (where the minor principal stress  $\sigma_3$  exceeds  $f_m$ ) are in the upper left hand and lower right hand corners. This figure also shows that the yielding area of the masonry wall (where the minor principal stress  $\sigma_3$  exceeds  $f_0$ ) is over a diagonal band stretching from the upper left hand corner to the lower right hand corner of the wall. The crushing and yielding patterns are consistent with the experimental results of Lotfi and Shing [14], as shown in Figure 12(b).

Using the DDA analysis, the predicted horizontal displacement at point Q in Figure 11 is 2.63 in. (6.68 cm) which is not consistent with the experimental value of 0.12 in. (0.3 cm) obtained by Lotfi and Shing [14]. One possible explanation for this discrepancy is that in the DDA model the joint behavior is relatively simple. In contrast, other numerical methods used for masonry use a more complex arrangement of normal and tangential springs and dashpots such as shown in Figure 13 [26].

In this shear wall example, the shear behavior of mortar joints needs to be simulated by tangential springs (and even by dashpots when creeping behavior is studied) and the normal behavior of tensile debonding also needs to be included. Therefore, sliding along the mortar joints can be highly reduced and the accuracy of the predicted displacement at point Q can be improved.

Given the blocky nature of masonry, the DDA method seems to have, in its current formulation, many features which would be highly desirable for the stability analysis of masonry structures. In particular, compared to the FEM method, it can handle in a more straight forward manner the geometric changes in the physical model as blocks yield and crack and interfaces slide. On the other hand, the finite element method requires updating and reformulation of the structural stiffness matrix to account for physical changes in the structure. Since DEM methods emphasize block contacts, many of the problems encountered with the FEM can be eliminated.

To be considered as a viable alternative method to the FEM for masonry applications, the DDA method would have to be modified to include more capabilities. Some of these modifications could provide the basis for further research:

(i) The method should be able to model (1) interface normal behavior such as tensile debonding, interface opening and closing, (2) interface shear behavior in the pre-and post-peak regions, and (3) interface damage during monotonic or cyclic loading, which have been observed in various laboratory experiments [22, 27, 28, 29, 30].

(ii) The method should be able to model fracturing, yielding and cracking of the block

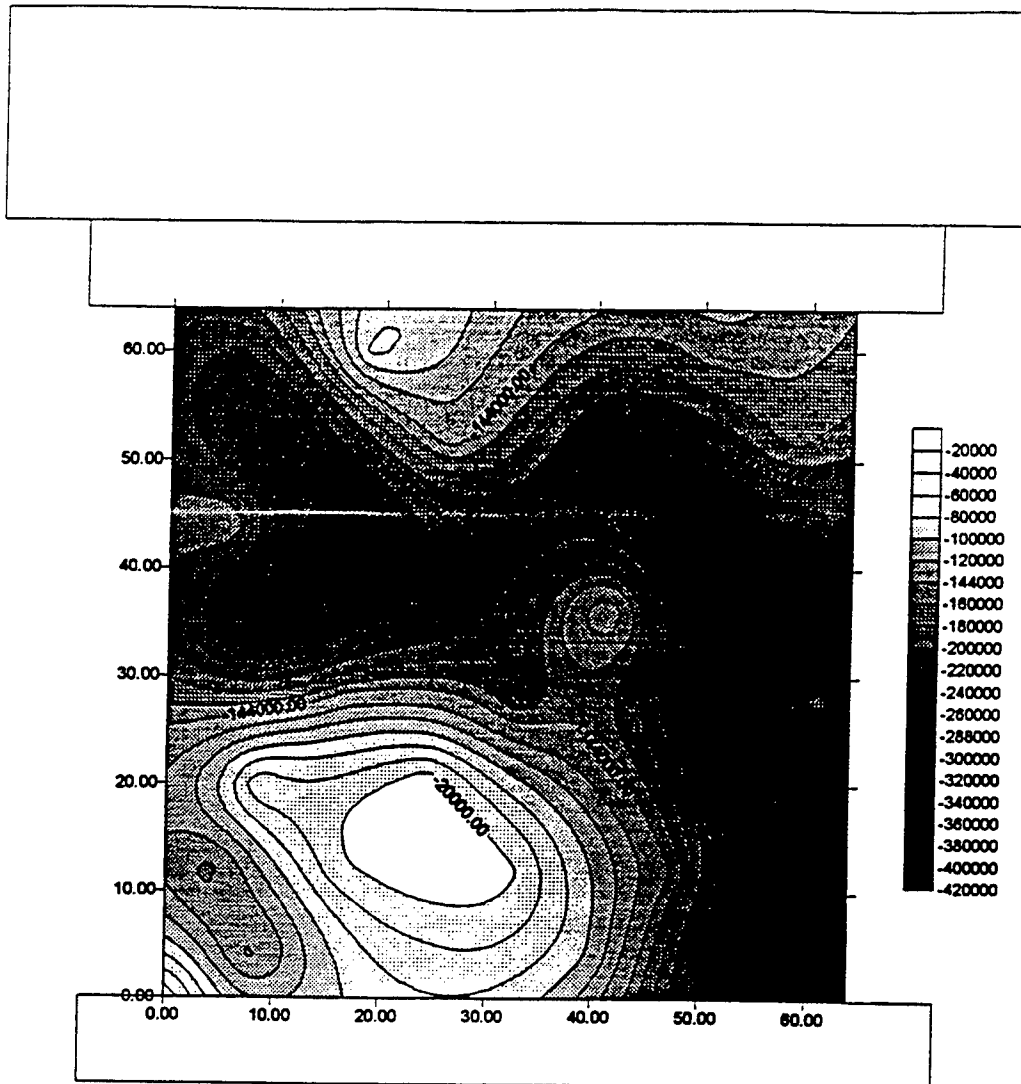


Figure12(a). Contour plot of  $\sigma_3$  (in psf) over a masonry shear wall.

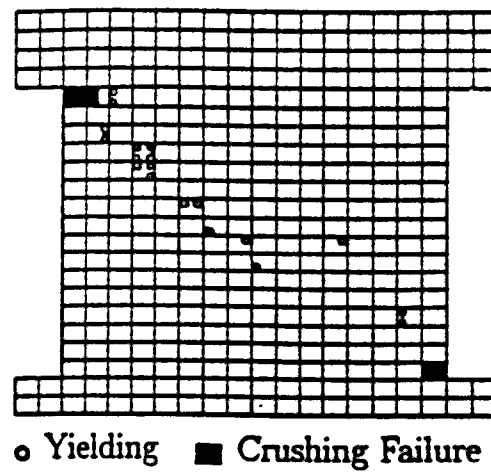


Figure12(b). Final yielding and crushing patterns over a masonry wall from Lotfi and Shing (1994).

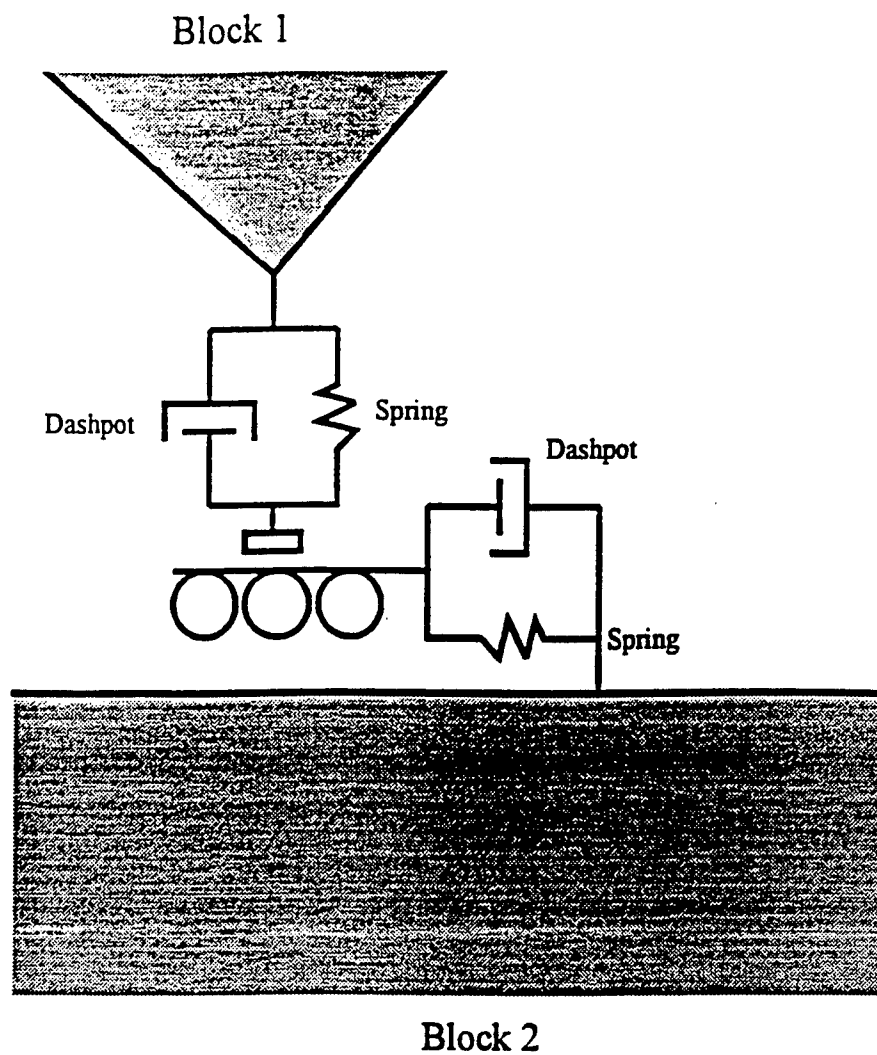


Figure13. Numerical joint modeling for block contact (after Ting et al. 1993).



elements and in particular how cracks, initiated in block elements, interact with existing masonry interfaces.

(iii) The method should be able to account for load changes as a function of time and to model the response of masonry to displacement and load control loading modes. This is particularly important when analyzing laboratory tests on structural elements.

(iv) The method should be able to model the effect of cyclic loading which is very important for the stability of masonry structures in earthquake areas.

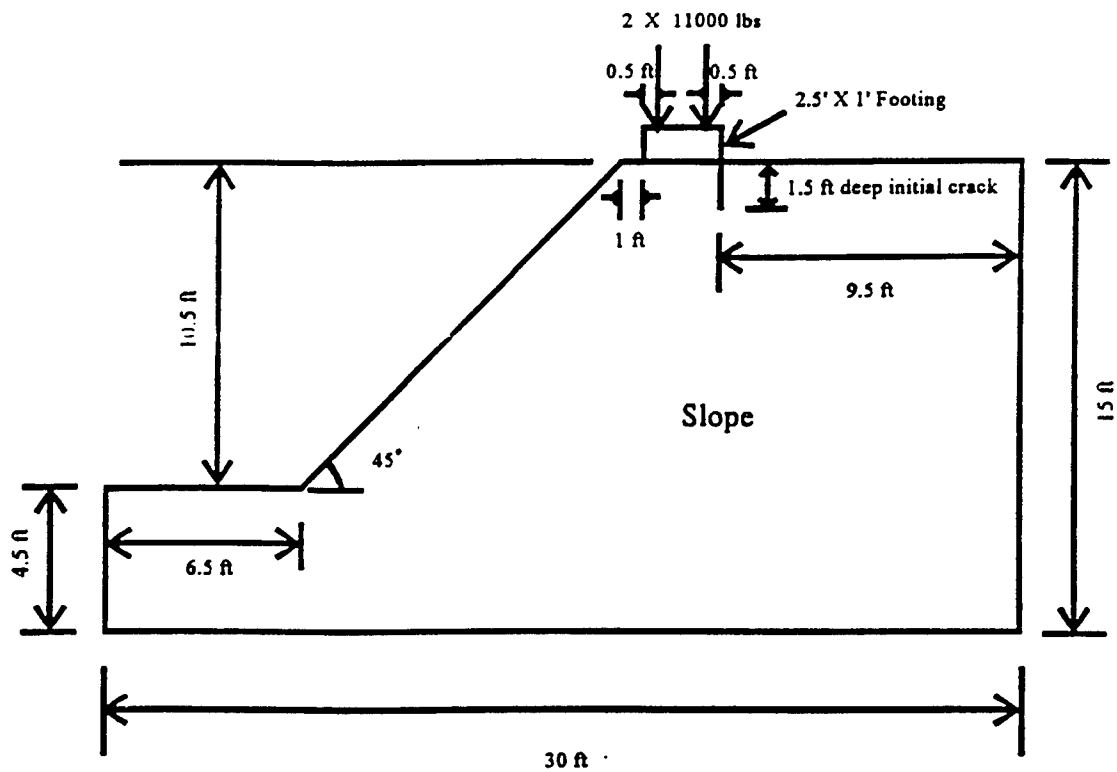
(v) The method should be able to model the effect of reinforcement which is important for modern masonry structures and older masonry structures that have been retrofitted. Methods of reinforcement such as grout injection, installation of reinforcing steel, and prestressing are of particular interest to engineers interested in structural masonry.

## Modeling slope stability

Gravity can cause instability in natural slopes, in slopes formed by excavation and in slopes of earth dams and embankments. Slope failure can be of three major types : rotational (circular or noncircular) slip, translational slip and compound slip. In classical soil mechanics, slope stability analysis is usually conducted using limiting equilibrium methods. Various techniques are available such as the Fellenius method, the Bishop method, the Morgenstern method, etc. .... [31]. Numerical approaches using the FEM method have also been used. These often incorporate a complex criterion, such as a visco-plastic model [32] or an elasto-plastic model [33, 34, 35] to analyze slope failure. The example presented below is used to show how the enhanced DDA method can predict rotational slip in slopes with homogeneous properties. It is also used to demonstrate the sub-blocking capability.

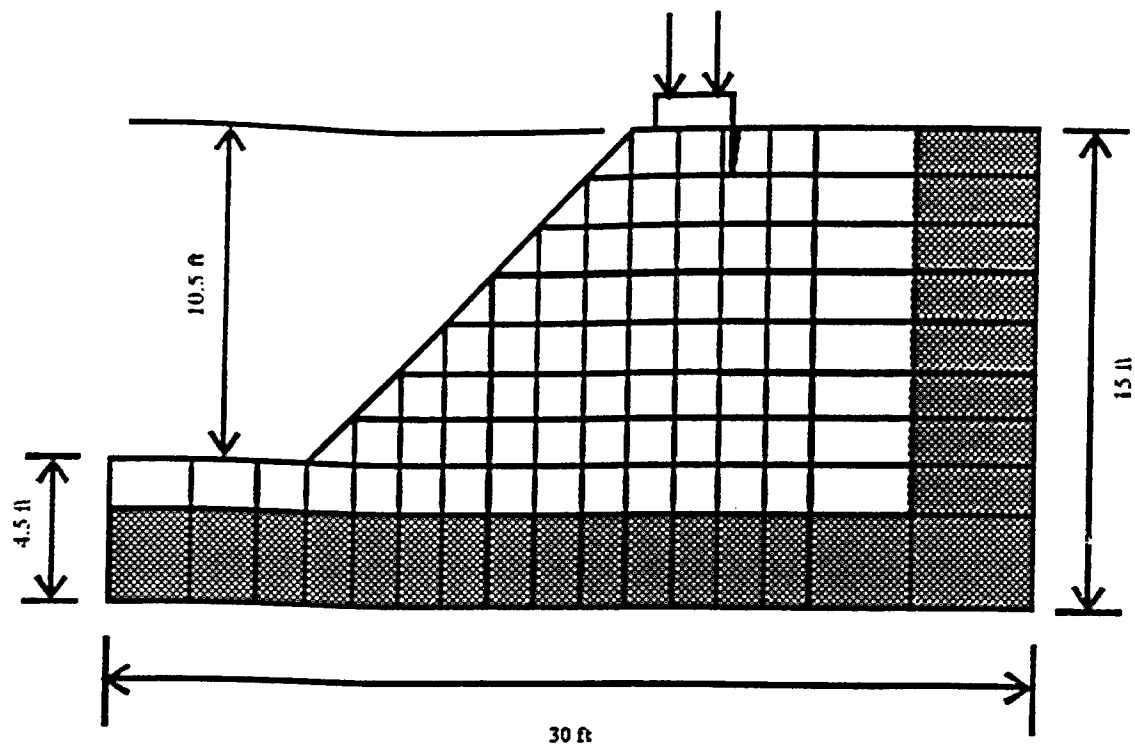
Consider a footing resting at the crest of a 10.5 ft (3.2 m) high slope with an angle of 45 degrees (Figure 14). A 1.5 ft (0.46 m) deep initial tension crack is located along the right side of the footing. Two vertical loads of 11 kips ( $4.9 \times 10^2$  MN) each are applied on the footing. The material in the slope is assumed to be homogeneous with a Young's Modulus  $E=1 \times 10^8$  psf (4,800 MPa), a Poisson's ratio  $\nu=0.3$ , a unit weight  $\gamma=130$  pcf ( $2 \times 10^2$  MN/m<sup>3</sup>), an inherent shear strength (cohesion)  $s_0=1000$  psf ( $4.8 \times 10^2$  MPa), a very high tensile strength, and a friction angle of 26°. In selecting a high tensile strength, only shear failure was allowed to occur. When shear fracturing occurs, the fracturing plane passes through the cracking front and is inclined at  $+(\pi/4-\phi/2)$  with respect to the minimum principal stress  $\sigma_3$ . The footing was assumed to have the same elastic properties as the slope material. In the DDA analysis, the footing was represented by one non-breakable block. The slope was represented by one block divided into 103 sub-blocks; 24 of which were fixed in the horizontal and vertical directions (Figure 15). The contact between the footing and the slope, the initial crack and all subsequent cracks were given a friction angle of 30 degrees and zero cohesion.

For the example shown in Figure 15, the DDA program was run with the following specifications:



(a)

Figure14. Problem geometry. Slope with a 1.5 ft (0.46 m) deep tension initial crack and a footing. The footing, loaded by two vertical loads 11,000 lbs (48.9 kN) each, rests at the corner of the slope.



(b)

Figure15. Msh and initial configuration. The blocks in the shaded area are fixed.

Initial Penalty Number	Time Step (seconds)	Max. No. of Iterations per Time Step	Residual Force Ratio ( $\epsilon$ ) (Eq. (17))
$1 \times 10^7$ lbs/ft ( $1.46 \times 10^2$ MN/m)	$6 \times 10^{-4}$	14	$\leq 0.1$

Figures 16(a)-(f) show the trajectory of crack propagation and the fractured and deformed slope after 5, 11, 150, 250, 300 and 500 time steps, respectively. Loading of the footing results in having the crack propagate in a rotational manner. After 11 time steps, the foundation starts fracturing at the initial crack tip and the crack propagates towards the slope. The slope is then divided into two distinct sections. The upper section continues to slide downward along the newly created crack surface. Large displacements along the footing-slope contact and the rotational slip surface can be noticed. The results clearly demonstrate that the assumption of a rotational failure surface is valid in this case. This validation also provides further confidence in the capability of the enhanced DDA model and the sub-blocking feature. It also suggests that the new DDA method may be a useful tool in the analysis of a range of slope stability problems.

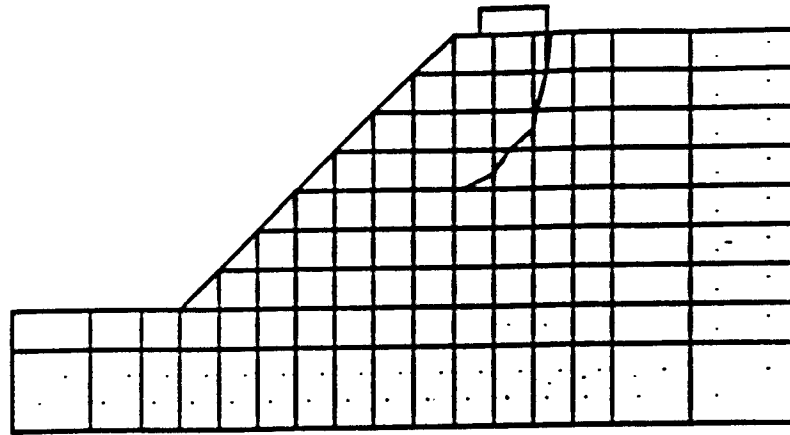
## Conclusions

Over the past three years, three major extensions to the DDA method have been implemented: (1) improvement of block contact, (2) calculation of stress distributions within blocks, and (3) block fracturing. Two numerical examples in this paper have shown that the modified DDA method with the three extensions is more applicable to a greater range of rock engineering problems than the original DDA method. More examples can be seen in Lin's thesis [2].

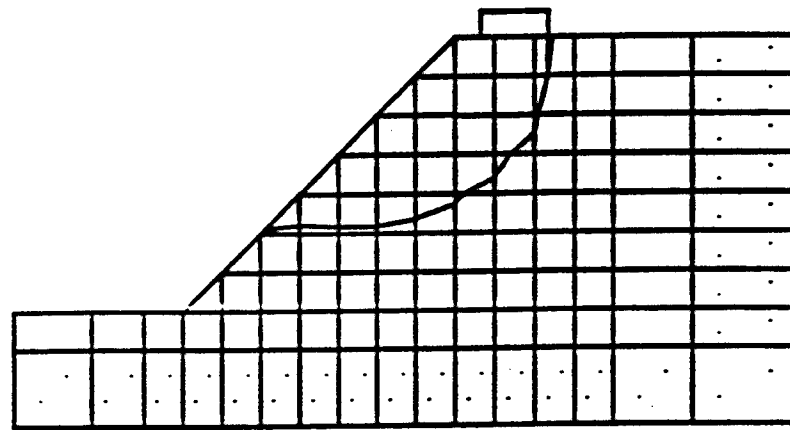
In the stability analysis of masonry structures, the DDA method can handle in a more straightforward manner than with the FEM method, the geometric changes observed in physical models as blocks yield and crack and slide along their interfaces. The DDA results showed that joint cohesion and brick internal friction have a significant effect on the deformation and fracturing of unreinforced masonry shear walls.

In modeling slope stability, the DDA sub-block analysis clearly demonstrates that not only the assumption of a rotational failure surface, which has been made by many researchers before, is valid, but also that large displacements along the footing-slope contact and the rotational slip surface can be captured.

In the near future development of the manifold method, extensions of (1) and (3) are to be implemented in the program to enhance the method to be more applicable to a greater range of rock mechanics problems and other engineering problems involving blocky systems.

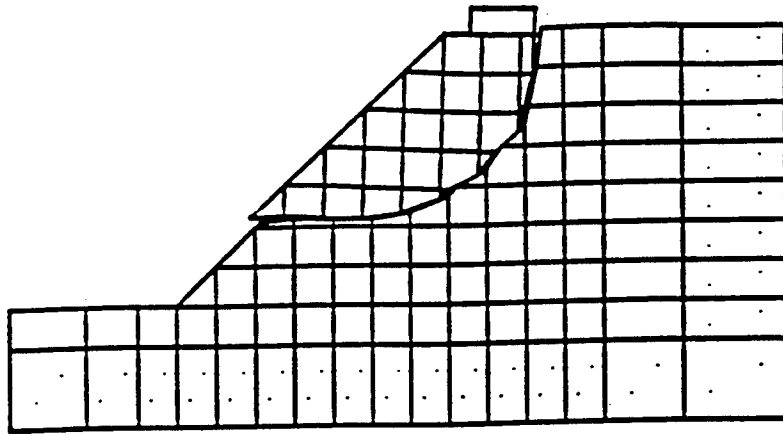


(a)

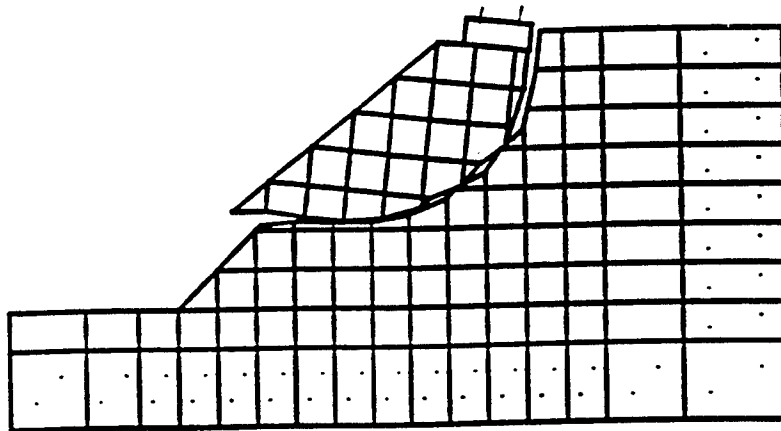


(b)

Figure16. Fractured slope after 5 and 11 time steps in (a) and (b).

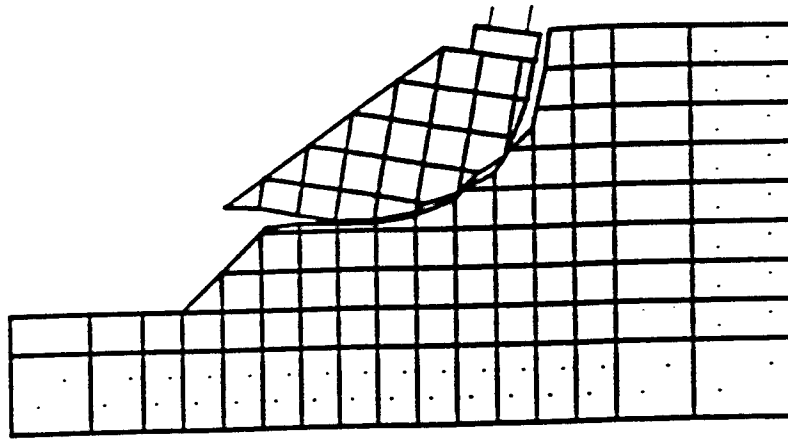


(c)

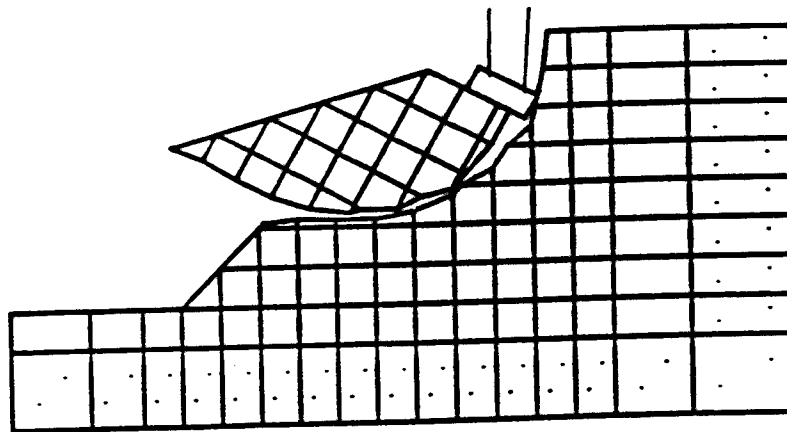


(d)

Figure16. Fractured slope after 150 and 250 time steps in (c) and (d).



(e)



(f)

Figure16. Fractured slope after 300 and 500 time steps in (e) and (f).

## References

1. Shi, G-H (1991) "Manifold method of material analysis." *Proceedings of Ninth Army Conference on Applied Mathematics and Computing*, June 18-21, Minneapolis, Minnesota.
2. Lin, C. T. (1995) "Extensions to the Discontinuous Deformation Analysis for jointed rock masses and other blocky systems." Ph.D thesis, University of Colorado, Boulder.
3. Campbell, J. S. (1974) "A penalty function approach to the minimization of quadratic functions in finite element analysis." *Proceedings of Finite Elements in Engineering*, University of South Wales.
4. Felippa, C. A. (1978) "Iterative procedures for improving penalty function solutions of algebraic systems." *International Journal of Numerical Methods in Engineering*, 12, pp. 821-836.
5. Felippa, C. A. (1986) "Penalty-function iterative procedures for mixed finite element formulations." *International Journal of Numerical Methods in Engineering*, 22, pp. 267-279.
6. Zienkiewicz, O. C., Li, Xi-Kui, and Nakasawa, S. (1984) "Iterative solution of mixed problems and the stress recovery procedures." Report C/R476/84, Institute for Numerical Methods in Engineering, Univ. College of Swansea, Wales, U. K.
7. Landers, J. A., and Taylor, R. L. (1986) "An Augmented Lagrangian Formulation for the Finite Element solution of contact problems." *Naval Civil Engineering Laboratory*, Port Hueneme, CA, Technical Report CR 86.008.
8. Shi, G-H (1988) "Discontinuous Deformation Analysis : a new numerical model for the statics and dynamics of block systems." PhD thesis, University of California, Berkeley.
9. Kanninen, M. F., and Popelar, C. H. (1985) "Advanced fracture mechanics." Oxford University Press, New York.
10. Arya, S. K., and Hegemier, G. A. (1978) "On nonlinear response prediction of concrete masonry assemblies." *Proceedings of North America Masonry Conference*, Masonry Society, Boulder, Colorado, 19.1-19.24.
11. Ali, S. S., and Page, A. W. (1988) "Finite element model for masonry subjected to concentrated loads." *Journal of Structural Engineering*, ASCE, 114(8), pp.1716-1784.
12. Lotfi, H. R., and Shing, P. B. (1991) "An appraisal of smeared crack models for masonry shear wall analysis." *Computers and Structures*, 41(3), pp. 413-425.
13. Lotfi, H. R., (1992) "Finite element analysis of fracture of concrete and masonry structures." PhD thesis, University of Colorado, Boulder.
14. Lotfi, H. R., and Shing, P. B. (1994) "Interface model applied to fracture of masonry structures." *Journal of Structural Engineering*, Vol. 120, No.1, pp. 63-80.
15. Rots, J. G. (1991) "Numerical simulation of cracking in structural masonry." *HERON*, 36(2), pp. 49-63.
16. Rots, J. G., and Lourenco, P. B. (1993) "Fracture simulation of masonry using non-linear interface elements." *Proceedings of 6th North America Masonry Conference*, pp. 983-993.
17. Dialer, C., and Karaca, M. (1993) "Application of DEM to problems in rock mechanics, structural engineering, and material testing." *Proceedings of 2nd International Conference on Discrete Element Methods*, MIT.
18. Dialer, C. (1992) "A Distinct Element approach for the deformation behavior of shear stressed masonry walls." *Proceedings of 6th Canadian Masonry Symposium*, Saskatoon.
19. Melbourne, C., and Gilbert, M. (1994) "The application of limit analysis techniques to masonry arch bridges." *Proceedings of 10th International Brick, Block, and Masonry Conference*, Calgary, pp. 359-368.



20. Melbourne, C., Gilbert, M., and Wagstaff, M. (1994) "The behavior of single and multi-span brickwork arch bridges." *Proceedings of 10th International Brick, Block, and Masonry Conference*, Calgary, pp. 339-347.
21. Middleton, J., Pande, G. N. (1991) "Computer methods in structural engineering." *International Symposium on Computer Methods in Structural Masonry*, Swansea, U. K.
22. Atkinson, R. H., Amadei, B., Saeb, S., and Sture S. (1989) "Response of masonry bed joints in direct shear." *Journal of Structural Engineering*, ASCE, Vol. 115, No. 9, pp. 2276-2296.
23. Meli, R. (1973) "Behavior of masonry walls under lateral loads." *Proceedings of 5th World Congress on Earthquake Engineering*, pp. 853-862.
24. Sinha, B. P., and Hendry, A. W. (1969) "Racking tests on Storey-height shear wall structures with openings, subjected to precompression." *Proceedings of International Conference on Masonry Structural Systems*, University of Austin, Texas, pp. 192-199.
25. Dawe, J. L., and McBride, R. T. (1985) "Experimental investigation of the shear resistance of masonry panels in steel frames." *Proceedings of 7th International Brick Masonry Conference*, Melbourne, Australia, Feb.
26. Ting, J. M., Khwaja, M., Meachum L. R., and Rowell J. D. (1993) "An ellipse-based discrete element model for granular materials." *International Journal for Numerical and Analytical Methods in Geomechanics*, Vol. 17, pp. 603-623.
27. Hegemeier, G. A. et al. (1978) "On the behavior of joints in concrete masonry." *Proceedings of North America Masonry Conference*, Boulder, Colorado.
28. Nuss, L. K., Noland, J. L., and Chinn, J. (1978) "The parameters in influencing shear strength between clay masonry units and mortar." *Proceedings of North America Masonry Conference*, Boulder, Colorado.
29. Drysdale, R. G., Vanderkeyl, R. V., and Hamid, A. A. (1979) "Shear strength of brick masonry joints." *Proceedings of 5th International Brick Masonry Conference*, Paper II-3, Washington DC, 1979.
30. Pook, R. L., Stylianou, M. A., and Dawe, J. L. (1986) "Experimental investigation of the influence of compression on the shear strength of masonry joints." *Proceedings of 4th Canada Masonry Symposium*, Fredericton, Canada.
31. Lambe, T. W., and Whitman, R. V. (1979) "Soil Mechanics, SI version." Wiley, New York.
32. Zienkiewicz, O. C., and Pande, G. N. (1977) "Time-dependent multilaminate model of rocks- a numerical study of deformation and failure of rock masses." *International Journal for Numerical and Analytical Methods in Geomechanics*, Vol. 1, pp. 219-247.
33. Prevost, J. H. (1984) "Localization of deformations in elastic-plastic solids." *International Journal for Numerical and Analytical Methods in Geomechanics*, Vol. 8, pp. 187-196.
34. Rowe, R. K., and Mylleville, B. L. J. (1993) "The stability of embankments reinforced with steel." *Canadian Geotechnical Journal*, Vol. 30, pp. 768-780.
35. Zienkiewicz, O. C., and Huang, M. (1995) "Localization problems in plasticity using finite elements with adaptive remeshing." *International Journal for Numerical and Analytical Methods in Geomechanics*, Vol. 19, pp. 127-148.

# **Manifold Method Application: Tunnel Roof Deflection**

Mary M. MacLaughlin

Department of Civil Engineering, University of California, Berkeley, CA 94720

## **Abstract**

The Manifold Method is applied to the problem of roof deflection in a tunnel through horizontally layered rock. In this problem, the roof is modeled first as a single beam and then as a two-layer system, with a thin beam overlying a thicker one. Analytical solutions are available for both cases. The Manifold Method results compare reasonably well with the analytical solutions. A cracked beam was also analyzed to show qualitatively that the deflections are greater than those of an intact beam.

## **Introduction**

The Manifold Method is a numerical method recently developed by Dr. Gen-hua Shi to model material behavior (Shi, 1992). The material may be deformable and may contain discontinuities. The domain of interest is modeled with a physical mesh and any number of mathematical meshes. The physical mesh, which consists of the boundaries and internal discontinuities of the material, defines the limits of the integration zones. The mathematical meshes are used to describe the behavior of the material within each integration zone. The details of the numerical aspects of the method are available elsewhere (Shi, 1991).

The current computer implementation of the method consists of a finite element type of mathematical mesh comprised of  $60^\circ$  constant strain triangles, with displacements along the discontinuities modeled according to the discontinuous deformation analysis method (Shi, 1993).

The ability to model both material deformability and displacements along discontinuities within the material makes the manifold method particularly appealing for modeling geologic materials, which are deformable and for the most part inherently discontinuous. In this study the method is applied to the problem of roof deflection in a tunnel through horizontally layered rock. The roof is modeled first as a single beam and then as a two-layer system, with a thin beam overlying a thicker one. A cracked beam is also analyzed to show qualitatively that the deflections are greater than those of an intact beam.

## Case 1: Beam Bending

Analytical solutions are available for the case of beam deflection under self-weight, for which (Lindeburg, 1980). Three boundary conditions were analyzed: clamped, pinned, and cantilever. The beam dimensions were 40 m long and 4 m thick. The mesh configuration used has two rows of triangular elements within the beam (Figure 1). The material parameters used are as follows:

Young's modulus:	$E = 4800000 \text{ kPa}$	Mass density:	$\rho = 2580 \text{ kg/m}^3$
Poisson's ratio:	$\nu = .25$	Unit weight:	$\gamma = 25.3 \text{ kN/m}^3$

The results are summarized in Table I. The solution computed by the manifold method are lower than the analytical solution, but equivalent to finite element solutions using constant strain triangles (Zienkiewicz, 1977).

**Table I.** Comparison of Analytical and Manifold Method solutions for deflection at the midpoint (clamped and pinned) or the end of the beam (cantilever).

<u>Beam Type</u>	<u>Analytical Solution</u>	<u>Manifold Method</u>
Clamped	.026 m	.010 m
Pinned	.132 m	.014 m
Cantilever	1.265 m	.258 m

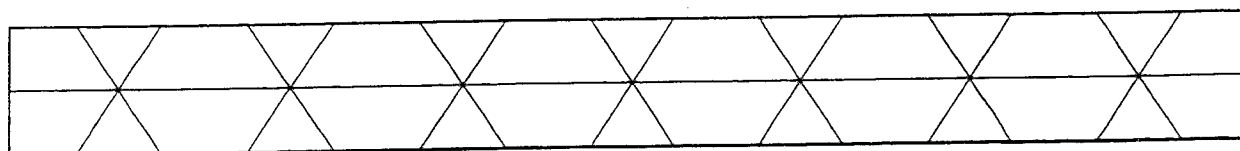


Figure 1: Beam configuration analyzed for Case 1.

## Case 2: Two-Layer System

The second problem analysed is the case of a thin layer overlying a thick layer, which also has an analytical solution (Goodman, 1989). The solution assumes that the beams are clamped. The length of the beams is 40 m and the thicknesses for the upper layer and the lower layer are 2 and 4 m, respectively. The material parameters are the same as those used for Case 1 above. The geometry is shown in Figure 2. Although the computed solution (.012) deviates from the analytical solution (.035), it is approximately 20 to 30% greater than the solution for the deflection of the lower layer alone (which indicates that there is a load transfer from the upper layer to the lower) as predicted by the analytical solution.

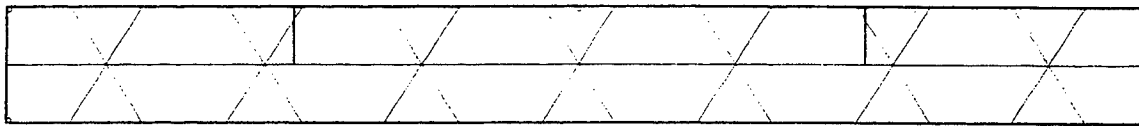


Figure 2: Beam configuration analyzed for Case 2.

## Case 3: Cracked Beam

The Manifold Method is also capable of modelling a material which contains discontinuities. This feature was used to model a 40 m long by 4 m thick beam containing several cracks. Again, the material parameters are the same as those for Case 1. The deformed configuration is shown in Figure 3. The calculated deflection ( $x$ ) is greater than that of an intact beam (.026 m).

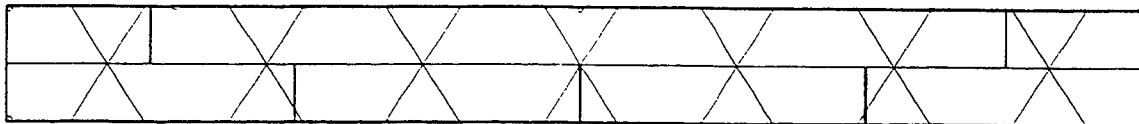


Figure 3

## REFERENCES

- Goodman, Richard E. (1989). *Introduction to Rock Mechanics, Second Edition*, John Wiley & Sons, New York, 562 pp.
- Lindeburg, Michael R. (1982). *Engineer in Training Review Manual, Sixth Edition*, Professional Publications Inc., Belmont, California, 520 pp.
- Shi, Gen-hua (1991). "Manifold Method of Material Analysis," *Transactions of the Ninth Army Conference on Applied Mathematics and Computing*, pp. 51-76.
- Shi, Gen-hua (1992). "Modelling Rock Joints and Blocks by Manifold Method," *Proceedings of the 33rd U.S. Symposium on Rock Joints*, pp. 639-648.
- Shi, Gen-hua (1993). *Block System Modeling by Discontinuous Deformation Analysis*, Computational Mechanics Publications, London, England, 209 pp.
- Zienkiewicz, O.C. (1977). *The Finite Element Method, Third Edition*, McGraw Hill Book Company Limited, London, 787 pp.

# REPORT DOCUMENTATION PAGE

Form Approved  
OMB No. 0704-0188

Public reporting burden for this collection of information is estimated to average 1 hour per response, including the time for reviewing instructions, searching existing data sources, gathering and maintaining the data needed, and completing and reviewing the collection of information. Send comments regarding this burden estimate or any other aspect of this collection of information, including suggestions for reducing this burden, to Washington Headquarters Services, Directorate for Information Operations and Reports, 1215 Jefferson Davis Highway, Suite 1204, Arlington, VA 22202-4302, and to the Office of Management and Budget, Paperwork Reduction Project (0704-0188), Washington, DC 20503.

1. AGENCY USE ONLY (Leave blank)		2. REPORT DATE August 1997	3. REPORT TYPE AND DATES COVERED Volume 1 of 2	
4. TITLE AND SUBTITLE Working Forum on the Manifold Method of Material Analysis, Volume I			5. FUNDING NUMBERS Work Units 33286 and 31700	
6. AUTHOR(S)				
7. PERFORMING ORGANIZATION NAME(S) AND ADDRESS(ES) U.S. Army Engineer Waterways Experiment Station 3909 Halls Ferry Road, Vicksburg, MS 39180-6199			8. PERFORMING ORGANIZATION REPORT NUMBER Miscellaneous Paper GL-97-17	
9. SPONSORING/MONITORING AGENCY NAME(S) AND ADDRESS(ES) U.S. Army Corps of Engineers Washington, DC 20314-1000			10. SPONSORING/MONITORING AGENCY REPORT NUMBER	
11. SUPPLEMENTARY NOTES Available from National Technical Information Service, 5285 Port Royal Road, Springfield, VA 22161.				
12a. DISTRIBUTION/AVAILABILITY STATEMENT Approved for public release; distribution is unlimited.			12b. DISTRIBUTION CODE	
13. ABSTRACT (Maximum 200 words)  Volume I of the "Working Forum on the Manifold Method of Material Analysis" contains papers presented by leading researchers on the subject of the numerical manifold method. The emphasis of each of the authors represents a different approach to extending the state of the art. Volume II presents the theoretical development of the numerical manifold and the simplex integration methods by Dr. Gen-hua Shi, the originator of both methods.				
14. SUBJECT TERMS Case studies                      Large deformations Continuum                        Numerical manifold Discontinuum                  Simplex integration Jointed rock			15. NUMBER OF PAGES 252	
			16. PRICE CODE	
17. SECURITY CLASSIFICATION OF REPORT UNCLASSIFIED	18. SECURITY CLASSIFICATION OF THIS PAGE UNCLASSIFIED	19. SECURITY CLASSIFICATION OF ABSTRACT	20. LIMITATION OF ABSTRACT	

AD NUMBER	DATE	DTIC ACCESSION NOTICE
1. REPORT IDENTIFYING INFORMATION		<b>REQUE</b> 1. Put you on reve 2. Comple 3. Attach maillec 4. Use ur. inform 5. Do not for 6  <b>DTIC:</b> 1. Assig 2. Retui
A. ORIGINATING AGENCY USAE WES		
B. REPORT TITLE AND/OR NUMBER MP-GL-97-17; VOLUME I		
C. MONITOR REPORT NUMBER		
D. PREPARED UNDER CONTRACT NUMBER		
2. DISTRIBUTION STATEMENT Approved for public release; Distribution is unlimited.		

DTIC Form 50  
DEC 91

PREVIOUS EDITIONS ARE OBSOLETE